



HAL
open science

Synthesis of ligand-functionalized core-cross-linked amphiphilic star block copolymers and application as catalytic nanoreactors

Hui Wang

► **To cite this version:**

Hui Wang. Synthesis of ligand-functionalized core-cross-linked amphiphilic star block copolymers and application as catalytic nanoreactors. Catalysis. Université Paul Sabatier - Toulouse III, 2021. English. NNT: 2021TOU30203 . tel-03677370

HAL Id: tel-03677370

<https://theses.hal.science/tel-03677370>

Submitted on 24 May 2022

HAL is a multi-disciplinary open access archive for the deposit and dissemination of scientific research documents, whether they are published or not. The documents may come from teaching and research institutions in France or abroad, or from public or private research centers.

L'archive ouverte pluridisciplinaire **HAL**, est destinée au dépôt et à la diffusion de documents scientifiques de niveau recherche, publiés ou non, émanant des établissements d'enseignement et de recherche français ou étrangers, des laboratoires publics ou privés.



THÈSE

En vue de l'obtention du
DOCTORAT DE L'UNIVERSITÉ DE TOULOUSE
Délivré par l'Université Toulouse 3 - Paul Sabatier

Présentée et soutenue par
HUI WANG

Le 9 novembre 2021

**Synthesis of ligand-functionalized core-cross-linked amphiphilic
star block copolymers and application as catalytic nanoreactors**

Ecole doctorale : **SDM - SCIENCES DE LA MATIERE - Toulouse**

Spécialité : **Chimie Macromoléculaire et Supramoléculaire**

Unité de recherche :

LCC - Laboratoire de Chimie de Coordination

Thèse dirigée par

Rinaldo POLI

Jury

Mme Jutta Rieger, Rapporteur

M. Sébastien Tilloy, Rapporteur

Mme Audrey Denicourt Nowicki, Examinatrice

M. Mathias Destarac, Examineur

M. Eric Manoury, Examineur

M. Rinaldo Poli, Directeur de thèse

Abbreviations and symbols

(1) Symbols

D_z	Z-average size, intensity-weighted harmonic mean particle diameter
PDI	polydispersity index
M_w	weight-average molecular weight
M_n	number-average molecular weight
$M_{n,exp}$	experimental number-average molecular weight
$M_{n,th}$	theoretical number-average molecular weight
DP_n	degree of polymerization
s	singlet NMR peak
d	doublet NMR peak
t	triplet NMR peak
q	quadruplet NMR peak
m	multiplet NMR peak
br	broad NMR peak
\mathcal{D}	dispersity
dn/dc	specific refractive index increment

(2) Abbreviations

ATRP	atom transfer radical polymerization
CCM	core-crosslinked micelle
CCM-N	CCM with the neutral outer shell
CCM-C	CCM with the cationic outer shell
CCM-A	CCM with the anionic outer shell
CMC	critical micelle concentration
DLS	dynamic light scattering
GC	gas chromatography
HPLC	high performance liquid chromatography reagent
ICP-MS	inductively coupled plasma mass spectrometry
LCST	lower critical solution temperature

macroRAFT	macromolecular RAFT agent
NMR	nuclear magnetic resonance
NG	core-crosslinked nanogel
NPs	nanoparticles
PISA	polymerization induced self-assembly
ppm	part per million
RAFT	reversible addition-fragmentation chain transfer
rpm	revolutions per minute
SEC	size exclusion chromatography
TEM	transmission electron microscopy
TOF	turnover frequency
TON	turnover number

(3) Chemical compounds

AIBN	azobisisobutyronitrile
ACPA	4,4'-azobis(4-cyanopentanoic acid)
acac	acetylacetonato
BMOPPP	bis(<i>p</i> -methoxyphenyl) phenylphosphine
CTPPA	4-cyano-4-thiothiopropyl-sulfanyl pentanoic acid
CDCl ₃	deuteration chloroform
DMSO- <i>d</i> ₆	deuteration dimethyl sulfoxide
D ₂ O	deuteration water
DEGDMA	diethylene glycol dimethacrylate
DPSP	4-(diphenylphosphino) styrene
DMF	N,N-dimethylformamide
EGDMA	ethyl glycol dimethyl methacrylate
HCl	hydrochloric acid
KCl	potassium chloride
NaHCO ₃	sodium bicarbonate
NaNO ₃	sodium nitrate
NEt ₃	triethylamine
Me	methyl

MeCN	acetonitrile
MeI	iodomethane
MAA	methyl acrylic acid
LiBr	lithium bromide
PAA	polyacrylic acid
PEG	poly(ethylene glycol)
PEGMA	poly(ethylene glycol) methacrylate
PEO	poly(ethylene oxide)
PMAA	polymethacrylic acid
PEOMA	poly(ethylene oxide) methyl ether methacrylate
P4VP	poly(4-vinylpyridine)
P4VPMe ⁺ I ⁻	poly(1-methyl-4-vinylpyridinium iodide)
PSt	polystyrene
St	styrene
SS ⁻ Na ⁺	sodium 4-vinylbenzenesulfonate
TPP/PPh ₃	triphenylphosphine
TPPTS	tris(3-sodium sulfonatophenyl) phosphine
4VP	4-vinylpyridine

Table of contents

Abbreviations and symbols	1
Introduction	15
Chapter I Literature survey	21
I.1 Catalyst recovery in the liquid/liquid biphasic catalysis	25
I.1.1 Heterogenized homogeneous catalysts in liquid/liquid biphasic catalysis.....	28
I.2 Aqueous-organic biphasic catalysis	32
I.2.1 The development of aqueous biphasic catalysis	33
I.2.2 Heterogenized homogeneous catalysts in aqueous biphasic catalysis.....	35
I.3 Micellar-type aqueous biphasic catalysis	40
I.3.1 Micelle-aided catalysis	44
I.3.2 Crosslinked micelle-aided catalysis	50
I.4 Objectives and scope of the thesis	53
Chapter II Synthesis and characterization of core-shell amphiphilic nanoreactor with a polycationic shell	57
II.1 Introduction	58
II.2 RAFT polymerization of phosphine-free cationic-shell copolymer	65
II.2.1 Preliminary optimization studies	66
II.2.2 Optimized synthesis and characterization of the amphiphilic P4VPMe ⁺ I ⁻ - <i>b</i> -PSt macroRAFT latex	77
II.2.3 Crosslinking of the amphiphilic P4VPMe ⁺ I ⁻ - <i>b</i> -PSt copolymer with high molar mass PSt block.....	85
II.2.4 Synthesis of a P4VPMe ⁺ I ⁻ - <i>b</i> -PSt- <i>b</i> -P(St- <i>co</i> -DEGDMA) NG	96
II.3 RAFT polymerization of phosphine-functionalized cationic copolymer	102
II.4 Conclusion	115
Chapter III Coordination studies and molecular rhodium-catalyzed biphasic hydrogenations	117
III.1 Introduction	118
III.2 [RhCl(COD)]₂ precatalyst coordination and migration studies	121
III.3 Biphasic catalytic hydrogenations	124
III.3.1 Hydrogenation of styrene in 1-nonanol	125
III.3.2 Hydrogenation of neat styrene.....	135
III.3.3 Hydrogenation of 1-octene.....	137
III.4 Conclusion	139
Chapter IV Rhodium nanoparticles generation and catalyzed biphasic hydrogenations	140
IV.1 Introduction	141
IV.2 Generation of rhodium nanoparticles in the CCM-N polymers	144

IV.3	Generation of rhodium nanoparticles in the CCM-C polymers	150
IV.4	Catalyzed hydrogenation of acetophenone	151
IV.5	Catalyzed hydrogenation of styrene	158
IV.6	Catalyzed hydrogenation of 1-octene	168
IV.7	Conclusion	170
Chapter V Synthesis and characterization of anionic core-shell amphiphilic copolymer		172
V.1	Introduction	173
V.2	P(SS⁻Na⁺) macroRAFT	175
V.3	P(SS⁻Na⁺)-<i>b</i>-PSt diblock macroRAFT	177
V.4	Crosslinking of the amphiphilic PSS⁻Na⁺-<i>b</i>-PSt copolymer with high molar mass	
	PSt block	181
V.4.1	Crosslinking by DEGDMA in the presence of styrene	181
V.4.2	Crosslinking with pure DEGDMA	182
V.4.3	Completeness of the crosslinking step	187
V.5	Conclusion	191
Chapter VI Experimental section		192
VI.1	Materials and characterization	193
VI.1.1	Materials	193
VI.1.2	Characterization techniques	196
VI.2	Synthesis and characterization of core-shell amphiphilic nanoreactors with a polycationic shell	199
VI.2.1	Preliminary optimization studies on phosphine-free copolymers with a cationic P4VPMe ⁺ I ⁻ shell	199
VI.2.2	Preparation of phosphine-functionalized polymers with a cationic P4VPMe ⁺ I ⁻ shell	206
VI.3	RAFT synthesis of core-crosslinked micelles and nanogels with an anionic PSS⁻Na⁺ shell	210
VI.3.1	Preparation of phosphine-free polymer with an anionic PSS ⁻ Na ⁺ shell	210
VI.4	General procedure for Rh complexation to the phosphine ligand within CCM or NG core	212
VI.5	General procedure for molecular rhodium-catalyzed biphasic hydrogenations	212
VI.5.1	Hydrogenation of styrene or 1-octene in solvent	212
VI.5.2	Hydrogenation of neat styrene	213
VI.6	Rhodium nanoparticles generation and general procedure for biphasic hydrogenations	213
VI.6.1	General procedure for the synthesis of Rh nanoparticles within the nanoreactors	213
VI.6.2	General procedure for Rh nanoparticles synthesis from a homogeneous phase	214
VI.6.3	General procedure for the catalytic hydrogenation	215
Conclusions and perspectives		218
References		222

Annexes..... 240

Index of figures

Figure I.1.0	Illustration of the Pd@TRGO-g-PEtOx catalyst recycling by thermal switching between dispersion and sedimentation behavior	25
Figure I.1.1	Schematic illustration of the flow Pickering emulsion strategy for organic-aqueous biphasic catalysis reactions.	26
Figure I.1.2	Various implementations of liquid/liquid biphasic catalysis.	28
Figure I.2.1	Gas uptake plots from a ballast vessel for the hydroformylation of various alkenes in the absence (grey) and presence (black) of [OctMim]Br.	35
Figure I.3.1	Schematic representation of a core-shell catalytic nanoreactor self-assembly process and of the hydroaminomethylation application.	48
Figure I.3.2	Schematic representation of the synthesis of shell crosslinked micelles.	50
Figure I.3.3	Schematic representation of the synthesis of a poly(2-oxazoline) crosslinked micelles with a Co ^{III} -salen-functionalized core.	51
Figure II.1.1	Chemical formulas of used cationic monomers for RAFT polymerization.	65
Figure II.2.1	Poly(4-vinylpyridinium) copolymers.	67
Figure II.2.2	(a) Conversion vs. time curve for the RAFT polymerization of 4VP and (b) SEC chromatogram of the resulting R ₀ -4VP ₅₆ -SC(S)SPr.	68
Figure II.2.3	¹ H NMR spectra in DMSO- <i>d</i> ₆ of (a) R ₀ -4VP ₅₆ -SC(S)SPr at the end of the polymerization and (b) isolated R ₀ -(4VPMe ⁺ I) ₅₆ -SC(S)SPr macroRAFT.	68
Figure II.2.4	¹ H NMR spectra in DMSO- <i>d</i> ₆ of the products obtained from the hydrolysis of DMF in water promoted by (a) HI and (b) MeI.	70
Figure II.2.5	(a) Conversion vs. time curve for RAFT polymerization of styrene in H ₂ O/EtOH using the R ₀ -4VP ₅₆ -SC(S)SPr macroRAFT agent and (b) SEC chromatograms for the R ₀ -4VP ₅₆ -SC(S)SPr macroRAFT and the R ₀ -4VP ₅₆ - <i>b</i> -St ₂₄₇ -SC(S)SPr copolymer.	73
Figure II.2.6	(a) DLS and (b) TEM characterizations for the R ₀ -4VP ₅₆ - <i>b</i> -St ₂₄₇ -SC(S)SPr latex.	73
Figure II.2.7	Synthesis of R ₀ -4VP ₁₃₇ -SC(S)SPr: (a) monitoring of the monomer consumption; (b) evolution of the molar mass and <i>D</i> vs. conversion from the SEC analysis; (c) SEC traces evolution with conversion.	74
Figure II.2.8	¹ H NMR spectra taken during the formation of R ₀ -4VP ₁₃₇ -SC(S)SPr.	75
Figure II.2.9	¹ H NMR spectra taken during the formation of R ₀ -4VP ₁₃₇ - <i>b</i> -St ₃₄₄ -SC(S)SPr.	76
Figure II.2.10	(a) DLS and (b) TEM characterizations of the [R ₀ -(4VPMe ⁺ I) ₁₃₇ - <i>b</i> -St ₃₄₄ -SC(S)SPr]·24(DMF) latex.	77
Figure II.2.11	¹ H NMR spectra taken during the formation of R ₀ -4VP ₁₃₇ - <i>b</i> -St ₄₈ -SC(S)SPr.	78
Figure II.2.12	¹ H DOSY NMR spectrum of R ₀ -4VP ₁₃₇ - <i>b</i> -St ₄₈ -SC(S)SPr in D ₂ O/CDCl ₃ .	79
Figure II.2.13	DLS and TEM characterization of the R ₀ -4VP ₁₃₇ - <i>b</i> -St ₄₈ -SC(S)SPr latex: (a) DLS in ethanol; (b) DLS in water/ethanol; (c) TEM.	79
Figure II.2.14	¹ H NMR spectrum of [R ₀ -(4VPMe ⁺ I) ₁₃₇ - <i>b</i> -St ₄₈ -SC(S)SPr]·38(DMF).	80
Figure II.2.15	DLS and TEM characterization of the R ₀ -(4VPMe ⁺ I) ₁₃₇ - <i>b</i> -St ₄₈ -SC(S)SPr latex.	81
Figure II.2.16	¹ H NMR monitoring of the styrene consumption in the chain extension of R ₀ -(4VPMe ⁺ I) ₁₃₇ - <i>b</i> -St ₄₈ -SC(S)SPr, leading to [R ₀ -(4VPMe ⁺ I) ₁₃₇ - <i>b</i> -St ₃₄₅ -SC(S)SPr]·38(DMF).	81

Figure II.2.17 (a) DLS and (b) TEM characterization of the $R_0-(4VPMe^+I^-)_{137}-b-St_{48}-b-St_{297}-SC(S)SPr$ latex.	82
Figure II.2.18 DLS study of a $R_0-(4VPMe^+I^-)_{140}-b-St_{48}-b-St_{297}-SC(S)SPr$ polymer latex.	83
Figure II.2.19 DLS of $R_0-(4VPMe^+I^-)_{137}-b-St_{48}-b-St_{297}-SC(S)SPr$ after freeze-drying the aqueous latex and redispersion.	85
Figure II.2.20 1H NMR monitoring of the styrene/DEGDMA consumption in the crosslinking of $R_0-(4VPMe^+I^-)_{137}-b-St_{345}-SC(S)SPr$, leading to $R_0-(4VPMe^+I^-)_{137}-b-St_{345}-b-(St_{157}-co-DEGDMA_{13})-SC(S)SPr$	87
Figure II.2.21 1H NMR spectrum of the final CCM $R_0-(4VPMe^+I^-)_{137}-b-St_{345}-b-(St_{157}-co-DEGDMA_{13})-SC(S)SPr$ swollen by $CDCl_3$ in D_2O	87
Figure II.2.22 DLS and TEM analyses of the $R_0-(4VPMe^+I^-)_{137}-b-St_{345}-b-(St_{157}-co-DEGDMA_{13})-SC(S)SPr$ CCM latex.	88
Figure II.2.23 DLS analysis of the $R_0-(4VPMe^+I^-)_{140}-b-St_{350}-b-(St_{135}-co-DEGDMA_{15})-SC(S)SPr$ latex.	90
Figure II.2.24 DLS analysis of $R_0-(4VPMe^+I^-)_{140}-b-St_{350}-b-(St_{135}-co-DEGDMA_{15})-SC(S)SPr$ after freeze-drying and redispersion.	91
Figure II.2.25 1H NMR monitoring in $DMSO-d_6$ of the crosslinking reaction with pure DEGDMA to yield the $R_0-(4VPMe^+I^-)_{137}-b-St_{345}-b-DEGDMA_{15}-SC(S)SPr$ latex.	93
Figure II.2.26 1H NMR spectrum of the $R_0-(4VPMe^+I^-)_{137}-b-St_{345}-b-DEGDMA_{15}-SC(S)SPr$ latex swollen by $CDCl_3$ in D_2O	93
Figure II.2.27 DLS and TEM analyses of the $R_0-(4VPMe^+I^-)_{137}-b-St_{345}-b-DEGDMA_{15}-SC(S)SPr$ CCM latex.	94
Figure II.2.28 DLS analysis of the $R_0-(4VPMe^+I^-)_{140}-b-St_{345}-b-DEGDMA_{15}-SC(S)SPr$ latex.	95
Figure II.2.29 DLS analysis of $R_0-(4VPMe^+I^-)_{140}-b-St_{345}-b-DEGDMA_{15}-SC(S)SPr$ after freeze-drying and redispersion.	96
Figure II.2.30 1H NMR monitoring in $DMSO-d_6$ of the $R_0-(4VPMe^+I^-)_{137}-b-St_{48}-b-(St_{300}-co-DEGDMA_{15})-SC(S)SPr$ nanogel synthesis.	97
Figure II.2.31 DLS analysis of the nanogel $R_0-(4VPMe^+I^-)_{137}-b-St_{48}-b-(St_{300}-co-DEGDMA_{15})-SC(S)SPr$ latex.	98
Figure II.2.32 TEM image of the $R_0-(4VPMe^+I^-)_{137}-b-St_{48}-b-(St_{300}-co-DEGDMA_{15})-SC(S)SPr$ nanogel particles.	98
Figure II.2.33 DLS analyses of (a) $R_0-(4VPMe^+I^-)_{137}-b-St_{48}-SC(S)SPr$ macroRAFT agent after equilibration with styrene and DEGDMA; (b) $R_0-(4VPMe^+I^-)_{137}-b-St_{48}-b-(St_{300}-co-DEGDMA_{15})-SC(S)SPr$; (c) as (b), after swelling with toluene; (d) TEM image of the final product.	100
Figure II.2.34 1H NMR spectrum of the $R_0-(4VPMe^+I^-)_{137}-b-St_{48}-b-(St_{300}-co-DEGDMA_{15})-SC(S)SPr$ latex swollen by $CDCl_3$ in D_2O	100
Figure II.2.35 DLS analysis of the $R_0-(4VPMe^+I^-)_{140}-b-St_{50}-b-(St_{300}-co-DEGDMA_{15})-SC(S)SPr$ nanogel latex.	101
Figure II.2.36 DLS analysis of $R_0-(4VPMe^+I^-)_{140}-b-St_{50}-b-(St_{300}-co-DEGDMA_{15})-SC(S)SPr$ after freeze-drying and redispersion. All measurements were carried out on unfiltered samples.	102
Figure II.3.1 1H NMR spectra of the latex of deblocks $R_0-(4VPMe^+I^-)_{140}-b-St_{50}-b-(St_{1-n}-co-DPPS_n)_{300}-SC(S)SPr$	104

Figure II.3.2	^1H NMR spectrum of the latex of deblocks swollen by CDCl_3 in D_2O .	105
Figure II.3.3	^1H NMR spectra of the CCM latexes.	106
Figure II.3.4	^1H NMR spectra of the CCM latexes swollen by CDCl_3 in D_2O .	107
Figure II.3.5	^1H NMR spectra of the NG latex swollen by CDCl_3 in D_2O .	108
Figure II.3.6	^{31}P NMR spectra of (a) DPPS in CDCl_3 and (b-g) of the various deblocks, CCMs and NG latexes swollen by CDCl_3 in D_2O .	109
Figure II.3.7	DLS and TEM images for CCMs and NG.	110
Figure II.3.8	DLS analyses of (a) $\text{R}_0\text{-(4VPMe}^+\text{T)}_{140}\text{-}b\text{-St}_{50}\text{-}b\text{-St}_{300}\text{-SC(S)SPr}$; (b) CCM-C-0.05; (c) CCM-C-0.1; (d) NG-C, after freeze-drying and redispersion in a DMSO/toluene.	111
Figure II.3.9	DLS analyses of the aqueous suspensions of CCM-C and NG-C particles after swelling.	114
Figure III.1.1	Photos of CCM latex: (a) pre-swelling latex with Rh complex chloroform solution; (c) after stirring and decantation.	118
Figure III.1.2	Particle-particle coupling resulting from interpenetration and Rh-TPP coordination.	120
Figure III.2.1	^{31}P NMR spectrum for the toluene-swollen CCM-C-0.1 latex, before (a) and after (b) equilibration with a $[\text{RhCl}(\text{COD})]_2$ toluene solution at a P/Rh ratio of 1:1.	122
Figure III.2.2	^{31}P NMR spectra recorded at different times after mixing equivalent amounts of CCM-C-0.2 latexes with 0 and 100% Rh loadings.	123
Figure III.3.1	Time dependence of the styrene conversion for the biphasic catalyzed by the CCM-C-0.1 latex.	126
Figure III.3.2	Comparison of the conversion vs. time between the $[\text{RhCl}(\text{COD})(\text{TPP}@ \text{CCM-C-0.1})]$ catalyst under biphasic conditions and the homogeneous $[\text{RhCl}(\text{COD})@ \text{PPh}_3]$ catalyst.	129
Figure III.3.3	Styrene conversion vs. recycle number for the biphasic catalyzed styrene hydrogenation by the CCM-C-0.1 latex in 1-nonanol.	132
Figure III.3.4	Styrene conversion vs. recycle number for the biphasic catalyzed styrene hydrogenation by the CCM-C-0.1 latex in 1-nonanol.	132
Figure III.3.5	Styrene conversion vs. recycle number for the biphasic catalyzed styrene hydrogenation by the CCM-C-0.1 latex in 1-nonanol.	133
Figure III.3.6	DLS and TEM images of: (a) CCM-C-0.1 latex after charging with $[\text{RhCl}(\text{COD})]_2$; (b) same latex, after one catalytic run; (c) same latex, after 9 recycles.	134
Figure III.3.7	DLS and TEM analysis of: (a) NG-C latex after charging with $[\text{RhCl}(\text{COD})]_2$ and (b) same latex, after the catalytic run.	134
Figure III.3.8	(a) Time dependence of the styrene conversion for the biphasic catalyzed hydrogenation of neat styrene by the CCM-C-0.1 latex.	136
Figure III.3.9	Conversion vs. time for the biphasic hydrogenation of 1-octene in 1-nonanol catalyzed by $[\text{RhCl}(\text{COD})(\text{TPP}@ \text{CCM-C-0.1})]$.	138
Figure III.3.10	Reaction vial for the biphasic hydrogenation of 1-octene in toluene catalyzed by $[\text{RhCl}(\text{COD})(\text{TPP}@ \text{CCM-C-0.1})]$.	139
Figure IV.1.1	Reaction vial for the biphasic hydrogenation of acetophenone in toluene catalyzed by $[\text{RhCl}(\text{COD})(\text{TPP}@ \text{CCM-C-0.1})]$.	141
Figure IV.2.1	TEM images of CCM-N-n polymer latexes after loading with $[\text{RhCl}(\text{COD})]_2$.	145

Figure IV.2.2	TEM images of the Rh NPs obtained from a toluene solution of [RhCl(COD)] ₂ in the presence of PEOMA ((a) and (b)) or macroRAFT-N ((c) and (d)).	147
Figure IV.2.3	TEM image of the RhNP@CCM-N-0.1 obtained from a 25% loaded latex.	148
Figure IV.2.4	TEM images of the CCM-N-0.2 polymer latex after loading with [RhCl(COD)] ₂ and reduction with H ₂ in the presence of NEt ₃ .	148
Figure IV.2.5	TEM images of the Rh NPs obtained from a toluene solution of [RhCl(COD)] ₂ in the presence of PPh ₃ .	149
Figure IV.3.1	TEM images of the CCM-C-0.1 polymer latex after loading with [RhCl(COD)] ₂ and reduction with H ₂ in the presence of NEt ₃ .	151
Figure IV.3.2	TEM images of RhNP@CCM-C-0.1 obtained with P/Rh = 1:1 and reduction with with different NEt ₃ /Rh ratios.	151
Figure IV.3.3	TEM images of RhNP@macroRAFT-C obtained by [RhCl(COD)] ₂ reduction.	151
Figure IV.4.1	TEM images of the RhNP@CCM-N-0.1 latex before and after the catalytic runs.	156
Figure IV.4.2	TEM image of the RhNP@CCM-C-0.1 latex after the catalytic run.	157
Figure IV.5.1	TEM images of the RhNP@CCM-N-0.1 latex after the catalytic run.	162
Figure IV.5.2	TEM images of the RhNP@CCM-C-0.1 latex after the catalytic run.	162
Figure IV.5.3	TEM images of the RhNP@NG-C-0.1 latex after the catalytic run.	163
Figure IV.5.4	(a) Conversion vs. recycle number for the hydrogenation of neat styrene catalyzed by RhNP@CCM-C-0.1 and with product recovery by extraction with diethyl ether.	166
Figure IV.5.5	(a) Conversion vs. recycle number for the hydrogenation of neat styrene catalyzed by RhNP@CCM-C-0.1 and with product recovery by extraction with toluene.	167
Figure IV.5.6	(a) Conversion vs. recycle number for the hydrogenation of neat styrene catalyzed by RhNP@NG-C-0.1 and with product recovery by extraction with toluene.	168
Figure V.2.1	¹ H NMR monitoring of the SS ⁻ Na ⁺ RAFT polymerization.	176
Figure V.2.2	Monitoring of the SS ⁻ Na ⁺ RAFT polymerization with SS ⁻ Na ⁺ /CTPPA = 140.	176
Figure V.2.3	DLS and TEM characterization of the R ₀ -(SS ⁻ Na ⁺) _x -SC(S)SPr macroRAFT.	177
Figure V.3.1	¹ H NMR monitoring of the R ₀ -(SS ⁻ Na ⁺) _x -SC(S)SPr macroRAFT chain extension with styrene.	178
Figure V.3.2	The photos of R ₀ -(SS ⁻ Na ⁺) _x -b-St _y -SC(S)SPr translucent dispersions.	179
Figure V.3.3	DLS and TEM characterization for the R ₀ -(SS ⁻ Na ⁺) _x -b-St _y -SC(S)SPr diblock macroRAFT agents.	180
Figure V.4.1	¹ H NMR monitoring of the crosslinking of the diblock R ₀ -(SS ⁻ Na ⁺) ₁₄₀ -b-St _y -SC(S)SPr macroRAFT micelles.	181
Figure V.4.2	DLS and TEM data for the R ₀ -(SS ⁻ Na ⁺) ₁₄₀ -b-St _y -b-(St _{0.9-co} -DEGDMA _{0.1}) ₁₅₀ -SC(S)SPr CCM.	182
Figure V.4.3	¹ H NMR monitoring of the crosslinking of the diblock R ₀ -(SS ⁻ Na ⁺) _x -b-St _y -SC(S)SPr macroRAFT micelles with neat DEGDMA.	183
Figure V.4.4	¹ H spectrum of R ₀ -(SS ⁻ Na ⁺) ₁₄₀ -b-St ₃₀₀ -b-DEGDMA ₁₅ -SC(S)SPr: (a) in DMSO- <i>d</i> ₆ and (b) in D ₂ O/CDCl ₃ .	183
Figure V.4.5	DLS and TEM data for the R ₀ -(SS ⁻ Na ⁺) _x -b-St _y -b-DEGDMA _z -SC(S)SPr CCM.	185
Figure V.4.6	Comparative DLS results of the R ₀ -(SS ⁻ Na ⁺) ₅₀ -b-St ₃₀₀ -SC(S)SPr latex without (a)	

and with (b) DEGDMA, prior to crosslinking.	185
Figure V.4.7 DLS monitoring of the core-swelling by toluene and chloroform for selected R_0 -(SS ⁻ Na ⁺) ₁₄₀ - <i>b</i> -St _{<i>y</i>} - <i>b</i> -DEGDMA _{<i>z</i>} -SC(S)SPr CCMs.	186
Figure V.4.8 DLS investigations of R_0 -St ₃₀₀ -SC(S)SPr as (a) synthesized in water and after freeze-drying and redispersion in (b) THF; (c) DMF; (d) acetone.	188
Figure V.4.9 DLS investigations of R_0 -(SS ⁻ Na ⁺) ₁₄₀ - <i>b</i> -St ₃₀₀ -SC(S)SPr after freeze-drying and redispersion in THF/H ₂ O and DMF/H ₂ O mixtures of various compositions.	189
Figure V.4.10 Comparison of the DLS in water and THF/H ₂ O 60/40 for the R_0 -(SS ⁻ Na ⁺) _{<i>x</i>} - <i>b</i> -St _{<i>y</i>} - <i>b</i> -(St _{<i>w</i>} - <i>co</i> -DEGDMA _{<i>z</i>})-SC(S)SPr CCMs polymers.	190
Figure VI.1.1 (a) DLS and (b) TEM characterizations for the R_0 -(MAA _{0.5} - <i>co</i> -PEOMA _{0.5}) ₃₀ - <i>b</i> -(St _{0.9} - <i>co</i> -DPPS _{0.1}) ₃₀₀ - <i>b</i> -(St _{0.9} - <i>co</i> -DEGDMA _{0.1}) ₁₀₀ -SC(S)SPr latex.	195
Figure A.0.1 (a) DLS in water/EtOH and (b) TEM characterization of the R_0 -4VP ₁₃₇ - <i>b</i> -St ₃₄₄ -SC(S)SPr latex.	240
Figure A.0.2 Excerpt in selected regions of the ¹ H NMR spectra in DMSO- <i>d</i> ₆ of R_0 -(4VPMe ⁺ I) ₁₃₇ - <i>b</i> -St ₃₄₄ -SC(S)SPr.	240
Figure A.0.3 ¹ H NMR spectrum of [R_0 -(4VPMe ⁺ I) ₁₃₇ - <i>b</i> -St ₃₄₄ -SC(S)SPr]·24(DMF).	241
Figure A.0.4 Molar mass and dispersity as a function of conversion for the chain extension of the R_0 -4VP ₁₃₇ -SC(S)SPr macroRAFT agent leading to R_0 -4VP ₁₃₇ - <i>b</i> -St ₄₈ -SC(S)SPr.	241
Figure A.0.5 Excerpt in selected regions of the ¹ H NMR spectra of R_0 -(4VPMe ⁺ I) ₁₃₇ - <i>b</i> -St ₄₈ -SC(S)SPr.	242
Figure A.0.6 DLS of R_0 -(4VPMe ⁺ I) ₁₃₇ - <i>b</i> -St ₄₈ - <i>b</i> -St ₂₉₇ -SC(S)SPr: (a) after freeze-drying and dispersion in DMSO at room temperature; (b) after heating for 24 h at 90 °C; (c) dependence of <i>D</i> _{<i>z</i>} on temperature.	242
Figure A.0.7 (a) DLS of R_0 -St ₂₆₃ -SC(S)SPr in toluene and (b) DLS of R_0 -(4VPMe ⁺ I) ₁₃₇ - <i>b</i> -St ₄₈ - <i>b</i> -St ₂₉₇ -SC(S)SPr after freeze-drying, dispersion in a DMSO/toluene, and heating for 24 h at 90 °C.	243
Figure A.0.8 DLS and TEM analyses of the R_0 -(MAA _{0.5} - <i>co</i> -PEOMA _{0.5}) ₃₀ - <i>b</i> -St ₃₅₀ - <i>b</i> -(St _{0.9} - <i>co</i> -DEGDMA _{0.1}) ₁₀₀ -SC(S)SPr CCM latex.	243
Figure A.0.9 DLS and TEM analyses of the R_0 -(MAA _{0.5} - <i>co</i> -PEOMA _{0.5}) ₃₀ - <i>b</i> -St ₅₀ - <i>b</i> -(St ₃₄₀ - <i>co</i> -DEGDMA ₁₀)-SC(S)SPr NG latex.	244
Figure A.0.10 DLS and TEM analyses of the R_0 -(MAA _{0.5} - <i>co</i> -PEOMA _{0.5}) ₃₀ - <i>b</i> -(St _{0.1} - <i>co</i> -DPPS _{0.9}) ₃₀₀ - <i>b</i> -(St _{0.9} - <i>co</i> -DEGDMA _{0.1}) ₁₀₀ -SC(S)SPr CCM latex.	244
Figure A.0.11 DLS analysis of the R_0 -(4VPMe ⁺ I) ₁₃₇ - <i>b</i> -St ₃₄₅ -SC(S)SPr latex used for the crosslinking with pure DEGDMA.	245
Figure A.0.12 Graphic representation of the data in Table III.3.1.	245

Index of tables

Table I.1.1 Comparison between homogeneous catalysis and heterogeneous catalysis.	24
Table II.3.1 Exploration of the morphology dependence for the diblock $R_0-(4VPMe^+I)_a-b-St_b-b-(St_{1-n-co-DPPS_n})_c-SC(S)SPr$ and for the CCM $R_0-(4VPMe^+I)_a-b-St_b-b-(St_{1-n-co-DPPS_n})_c-b-(St_d-co-DEGDMA_e)-SC(S)SPr$ as a function of hydrophilic and hydrophobic chain lengths and of the amount of monomers used in the crosslinking step.	113
Table III.3.1 Hydrogenation of styrene in 1-nonanol with different nanoreactors and different P/Rh ratios.	128
Table III.3.2 Recycling experiments for the hydrogenation of styrene in 1-nonanol with CCM-C-0.1.	131
Table III.3.3 Hydrogenation of neat styrene with CCM-C-0.1.	136
Table III.3.4 Hydrogenation of 1-octene with CCM-C-0.1.	138
Table IV.4.1 Acetophenone hydrogenation catalyzed by Rh NPs.	153
Table IV.5.1 Styrene hydrogenation catalyzed by Rh NPs.	159
Table IV.5.2 Effect of reaction time, temperature and TPP content on the biphasic hydrogenation of styrene catalyzed by RhNP@CCM-C.	164
Table IV.6.1 1-octene hydrogenation catalyzed by RhNP@CCM-C-0.1.	169
Table V.3.1 Conversion and polymer characterization during the chain extension of the $R_0-(SS^-Na^+)_{140}-SC(S)SPr$ macroRAFT agent with styrene.	178
Table VI.2.1 List of all polymers synthesized in this study and reference to their characterization.	209

Index of schemes

Scheme I.1.1	Reaction of Na ₃ tppts with [Rh(acac)(CO) ₂] in polar solvents.	29
Scheme I.1.2	Fluorous-organic biphasic catalysis.	30
Scheme I.1.3	Classical biphasic catalysis based on two immiscible liquids.	31
Scheme I.1.4	Principle of phase transfer catalysis.	32
Scheme I.2.1	General arrangement for aqueous biphasic catalysis.	33
Scheme I.2.2	Thermomorphic aqueous biphasic catalysis.	37
Scheme I.2.3	Principle of CD/cationic surfactant combination to perform interfacial catalysis in thermoregulated emulsion.	39
Scheme I.2.4	Illustration of CO ₂ -responsive Pickering emulsion for biphasic system.	40
Scheme I.3.1	Schematic representation of micelles.	41
Scheme I.3.2	Synthetic scheme of the micelle supported metal catalyst.	42
Scheme I.3.3	Schematic representation of core-shell catalytic nanoreactor prepared by RAFT polymerization.	43
Scheme I.3.4	Assembly of catalyst functionalized amphiphilic block copolymers into polymer micelles and vesicles.	44
Scheme I.3.5	RAFT polymerization of core-shell catalytic nanoreactor and hydroaminomethylation application.	46
Scheme I.3.6	Core-shell catalytic nanoreactor and acylation application.	47
Scheme I.3.7	Amphiphilic triphenylphosphane-functionalized poly(2-oxazoline) block copolymer.	48
Scheme I.3.8	Catalysts and block copolymer structure.	49
Scheme I.3.9	Catalyst encapsulation approach for ethylene polymerization in water.	49
Scheme I.3.10	Synthesis of metal-star catalysts by tandem catalyst interchange and star-polymer-catalyzed living radical polymerization.	52
Scheme I.4.1	Synthesis of neutral shell CCM by a three-step one-pot RAFT-PISA process in water.	54
Scheme II.1.1	General strategy for the construction of core-crosslinked amphiphilic star-block copolymers.	58
Scheme II.1.2	Atom transfer process for poly(St-co-DPPS) made by ATRP.	59
Scheme II.1.3	(a) convergent polymer synthesis by arm-first method and (b) divergent polymer synthesis by core-first method.	60
Scheme II.1.4	Synthesis pathway toward block copolymer nanoreactor with a neutral-shell. ...	62
Scheme II.2.1	Synthesis of the R ₀ -(4VPMe ⁺ I ⁻) _x -b-St _y -SC(S)SPr diblock copolymer.	67
Scheme II.2.2	Proposed mechanism for the MeI-promoted hydrolysis of DMF.	70
Scheme II.2.3	Proposed alternative mechanism.	71
Scheme II.2.4	Crosslinking step for the synthesis of the CCM with a polycationic P4VPMe ⁺ I ⁻ shell.	86
Scheme II.3.1	Synthesis pathway toward block copolymer nanoreactor with a polycationic shell.	103

Scheme III.1.1	Coordination reaction between Rh precatalyst and nanoreactor (CCM).	119
Scheme III.3.1	Products resulting from the hydrogenation of styrene catalyzed by molecular Rh ^I	126
Scheme III.3.2	Products resulting from the hydrogenation of 1-octene catalyzed by molecular Rh ^I	137
Scheme IV.4.1	Products resulting from the hydrogenation of acetophenone catalyzed by Rh NPs.	154
Scheme IV.5.1	Products from the hydrogenation of styrene catalyzed by Rh NPs.	158
Scheme V.1.1	Synthesis pathway toward block copolymer nanoreactor with a polyanionic shell.	174
Scheme VI.1.1	Synthesis route of CTPPA RAFT agent.	195

Introduction

Since a few years, the chemical industry's major goal of economic interest has combined with environmental concerns. For this purpose, catalysis is becoming an essential component in order to conduct a chemical reaction under milder conditions, at lower costs and with higher product selectivity, participating in more than 80% of the industrial production processes. A variety of catalytic reactions have been investigated over last few decades at the academic and industrial levels, including the ammonia synthesis^[1], Fischer-Tropsch processes^[2], Ziegler-Natta catalysis^[3], enzyme catalysis^[4] and so forth.

Nowadays, environmental concerns deeply influence the direction of new advances in the catalysis field. Among the demands in line with the 12 green chemistry principles^[5], efficient catalyst recovery and recycling attracts greater and greater attention. It requires simple protocols that avoid the use of volatile solvents and costly distillation procedures. In this respect, the liquid/liquid biphasic protocol^[6] is attractive because the catalyst is located in a different liquid phase from that of the substrates and products at the end of the catalytic reaction. This simplifies phase separation and subsequent catalyst recycling by decantation. There has been increasing research on the application of biphasic reaction media with innovative solvents, such as fluoruous solvents^[7] and ionic liquids^[8], yielding successful developments like the Difasol process^[9]. However, the use of water to solubilize the catalyst has the advantage of driving the system toward sustainability and diminishing costs. This is named aqueous biphasic catalysis. For instance, the Rhône-Poulenc/Ruhrchemie Rh-catalyzed hydroformylation of propene to butanal has been a great industrial success.^[10] However, this principle is not adaptable to the heavy olefins because of their insufficient water solubility, giving low, mass transport-limited rates.

Great effort has been devoted to increase mass transport, to homogenize the system or increase the interface area, to anchor molecular catalysts on solid supports (recovery by filtration) or on high molecular-weight soluble polymers or dendrimers (recovery by ultrafiltration through membranes) and to various liquid/liquid biphasic variations.

Among several possible variations, the micellar approach is one of the most promising. This consists in catalyst anchoring to the hydrophobic part of surfactants or amphiphilic copolymers that self-organized as micelles in water (reaction occurring in the micellar core). This approach is elegant because the substrate/product and the catalyst are confined in two separate phases at all times. It is also versatile because recent advances in living/controlled polymerization allow easy access to a host of chain-functionalized copolymers. However, it suffers from excessive micelle swelling with generation of stable emulsions, retarding decantation/separation, and from the surfactant/micelle equilibrium, even when the critical micellar concentration is very low, which is a source of catalyst leaching because the free surfactant places itself at the oil/water interface or as inverse micelles in the oil phase.

In a recently introduced approach, unimolecular polymeric objects removed both limitations because swelling of these particles is limited by the dimensions of the resulting macromolecule and the micellar equilibrium with the free arms is removed. A few examples of unimolecular macrostructures that achieve a favourable environment for efficient catalysis in water are available in the open literature. This approach may be called crosslinked micelle-aided catalysis. These examples prove that the performance and stability of such macrostructures require suitable loading and location of the catalytic moieties, as well as a good match between the hydrophobic character of the substrate and the polymer core.

Inspired by this industrial challenge and taking advantage of its multiple research interests, which comprise catalysis and polymer synthesis by controlled radical polymerization, our group (*Ligands, architectures complexes et catalyse, LAC₂*) has recently introduced an innovative approach. It consists of tying together the hydrophobic chain ends of amphiphilic block copolymers to generate unimolecular nano-objects, called core-crosslinked micelles (CCMs) that function as unimolecular amphiphilic nanoreactors. These polymers are assembled straightforwardly by a three-step one-pot process that uses the “reversible addition-fragmentation chain transfer”

(RAFT) radical polymerization methodology. During one of the synthetic steps, a phenomenon known as “polymerization-induced self-assembly” (PISA) occurs, with direct generation of a latex. These CCMs are characterized by a hydrophilic neutral P(MAA-*co*-PEOMA) shell and a hydrophobic polystyrene-based core bearing phosphine ligands, which is crosslinked in the last step. The application of this CCM latex, after loading with a rhodium precatalyst, to the aqueous biphasic hydroformylation and hydrogenation of highly hydrophobic substrates has shown high activity and selectivity and good recyclability with low catalyst leaching.

However, these nanoreactors still suffered from non-negligible catalyst losses in the organic product phase and from slow decantation. These phenomena were shown to result from the high-temperature lipophilicity of the neutral P(MAA-*co*-PEOMA) shell and from particle aggregation. The latter is the consequence of particle interpenetration. In order to correct these problems, it was then envisaged to modify the polymer scaffold by replacing the hydrophilic neutral-shell with a polyelectrolytic one, which is the major objective of this thesis.

In this research, copolymer micelles with polycationic (polyvinylpyridium, P4VPM^{+I}) or polyanionic (polystyrenesulfonate, PSS^{-Na⁺}) shells were prepared by the RAFT-PISA strategy in water, and then crosslinked by diethylene glycol dimethacrylate (DEGDMA) to form unimolecular objects. Depending on the different crosslinking strategy, two polymer architectures were obtained: CCM and nanogel (NG). The phosphine ligand-containing monomer, 4-(diphenylphosphino) styrene (DPPS), was copolymerized by diluting it with styrene outside the crosslinked part (in case of CCM) or in the crosslinked part (in case of NG). The resulting functionalized micelles were loaded with [RhCl(COD)]₂ into the cores to form catalytic nanoreactors. The molecular catalysts and metallic nanoparticles that formed under specific conditions were used for the aqueous biphasic hydrogenation of styrene, acetophenone and 1-octene.

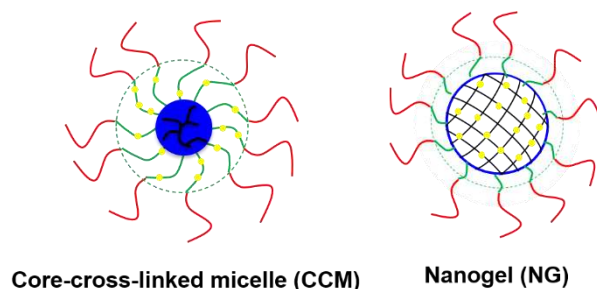


Figure I.1 The structure of two unimolecular micelles: CCM and NG.

The first chapter gives an overview of the heterogenized homogeneous catalysis principles and a few significant applications. The liquid/liquid biphasic catalysis will first be presented in terms of its history, classifications and corresponding catalyst recovery methods. Then the chapter is focused on aqueous biphasic catalysis, especially micellar catalysis. In the end, the recent examples making use of unimolecular nanoreactor catalysis are detailed, with specific focus on the catalytic activity, selectivity and catalyst recovery and leaching issues.

The second chapter in this thesis deals with the preparation of non-functionalized copolymers and phosphine-functionalized copolymers with a positively charged shell, using the RAFT method in three steps: polymerization of water-soluble monomers to build the hydrophilic shell blocks, chain extension with a hydrophobic monomer with or without ligands incorporation and featuring self-assembly (PISA), and finally further chains extension and core crosslinking. The shells consist of polycationic P4VPMe⁺I⁻ chains. DLS and TEM characterization demonstrates the well-defined spherical morphology and size distribution of the unimolecular particles.

The third chapter shows the investigation of the nanoreactor loading with the [RhCl(COD)]₂ complex via coordination to the core-anchored phosphine ligands. A point of interest is the totally different interparticle ligand exchange and metal migration behaviours compared to the first-generation neutral-shell nanoreactors. The catalytic performance (activity, selectivity, metal leaching) in hydrogenation of styrene and 1-octene under aqueous biphasic condition will also be discussed in this part.

The fourth chapter will report the generation of metallic nanoparticles within the

nanoreactor cores as a function of base addition, nature of the outer shell, ligand concentration in the core and other variables. These rhodium nanoparticles will also be used for the hydrogenation of styrene, acetophenone or 1-octene under aqueous biphasic conditions. The catalyst recovery tests were done by extraction with toluene or diethyl ether, showing different recycling behaviours.

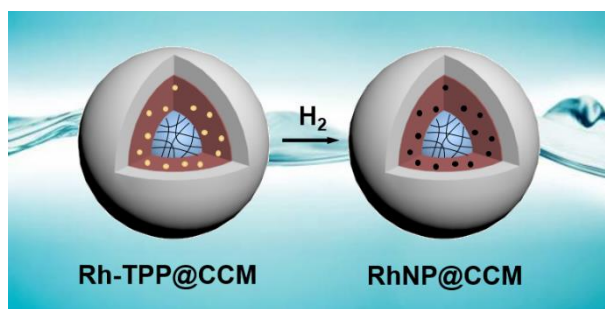


Figure I.12 The rhodium nanoparticles synthesis in the nanoparticle core.

The fifth chapter describes the preparation of CCMs and NGs with a polyanionic shell, which consists of PSS⁻Na⁺ chains. The preparation is again a one-pot synthesis like that of the neutral-shell copolymers. The resulting particles were also studied by DLS and TEM measurements.

The last chapter reports the polymerization, metal complexation, and catalysis procedures, the characterization techniques and the corresponding used chemicals.

Chapter I

Literature survey

The discovery of catalysis by Berzelius in 1836 and its scientific definition by Ostwald in 1894^[11] provided a powerful mean to fabricate desired chemicals. Growing recognition of the catalysis theory, associated with the innovative works from subsequent scientists such as Berzelius, Kirchhoff, Humphry, Henry, Dobereiner, Faraday, Phillips, Sabatier and so on, led to the development of catalysis as a topic of its own. The concept of catalysis as a phenomenon includes the effect on the increasing rate of achieving an equilibrium of a chemical reaction in the presence of a relatively small amount of a substance, named catalyst, which is not itself chemically changed or consumed. Catalysts function by forming activated intermediates of lower energy with reactants to decrease the activation barrier along the reaction energy profiles. On the other hand, although a catalyst does not influence the equilibria of reversible reactions, it may have an unequal influence on several reaction pathways, affecting the product selectivity. These acceleration and selectivity actions make catalysis a promising tool for fast and high-efficiency industrial production of chemicals. Nearly 80% of the worldwide chemical manufacturing in a variety of sectors such as food processing, pharmaceuticals, textile, fuels and construction involves catalyzed processes.

Catalytic processes can be classified as homogeneous and heterogeneous, depending on whether the catalyst is in the same phase as the reagents, or in a different one. The phase of the reagents must be a fluid (most frequently liquid). In heterogeneous catalysis, the catalyst is in most cases a solid and the “heterogeneous catalysis” terminology is typically reserved to this situation. However, a catalyst may also be confined in a different liquid, which is immiscible with the reagents phase. This also falls under the definition of heterogeneous catalysis, but is typically referred to as “biphasic catalysis”, or more precisely liquid/liquid biphasic catalysis. It is also necessary to underline that the distinction between homogeneous and heterogeneous is not always clear-cut, like the distinction between one-phase and two-phase systems. When the domain size of the minority phase, which is dispersed in the majority (continuous) phase, gets smaller and smaller, there is a continuous transition from

emulsion (liquid/liquid) or suspension (solid/liquid) two-phase systems, through an intermediate situation of “colloidal dispersions”, to finally obtain a one-phase solution. The typical accepted boundaries of the domain size are $> 1 \mu\text{m}$ for the two-phase systems or “coarse dispersions” and $< 1 \text{ nm}$ for the single-phase solutions, thus leaving the intermediate size range ($1 \text{ nm} < d < 1 \mu\text{m}$) for the intermediate area of the colloidal dispersions.^[12] Therefore, the classification of certain situations of nanosized catalysts, both hard (*e.g.* metallic nanoparticles) and soft (*e.g.* anchored on polymers either above or below the glass transition temperature), as homogeneous or heterogeneous is ambiguous. Another special situation is that of “enzyme catalysis”. In terms of phase behavior, this can be classified as either homogeneous or heterogeneous (or in the middle “grey” area). This terminology, however, is commonly used and reserved to catalytic process occurring in biological systems.

The homogeneous and heterogeneous processes can be assessed in terms of several parameters, *i.e.*, activity, selectivity, lifetime, catalyst recovery and recycling (Table I.1.1).^[13] Heterogeneous catalysis (in the typical meaning of solid catalysts) is usually characterized by lower activity, lower selectivity and high tolerance for harsh reaction conditions (higher temperature and/or pressure). Furthermore, the complicated diffusion, mass transport of reactants and heat transfer in the heterogeneous catalysis system brings in much difficulty in the exploration of kinetics. Apart from these drawbacks, the separation of the catalyst from the products can be accomplished much more easily and less costly simply by interphase separation. Conversely, the recovery of homogeneous catalysts requires additional separation techniques such as distillation, precipitation, extraction, or ultrafiltration, which are quite demanding due to the use of specific equipment and a large number of solvents. In addition, homogeneous catalysts might more readily contaminate the products or suffer from deactivation and serious loss during the separation and recovery procedures. On the other hand, the molecular nature of the homogeneous catalyst leads to greater activities (all catalyst molecules are accessible to the substrate without mass transport limitations) and selectivities. Because

of the inherent difficulty in homogeneous catalyst recovery, which conduces to complicated catalyst recycling strategies and high costs, heterogeneous catalysis occupies most of the chemical manufacturing market.

Table I.1.1 Comparison between homogeneous catalysis and heterogeneous catalysis.

Property	Homogeneous catalysis	Heterogeneous catalysis
Physical state ^a	l-l, g-g	l-l, l-g, s-l, g-s
Activity	high	medium
Selectivity	high	medium
Mechanistic investigations	facile	difficult
Catalyst lifetime	medium	long
Catalyst recovery	hard	easy
Reaction solvents	more	less
Reaction rate control	dynamics	diffusion
Reaction condition	mild	harsh
Industrial application	few	many
Typical implementation	batch process	continuous process

^al = liquid; g = gas; s = solid.

In order to combine the advantages of the heterogeneous and homogeneous processes, numerous strategies for catalyst recovery have been explored, such as thermal and chemical methods,^[14] catalyst heterogenization,^[15] membrane technology^[16] and multiphase catalysis.^[13b] For example, Rolf Mülhaupt *et al.*^[17] prepared a thermoresponsive material based on poly(2-ethyl-2-oxazoline) grafted on graphene oxide (TRGO-g-PEtOx) as a palladium catalyst support. The grafted PEtOx chains enabled the transition between dispersion and sedimentation through temperature regulation. Above the lower critical solution temperature (LCST), the TRGO-g-PEtOx support agglomerates and sedimented, making the anchored catalyst

recycling straightforward by simple hot filtration (see Figure I.1.0). The recycled catalysts retained the close catalytic activity after five recycles.



Figure I.1.0 Illustration of the Pd@TRGO-g-PETox catalyst recycling by thermal switching between dispersion and sedimentation behavior.^[17]

I.1 Catalyst recovery in the liquid/liquid biphasic catalysis

Apparently, the easiest and most cost-effective solution is to confine the molecular catalyst in a different phase from that of the reactants and products, while maintaining its molecular constitution and therefore its performance characteristics but at the same time leading to simplified recovery. The catalyst support may be either solid or liquid. The former case is usually described as “heterogenized homogeneous” catalysis, whereas the latter one is referred to as liquid/liquid biphasic catalysis. In the first case, the molecular catalyst is immobilized on the surface of insoluble polymers (typically crosslinked resins)^[18] or inorganic oxides (*e.g.* silica, alumina, titania, *etc.*)^[19] The former polymeric supported catalysis might attain better product selectivity and the inorganic oxides supported catalysis is able to suffer from severe thermo or oxidative condition. The immobilization methods include covalent binding and adsorption such as physisorption,^[20] hydrogen bonding,^[21] encapsulation^[22] and so on. Among these anchoring interactions, covalent bonds provide the strongest link, making the bonded metal precatalyst more difficult to leave the solid supports under harsh reaction

conditions.

In liquid/liquid biphasic catalysis, the catalyst is “solubilized” into a liquid phase that is immiscible with that of the substrates/products. Both approaches still suffer from the problems of catalyst loss and mass transport restrictions, but the solid immobilization approach also suffer from lower rates, sometimes lower selectivity caused by the steric hindrance of the supports.^[23]

In the liquid/liquid biphasic method, the catalyst and the substrates may come into contact in one of four different ways: in the bulk of catalyst phase, in the substrates/products phase, at the interface or in another confined space such as nanosized micelles, where the catalyst may be immobilized, dispersed in a second liquid phase. Once the reaction is finished and stirring is stopped, the biphasic mixture is decanted with separation of catalyst and products in the respective phases. The catalyst solution can then be reused directly. This technology not only keeps the catalyst high activity and selectivity but also allows catalyst/product separation more efficiently and with less maintenance-intensive equipment. As an illustration, Hengquan Yang *et al.*^[24] developed a water-in-oil Pickering emulsion with the help of a solid emulsifier for the liquid/liquid interfacial approach (indicated as Figure I.1.1). The water-soluble catalyst was distributed in water droplets which lay in the continuous organic (oil) phase. This method exhibited great durability (over 2000 h) and enhanced catalysis efficiency.

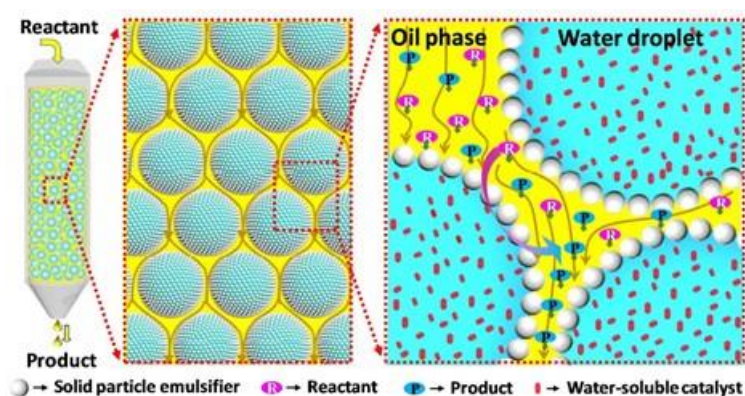


Figure I.1.1 Schematic illustration of the flow Pickering emulsion strategy for organic-aqueous biphasic catalysis reactions.^[24]

After the initial proposition of liquid/liquid catalysis by Manassen^[25] in 1973, the technique was developed by early work of Joó^[26] and Keim,^[27] leading to the commercial implementation of a catalyzed ethylene oligomerization process known as the Shell Higher Olefin Process (SHOP). Before this technology, ethylene oligomerization was homogeneously catalyzed by P-O chelate nickel complexes in toluene to yield linear α -olefins in > 98% chemoselectivity and > 99% regioselectivity (< 1% of branched olefins). As mentioned above, the high cost of catalyst recovery made this process unrealistic for industrial development. However, upon replacing the toluene solvent with 1,4-butanediol, Keim and Nabong^[28] noted that the reaction mixture yielded two phases at the end of the reaction. Therefore, when the ethylene oligomerization was complete, the nonpolar phase containing the α -olefins was easily separated.

It was not until Kuntz, in collaboration with Rhône-Poulenc, developed the synthesis of water-soluble phosphines,^[29] followed by research work at Ruhrchemie,^[30] that the first large-scale application of liquid/liquid biphasic homogeneous catalysis, known as the Ruhrchemie/Rhône-Poulenc (RCH/RP) hydroformylation, was implemented. This process uses a rhodium carbonyl catalyst stabilized by a triphenylphosphine trisulfonate ligand in the aqueous phase to hydroformylate alkenes, yielding mostly linear, water-insoluble aldehydes. In this process, the reaction occurs in the catalyst phase and is limited to the light olefins (propene, butene) with sufficient water solubility to ensure the absence of mass transport limitations.

In the past five decades, apart from the SHOP process (organic/organic, the reaction occurs in the catalyst phase) and the RCH/RP process (organic/aqueous, the reaction occurs in the catalyst phase), additional industrial implementation of the liquid/liquid biphasic catalysis protocol comprises the Kuraray telomerization process (organic/aqueous, the reaction occurs in the catalyst phase),^[31] the IFP Difasol process (organic/ionic liquid, the system becomes one-phase above 70 °C),^[9] the ring opening metathesis polymerization (ROMP) process (organic/organic)^[32] and others.

I.1.1 Heterogenized homogeneous catalysts in liquid/liquid biphasic catalysis

biphasic catalysis

As shown by the above-mentioned examples, liquid/liquid biphasic catalysis may use mixtures of different solvents with limited miscibility. In addition to the traditional aqueous-organic system and organic-organic solvent system,^[13b, 33] various novel hybrid systems are proposed which could be categorized into solvent systems, phase transfer catalysis (PTC) systems and nano- and microdispersed systems (indicated as Figure I.1.2).



¹ Solvent system.^[34]

^{2, 3, 4} PTC system: PTC by crown ethers,^[35] PTC by onium salts,^[36] PTC by cyclodextrins.^[37]

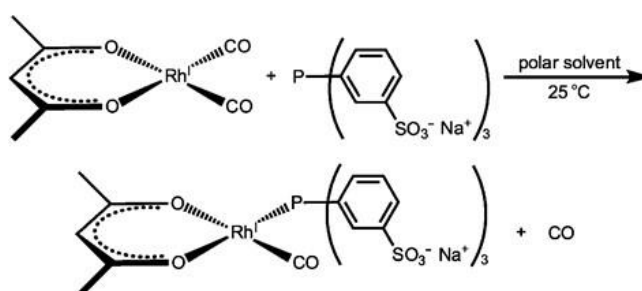
^{5, 6, 7} nano- and microdispersed system: micellar catalysis; microemulsion catalysis; Pickering emulsion catalysis.

Figure I.1.2 Various implementations of liquid/liquid biphasic catalysis.^[38]

Solvent system

In the solvent systems, in addition to the preferred water (because of low cost and hazard considerations), common choices for the catalyst phase are ionic liquids,^[8, 39] fluororous solvents,^[7] supercritical fluids^[40] and immiscible organic liquids. Newly-

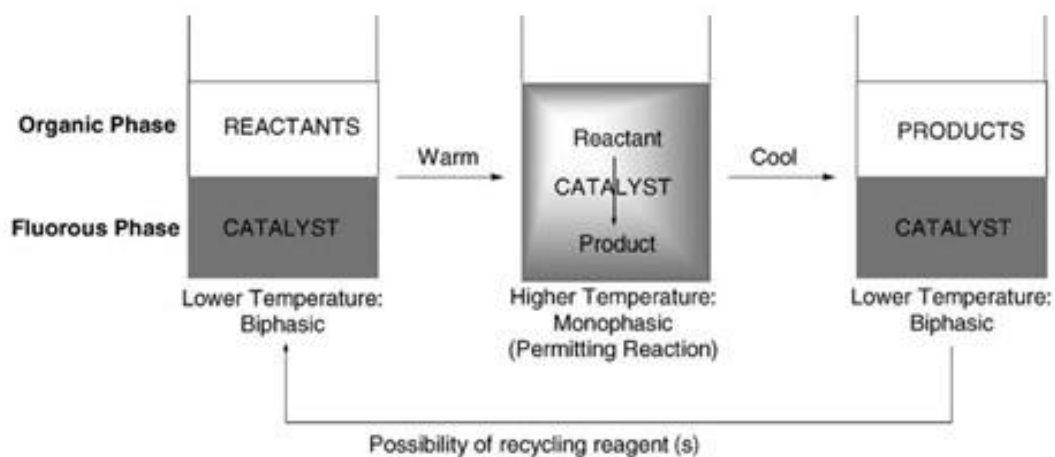
developed strategies make use of an ionic liquid in combination with either water or an immiscible organic solvent. Ionic liquids have an extraordinarily low vapor pressure which prevents the solvent volatilization during the catalytic reaction. Secondly, certain ionic liquids, especially with the $[\text{AlCl}_4]^-$, $[\text{PF}_6]^-$, $[\text{BF}_4]^-$ *etc.* anions, have weaker coordination ability than many organic solvents, weakening the competition between ligands and solvents for immobilizing metal atoms. Thus, ionic liquids are a promising medium for the liquid/liquid biphasic implementation of various catalyzed reactions. For example, Hans-Peter Steinrück *et al.*^[41] studied the location of the $[\text{Rh}(\text{acac})(\text{CO})_2]/\text{tris}(3\text{-sodium sulfonatophenyl})$ phosphine (TPPTS) precatalyst (Scheme I.1.1) as a function of the counterion of typical imidazolium ionic liquids, providing important information on the processes occurring at the phase boundary in hydroformylation catalysis. Carine Julcour Lebigue *et al.*^[42] utilized the same Rh@TPPTS precatalyst in a $[\text{PF}_6]^-$ ionic liquid for the biphasic hydroformylation of 1-octene. Since J. S. Wilkes and Y. Chauvin^[43] developed the first biphasic olefin polymerization/oligomerization reaction in ionic liquids in 1990, the Institut Français du Pétrole (IFP) developed the Difasol technology by using a nickel catalyst in a $[\text{AlCl}_4]^-$ ionic liquid for a high-selectivity olefin dimerization.



Scheme I.1.1 Reaction of Na_3tppts with $[\text{Rh}(\text{acac})(\text{CO})_2]$ in polar solvents.

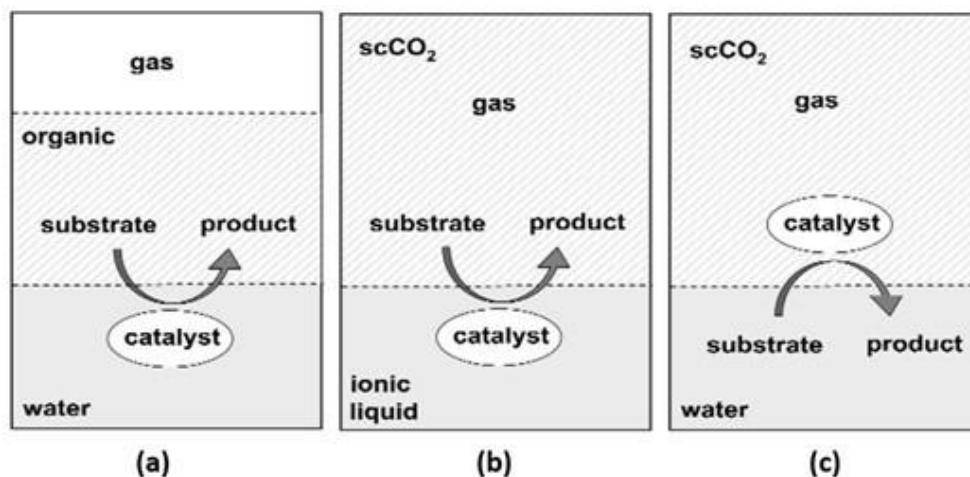
As widely known, perfluorinated compounds are hardly miscible with common organic solvents or water at low temperatures but become miscible at higher temperatures.^[44] Based on this thermomorphic property, fluoruous solvents become suitable candidates for the liquid/liquid biphasic protocol to simplify catalyst recovery.

Fluorous is a term referring to the high level of fluorination. This kind of systems are homogeneous under the high temperature conditions of the reaction, but heterogeneous during the separation process, which is usually carried out at low temperature (Scheme I.1.2). In order to favor dissolution of the metal precatalyst in the fluorous phase, the coordinated ligands are generally fluorinated. From the research by Horvath^[45] in the 1990s, fluorous-organic biphasic catalysis has been exploited for hydroformylation, hydrogenation, oxidation, hydroboration, nitration, Heck reaction and other catalyzed transformations.



Scheme I.1.2 Fluorous-organic biphasic catalysis.^[46]

Supercritical fluids are pure compounds or mixtures under temperature and pressure conditions beyond their critical point. Even though the supercritical fluids are not regarded as traditional liquids, they can also act as one of the two phases in the liquid/liquid biphasic catalysis protocol (Scheme I.1.3).



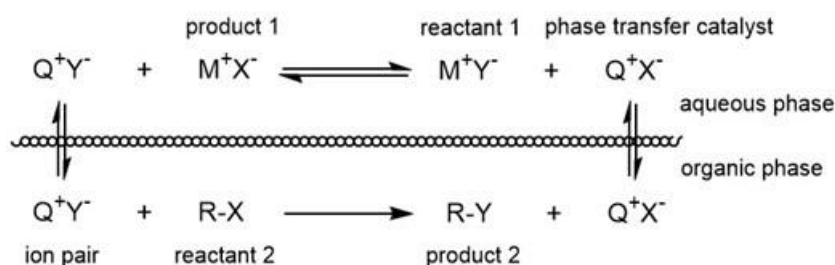
Scheme I.1.3 (a) Classical biphasic catalysis based on two immiscible liquids; (b) supercritical fluids-organic biphasic catalysis: ionic liquid/scCO₂ catalysis for CO₂-soluble substrates and products and (c) inverted scCO₂/aqueous phase catalysis for highly polar substrates and products.^[47]

The use of supercritical liquids as the catalytic phase brings a few benefits. Firstly, they are “good solvents” for a lot of organic substrates and can also dissolve hydrogen and oxygen at high concentrations. Secondly, compared to traditional liquids, supercritical fluids have higher diffusion coefficients, lower viscosity and lower surface tension, which favor substrate diffusion. Thirdly, in contrast to the normal gases, supercritical fluids have high heat conductivity. Therefore, the use of supercritical liquids will assist in speeding up the reaction. Finally, the solubility of substrates and products may also be regulated through a change of temperature or pressure, facilitating their separation from the supercritical fluid phase.^[48] Since CO₂ is naturally abundant, non-toxic and inert, it is the most popular supercritical liquid in biphasic catalysis.^[47]

Phase transfer catalysis system

In the protocol known as phase transfer catalysis (PTC),^[49] the type of process and the roles of the two immiscible solvents are totally different. In biphasic catalysis operating through the “solvent system” protocol, the reagents are in one liquid phase and the catalyst is in the second one. On the other hand, in PTC the two reagents cannot

be dissolved in the same solvent. Usually, one reagent is an organic hydrophobic substance and the second one is an anion coming from a water-soluble alkali metal salt, M^+Y^- . Therefore, a catalyst is needed to transport the anion to the organic phase. The phase transfer catalysts, Q^+X^- , are usually quaternary ammonium or phosphonium salts. They are able to exchange their counterion with M^+Y^- in the aqueous phase to form the ion pair Q^+Y^- , which is more lipophilic and can be transported to the organic phase. The reaction can then take place in the organic phase to produce the targeted product $R-Y$, and the regenerated Q^+X^- returns to the aqueous phase for the next ion exchange reaction (Scheme I.1.4). This will be discussed in more detail in the next section.

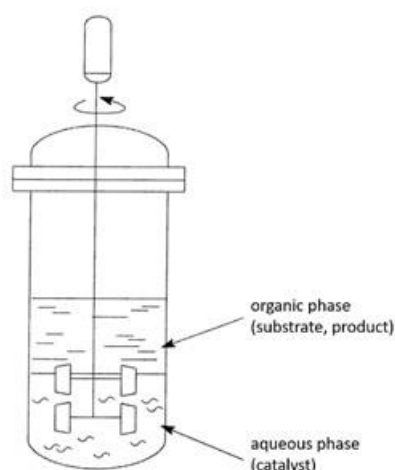


Scheme I.1.4 Principle of phase transfer catalysis.

I.2 Aqueous-organic biphasic catalysis

With the increasing concerns about environmental protection, renewable resources and sustainable development, green chemistry is currently attracting more and more attention. Water is a safe, environmentally friendly, renewable and inexpensive solvent, thus aqueous-organic biphasic catalysis (usually abbreviated as “aqueous biphasic catalysis”) is playing a dominant role in scientific research and industrial process. During the catalysis, the reactants mixture is stirred to enable the interaction between catalyst and substrate. Once the reaction reaches to the intended time, the stirring is stopped and the mixture separates into two phases, the organic phase containing products and residual substrates and the aqueous phase containing catalysts, as shown

in Scheme I.2.1.



Scheme I.2.1 General arrangement for aqueous biphasic catalysis.^[6b]

I.2.1 The development of aqueous biphasic catalysis

As noted above, the development history of aqueous biphasic catalysis began from the initial attempt by Manassen^[25] to hydroformylate propene and was followed by corresponding research leading to the first large-scale utilization of the aqueous biphasic catalysis (RCH/RP)^[30] in the early part of the 1980s. This process occurs homogeneously in the aqueous phase by the Rh catalyst coordinated by the water-soluble triphenylphosphine monosulfonate (TPPMS). Owing to the low but sufficient water solubility of propene, this catalytic reaction is not negatively affected by a mass transport restriction. Apart from this industrial application, aqueous biphasic catalysis is utilized in a number of additional processes. The Kuraray Corporation in Japan uses a palladium complex with the lithium salt of TPPMS, as the water-confined catalyst, for the hydrodimerization of butadiene to produce 2,7-octadien-1-ol, which is then hydrogenated to 1-octanol.^[50] The Rhône-Poulenc group in France has developed a synthesis of vitamin A and E precursors by the ruthenium-catalyzed C-C coupling of myrcene and ethyl acetonate to produce geranyl acetone. The Ru precatalyst is

coordinated by the TPPTS ligand.^[51] The BASF Corporation in Germany has established a Rh-catalyzed aqueous biphasic hydroformylation of olefins to produce the corresponding aldehyde and/or alcohol using a precatalyst stabilized by a chelating water-soluble ligand.^[52] The same company also designed a production line for 2-ethyl-1-hexanol and butanol by a hydroformylation catalyzed by cobalt formate and cobalt acetate, and this technique is still adopted by the Hills, DOW Chemical and W.R. Grace Corporations. Moreover, in earlier academic research, a Pd precatalyst modified with TPPMS was used for the Suzuki coupling of 2-chlorobenzonitrile and *p*-tolylboronic acid to synthesize 2-cyano-4'-methylbiphenyl.^[53] Nowadays, less expensive chlorinated aromatics and PdCl₂/TPPTS are used for the same catalyzed coupling in large-scale industrial production.^[54]

The scientific institutes and industrial manufacturing companies have been paying much attention to the study of aqueous biphasic catalysis for several years, because this method allows the efficient catalyst separation for recovery and recycling through simple decantation at low cost. However, in view of the bad water solubility of higher olefins, the mass transfer process of organic substrates to the aqueous phase becomes a barrier for the reaction rate improvement. This is clearly shown in Figure I.2.1, where a Rh-catalyzed aqueous biphasic hydroformylation of higher α -olefins becomes slower for longer chain (less soluble) olefins.^[55] In addition, the reaction is accelerated in the presence of 1-octyl-3-methyl imidazolium bromide as a weak surfactant. As already mentioned above, several strategies have been proposed over the last decades to promote the mass transport of reactants to the active reaction sites.

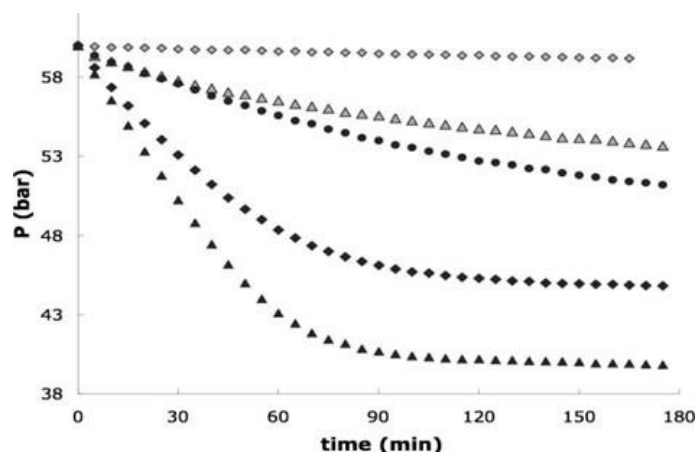


Figure I.2.1 Gas uptake plots from a ballast vessel for the hydroformylation of various alkenes in the absence (grey) and presence (black) of [OctMim]Br (0.5 mol dm^{-3}). ▲ 1-hexene, ◆ 1-octene, ● 1-decene. Reaction conditions: precatalyst: [Rh(acac)(CO)₂]; ligand: TPPTS; T = 100 °C; p = 20 bar (CO/H₂ = 1:1); stirring rate = 1000 rpm; 3 h; [Rh]_{aq} = $1.25 \times 10^{-3} \text{ mol dm}^{-3}$; alkene: 2 ml^3 .^[55]

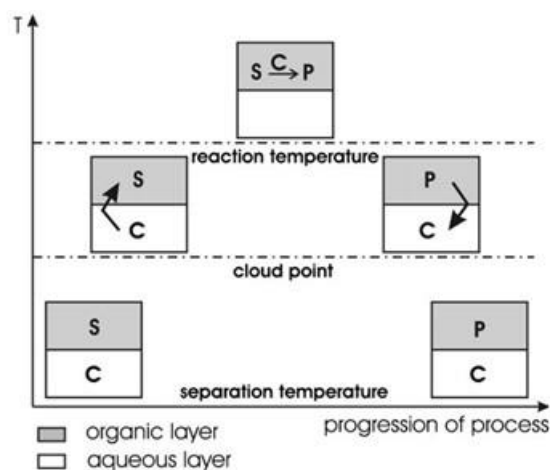
I.2.2 Heterogenized homogeneous catalysts in aqueous biphasic catalysis

In aqueous biphasic protocols, as already stated above, the catalyzed transformation may take place in one of four distinct environments: (1) in the substrate/product phase, if the catalyst can be transported to that phase by a temperature stimulus (thermomorphic catalysis) or by a phase-transfer agent; (2) in the catalyst phase, if the substrates are sufficiently water-soluble; (3) at the interface, if neither component is sufficiently soluble in the other component phase; and (4) within the homogeneous environment of catalytic nanoreactors such as functionalized micelles that generate a stable dispersion in water (latex). These ideas can be accomplished by introducing additives such as co-solvents, surfactants, polyethylene glycol, phase transfer agents or activated carbon,^[56] by varying the ligand structure or composition, or by using hydrophilic polymeric supports.

In the substrate/product phase

This can be accomplished by either the thermomorphic or by the phase transfer agent approach. In the former one, the catalyst is anchored on a thermoregulated ligand or polymeric support which is water soluble at low temperatures but becomes lipophilic above the LCST.^[57] In such a way, the catalyst migrates toward the substrate phase at the reaction temperature and the reaction occurs entirely in the homogeneous organic phase. When the reaction is finished and the mixture is cooled down below the LCST, the catalyst returns to the aqueous phase and can be separated, as indicated in Scheme I.2.2. Thus, the thermomorphic ligands or supports are selected according to the required reaction temperature.

A number of thermomorphic aqueous biphasic catalytic reactions have been reported. Chantal Larpent *et al.*^[58] attempted to use a thermo-responsive polyoxyethylene (decyloctaethyleneglycol) with covalently anchored 2,2'-dipyridylamine as a ligand for a Pd precatalyst applied to the Heck reaction of iodobenzene with ethyl acrylate and styrene. The reaction was conducted at 120 °C and the catalyst recycling was achieved by cooling until the catalyst went back to the aqueous phase. After recycling, the aqueous phase could be reused until the fourth run. The decreasing catalytic activity over the subsequent recycles could be rationalized by the influence of the inorganic salts on the phase transfer behavior of the thermoresponsive polymer.^[59] Poly(ethylene glycol) (PEG) and poly(ethylene glycol) derivatives form hydrogen bonds with water molecules, but this interaction is weakened at high temperatures, leading to increased hydrophobicity. This behavior allows the application of phosphine and phosphite ligands containing PEG substituents on the rhodium-catalyzed hydroformylation or hydrogenation in thermomorphic aqueous biphasic catalysis.^[60]



Scheme I.2.2 Thermomorphic aqueous biphasic catalysis: C = catalyst, S = substrate, P = product.^[61]

Concerning the phase transfer agent approach, as mentioned above, the unique character of the phase transfer agents also provides a route for the heterogenization of homogeneous catalysts in aqueous biphasic catalysis. This method includes normal phase transfer catalysis, inverse phase-transfer catalysis and phase-boundary catalysis. The first kind regularly employs salts or compounds that are soluble in both water and organic solvents as phase transfer agents. They are able to transport the catalyst from the aqueous phase to the organic phase without any emulsion formation. The inverse PTC operates a transport in the opposite direction. For instance, cyclodextrins (CD) and calixarenes are used to transport organic substrates to the catalytic aqueous phase.^[62] Finally, phase-boundary catalysis indicates that an amphiphilic phase transfer agent is located at the interface between the organic phase and the aqueous phase. In some cases, the ionic liquids could act as both a separate phase and as the phase transfer agent in biphasic catalysis.^[63]

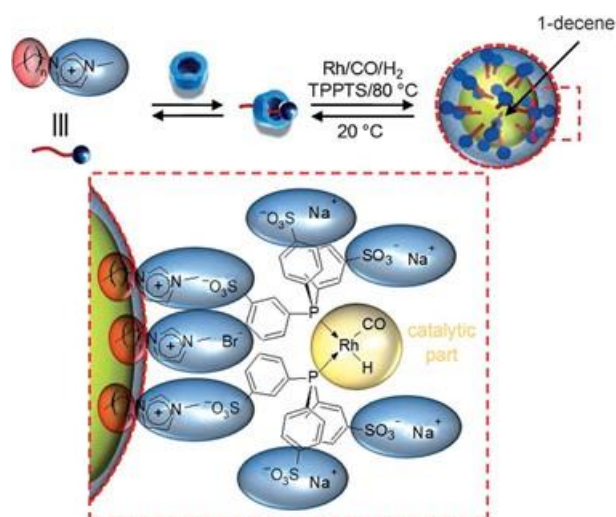
In the catalyst phase

Among the above additives, the co-solvents (alcohols, acetone or acetonitrile) increase the solubility of hydrophobic substrates in the catalytic aqueous phase.^[64] Nitin S. Pagar and Raj M. Deshpande^[65] reported a palladium catalyst coordinated by a water

soluble phosphine ligand for the Heck reaction in aqueous biphasic catalysis. To solve the mass transport limitation caused by the poor water solubility of the substrates, a co-solvent such as morpholine, NMP or 1,4-dioxane was used. The recovered catalyst gave a similar activity for two recycles, with 21%, 22% and 21% conversions respectively. Analysis by atomic absorption spectroscopy (AAS) proved that there was no leaching of the Pd catalyst into the organic phase after separation.

At the interface

When the catalyst solubility in the organic substrate phase and the substrate solubility in the catalyst aqueous phase are very low and mass transport severely limits the reaction, the major fraction (or totality) of the transformation may occur at the interface. In that case, adoption of a phase transfer agent, an amphiphilic copolymer or a surfactant leads to the formation of a water-in-oil (w/o) or oil-in-water (o/w) emulsion and increases the rate of the process via the increase of the interface surface. Andreea R. Schmitzer *et al.*^[37] demonstrated that the combination of a cationic imidazolium surfactant with α -CD favored the aqueous rhodium-catalyzed hydroformylation of higher olefins. The complexation ($T = 20\text{ }^{\circ}\text{C}$) and dissociation ($T = 80\text{ }^{\circ}\text{C}$) of α -CD and surfactants are reversible (Scheme I.2.3). At the reaction temperature, the dissociated surfactant molecules build up the oil droplets by emulsification. The water-soluble anionic TPPTS ligands and the rhodium precatalysts are stabilized on the organic droplet surface, favoring contact between the catalyst and the substrate at the interface and speeding up the reaction. After cooling down at the end of the reaction, the α -CD helps breaking the surfactant self-assemblies, leading to fast phase separation and catalyst recovery.



Scheme I.2.3 Principle of CD/cationic surfactant combination to perform interfacial catalysis in thermoregulated emulsion. Bottom: a possible active rhodium species during hydroformylation reaction.^[38]

Jianli Wang *et al.*^[66] synthesized an amphiphilic block copolymer made of 2,2,6,6-tetramethyl-4-piperidylmethacrylate (TPM, ligand-functionalized monomer for catalyst anchoring), methyl methacrylate (MMA, hydrophobic part) and 2-(dimethylamino) ethyl methacrylate (DMA, hydrophilic and CO₂-responsive part^[67]) through RAFT polymerization. This copolymer acted as surfactant to stabilize the reactants in water droplets dispersed into the organic phase, namely forming a Pickering emulsion (Scheme I.2.4). The 2,2,6,6-tetramethylpiperidine-1-oxyl (TEMPO) catalyst was immobilized on the fabricated amphiphilic P(TPM-*co*-DMA)-*b*-MMA) block polymer and then applied to the alcohol oxidation in interfacial aqueous biphasic catalysis, leading to a 4-fold increase of catalytic activity relative to the catalysis without emulsification. Moreover, the Pickering emulsion could be reversibly broken and reformed for 5 runs just by bubbling CO₂ and N₂, respectively.

The last protocol, the aqueous biphasic catalysis within the homogeneous environment of catalytic nanoreactors based on ligand-functionalized polymers has recently attracted considerable attention, because kinetically stable micelles can be easily formed by assembling amphiphilic diblock copolymers in water.^[68] This protocol may be defined as micellar-type aqueous biphasic catalysis and will be discussed in

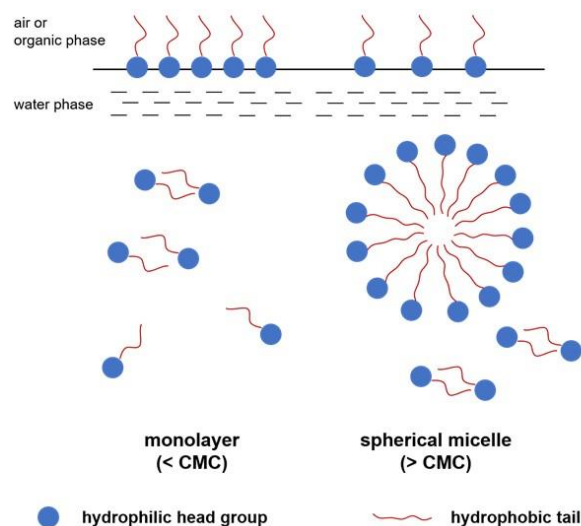
detail in the next section.



Scheme I.2.4 Illustration of CO₂-responsive Pickering emulsion for biphasic system.

I.3 Micellar-type aqueous biphasic catalysis

The hydrophilic head groups and hydrophobic tails in the amphiphilic polymer chains enable their interaction with both polar and nonpolar environments. The amphiphilic macromolecules initially form a unimolecular layer at the interface between the two phases to reduce the interfacial tension. At greater concentration, an equilibrium is established between this interfacial monolayer (also known as Langmuir-Blodgett layer) and free chains in the bulk solvents. When the concentration reaches the lower critical micelle concentration (CMC), a second equilibrium is established between the free chains and the micelle.^[69] Micelles can in principle be formed in both phases. Typically, in a aqueous/organic biphasic system, the objects formed in the aqueous phase are called micelles and those in the organic phase are called inverse micelles.^[70] This micelle assembly process is illustrated in Scheme I.3.1.

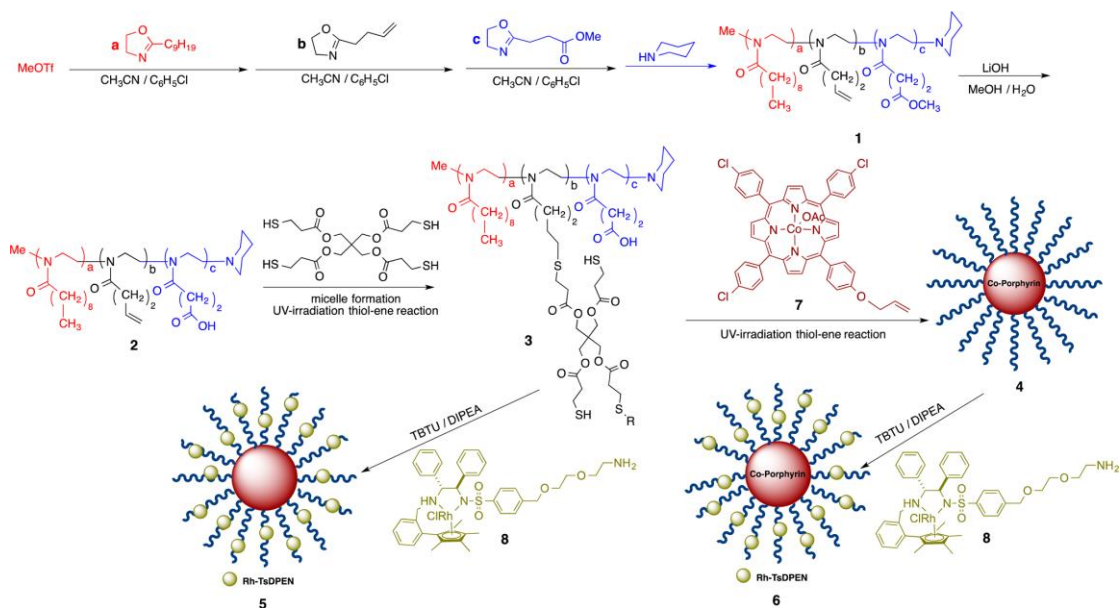


Scheme I.3.1 Schematic representation of micelles.

The use of functionalized micelles as nanoreactors in stable aqueous dispersions has recently attracted considerable attention, because kinetically stable micelles can be easily formed by assembling surfactants or amphiphilic diblock copolymers in water. In particular, amphiphilic diblock copolymers have the advantage of lower CMC and slower micelle/free arm equilibria, provided the chains are sufficiently long, thus producing more stable and persistent micelles. Since these micelles have nanoscale dimensions, they are usually called catalytic nanoreactors. Besides micelles, there are other types of macromolecular nanoreactors, for instance polymersomes,^[4] dendrimers^[71] and nanogels.^[72] This section focuses on micellar catalysis based on the polymeric micelles.

Polymeric micelles are composed of amphiphilic di(multi)block copolymers that form nanosized micellar structures with a hydrophobic core and a hydrophilic shell (for dispersion in water), or an inverse structure (for dispersion in a low-polarity solvent), which provides stability to the micelle in the desired medium.^[73] The catalyst must be anchored to the micellar core, in order to operate the catalyzed transformation in a medium that is compatible with the substrate phase and incompatible with the micelle-stabilizing phase. This ensures a high local substrate concentration and therefore a faster chemical process. To achieve this core functionality, ligands able to coordinate the

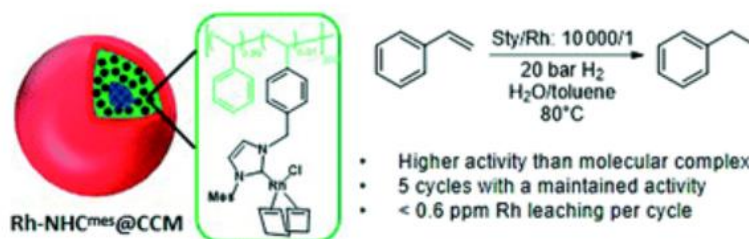
metal precatalyst can either be introduced in already assembled micelles by specific chemical reactions^[74] or by copolymerization of ligand-functionalized comonomers during the amphiphilic copolymer synthesis. As an illustrating example of loading through chemical reaction, Marcus Weck *et al.*^[75] synthesized poly(2-oxazoline) triblock copolymers via cationic ring-opening polymerization. The DLS proved the micelle formation by dispersing polymer **2** in water at a concentration higher than CMC. The multivalent tetrathiol crosslinker was used to functionalize the intermediate block via a thiol-ene reaction with the terminal vinyl groups (the black units shown in Scheme I.3.2) under UV-irradiation, resulting in crosslinking at the intermediate corona level. The remaining thiol groups were used to anchor Co-porphyrin catalysts to fabricate catalytic nanoreactors for the Co-catalyzed hydration of alkyne.



Scheme I.3.2 Synthetic scheme of the micelle supported metal catalyst.^[75]

The second method was utilized by our group to prepare a catalytic nanoreactor bearing Rh catalysts for styrene hydrogenation in aqueous biphasic catalysis.^[76] A rhodium complex bearing a styrene-functionalized NHC ligands was copolymerized into amphiphilic polymer chains which self-assembled as a core-shell architecture nanoreactor in the water phase. The synthesized nanoreactor latex was quite stable and

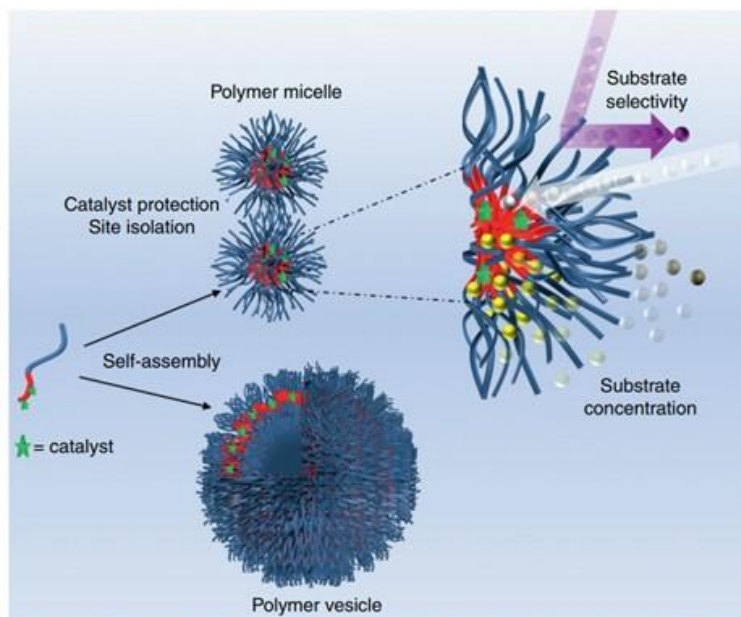
could be recycled up to four times with no obvious catalytic activity loss. In addition, the catalytic performance of this latex was superior to that of the molecular species in a homogeneous solution^[77] and without noticeable decomposition to metallic Rh nanoparticles, which was rationalized by the site isolation of the catalytic centers.^[76]



Scheme I.3.3 Schematic representation of core-shell catalytic nanoreactor prepared by RAFT polymerization.

By altering the hydrophilic/hydrophobic ratio, copolymer composition, molar mass, concentration, nature of solvents, temperature and additives, the polymer chains may self-assemble in different morphologies, such as spherical micelles, toroids, rods, fibers, vesicles and tubes.^[78] The emphasis in this section is on the spherical micelles, which are ideal for use as catalytic nanoreactors.

By applying this catalyst-loaded micelle to an aqueous-organic biphasic catalytic process, due to the hydrophobic affinity of the organic substrates for the micellar core, these can permeate through the shell into the hydrophobic core, accordingly increasing the reactants concentration and then the catalytic activity (Scheme I.3.4).^[57b] Therefore, this implementation combines the advantages of both homogeneous and heterogeneous catalysts.



Scheme I.3.4 Assembly of catalyst functionalized amphiphilic block copolymers into polymer micelles and vesicles.^[68]

The earliest report on micellar catalysis dates from the late 1970s, revealing the formation of micelles with surfactant effect.^[79] Since then, this area has witnessed a rapid development by the virtue of not only the emergence of various micelle-formation pathways, but also their suitability for different organic reaction processes. At the same time, it has to be recognized that the current commercially available surfactant species cannot meet the multitude of catalytic needs. Therefore, diverse research efforts have focused on the polymeric micelle nanoreactor preparations, features and catalytic implementation.^[69, 80]

I.3.1 Micelle-aided catalysis

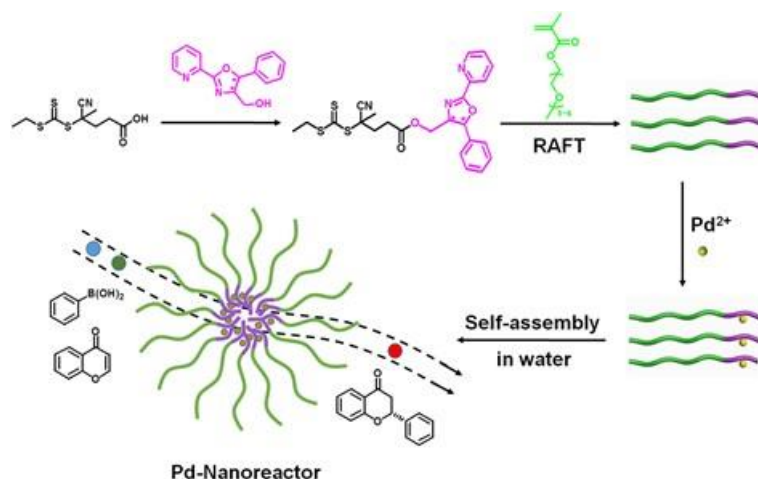
The introduction of the catalyst into the core of micellar nanoreactor can be accomplished by the copolymerization of catalyst-functionalized monomers into the hydrophobic segments followed by the self-assembly process, or by the coordination of the molecular precatalysts to the ligand-functionalized core after self-assembly.

Catalyst introduction by polymerization before micelle self-assembly

In this method, a monomer that is already functionalized with a (pre)catalyst is copolymerized into the amphiphilic chain. Various polymerization methods have been adopted to fabricate amphiphilic copolymer nano-objects^[81], such as anionic polymerization^[82], ring-opening metathesis polymerization,^[83] cationic polymerization^[84] and controlled/living radical polymerization. Among various methods, the controlled radical polymerization method dominates^[68], including nitroxide-mediated polymerization (NMP)^[85], atom transfer radical polymerization (ATRP)^[86] and RAFT^[87]. The radical polymerization has higher tolerance for water and can be used for a wide range of monomer types. Especially RAFT polymerization could be applied for one-pot or two-pot processes in order to copolymerize both hydrophilic and hydrophobic monomers with good control up to high molecular masses.^[88]

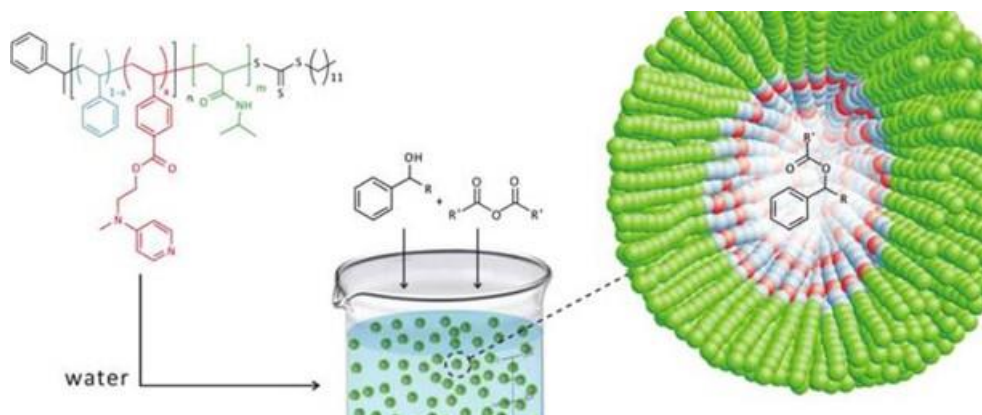
A Pd-loaded nanoreactor was fabricated by RAFT polymerization of hydrophilic oligo(ethylene glycol) methyl ether methacrylate (OEGMA₃₆), which was then chain capped by esterification of the RAFT transfer agent with the (S,S)-4-hydroxymethyl-5-phenyl-2-(2'-pyridinyl)-1,2-oxazoline (PyOx) ligand.^[87b] The Pd(TFA)₂ precatalyst was then coordinated to the pyridine-oxazoline group to afford a polymer supported palladium complex POEGMA₃₆-PyOx-Pd(II). These palladium-capped polymer chains were placed into water at room temperature (below the LCST), generating self-assembled spherical micelles, which served as nanoreactors for the asymmetric catalytic synthesis of flavanone under aqueous biphasic conditions as illustrated in Scheme I.3.5. Although the catalysis gave better results than those of unsupported pyridine-oxazoline-palladium catalysis, the catalyst recovery suffered from a great loss problem. The recycling was carried out thanks to the thermo-sensitive characteristic of the polymer. Specifically, after catalysis the product and the unreacted substrate were extracted by dichloromethane and the water phase was heated up to the phase transition temperature of the polymer. The water solution became turbid and centrifuged to recover the catalyst. The non-negligible catalyst loss might be due to the high LCST of

the polymer, leading to physical losses in the recovery process because of incomplete precipitation.^[57b, 89]



Scheme I.3.5 RAFT polymerization of core-shell catalytic nanoreactor and hydroaminomethylation application.

Besides this temperature-responsive amphiphilic core-shell polymeric nanoreactor, Rachel K. O'Reilly *et al.*^[90] synthesized a polymer with a hydrophilic poly(*N*-isopropylacrylamide) (PNIPAM) shell and a hydrophobic poly[4-(dimethylamino)pyridine]-*co*-polystyrene (PDMAP-*co*-PSt) core by RAFT polymerization techniques. The DMAP functionality in the core of the self-assembled micelle is a common nucleophilic organocatalyst for the acylation reaction in aqueous biphasic catalysis.^[91] The activity of the catalyst loaded in this nanoreactor was found to be very high compared to that of unsupported DMAP in THF. The polymeric catalyst could be reused 6 times without loss of activity. This kind of polymeric micelle can be disassembled by heating above the LCST. The polymer became a fine powder and could be recovered by centrifugation.

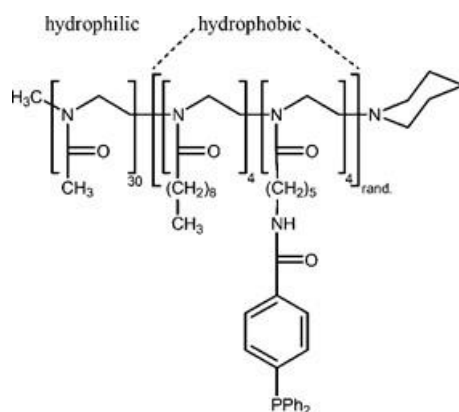


Scheme I.3.6 Core-shell catalytic nanoreactor and acylation application.

Catalyst introduction by coordination after micelle self-assembly

Another method for the catalyst introduction into the micellar core consists of binding the molecular precatalyst by coordination to the ligands that are already anchored in the core. This can be accomplished by transfer of the catalyst solution through the shell.

Ralf Weberskirch *et al.*^[92] prepared an amphiphilic poly(2-oxazoline) block copolymer with triphenylphosphane functions, shown in Scheme I.3.7. The block copolymer was loaded with $[\text{Rh}(\text{acac})(\text{CO})_2]$ or $[\text{Rh}(\text{acac})(\text{CO})_2]/[\text{Ir}(\text{coe})_2\text{Cl}]_2$ for the single-metal (Rh) or bimetallic (Rh/Ir) catalyzed hydroaminomethylation of 1-octene (Figure I.3.1). For the single-metal catalysts, a competition between amines and phosphanes for Rh coordination, as well as catalyst deactivation, resulted in an extremely low yield of the desired amine. Using the dual Rh/Ir catalyst system was found to overcome these problems: Rh was used for the olefin hydroformylation and Ir accomplished the selective hydrogenation of the enamine intermediate. The bimetallic required only 130°C and gave slightly better performances (yield: 24%, n/iso selectivity: 11 and TOF: 600 h⁻¹) than the single-metal system at 150°C (yield: 22%, n/iso selectivity: 7.5 and TOF: 461 h⁻¹).



Scheme I.3.7 Amphiphilic triphenylphosphane-functionalized poly(2-oxazoline) block copolymer.

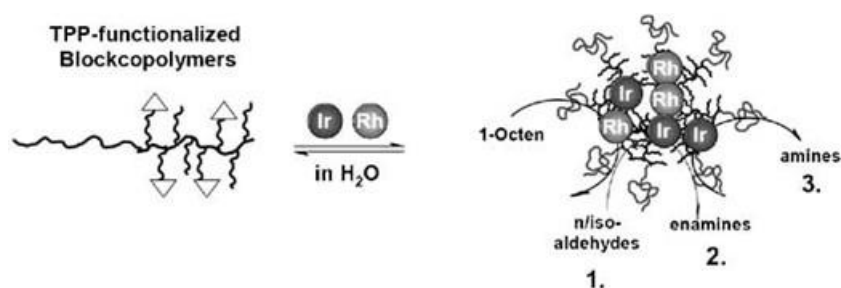
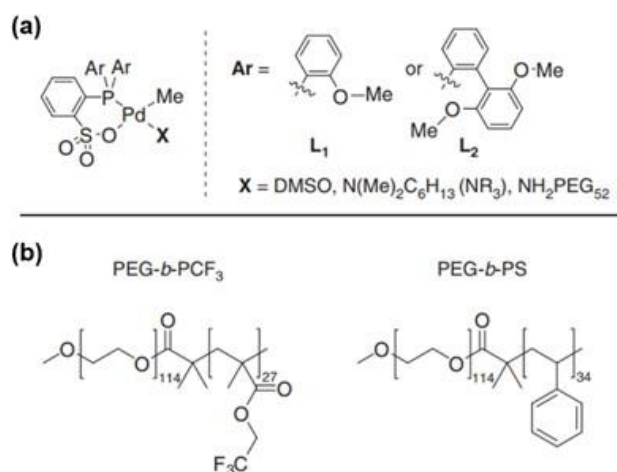


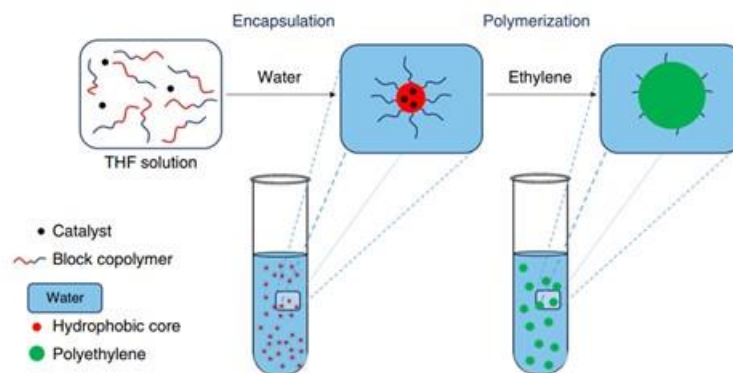
Figure I.3.1 Schematic representation of a core-shell catalytic nanoreactor self-assembly process and of the hydroaminomethylation application.

Damien Guironnet *et al.*^[93] developed a series of amphiphilic diblock copolymers as spherical micellar nanoreactors for the coordination/insertion polymerization of ethylene under aqueous biphasic conditions. These polymers were prepared by ATRP method from a chain-end-functionalized PEG macroinitiator as hydrophilic unit. The chosen hydrophobic monomers were poly (2,2,2-trifluoroethyl methacrylate (PCF₃) and polystyrene (PSt) to produce PEG-*b*-PCF₃ and PEG-*b*-PSt, see Scheme I.3.8. The micelle formation step was accomplished via an indirect method, dissolving the block copolymers in a water-miscible organic solvent (THF) followed by the addition of water, which induced aggregation and formation of stable micelles in the solvent mixture. The metal precatalyst was loaded into the micelle cores by addition as a solution in N,N-dimethylhexylamine and was assumed to remain core-confined. During the catalytic reaction, the ethylene migrated into the hydrophobic core where Pd catalyst is located.

The whole process is displayed in Scheme I.3.9. The encapsulated catalysts were found to have a significantly better performance than those obtained from the same precatalyst using a traditional miniemulsion strategy.



Scheme I.3.8 Catalysts and block copolymer structure. (a) catalysts: L₁Pd-X and L₂Pd-DMSO catalysts and (b) block copolymers: PEG-*b*-PCF₃ and PEG-*b*-PSt.



Scheme I.3.9 Catalyst encapsulation approach for ethylene polymerization in water.

The results obtained from the above examples reveal drawbacks for the micelle-aided aqueous biphasic catalysis, which are related to the equilibrium between micelles and free arms. These consist of catalyst losses at the liquid/liquid interface and as inverse micelles in the substrate/product phase (leaching), and extensive swelling, which may lead to stable emulsions and slower decantation.^[94] In that spirit, new types of unimolecular amphiphilic core-shell polymeric particles (crosslinked micelles) with

a functionalized hydrophobic core and a hydrophilic shell have attracted the research interests in recent years.

I.3.2 Crosslinked micelle-aided catalysis

Arm crosslinking in a self-assembled micelle leads to a unimolecular core-shell polymeric nano-object, in which all the amphiphilic polymer chains are tied together. Hence, the crosslinked micelle cannot excessively swell and cannot dissociate free single diblock chains. In reported contributions, unimolecular polymers of this type micelle by crosslinking reactions on the shell,^[82b, 86, 95] in the intermediate corona,^[83, 96] or in the core.^[97]

Shell- or corona-crosslinked catalytic nanoreactors

Rachel K. O'Reilly^[95c] reported water-dispersed spherical micelles with the shell crosslinked by an amidation reaction. The nanoreactor, shown in Figure I.3.2, contains terpyridine ligands linked to the hydrophobic core domain, which were used to coordinate a few metals (Fe, Ru and Cu) as precatalysts for click cycloadditions reactions.

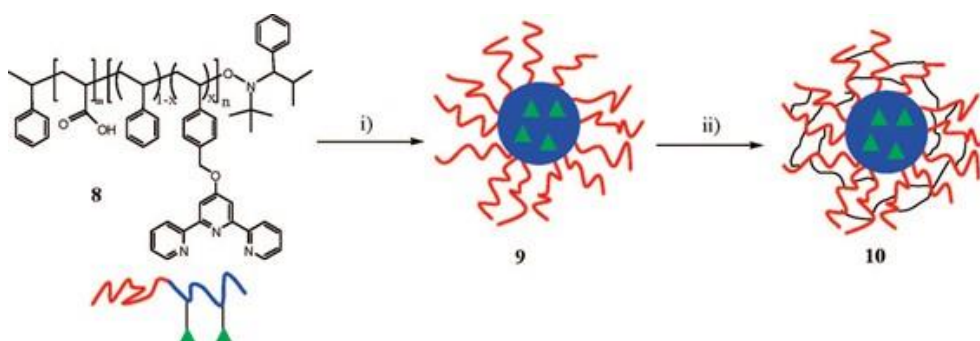


Figure I.3.2 Schematic representation of the synthesis of shell crosslinked micelles. i): self-assembly process and ii): crosslinking process by addition of 2,2'-(ethylenedioxy)bis(ethylamine).

It should be noticed that the aimed crosslinking degree was only 50% of the available acidic functions in order to maintain a certain permeability of the shell layer, ensuring the passageway for small molecules toward and out of the core. A potential problem in the preparation of these crosslinked polymers is interparticle crosslinking in concentrated solutions.

Marcus Weck *et al.*^[84b] synthesized poly(2-oxazoline)-based micelles crosslinked at the level of an intermediate corona and containing Co^{III}-salen complexes in the core and studied their use as catalytic nanoreactors for the hydrolytic kinetic resolution of terminal epoxides. The polymer synthesis route is illustrated in Figure I.3.3: the crosslinked layer was constructed by the UV activated [2+2] cycloaddition of cinnamate side chains. The micelles were loaded with Co^{II} acetate by coordination to the core-anchored salen ligands and then oxidized to produce a core-confined Co^{III}-salen catalyst. This catalyst showed high catalytic efficiency and substrate selectivity that depends on hydrophobicity. The recycling was accomplished by an ultrafiltration membrane with a molecular-weight cutoff of 30000 without apparent cobalt leaching and activity decrease until the 7th run.

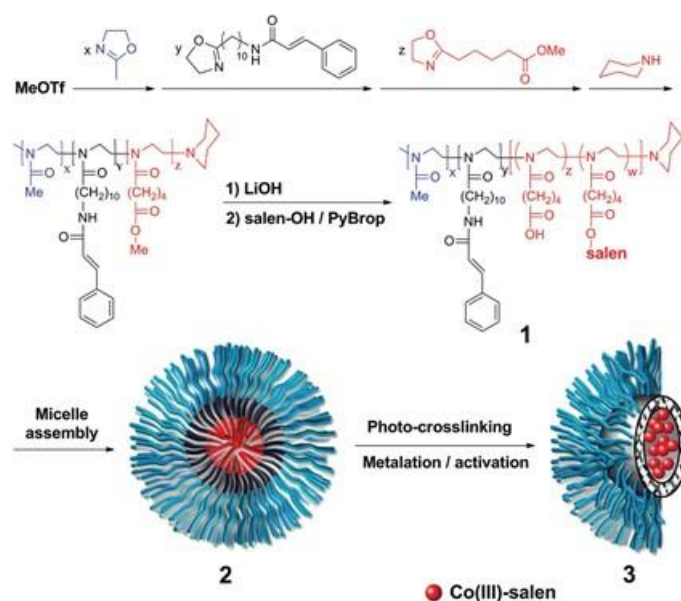
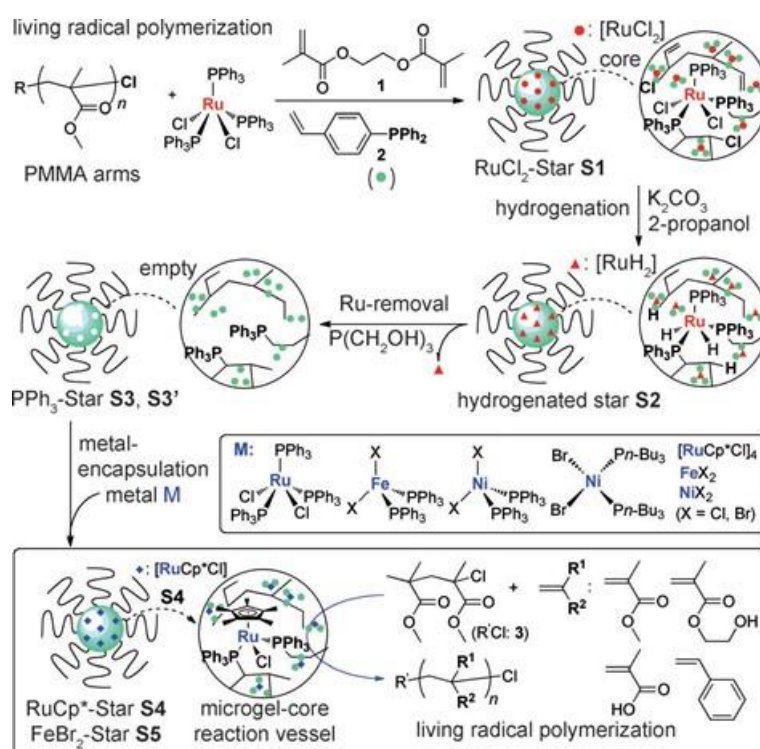


Figure I.3.3 Schematic representation of the synthesis of a poly(2-oxazoline) crosslinked micelles with a Co^{III}-salen-functionalized core.

Core crosslinked catalytic nanoreactors

Takaya Terashima, Mitsuo Sawamoto *et al.*^[98] reported an amphiphilic star polymer with a crosslinked core prepared by ruthenium-catalyzed living radical polymerization and its catalyst loading procedure. After the polymerization reaction, the core-linked phosphines were already linked to the ruthenium ATRP catalyst. By an *in-situ* ligand exchange reaction with a better ligating phosphine, tris(hydroxymethyl)phosphine, P(CH₂OH)₃, nanoreactors with metal-free core were obtained. Then new metal complexes such as [RuCp*Cl]₄, FeX₂ or NiX₂ (X = Cl, Br) were introduced to generate a variety of catalytic nanoreactors. As an example, the RuCp*@star-polymer was used for the ATRP of a variety of monomers, as shown in Scheme I.3.10, yielding a well-controlled polymerization process in contrast with an uncontrolled process for a chemically related insoluble RuCp*-Gel system. The catalyst was recycled by precipitation and reused without any activity reduction. These nanoreactors were also applied to other various catalyzed reactions, including but not limited to the hydrogenation of ketones.^[99]



Scheme I.3.10 Synthesis of metal-star catalysts by tandem catalyst interchange and star-polymer-catalyzed living radical polymerization.

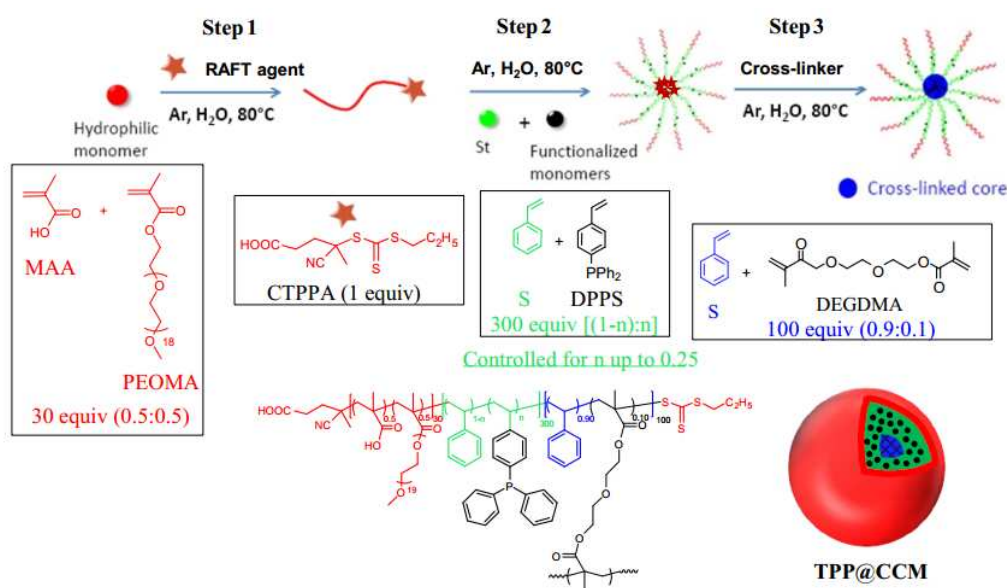
The affinity of the core structure for the substrates (core swelling) ensures the catalyst functioning in the same manner as in homogeneous catalysis and the high local concentration of both the active sites and the substrate in the nanoreactor core ensures a high rate for the catalyzed process. However, the premise of the interaction between catalysts and substrates within the nanoreactor core is efficient mass transfer of the substrates from the organic bulk phase toward the hydrophobic core through the hydrophilic shell. Based on these considerations, the composition of shell and core, the catalyst concentration, the solvent, the crosslinking density, the core dimensions *etc.* are key factors for the efficiency of the unimolecular micelle-aided aqueous biphasic catalysis.

I.4 Objectives and scope of the thesis

As stated in the previous section, unimolecular micelle-aided aqueous biphasic catalysis is an attractive way to efficiently separate and recycle catalysts from the substrate and products through the liquid/liquid biphasic implementation. It involves catalyst confinement in the core of nanoreactors, which remain confined as a stable colloidal dispersion in the aqueous phase, thus allowing catalyst recovery by decantation. This strategy has been implemented for a few molecular catalysts.

This thesis aimed at using core-crosslinked unimolecular polymers, called core-crosslinked micelles (CCM) or nanogels (NG) depending on the crosslinking strategy. The first-generation copolymers developed in our group consisted of tying together the hydrophobic chain ends of amphiphilic block copolymers with a neutral outer shell consisting of P(MAA-*co*-PEOMA) (see Scheme I.4.1). These polymers were assembled straightforwardly (multiple-gram, scalable amounts can be made in < 1 day) by a three-step one-pot process. The generated low-viscosity latex contained up to 30 wt% of well-defined triphenylphosphine-functionalized core-crosslinked micelles with

controlled diameter ($D_z = 80\text{-}110\text{ nm}$) and low polydispersity ($\text{PDI} < 0.2$). However, due to the increased lipophilicity of the outer shell at the catalyzed reaction temperatures and to micelle aggregation, the catalytic applications of this series nanoreactor suffered from significant catalyst loss and recovery problems. Therefore, we have targeted new nanoreactors where the neutral outer shell is replaced by a polyelectrolytic one.



Scheme I.4.1 Synthesis of neutral shell CCM by a three-step one-pot RAFT-PISA process in water.^[100]

These polymers were designed with a hydrophilic polycationic shell consisting of polyvinylpyridium (P4VPM^{+I}) and a hydrophobic polystyrene core, which is crosslinked by diethylene glycol dimethacrylate (DEGDMA). The polymer preparation will be performed by RAFT polymerization via the polymerization-induced self-assembly (PISA) strategy. The first objective of this thesis was the optimization of the synthetic route and polymer composition. For this purpose, the choice of outer hydrophilic shell was based on the assumption that the particle interpenetration and agglomeration problems would be corrected thanks to the increased repulsive force coming from the charged nature of the outer shell. Moreover, contrary to the neutral

P(MAA-*co*-PEOMA), the charged P4VPM⁺ is not characterized by high-temperature hydrophobicity. This part of work has been implemented in collaboration with the C₂P₂ team headed by Muriel Lansalot and Franck D'Agosto at the CPE Lyon (France).

Subsequently, triphenylphosphine-functionalized versions of these particles (TPP@CCM and TPP@NG) were prepared and characterized. These macroligands were investigated in terms of their coordination chemistry with [RhCl(COD)]₂, of interparticle metal migration, and finally applied to the aqueous biphasic hydrogenation of styrene and 1-octene as model substrates.

It was serendipitously discovered that the core-confined [RhCl(COD)(TPP@CCM)] complexes are reduced under certain conditions to generate Rh⁰ nanoparticles (NPs). Therefore, a systematic investigation of this reduction process and of the effect of various parameters on the size and morphology of the produced Rh NPs was carried out. Finally, the nanoreactor-embedded Rh NPs were applied to the catalyzed acetophenone, styrene and 1-octene hydrogenation. The catalytic performance was investigated also in terms of catalyst stability and recycling, providing useful new information about the Rh NP stabilization and mobility in the amphiphilic polymer environment.

The last part of this thesis was dedicated to the attempted preparation of non-functionalized CCMs with a polyanionic shell consisting of polystyrenesulfonate (PSS⁻ Na⁺). These negatively charged polymers are more easily accessible than the positively charged ones. This new type of outer shell is also supposed to block the particle interpenetration.

The significance of this thesis is to illustrate a novel preparation method for unimolecular micellar nanoreactors with a charged outer shell. This feature blocks the particle interpenetration with core-core contact, which was previously found to be the cause of particle-particle coupling after loading with the metal precatalyst. Equally important, this series of micellar nanoreactors lead to lower high-temperature lipophilicity, lower catalyst leaching and faster decantation than the corresponding

nanoreactors with a P(MAA-*co*-PEOMA) neutral shell and therefore have a high potential for various metal catalyzed reactions.

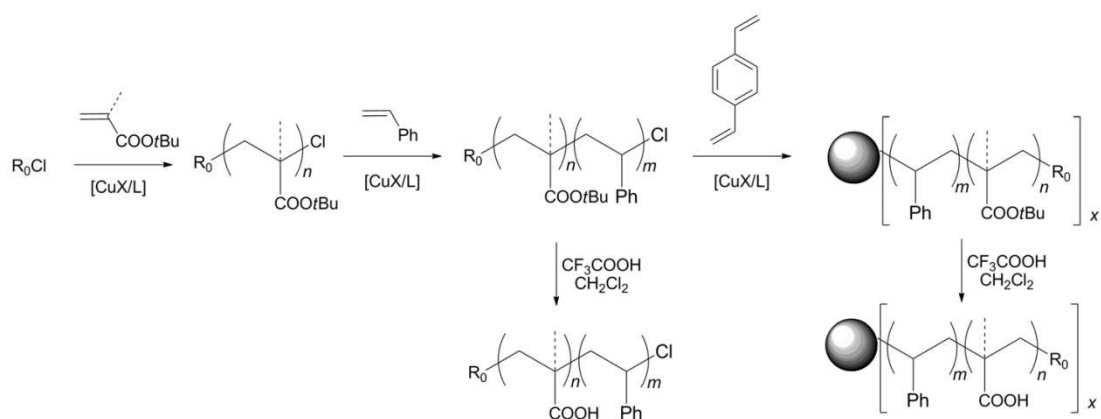
Chapter II

Synthesis and characterization of core-shell amphiphilic nanoreactor with a polycationic shell

II.1 Introduction

As mentioned in the Chapter I, in the multimolecular micelle aided catalysis protocol, the micelles would suffer from excessive core swelling and from the free arm-micelle equilibrium, which results in losses. To remove these limitations, the micelles can be made unimolecular by crosslinking the arms at the shell, corona or core levels.

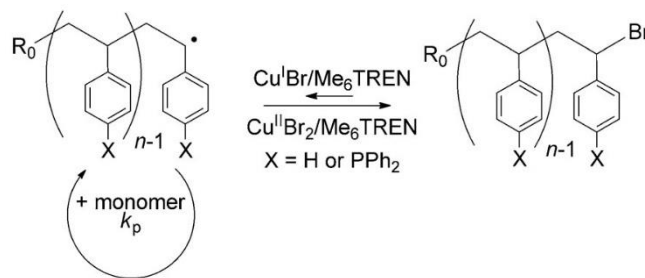
In the preliminary studies carried out by the “*Ligands, Architectures Complexes et Catalyse*” team (LAC₂) at LCC, first-generation core-crosslinked amphiphilic polymers were prepared by copper-catalyzed ATRP via the arm-first approach.^[101] This star-block polymer was designed with polymethacrylic acid (PMAA) or polyacrylic acid (PAA) hydrophilic shells and polydivinylbenzene crosslinked cores (see Scheme II.1.1). The shell blocks were obtained by the hydrolysis of linear macroinitiators poly(*tert*-butyl methacrylate)-*b*-polystyrene and poly(*tert*-butyl acrylate)-*b*-polystyrene. Then they were crosslinked by DVB and hydrolyzed to PMAA and PAA to obtain the deprotonated shells. However, the syntheses suffered from incomplete crosslinking, leaving a significant fraction of free linear diblock chains, which is a frequently encountered limitation for this convergent method of syntheses.



Scheme II.1.1 General strategy for the construction of core-crosslinked amphiphilic star-block copolymers.^[101]

In order to make use of these polymers as catalytic nanoreactors, they are required

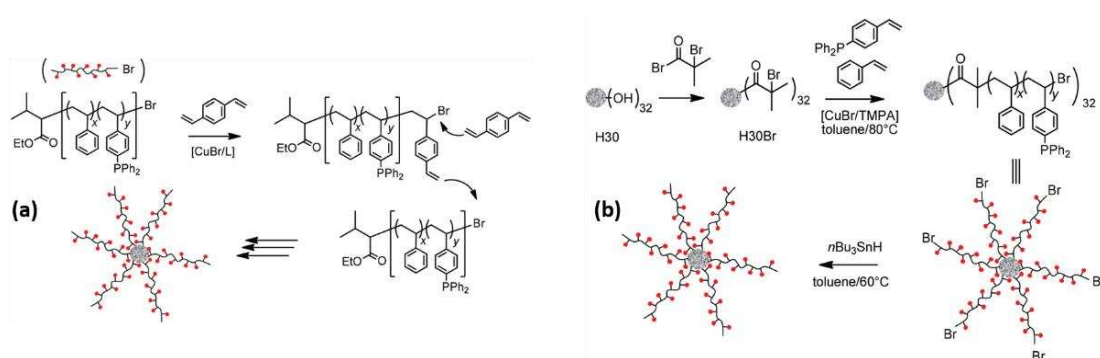
to be contain covalently bonded ligands to anchor the catalytic centers.^[102] For that purpose, another polymer was developed. A first investigation was devoted to the ATRP copolymerization of styrene and 4-diphenylphosphinostyrene, which had not been previously reported using a copper catalyst (see Scheme II.1.2), in order to generate triphenylphosphine-functionalized polystyrene chains, P(St-*co*-DPPS). In the end of the reaction, the copper catalyst was almost completely removed (the residual copper was estimated to be 1.5% of the amount used for the polymer synthesis). The obtained copolymers were coordinated with [Rh(acac)(CO)₂] and used for hydroformylation of octene under homogeneous conditions in toluene. It was found that the linear-to-branched (l/b) selectivity for the Rh@polymer-catalyzed reaction improved a little compared to the reaction catalyzed by the molecular analogue (Rh@PPh₃).



Scheme II.1.2 Atom transfer process for poly(St-*co*-DPPS) made by ATRP.^[102]

Given the success of the atom transfer copolymerization of styrene and DPPS to yield well-controlled blocks, core-crosslinked star-block copolymers synthesized by arm-first (Scheme II.1.3a) or core-first (Scheme II.1.3b) methods via copper-catalyzed ATRP.^[103] In the former strategy, the styrene and DPPS were first copolymerized by ATRP or ARGET (Activator Regenerated by Electron Transfer)-ATRP methods, followed by crosslinking with *p*-divinylbenzene (DVB). However, because of the imperfect chain-end bromide functionality in the macroinitiators, the DVB crosslinking step yielded star polymers contaminated with a significant amount of non-extended linear chains. An alternative crosslinking step by EGDMA (ethyl glycol dimethyl methacrylate) lead to macrogelation.

The strategy was therefore turned to the divergent approach (core-first method). The H30Br macroinitiator containing 32 Br-functional ends was designed from the commercial initiator Boltorn™ H30 shown as Scheme II.1.3b. After the ATRP of the styrene-DPPS mixture from these 32 arms, the resulting star copolymer had a controlled size distribution. Being loaded with $[\text{Rh}(\text{acac})(\text{CO})_2]$, this copolymer was also applied in the 1-octene hydroformylation under homogeneous conditions, yielding a lower rate relative to the catalyst anchored on the linear copolymer and a slightly higher l/b ratio.



Scheme II.1.3 (a) convergent polymer synthesis by arm-first method and (b) divergent polymer synthesis by core-first method.^[103]

In order to make use of this kind of unimolecular core-shell copolymer into the aqueous biphasic homogeneous catalysis, the subsequent work in our team aimed at constructing a star copolymer with a hydrophilic shell and a hydrophobic core where the catalytic reaction occurs. Considering the problem that part of the Cu catalyst might remain entrapped in the star polymer core, ATRP would not be optimal synthetic method.

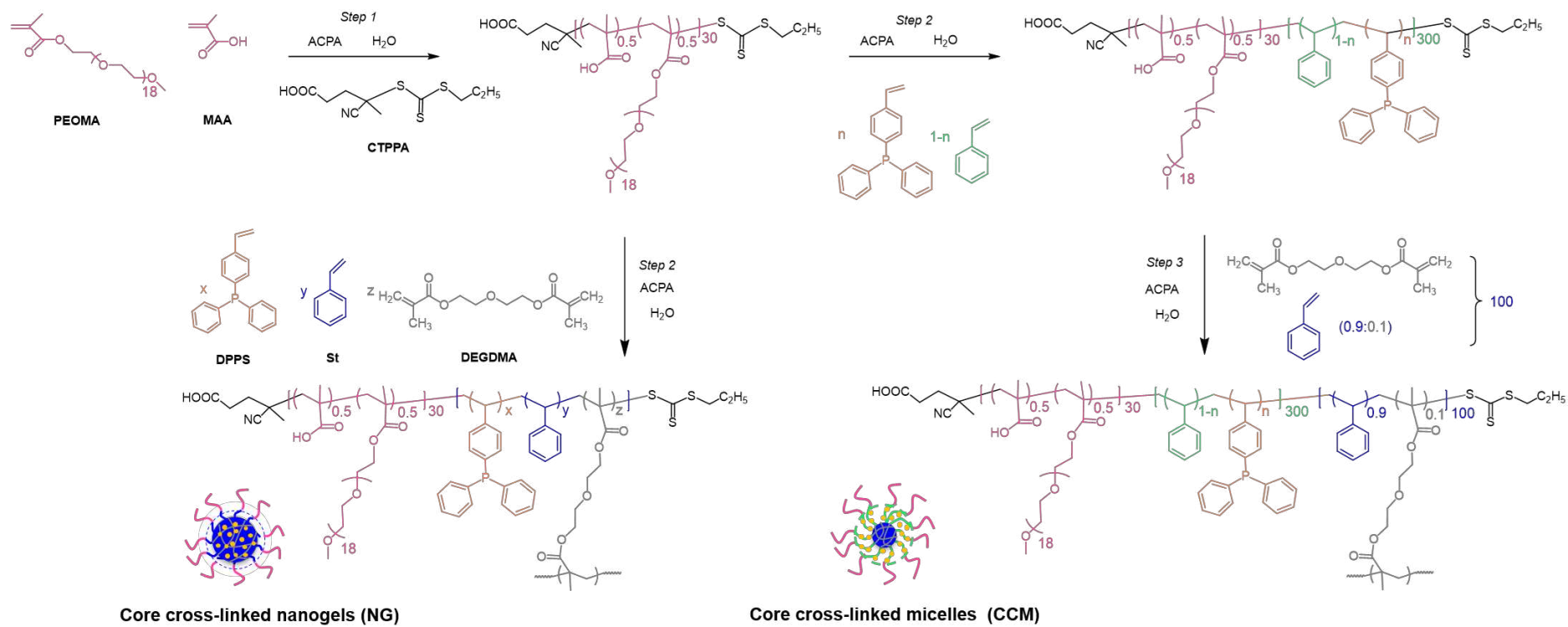
As discussed in Chapter I, RAFT polymerization combined with the PISA strategy could be extrapolated to a one-pot or two-pot process for preparing amphiphilic copolymers in many solvents. On the other hand, this strategy is widely used for the polymerization of a variety of monomers, including neutral, cationic, anionic and zwitterionic monomers. The obtained polymers are characterized by controlled molecular weights and low polydispersity and can be made with different morphologies,

such as spheres, nanofibers, vesicles, cylinders and so on.

Thus, further efforts within the LAC₂ team to access core-shell amphiphilic unimolecular polymer-based nanoreactors for aqueous biphasic catalysis was reoriented toward the emulsion polymerization mediated by RAFT via the PISA approach. The first generation nanoreactor was designed with a polystyrene core anchored ligands, a neutral hydrophilic shell based on randomly copolymerized methacrylic acid (MAA) and poly(ethylene oxide) methyl ether methacrylate (PEOMA), and crosslinked via the use of diethylene glycol dimethacrylate (DEGDMA).^[104] This choice was suggested by the already optimized synthesis of self-assembled micelles of linear P(MAA-*co*-PEOMA)-*b*-PSt by RAFT-PISA in the laboratory of our collaborators (C2P2 team at CPE Lyon).^[104a] Hence, core phosphine-functionalized analogues were developed and finally crosslinked at the core with DEGDMA, diluted with styrene (10/90). The resulting polymer architecture is named “core-crosslinked micelle” (CCM) and the average formula of a single polymer chain is $R_0-(MAA_{0.5}\text{-}co\text{-}PEOMA_{0.5})_{30}\text{-}b\text{-}(St_{1-n}\text{-}co\text{-}DPPS_n)_{300}\text{-}b\text{-}(St_{0.9}\text{-}co\text{-}DEGDMA_{0.1})_{100}\text{-}SC(S)SPr$, where the chain ends ($R_0 = C(CH_3)(CN)CH_2CH_2COOH$ and $SC(S)SPr$) are provided by the initial trithiocarbonate RAFT agent (CTPPA) (see **Scheme II.1.4**).

This work was carried out in collaboration with the C2P2 group for the polymer synthesis and with a group in the Laboratoire de Génie Chimique (Toulouse, France) for the hydroformylation catalysis tests.^[94, 105] It is important to point out that the crosslinking step led to spherical and well-defined single CCMs with narrow size distribution (as verified by the DLS and TEM characterization) only when DEGDMA was highly diluted in styrene. Using neat DEGDMA or a more concentrated (> 10% v/v) DEGDMA solution in styrene led to the formation of a macrogel. This phenomenon can be attributed to a dynamic interpenetration of the micelles (as proven by metal migration studies),^[72] which leads to core-core contact and interparticle crosslinking.

Scheme II.1.4 Synthesis pathway toward block copolymer nanoreactor with a neutral-shell.



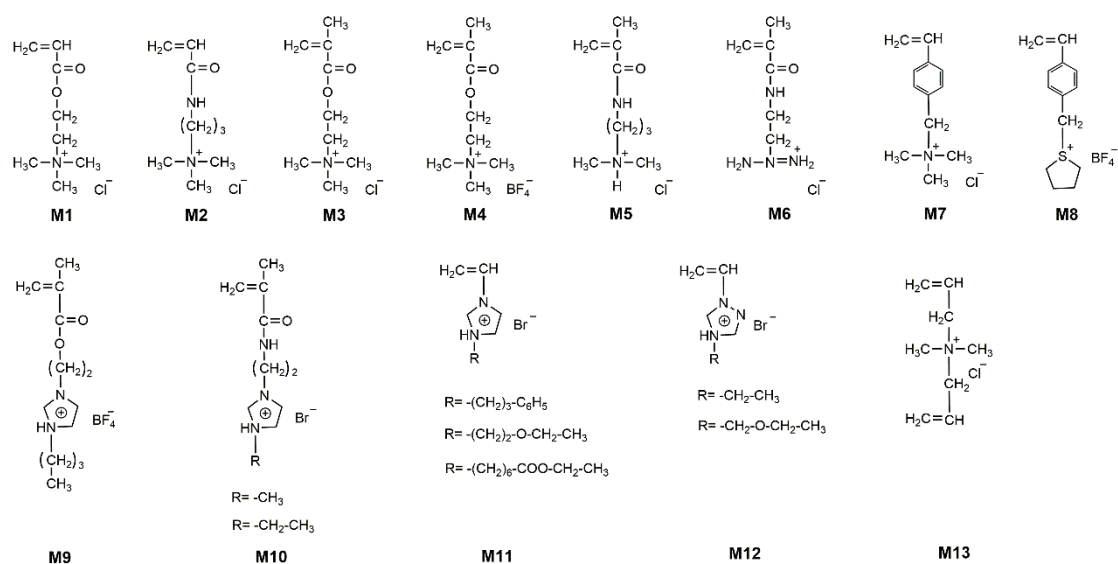
In subsequent work, analogous CCMs with different core-linked ligands were also made: bis(*p*-methoxyphenyl)phenylphosphine (BMOPPP) and nixantphos, by copolymerizing appropriately functionalized styrenes with regular styrene: 4-(bis(*p*-methoxyphenyl) phosphinostyrene^[106] and a 4-styryl-functionalized nixantphos^[107]. In order to use this CCM as catalytic nanoreactor, the metal precursor, [Rh(acac)(CO)₂], was introduced into the toluene-swollen cores and coordinated to the phosphine ligands. These nanoreactors were applied to the aqueous biphasic hydroformylation of 1-octene and showed excellent activity and moderate catalyst leaching.^[106] In both cases, CCMs with spherical shape and narrow size distribution could be obtained. However, the maximum amount of ligand-functionalized monomer was lower in these cases (5% in the former case, 1% in the latter, vs. 25% in the case of DPPS). The reason for this is the need to dissolve completely the ligand-functionalized comonomer into styrene, in order to obtain a well-behaved two-phase emulsion polymerization system before self-assembly.

A different type of architecture, having a fully crosslinked hydrophobic core and named “nanogel” (NG) resulted from the combination of steps 2 (chain extension of the hydrosoluble R₀-(MAA_{0.5}-*co*-PEOMA_{0.5})₃₀-SC(S)SPr macroRAFT agent) and 3 (crosslinking) into a single step (see **Scheme II.1.4**). This NG was prepared by chain extension of R₀-(MAA_{0.5}-*co*-PEOMA_{0.5})₃₀-SC(S)SPr by the RAFT-PISA copolymerization of styrene, DPPS and DEGDMA monomers. This procedure also led to well-defined spherical polymer particles with narrow size distribution. However, it was later found that the nanogel generation step (simultaneous chain extension and crosslinking) works more reliably if it is preceded by a chain extension of the hydrosoluble macroRAFT agent with a short polystyrene block (*e.g.* 50 monomer units), sufficient to lead to micellar self-assembly. This makes the subsequent step more robust, with lower risk of macrogelation. The major difference between the CCM and NG particles is that polymer-bonded ligands for catalyst anchoring are outside of the crosslinked part for the CCM and inside for the NG.^[72]

The efficiency of the CCM and NG particles, after metal coordination, was demonstrated in the aqueous biphasic rhodium-catalyzed hydroformylation of a model water-insoluble α -olefin (1-octene^[72, 94, 105-106, 108]) and in the Rh-catalyzed hydrogenation of 1-octene and styrene^[109]. The biphasic nature of the reaction system allowed the simple recovery of the catalyst phase by decantation and its reuse in subsequent cycles.

In spite of their remarkable efficiency in catalysis, these nanoreactors still suffered from non-negligible catalyst losses in the organic product phase and from slow decantation. These phenomena were shown to result from the high-temperature lipophilicity of the neutral P(MAA-*co*-PEOMA) shell and from particle aggregation. The latter is the consequence of particle interpenetration.^[100] In order to correct these problems, it was then envisaged to modify the polymer scaffold by replacing the neutral hydrophilic shell with a polyelectrolytic one. This is the major objective of my thesis.

Thanks to the intense research on the RAFT polymerization of cationic monomers (shown in Figure II.1.1), the first targeted polymer involved a polycationic shell. This polymer was designed with a P4VPMe^{+I}⁻ cationic shell. The synthesis of the corresponding phosphine-functionalized nanoreactors is described in the next section.



- M1: 2-(acryloyloxy)ethyl trimethylammonium chloride ^[110]
 M2: 2-(methacryloylamino)propyl trimethylammonium chloride ^[111]
 M3: 2-(methacryloyloxy)ethyl trimethylammonium chloride ^[112]
 M4: 2-(methacryloyloxy)ethyl trimethylammonium tetrafluoroborate ^[113]
 M5: 2-(methacryloylamido)propyl dimethylmethanaminium chloride ^[114]
 M6: N-(2-guanidinoethyl)methacrylamide hydrochloride ^[87c]
 M7: 2-vinylbenzyl trimethylammonium chloride ^[115]
 M8: 4-vinylbenzyltetrahydrothiophenium tetrafluoroborate ^[116]
 M9: 2-(1-butylimidazolium-3-yl)ethyl methacrylate tetrafluoroborate ^[117]
 M10: 2-(1-methylimidazolium-3-yl)ethyl methacrylate bromide and 2-(1-ethylimidazolium-3-yl)ethyl methacrylate bromide ^[118]
 M11: 1-vinylimidazolium bromide ^[119]
 M12: 1-vinyltriazolium bromide ^[120]
 M13: diallyldimethylammonium chloride ^[121]

Figure II.1.1 Chemical formulas of used cationic monomers for RAFT polymerization.

II.2 RAFT polymerization of phosphine-free cationic-shell copolymer

In this section, the synthesis of the first example of a polyelectrolytic shell CCM with a hydrophobic PSt core and a polycationic shell based on quaternized (methylated) 4-vinylpyridine (4VP) units, $-\text{[CH}_2\text{-CH(4-C}_5\text{H}_4\text{NMe}^+\text{I}^-)]_n-$ (4VPM $^+\text{I}^-$) will be described. In order to optimize the synthesis of these new objects, polymers with non-

functionalized PSt chains in the hydrophobic core were first developed. In order to simplify the symbol in this thesis, the neutral-shell polymers are acronymized as CCM-N and NG-N, cationic-shell polymers are CCM-C and NG-C.

II.2.1 Preliminary optimization studies

To obtain a P4VPMe⁺I⁻ shell, the initial attempts were made to directly polymerize 1-methyl-4-vinylpyridinium iodide, CH₂=CH-4-C₅H₄NMe⁺I⁻ to form a hydrosoluble R₀-(4VPMe⁺I⁻)_x-SC(S)SPr macroRAFT agent under conditions identical to those previously optimized for the CCM with the neutral P(MAA-*co*-PEOMA) shell.^[122] However, this polymerization was unsuccessful. In a control experiment, no polymerization of this monomer was observed with either ACPA or azobisisobutyronitrile (AIBN) as radical initiator in a 1:2 dioxane-water solution. In this respect, it can be noted that vinylpyridinium monomers can undergo free radical polymerization,^[123] but the kinetic behavior is peculiar with a high reaction order in the monomer (*e.g.* 2.7),^[123a] and thus, the polymerization is too slow in dilute solutions. The RAFT polymerization of a vinylpyridinium salt has apparently never been reported, although it has been shown that a controlled RAFT polymerization takes place for other cationic monomers, like imidazolium, ammonium, phosphonium salts (Figure II.1.1). Poly(4-vinylpyridinium) copolymers have also been obtained by free radical polymerization of 4-vinylpyridine followed by quaternization with different alkyl bromides such as decyl bromide (P4VPBrD),^[124] isopentyl bromide (P4VPIPBr)^[124] and octyl bromide (P4VP-C₈Br),^[125] see Figure II.2.1.

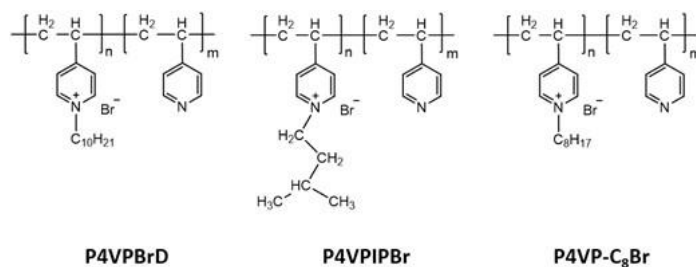
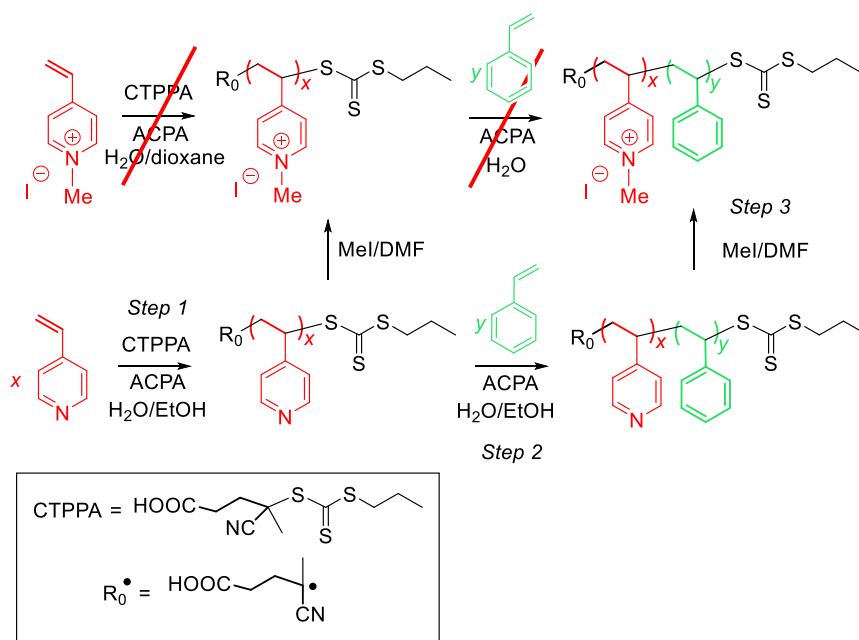


Figure II.2.1 Poly(4-vinylpyridinium) copolymers.

In order to overcome this obstacle, the first step of the synthesis was then turned into a RAFT polymerization of neutral 4VP, which required using a water/ethanol mixture in order to keep the system homogeneous and maintain good conditions for further PISA under the same operating conditions. The successful polymer synthesis required removing a few bottlenecks, see Scheme II.2.1.



Scheme II.2.1 Synthesis of the $R_0\text{-(4VPMe}^+\text{I}^-)_x\text{-}b\text{-St}_y\text{-SC(S)SPr}$ diblock copolymer.

The RAFT polymerization of 4VP has already been reported in the literature in bulk,^[126] toluene/ethanol mixture,^[127] isopropanol,^[128] ethanol,^[129] and THF^[130] but apparently never in a water/ethanol mixture. It was carried out in 70/30 (v/v) water/ethanol at 70 °C, initially targeting a low degree of polymerization (step 1 in

Scheme II.2.1 with $x = 60$). The polymerization proceeded to a 93% monomer consumption, and the resulting R_0 -4VP₅₆-SC(S)SPr product showed a narrow molar mass distribution ($D = 1.09$) with $M_n = 5800 \text{ g mol}^{-1}$ (vs. a theoretical value of 6100 g mol^{-1}), indicating a good control. The conversion versus time curve and the SEC analysis are available in the Figure II.2.2, and the NMR spectrum of the final solution is shown in Figure II.2.3a. Additional control experiments have shown the absence of reactivity between the RAFT agent and the monomer, as well as between the RAFT agent and MeI.

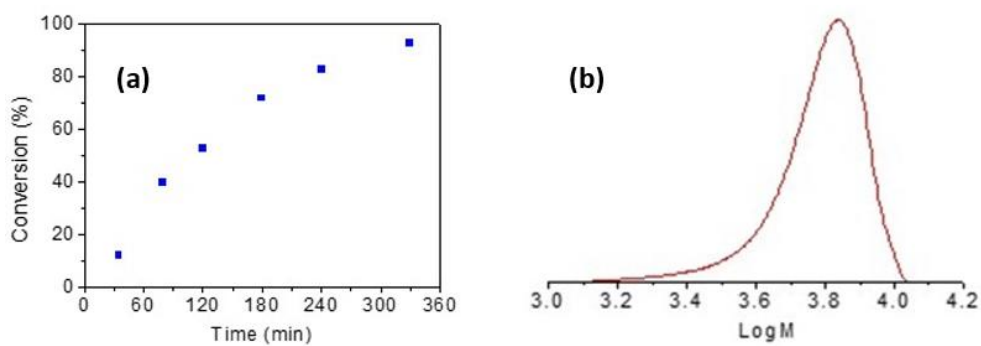


Figure II.2.2 (a) Conversion vs. time curve for the RAFT polymerization of 4VP and (b) SEC chromatogram of the resulting R_0 -4VP₅₆-SC(S)SPr.

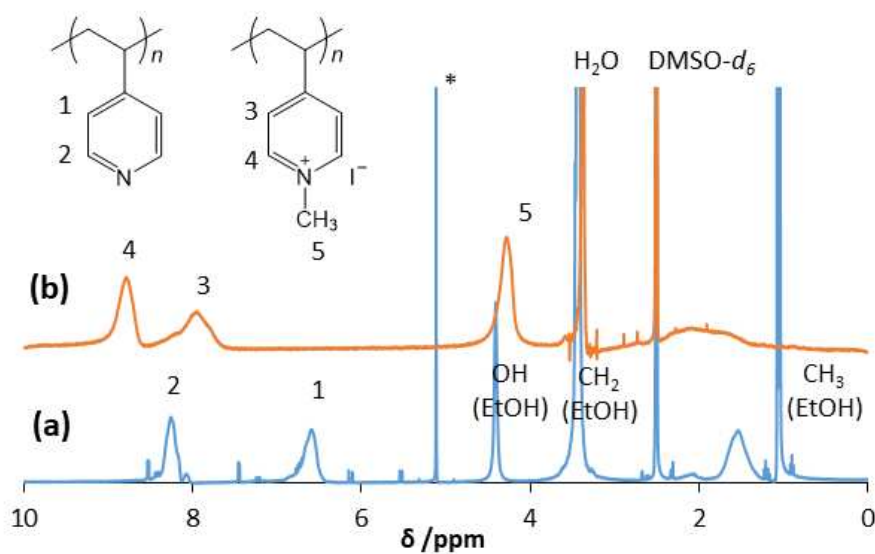


Figure II.2.3 ¹H NMR spectra in DMSO-*d*₆ of (a) R_0 -4VP₅₆-SC(S)SPr at the end of the polymerization and (b) isolated R_0 -(4VPMe⁺I)₅₆-SC(S)SPr macroRAFT. In spectrum (a),

the methylene resonance of the ethanol co-solvent overlaps with the stronger water resonance and the starred resonance is the 1,3,5-Trioxane internal standard used to monitor the monomer conversion.

Full quaternization of the P4VP block in this polymer was then accomplished by reaction with excess MeI in dimethylformamide (DMF) to yield $R_0-(4VPMe^+I^-)_{56}-SC(S)SPr$, aiming at a direct chain extension with a PSt block. The product was obtained as a yellowish solid after removing DMF by dialysis against pure water and freeze-drying. This procedure also removed the water-soluble $Me_2NH_2^+I^-$ coproduct, the formation of which was evidenced by NMR study.

Control experiments for the generation of $Me_2NH_2^+$ from the reaction of MeI with DMF in water

No reaction takes place between DMF and water in the absence of acidity. The addition of MeI to water or to water-EtOH mixtures does not generate any acidity (*e.g.* HI) because of immiscibility. However, the addition of a Brønsted acid (HCl or HI) to an aqueous solution of DMF induces hydrolysis of DMF with generation of $Me_2NH_2^+$ and formic acid (HCOOH), Figure II.2.4. The alternative addition of MeI equally generates the $Me_2NH_2^+$ ion, formic acid and MeOH, plus a small amount of methyl formate, which led us to propose the mechanism for the action of MeI (see Scheme II.2.2 and Scheme II.2.3). The hydrolysis promoted by MeI generates HI, which then takes over to promote faster hydrolysis with formation of formic acid and methanol.

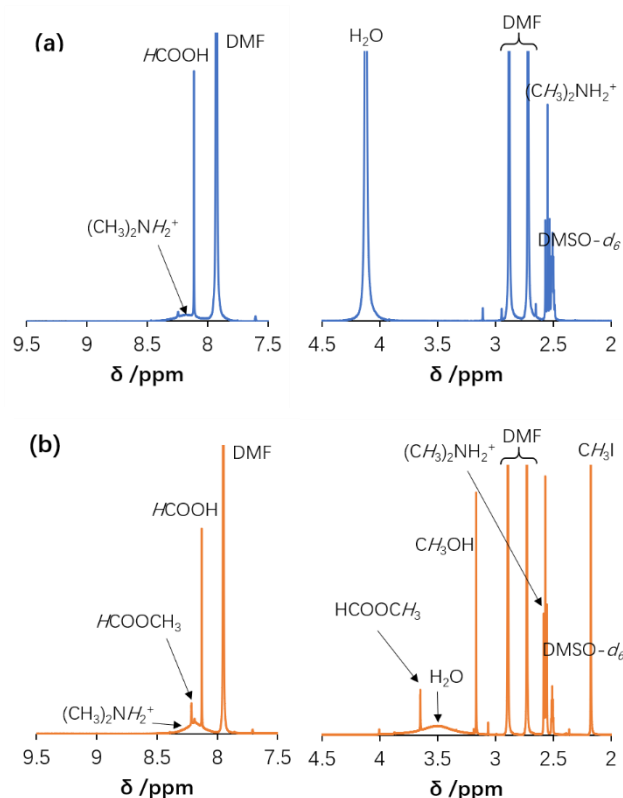
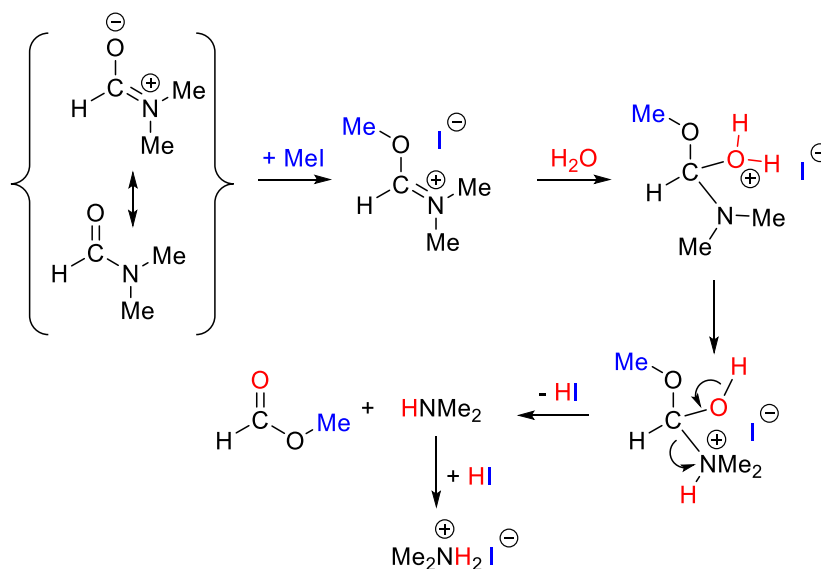
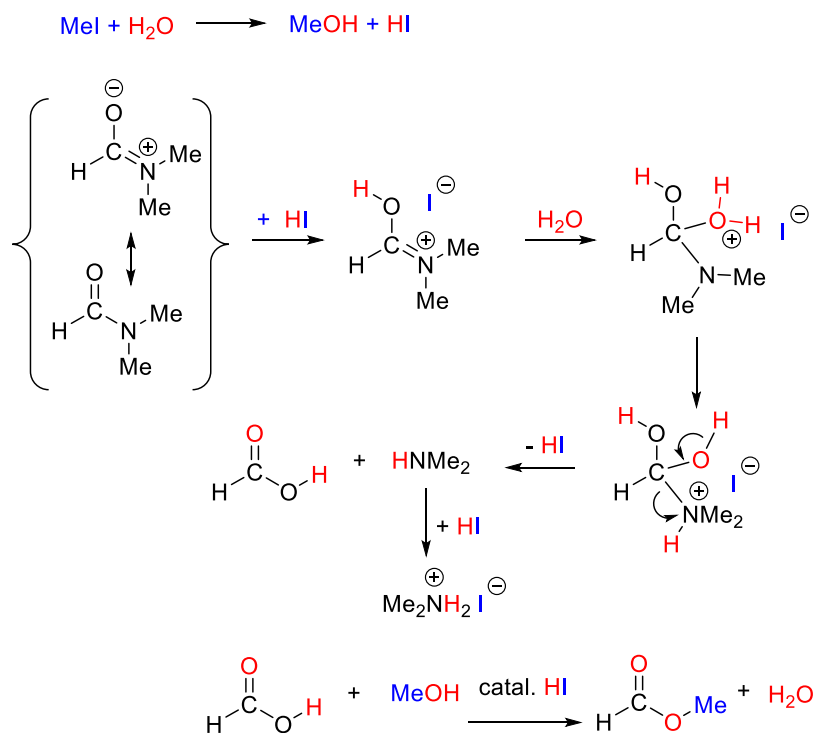


Figure II.2.4 ^1H NMR spectra in $\text{DMSO-}d_6$ of the products obtained from the hydrolysis of DMF in water promoted by (a) HI and (b) MeI.



Scheme II.2.2 Proposed mechanism for the MeI-promoted hydrolysis of DMF. It is also possible to envisage the same mechanism with initial hydrolysis of MeI to HI (see Scheme II.2.3 below), which would however lead to HCOOH directly. The observed ^1H NMR resonance of HCOOCH₃ (Figure II.2.4b) indicates that, if this happens, the formate ester must be formed again by HI-catalyzed esterification.



Scheme II.2.3 Proposed alternative mechanism.

The ^1H NMR spectrum of the isolated $\text{R}_0\text{-(4VPMe}^+\text{I}^-)_{56}\text{-SC(S)SPr}$ in $\text{DMSO-}d_6$ (Figure II.2.3b) shows that the proton resonances of the P4VP aromatic CH protons at δ 8.21 and 6.55 ppm have been fully replaced by those of the $-\text{C}_5\text{H}_4\text{NMe}^+$ rings of the $\text{P4VPMe}^+\text{I}^-$ block at δ 8.77 and *ca.* 8 ppm (br) plus the Me resonance at δ 4.2 ppm.

After redispersion in water, a chain extension with styrene was attempted. However, after 3 h at 80 °C in the presence of ACPA, the conversion was very low (< 5%), and no latex was formed. Prolonging the reaction overnight did not lead to higher conversions. A possible rationalization of the lack of chain extension is based on the charged nature of the macroRAFT agent. As already mentioned in the literature, the charged nature of the macroRAFT may disturb the first addition-fragmentation steps.^[131] Armes *et al.*^[132] have recently synthesized anionic diblock copolymer nanoparticles via RAFT-PISA aqueous dispersion polymerization formulation. They showed that the extension of a poly(2-hydroxypropyl methacrylate) block with an hydrophilic anionic block based on poly(potassium 3-sulfopropyl methacrylate) (PKSPMA) led to the formation of ill-defined micellar aggregates. This is most likely

due to the strong polyelectrolyte nature of the PKSPMA block, which results in lateral repulsive electrostatic forces between monomers and macroradicals, thus impeding their efficient contacts and micellar self-assembly. Meanwhile, D'Agosto and Lansalot *et al.*^[88] adopted the same procedure to prepare poly(acrylic acid)-*b*-polystyrene latexes at different pH values. Probably for the same reason, the RAFT polymerization of styrene with a PAA macroRAFT agent showed an inhibition period that increased from 3 h (reaction system pH = 2.5) to 3.5 h (reaction system pH = 3.5) or even to 8 h (reaction system pH = 4.5), corresponding to the gradual PAA macroRAFT ionization from a non-ionized system to a fully ionized one. However, successful chain extensions by RAFT-PISA were reported for quaternized poly[2-(dimethylamino)ethyl methacrylate] with 2-hydroxypropyl methacrylate^[133] and for poly(imidazolium-substituted methacrylate) with 2-vinylpyridine.^[134]

In order to circumvent this new obstacle, the direct chain extension of R₀-4VP₅₆-SC(S)SPr with a PSt block was then carried out before methylation (step 2 in Scheme II.2.1 with $y = 247$). In this respect, the literature shows the use of the same strategy, using NMP, to synthesize a related diblock copolymer, P(4VPR⁺Br⁻)-*b*-PDMAA: initial 4VP polymerization, followed by extension with DMAA and final quaternization of the P4VP block pyridine rings by RBr.^[135] The RAFT method has previously been used to generate PSt-*b*-P4VP polymers by sequential monomer addition by extending a PSt macroRAFT chain with a P4VP block in a variety of solvents (DMF,^[136] MeOH,^[137] and CO₂/isopropanol^[128b]) or in bulk^[138] and also by extending a P4VP macroRAFT with a PSt block in methanol^[139] or methanol/water^[87a] involving PISA. Starting with the R₀-4VP₅₆-SC(S)SPr macroRAFT agent led to the formation of a R₀-4VP₅₆-*b*-St₂₄₇-SC(S)SPr product with $\bar{D} = 1.1$ for $M_n = 35500 \text{ g mol}^{-1}$, versus a theoretical molar mass of 32000 g mol^{-1} . The conversion as a function of time (Figure II.2.5a) is characterized by an induction time, typical of PISA, as in the previously developed CCM with the neutral P(MAA-*co*-PEOMA) shell.^[94] After 2 h, the conversion already reached a maximal value (~82%), and a stable latex was obtained. The SEC traces (Figure II.2.5b)

illustrate a good control of the polymerization, while DLS revealed the formation of particles with a diameter around $D_z = 38$ nm and narrow size distribution (PDI = 0.09), see Figure II.2.6a. The particle morphology was observed by TEM, Figure II.2.6b, indicating the formation of small spherical particles, consistent with the DLS analysis. It is worth mentioning here that the nonquantitative conversion of 4VP in the first step (93%) is not an impediment for a successful self-assembly during the PSt block growth.

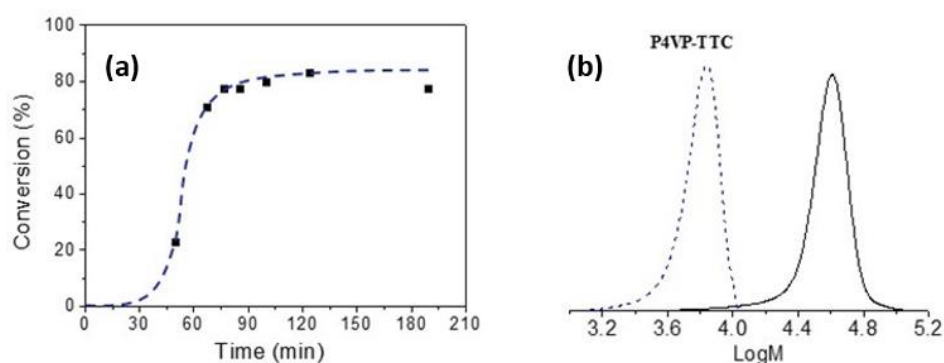


Figure II.2.5 (a) Conversion vs. time curve for RAFT polymerization of styrene in $\text{H}_2\text{O}/\text{EtOH}$ (70/30, v/v) mixture at 80°C using the $\text{R}_0\text{-4VP}_{56}\text{-SC(S)SPr}$ macroRAFT agent (experimental points and arbitrary smoothed dashed line) and (b) SEC chromatograms for the $\text{R}_0\text{-4VP}_{56}\text{-SC(S)SPr}$ macroRAFT and the $\text{R}_0\text{-4VP}_{56}\text{-}b\text{-St}_{247}\text{-SC(S)SPr}$ copolymer.

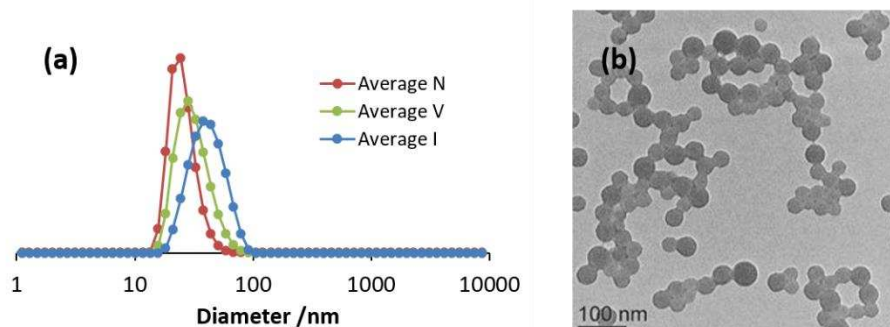


Figure II.2.6 (a) DLS (unfiltered sample) and (b) TEM characterizations for the $\text{R}_0\text{-4VP}_{56}\text{-}b\text{-St}_{247}\text{-SC(S)SPr}$ latex.

The third step of the polymer synthesis was the methylation of the P4VP block by MeI. For this purpose, a polymer with a slightly different block molar mass was initially used, $\text{R}_0\text{-4VP}_{137}\text{-}b\text{-St}_{344}\text{-SC(S)SPr}$, because this block molar mass would be suitable for

generating spherical particles by direct crosslinking according to our previous studies on the neutral polymers.^[94] The low slope of kinetic monitoring curve (Figure II.2.7) on this polymerization indicates the presence of an induction time identical to the polymerization of 56 4VP units.

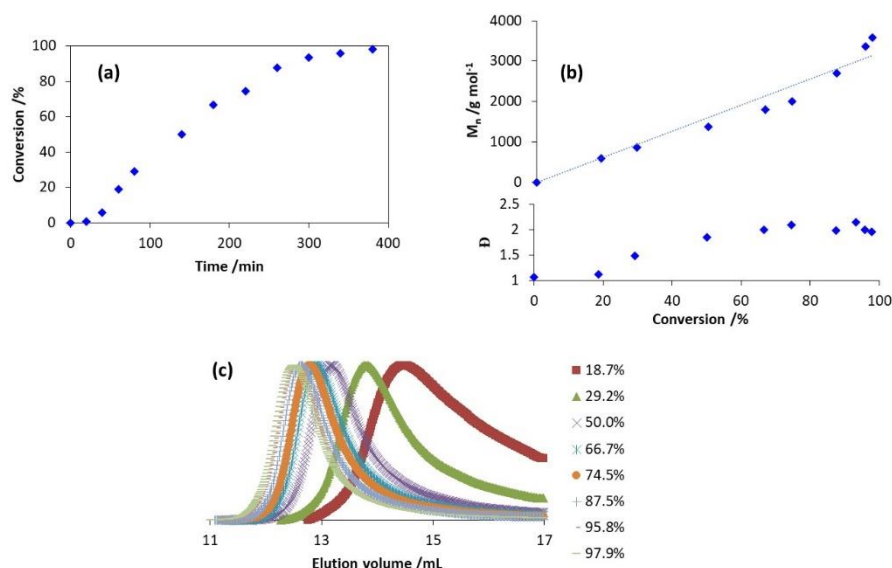


Figure II.2.7 Synthesis of R_0 -4VP₁₃₇-SC(S)SPr: (a) monitoring (from the ^1H NMR data) of the monomer consumption; (b) evolution of the molar mass and \bar{D} vs. conversion from the SEC analysis in DMF with 10 mM LiBr; (c) SEC traces evolution with conversion.

The ^1H NMR characterization of 4VP polymerization is given in Figure II.2.8. The 4VP monomer resonances at δ 5.50 ($-\text{CH}_2-\text{CH}-$, d), 6.10 ($-\text{CH}_2-\text{CH}-$, d) and 6.72 ($-\text{CH}_2-\text{CH}-$, dd) at t_0 disappeared in the end of polymerization, indicating the total monomer consumption. The P4VP alkyl CH protons at δ 1.54 ppm, aromatic CH protons at δ 8.21 and 6.55 ppm increased, as shown in Figure II.2.8b. The ^1H NMR monitoring of the chain extension with 350 St is given in Figure II.2.9. From the residual styrene resonances (δ 5.26 ($-\text{CH}_2-\text{CH}-$, d), 5.83 ($-\text{CH}_2-\text{CH}-$, d) and 6.74 ($-\text{CH}_2-\text{CH}-$, dd)), the monomer conversion is calculated as 98.4%, corresponding to the average polymer composition R_0 -4VP₁₃₇-*b*-St₃₄₄-SC(S)SPr. However, the PSt block is not solvated by DMSO- d_6 /EtOH/H₂O and thus it is not visible in this solvent combination.

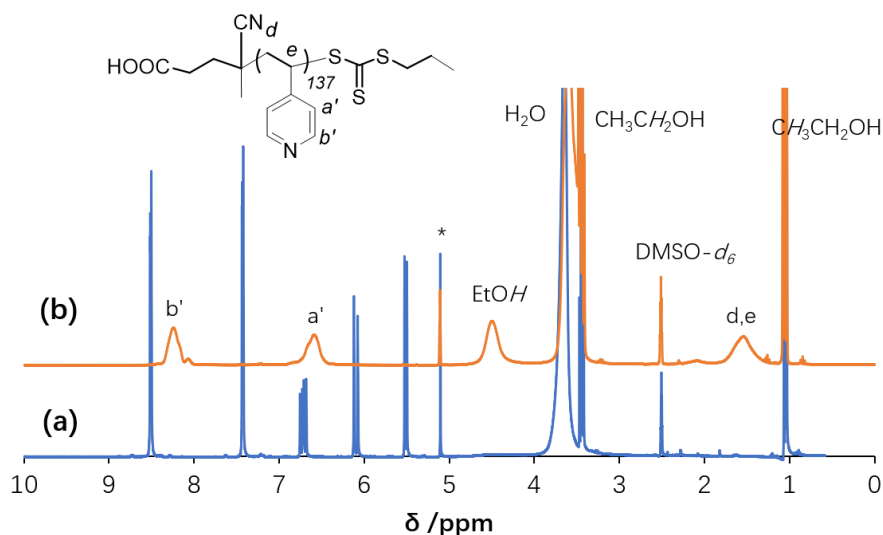


Figure II.2.8 ^1H NMR spectra taken during the formation of $\text{R}_0\text{-4VP}_{137}\text{-SC(S)SPr}$ at $t = 0$ (a, blue) and 20 h (b, orange) by diluting an aliquot of the reaction mixture in $\text{DMSO-}d_6$. The RAFT agent CTPPA resonances are not observed at $t = 0$ because the compound is not soluble at room temperature.

The DLS of this sample (see Annex, Figure A.0.1a) shows a slightly larger average size and dispersity ($D_z = 63$ nm and $\text{PDI} = 0.39$) than the equivalent polymer with shorter blocks. This is evidence of a certain degree of agglomeration, which is confirmed by the TEM analysis (Figure A.0.1b).

The methylation step was accomplished by addition of a DMF solution of MeI to the $\text{P4VP-}b\text{-PSt}$ latex in the $\text{H}_2\text{O/EtOH}$ mixture. The ^1H NMR monitoring before polymer isolation not only confirmed the quantitative methylation but also revealed the formation of a significant amount of Me_2NH_2^+ , identified by the NMR resonances at δ 2.56 (CH_3 , t, $J = 5.6$ Hz) and 8.16 ppm (NH_2 , broad), and HCOOH , identified by a sharp resonance at δ 8.10 ppm (see the NMR characterization in Figure A.0.2 and Figure A.0.3) and confirmed by control experiments (see Figure II.2.4). This product is formed because of the simultaneous presence of DMF, water, and MeI, see the proposed mechanism in Scheme II.2.2.^[140] Solvent removal by vacuum filtration (leading to a viscous residue), followed by thorough washing with water to completely remove the dimethylammonium salt byproduct and final vacuum-drying, led to a gummy and sticky final product in relatively low yields, which variable amounts of water and retained

DMF (24 molecules per chain according to NMR integration ratio between the DMF proton peak at δ 2.89 (-CH₃, 3H) and P4VPM⁺I⁻ proton peak at δ 4.25 (Me, 3H).

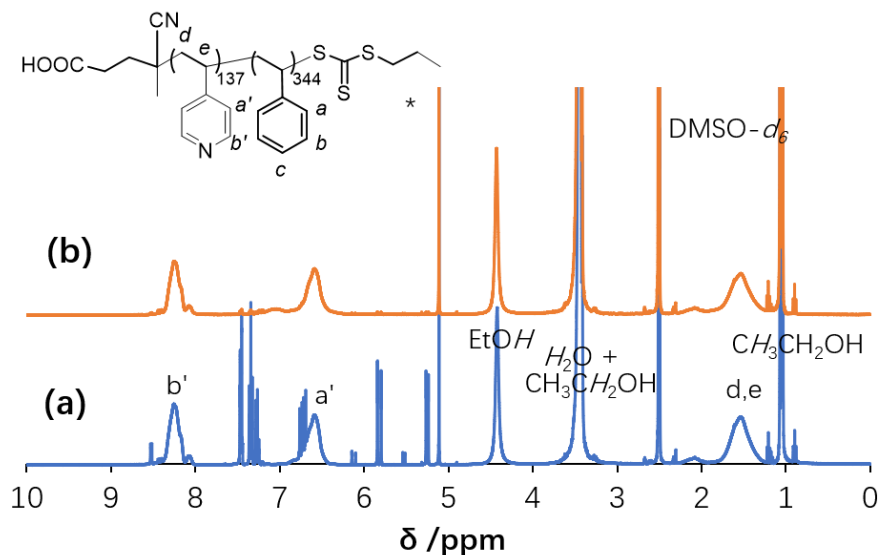


Figure II.2.9 ¹H NMR spectra taken during the formation of R₀-4VP₁₃₇-*b*-St₃₄₄-SC(S)SPr at $t = 0$ (a, blue) and 100 min (b, orange) by adding an aliquot of the reaction mixture to DMSO-*d*₆. Unfortunately, neither CDCl₃ nor C₆D₆ was able to solvate the PSt block.

The DLS ($D_z = 236$ nm and PDI = 0.13) and TEM analyses of the isolated and cleaned polymer after redispersion in water (see Figure II.2.10) demonstrate the regular spherical shape and relatively narrow size dispersity for the self-organized diblock R₀-(4VPM⁺I⁻)₁₃₇-*b*-St₃₄₄-SC(S)SPr chains. The very large increase in the particle size upon cationization may be attributed not only to the much better solvated outer shell in the aqueous solvent but also to the formation of aggregates upon redispersion, entrapping block copolymer chains. Although the DLS and TEM characterizations suggest that this product might be suitable for further macromolecular synthesis by crosslinking, its poorly tractable nature and the low yields led us to develop an alternative, optimized procedure.

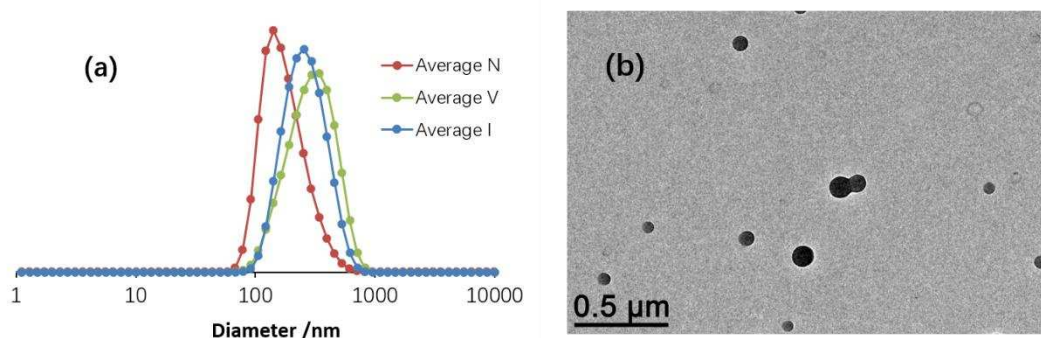


Figure II.2.10 (a) DLS (unfiltered sample) and (b) TEM characterizations of the $[R_0-(4VPMe^+I^-)_{137}-b-St_{344}-SC(S)SPr] \cdot 24(DMF)$ latex.

II.2.2 Optimized synthesis and characterization of the amphiphilic $P4VPMe^+I^-$ -*b*-PSt macroRAFT latex

Because of the above-mentioned difficulties in handling the $R_0-4VP_{137}-b-St_{344}-SC(S)SPr$ product, the final strategy consisted in synthesis of a $P4VP$ -*b*-PSt diblock with a shorter PSt block ($DP = 50$), sufficient to induce micelle formation, followed by cationization of the $P4VP$ block and then further chain extension with a longer PSt chain. Incidentally, this allows additional flexibility for the potential synthesis of other objects, such as ligand-functionalized cores,^[94] or NG core^[72, 106] architectures, which indeed correspond to the final targets of our research efforts.

The same macroRAFT agent of average formula $R_0-4VP_{137}-SC(S)SPr$, used in the above optimization studies, was extended in step 2 (Scheme II.2.1) with a short PSt block to obtain $R_0-4VP_{137}-b-St_{48}-SC(S)SPr$. The SEC monitoring showed the expected molar mass increase as a function of conversion (Figure A.0.4), in good agreement with the calculated values, while the dispersity remained low ($PDI = 1.25$), and the 1H NMR monitoring (Figure II.2.11) confirmed the nearly complete monomer consumption. The PSt block is solvated by $CDCl_3$ (Figure II.2.11c) but not by $DMSO-d_6/EtOH$ (Figure II.2.11b) and thus it is not visible in this solvent combination. By relative integration of

the broad resonances attributed to aromatic CH protons from P4VP at δ 8.25 ppm ($-C_5H_4N$, ortho-H, 2H), δ 6.56-6.30 ppm ($-C_5H_4N$, meta-H, 2H) in DMSO- d_6 , and PSt at δ 7.02 ppm ($-C_6H_5$, ortho-H and para-H, 3H) in D₂O/CDCl₃, the 4VP/St ratio is approx. 3:1, which is in agreement with the expected value.

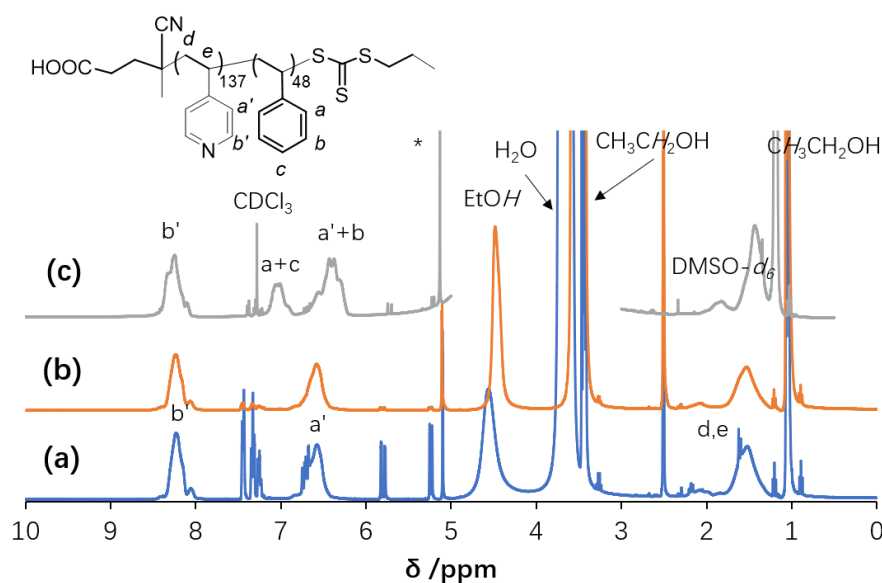


Figure II.2.11 ¹H NMR spectra taken during the formation of R₀-4VP₁₃₇-*b*-St₄₈-SC(S)SPr at $t = 0$ (a, blue) and 4.5 h by adding an aliquot of the reaction mixture to DMSO- d_6 (b, orange) or to D₂O/CDCl₃ (c, grey).

In addition, the DOSY NMR spectrum (Figure II.2.12) confirmed that all polymer signals, notably the aromatic CH signals of both pyridine and phenyl rings, correspond to a single diffusion coefficient. Since this copolymer R₀-4VP₁₃₇-*b*-St₄₈-SC(S)SPr cannot be solubilized by pure water before quaternization, the DLS analyses were done in ethanol or 75/25 (v/v) water/ethanol mixture (Figure II.2.13a and b). It shows a relatively narrow distribution with $D_z = 24.4$ nm and PDI = 0.14 in ethanol, and $D_z = 30.0$ nm and PDI = 0.48 in 75/25 (v/v) water/ethanol, though containing a few large agglomerates, and particles with a spherical morphology (see TEM in Figure II.2.13c), respectively.

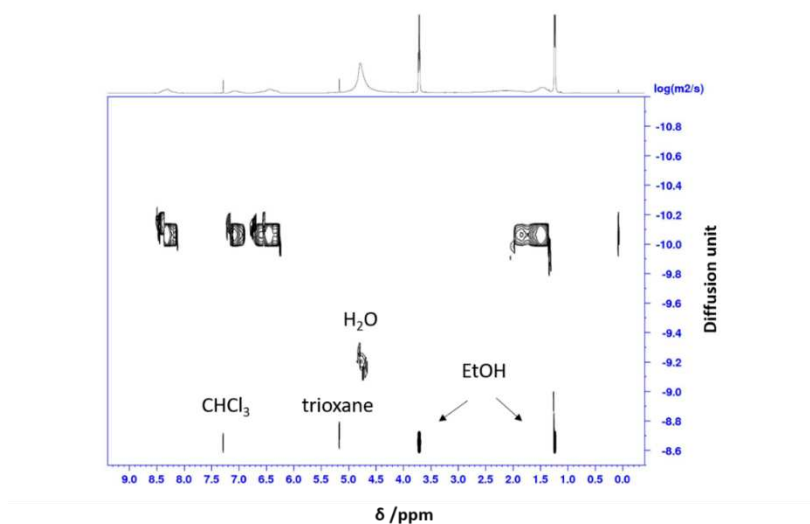


Figure II.2.12 ^1H DOSY NMR spectrum of $\text{R}_0\text{-4VP}_{137}\text{-}b\text{-St}_{48}\text{-SC(S)SPr}$ in $\text{D}_2\text{O}/\text{CDCl}_3$.

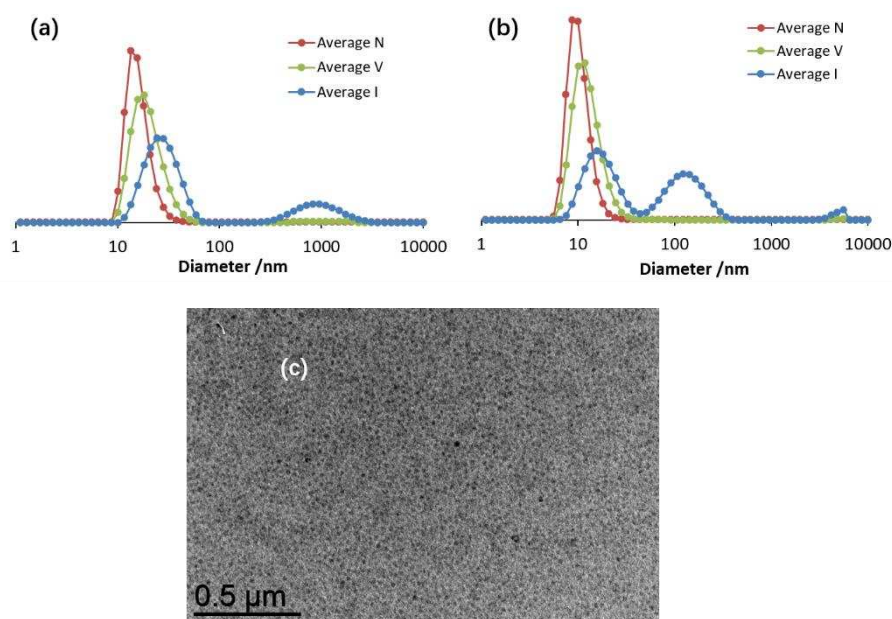


Figure II.2.13 DLS and TEM characterization of the $\text{R}_0\text{-4VP}_{137}\text{-}b\text{-St}_{48}\text{-SC(S)SPr}$ latex: (a) DLS in ethanol (unfiltered sample); (b) DLS in 75/25 (v/v) water/ethanol (unfiltered sample); (c) TEM.

The cationization with MeI in DMF in step 3 in Scheme II.2.1 proceeded as smoothly as for the diblock copolymer with the longer PSt block. In this case, however, the final polymer extensively precipitated and could be efficiently separated from the liquid phase by centrifugation. Because the Me_2NH_2^+ salt byproduct is quite soluble in

DMF, it could be fully eliminated from the isolated polymer (Figure A.0.5) by repetitive washings with DMF, followed by a final solvent change to diethyl ether until the washing solution becomes colorless and then drying. The global yield of the cationization step after several washings was 67% measured by weight. Integration of the ^1H NMR spectrum (Figure II.2.14) indicates that the isolated material retains a significant amount of DMF, $[\text{R}_0\text{-(4VPMe}^+\text{I}^-)_{137}\text{-}b\text{-St}_{48}\text{-SC(S)SPr}]\cdot 38(\text{DMF})$. This copolymer was then redispersed in water for further chain extension.

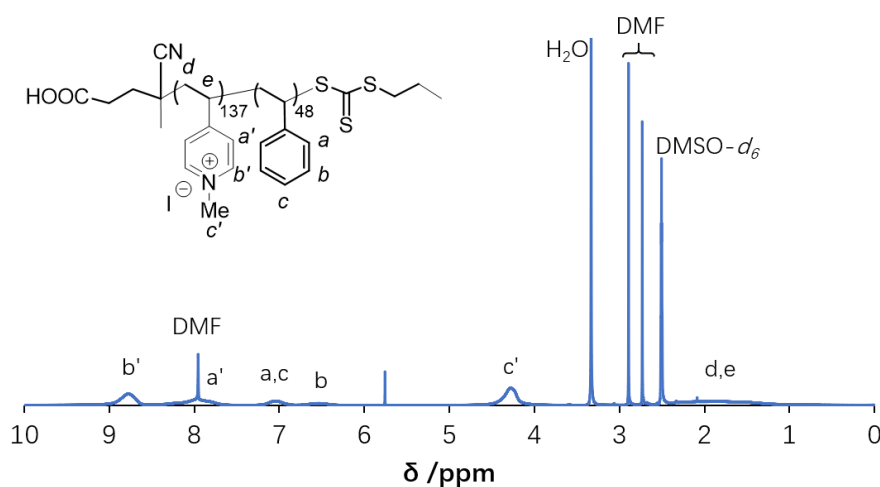


Figure II.2.14 ^1H NMR spectrum in $\text{DMSO-}d_6$ of $[\text{R}_0\text{-(4VPMe}^+\text{I}^-)_{137}\text{-}b\text{-St}_{48}\text{-SC(S)SPr}]\cdot 38(\text{DMF})$.

After redispersion in water, the resulting dispersion showed the presence of large agglomerates (Figure II.2.15b) and a broad size distribution in DLS, with $D_z = 276$ nm and $\text{PDI} = 0.25$ (see Figure II.2.15a). This could indicate the formation of large compound micelles that trap a certain number of $\text{R}_0\text{-(4VPMe}^+\text{I}^-)_{137}\text{-}b\text{-St}_{48}\text{-SC(S)SPr}$ block copolymer micelles into aggregates.^[141] However, this did not hamper the use of this macroRAFT intermediate to ultimately generate unimolecular polymeric nanoparticles of small size and narrow size distribution (vide infra).

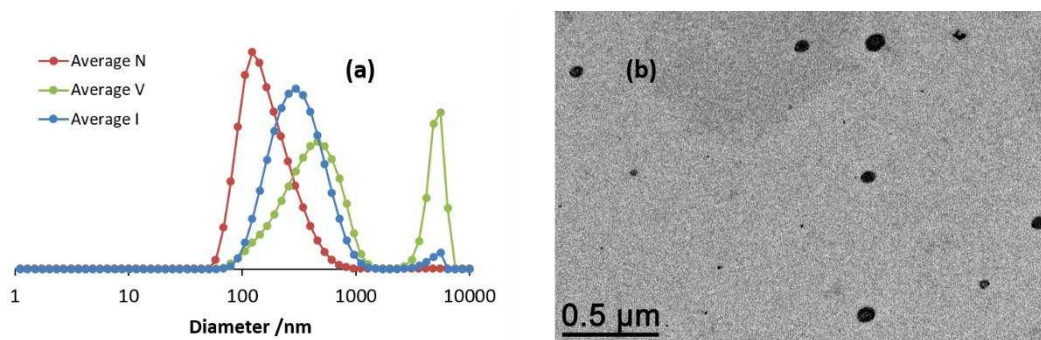


Figure II.2.15 DLS and TEM characterization of the $R_0-(4VPMe^+I)_{137}-b-St_{48}-SC(S)SPr$ latex: (a) DLS in water and (b) TEM.

Further chain extension in water of $R_0-(4VPMe^+I)_{137}-b-St_{48}-SC(S)SPr$ in a fourth step with additional styrene (297 equiv. per chain) resulted in nearly total styrene incorporation (Figure II.2.16) and formation of a stable latex with small-size individual particles ($D_z = 115.9$ nm and PDI = 0.06, Figure II.2.17a). The TEM analysis also confirmed the spherical morphology and narrow size distribution of the polymer micelles (Figure II.2.17b). The narrowness of the particle size distribution and the lower particle size obtained after polymerization are good indications that the chain extension was successful and that a $R_0-(4VPMe^+I)_{137}-b-St_{48}-b-St_{297}-SC(S)SPr$ block copolymer was obtained.

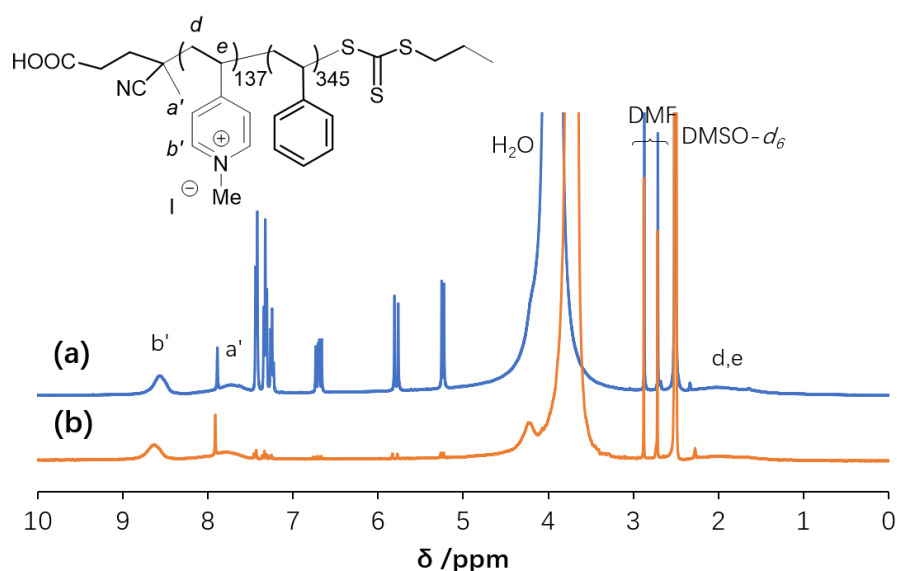


Figure II.2.16 1H NMR monitoring in $DMSO-d_6$ of the styrene consumption in the chain extension of $R_0-(4VPMe^+I)_{137}-b-St_{48}-SC(S)SPr$, leading to $[R_0-(4VPMe^+I)_{137}-b-St_{345}-SC(S)SPr] \cdot 38(DMF)$: initial spectrum (a, blue) and final spectrum (b, orange).

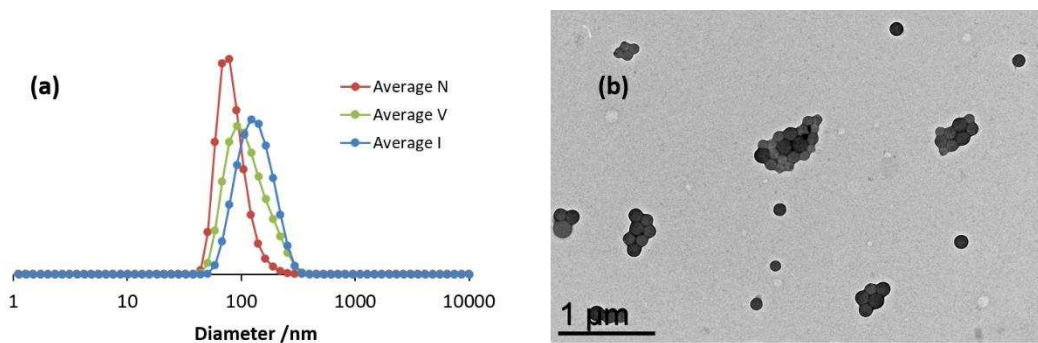


Figure II.2.17 (a) DLS (unfiltered sample) and (b) TEM characterization of the R_0 - $(4VPMc^+I)_{137}$ - b - St_{48} - b - St_{297} - $SC(S)SPr$ latex.

In all evidence, extension of the amphiphilic diblock PSt chains results in a breakdown of the large aggregates and in a reorganization in the form of spherical micelles ($D_z = 94.6$ nm and $PDI = 0.14$) shown in Figure II.2.18a. These micelles are kinetically quite stable because addition of toluene and vigorous stirring of the latex at room temperature ($D_z = 98.2$ nm and $PDI = 0.10$) led to neither excessive swelling nor to the formation of emulsions, as shown by DLS in Figure II.2.18b. Prolonged heating at high temperature for several hours led to micelle reorganization with formation of smaller objects ($D_z = 48.5$ nm and $PDI = 0.03$) (Figure II.2.18c) for the unswollen micelles and to significant expansion for the swollen ones ($D_z = 312.6$ nm and $PDI = 0.17$) (Figure II.2.18d).

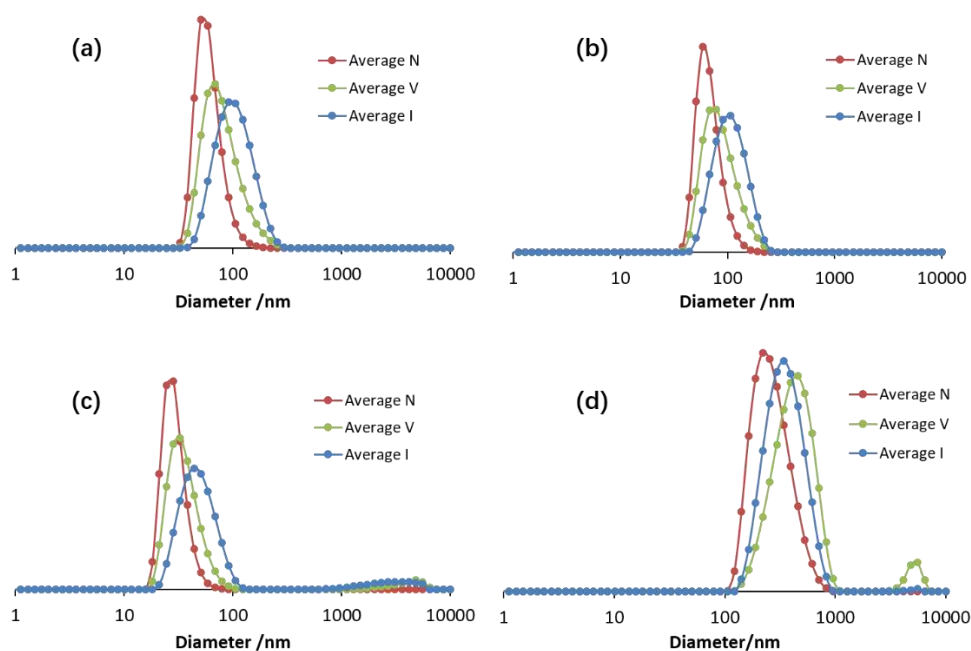


Figure II.2.18 DLS study of a $R_0-(4VPMe^+I)_{140}-b-St_{48}-b-St_{297}-SC(S)SPr$ polymer latex: (a) as synthesized; (b) after swelling with toluene at room temperature; (c) as (a), after heating for 24 h at 90 °C; (d) as (b), after heating for 18 h at 80 °C. All measurements were carried out on unfiltered samples.

A determination of whether the CCM product contains residual non-crosslinked arms is not simple because any free arm would remain entrapped in the CCM particles by self-assembly and would thus remain undetected by DLS and TEM. In addition, free arms and crosslinked polymers are indistinguishable by NMR spectroscopy. The separation of non-crosslinked free arms from the crosslinked particles is only possible by dispersion in a medium with good solvent properties for both core and shell. The presence of any free diblock chain can then be assessed by an investigation of size-dependent properties such as diffusion (DOSY NMR) or light scattering (DLS). Due to this limitation, the DOSY NMR cannot be used for investigation this problem. Thus, we opted to use the DLS methodology.

To make sure crosslinking reaction is complete, a compatibilizing solvent for the two blocks, $R_0-(4VPMe^+I)_{140}-b-St_{48}-b-St_{297}-SC(S)SPr$ was searched. In this solvent, the non-crosslinked chains that remained trapped in the cores could be drawn out and the non-crosslinked micelles could dissociate to smaller-size free chains, while the

crosslinked micelles would maintain their larger size. In the first attempt, this polymer was freeze-dried and redispersed in DMSO, yielding again micelles ($D_z = 43.8$ nm and $PDI = 0.22$, Figure A.0.6a). This micellar structure was maintained, though some agglomeration occurred, after heating the dispersion for 24 h at 90 °C ($D_z = 96.2$ nm and $PDI = 0.42$, Figure A.0.6b). A variable-temperature DLS study showed a steady D_z decrease as the temperature was increased (Figure A.0.6c), while the size distribution remained monomodal. The smaller size of these micelles relative to those in the water dispersion may be attributed to a poorer solvation of P4VPM e^+I^- by DMSO and/or to a lower aggregation number in this medium, though the continuous shrinking as the temperature is increased rather suggests the importance of the solvation effect. The addition of increasing amounts of toluene, which is a good solvent for the PSt core and is fully miscible with DMSO, maintained a stable dispersion up to 40% (v/v), whereas greater toluene fractions led to polymer precipitation. Incidentally, the precipitated polymer showed the same PVPMe $^+I^-$ /PSt ratio as the freeze-dried residue in the 1H NMR spectrum, whereas no detectable polymer resonances were found in the mother liquor, indicating the absence of PSt homopolymer chains.

The DLS analyses of the dispersions obtained at variable DMSO/toluene ratios at room temperature show a smaller size distribution below 10 nm, suggesting the disaggregation of the micelles and an equilibrium with free chains, which is already quite extensive for the 80/20 mixture (Figure II.2.19b and c). In order to support the assignment of the small diameter distribution to single chains, a DLS measurement was carried out for a toluene solution of a specially synthesized PSt homopolymer, R $_0$ -St $_{263}$ -SC(S)SPr, yielding a major distribution with $d < 10$ nm (Figure A.0.7a). Therefore, the DMSO/toluene mixture, even with only 20% toluene, appears to solvate both blocks as free chains instead of micelles, without polymer precipitation. Finally, the freeze-dried sample was redispersed in the 80/20 DMSO/toluene mixture and heated for 24 h at 90 °C. In this case, the DLS analysis of the resulting dispersion showed a trimodal distribution, suggesting the presence of micelles, middle-size nanoaggregates, and

much larger particles stabilized by the diblock copolymer (Figure A.0.7b) but no single chains (no distribution with diameter < 10 nm).

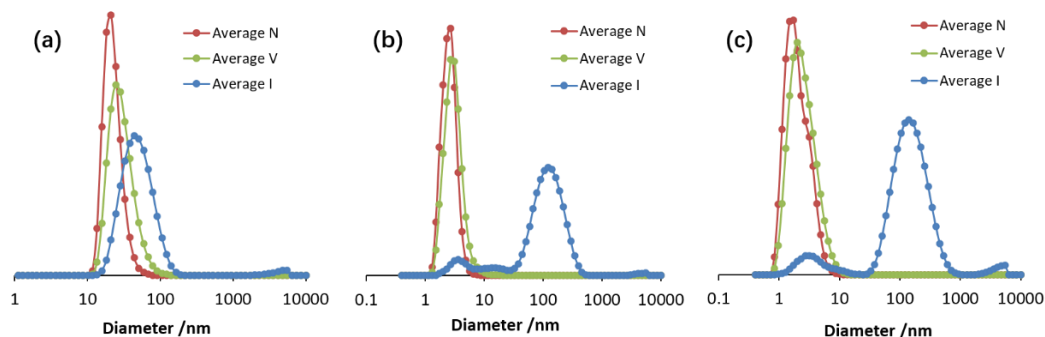


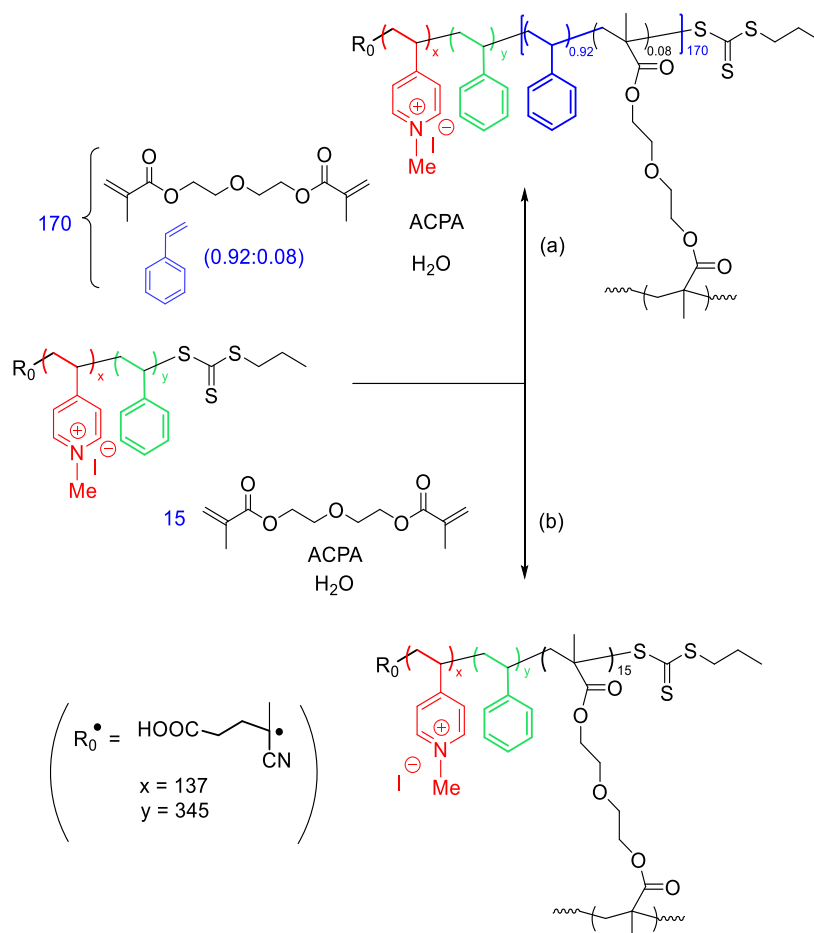
Figure II.2.19 DLS of $R_0-(4VPMe^+I^-)_{137}-b-St_{48}-b-St_{297}-SC(S)SPr$ after freeze-drying the aqueous latex and redispersion in (a) neat DMSO; (b) DMSO/toluene 80/20 (v/v); (c) DMSO/toluene 60/40 (v/v). The solutions were measured after equilibration of the dispersion for at least one night at room temperature.

II.2.3 Crosslinking of the amphiphilic $P4VPMe^+I^-$ -*b*-PSt copolymer with high molar mass PSt block

Crosslinking by DEGDMA in the presence of styrene

The particles resulting from the synthesis outlined above, henceforth written as $R_0-(4VPMe^+I^-)_{137}-b-St_{345}-SC(S)SPr$, were first crosslinked according to the previously published protocol,^[94] which made use of a DEGDMA/styrene mixture. As already stated in section II.1, dilution of the DEGDMA crosslinker with a large amount of styrene was found necessary, in the previous synthesis of the CCM-N particles containing the neutral P(MAA-*co*-PEOMA) hydrophilic shell,^[72, 94] to avoid macrogelation. As already mentioned in the literature,^[85] poly(sodium acrylate)-*b*-poly(N,N-diethylacrylamide) diblock copolymer chains underwent chain extension along with crosslinking reaction by crosslinker N,N'-methylenebisacrylamide and N,N-diethylacrylamide. Individual particles were formed when the concentration of the difunctional crosslinker was low (< 3 mol% based on the monomers), whereas

macrogelation was observed at a larger concentration. The microphase separation at an early stage of this dispersion polymerization was found to be one reason for the avoidance of macrogelation.^[142]



Scheme II.2.4 Crosslinking step for the synthesis of the CCM with a polycationic P4VPMe⁺I⁻ shell.

Application of the same conditions as in the previous synthesis of the polymer with the neutral-shell, using a DEGDMA/styrene molar ratio of 7.7/92.3 for a total of 170 equiv. per chain (Scheme II.2.4, path (a)), yielded R₀-(4VPMe⁺I⁻)₁₃₇-*b*-St₃₄₅-*b*-(St₁₅₇-*co*-DEGDMA₁₃)-SC(S)SPr according to the 89% conversion of styrene and complete consumption of DEGDMA (Figure II.2.20), in which each polymer chain has an average molar mass of $9.17 \times 10^4 \text{ g mol}^{-1}$. The ¹H NMR spectrum in DMSO-*d*₆ does not show the PSt core because this solvent and H₂O are not able to swell it. However,

all polymer parts become visible in a colloidal dispersion in D₂O with the particle core swollen by CDCl₃, see Figure II.2.21.

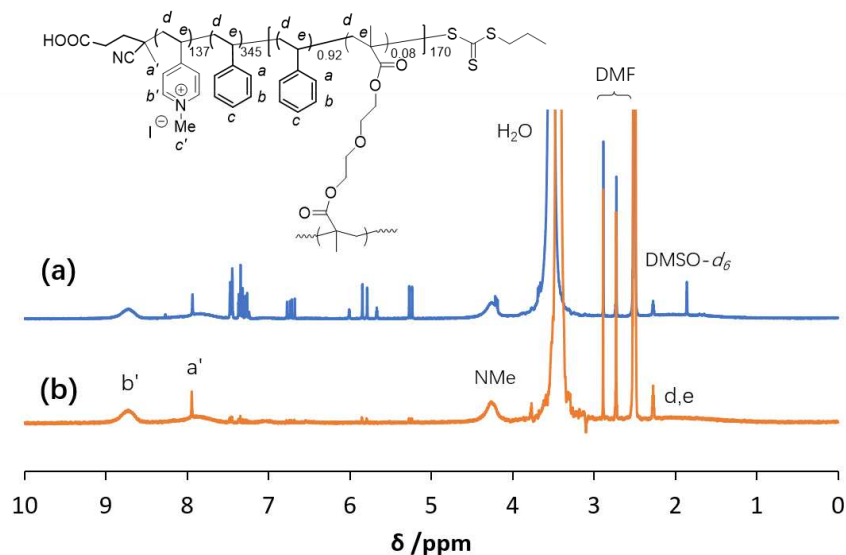


Figure II.2.20 ¹H NMR monitoring in DMSO-*d*₆ of the styrene/DEGDMA consumption in the crosslinking of R₀-(4VPMe⁺I)⁻₁₃₇-*b*-St₃₄₅-SC(S)SPr, leading to R₀-(4VPMe⁺I)⁻₁₃₇-*b*-St₃₄₅-*b*-(St₁₅₇-*co*-DEGDMA₁₃)-SC(S)SPr: (a) initial spectrum and (b) final spectrum.

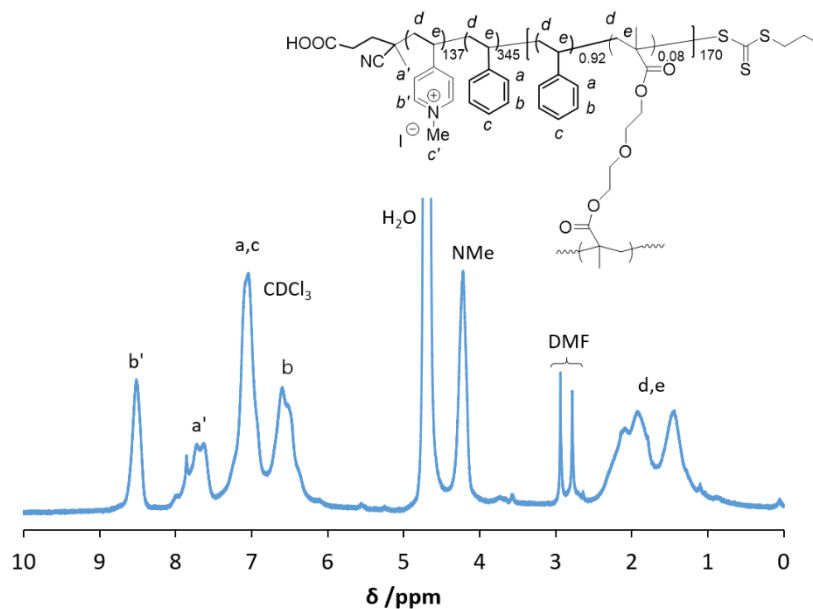


Figure II.2.21 ¹H NMR spectrum of the final CCM R₀-(4VPMe⁺I)⁻₁₃₇-*b*-St₃₄₅-*b*-(St₁₅₇-*co*-DEGDMA₁₃)-SC(S)SPr swollen by CDCl₃ in D₂O.

The final latex has once again the aspect of a homogeneous and stable white

dispersion. The DLS results (Figure II.2.22a) revealed one population of objects with a narrow size distribution (PDI = 0.09) and an average D_z of 143 nm. The measurement was repeated after stirring the sample with excess toluene, resulting in particle swelling, followed by fast decantation, yielding $D_z = 156$ nm (PDI = 0.04), see Figure II.2.22b. The swelling process was rapid (shaking for < 1 min), as indicated visually by the change of relative volumes, before and after shaking, of the aqueous and organic phases. This biphasic mixture decanted in 1 min and the top organic phase was clear. This demonstrates the feasibility of fast mass transport for small organic molecules compatible with PSt through the hydrophilic polymer shell toward the particle core. This is consistent with the reported conclusion for the P(MAA-*co*-PEOMA) shell CCM (see Figure A.0.8a-c). This feature enables the introduction of metal complex precatalysts into the core for catalytic nanoreactor application (*vide infra*).

On the basis of a spherical shape (Figure II.2.22c), the average volume increase by swelling can be calculated as 29.8% and $\Delta V = (4/3)\pi[(156/2)^3 - (143/2)^3] = 4.57 \times 10^5 \text{ nm}^3$. Using the density (0.865 g cm^{-3}) and molecular weight (92.14 g mol^{-1}) of toluene and Avogadro's number, this allows to estimate an average of $\approx 2.6 \times 10^6$ toluene molecules per swollen particle.

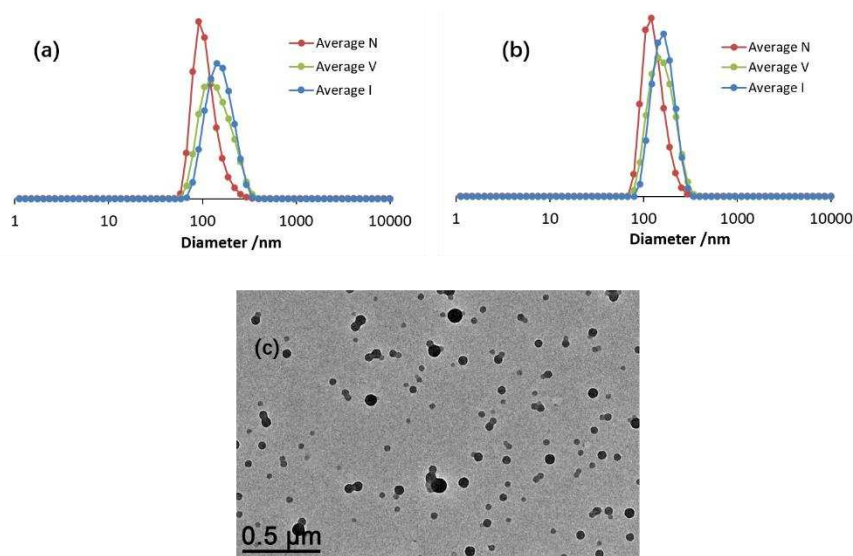


Figure II.2.22 DLS and TEM analyses of the R_0 -(4VPMe⁺I⁻)₁₃₇-*b*-St₃₄₅-*b*-(St₁₅₇-*co*-DEGDMA₁₃)-SC(S)SPr CCM latex: (a) DLS (unfiltered sample); (b) DLS after swelling with toluene (unfiltered sample); (c) TEM.

Several experiments were conducted in order to assess the stability of the CCM scaffold and the extent of the crosslinking step (Figure A.0.8d). A latex of the neutral-shell $R_0\text{-(MAA}_{0.5}\text{-}co\text{-PEOMA}_{0.5})_{30}\text{-}b\text{-(St}_{0.9}\text{-}co\text{-DPPS}_{0.1})_{300}\text{-}b\text{-(St}_{0.9}\text{-}co\text{-DEGDMA}_{0.1})_{100}\text{-SC(S)SPr CCM}$ was tested for stability as a function of temperature at 90 °C. These conditions are identical to those used for the olefin hydroformylation reaction, except for the absence of the high-pressure syngas. After stirring for 5 days, both D_z and PDI had increased (from 80 nm to 100 nm), indicating the appearance of particle coagulation.^[94]

A latex of the closely related cationic-shell $R_0\text{-(4VPMe}^+\text{I}^-)_{140}\text{-}b\text{-St}_{350}\text{-}b\text{-(St}_{135}\text{-}co\text{-DEGDMA}_{15})\text{-SC(S)SPr CCM}$, characterized by a narrow size distribution ($D_z = 110.6$ nm and PDI = 0.10, Figure II.2.23a), was heated for 24 h at 90 °C in order to probe its thermal stability. The treatment gave no evidence of alteration; notably, the latex remained a stable colloidal suspension with no sign of coagulation, but the DLS analysis after the treatment revealed slightly smaller particles ($D_z = 89.7$ nm and PDI = 0.10, Figure II.2.23b). This behavior is similar to that observed for the precursor micelles, raising doubts about a possible incomplete crosslinking step, because the contraction may result from reorganization with loss of free arms. On the other hand, a slight contraction may also result from relaxation of the glassy PSt core upon prolonged treatment under conditions close to the glass transition temperature. The same thermal treatment was also carried out on the same latex after swelling with toluene: the swollen particles ($D_z = 112.3$ nm and PDI = 0.10, Figure II.2.23c) showed an expansion and a significant increase of the size distribution ($D_z = 254.1$ and PDI = 0.24, Figure II.2.23d) after heating for 24 h at 90 °C, with evidence of formation of larger aggregates, in close analogy to the behavior of the precursor diblock arm micelles. Freeze-drying, followed by redispersion in water, gave a size distribution similar to that of the latex from synthesis, with no evidence of coagulation ($D_z = 112.3$ nm and PDI = 0.09, Figure II.2.23e).

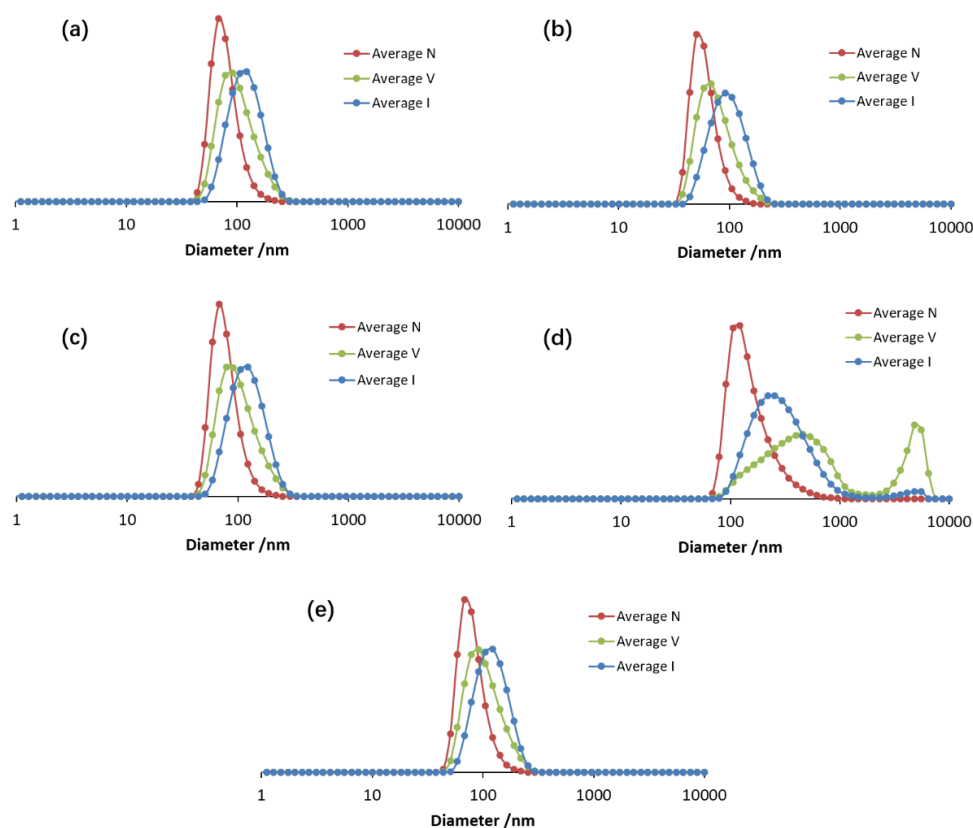


Figure II.2.23 DLS analysis of the R_0 -(4VPMe⁺I)₁₄₀-*b*-St₃₅₀-*b*-(St₁₃₅-*co*-DEGDMA₁₅)-SC(S)SPr latex: (a) as synthesized; (b) after heating at 90 °C for 24 h; (c) swollen with toluene; (d) swollen and then after heating for 24 h at 90 °C; (e) after freeze-drying and redispersion in water.

In order to further probe the possible presence of non-crosslinked arms, the freeze-dried polymer was also redispersed in both neat DMSO and a DMSO/toluene (80/20, v/v) mixture because the dispersion in the mixed solvent was shown to release single chains from the micelles, as evidenced by the DLS analysis (vide supra). The dispersion in neat DMSO was monomodal with significantly smaller D_z than when the same particles are dispersed in water ($D_z = 63.6$ nm and PDI = 0.09, Figure II.2.24a). Warming for 24 h at 90 °C showed only a slight increase of size and size distribution ($D_z = 94.3$ nm and PDI = 0.25) with evidence of a few large aggregates (Figure II.2.24b). The dispersion in the mixed solvent, on the other hand, contrary to the dispersion of the precursor diblock micelles (Figure II.2.19b), only showed a single size distribution ($D_z = 130.2$ nm and PDI = 0.15, Figure II.2.24c) and notably the absence of a small size distribution attributable to single chains. After heating for 24 h at 90 °C, the average

diameter decreased while the size distribution remained narrow ($D_z = 95.8$ nm and PDI = 0.13, Figure II.2.24d). This result clearly suggests that the core crosslinking step of the polymer synthesis is essentially quantitative, with an undetectable amount of residual free arms even at high temperature. Incidentally, the smaller particle average diameter in pure DMSO than in water, as also observed for the diblock copolymer micelles, given the absence of free arms, must be attributed to the poorer ability of DMSO, relative to water, to solvate the outer P4VPMe⁺I⁻ shell.

It has to be mentioned that, while the PISA process has the advantage of producing various ordered structures (including cylindrical micelles and vesicles) by altering the hydrophilic/hydrophobic ratio, the targeted application as nanoreactors for biphasic catalysis would not find any specific advantage in using alternative morphologies relative to spherical particles.

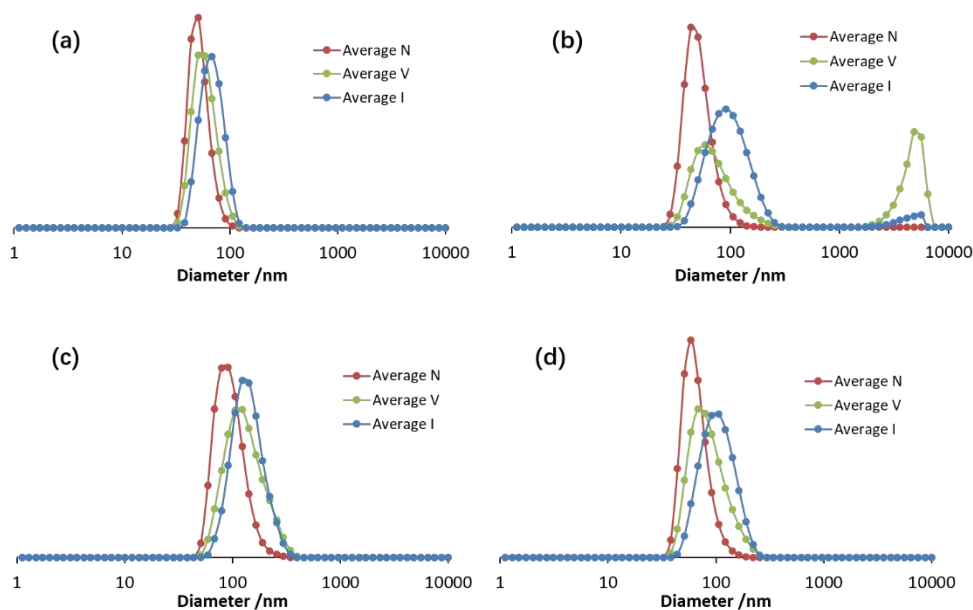


Figure II.2.24 DLS analysis of $R_0-(4VPMe^+I)_{140}-b-St_{350}-b-(St_{135}-co-DEGDMA_{15})-SC(S)SPr$ after freeze-drying and redispersion: (a) in neat DMSO at room temperature; (b) as (a) after heating at 90 °C for 24 h; (c) in DMSO/toluene 80/20 (v/v) at room temperature; (d) as (c) after heating at 90 °C for 24 h. All measurements were carried out on unfiltered samples.

Crosslinking by pure DEGDMA

The P4VPMe⁺I⁻-*b*-PSt-SC(S)SPr macroRAFT chains with the long PSt block were also crosslinked in the last step by pure DEGDMA (absence of styrene, Scheme II.2.4, path (b)). The motivation to attempt this synthesis was the previous failure to obtain well-defined spherical CCM particles, when using pure DEGDMA in the last step, in the presence of a neutral P(MAA-*co*-PEOMA) hydrophilic shell.^[94] Rather, such polymerization resulted in the formation of a macrogel because of particle-particle interpenetration,^[100] as already mentioned in section II.1. The previous investigation^[100] also proved that the interpenetration is completely stopped after complete deprotonation of the shell carboxylic acid functions with NaOH at high pH to yield a P(MAA⁻Na⁺-*co*-PEOMA) shell, which was attributed to the introduction of repulsive Coulombic forces between the different particles. On these grounds, it was of interest to probe whether the analogous interparticle Coulombic repulsion induced by the positively charged outer shell of our current micelles would allow crosslinking without macrogelation.

For this purpose, a new macroRAFT agent of average formula R₀-(4VPMe⁺I⁻)₁₃₇-*b*-St₄₈-SC(S)SPr was extended by PSt₂₉₇ and converted into R₀-(4VPMe⁺I⁻)₁₃₇-*b*-St₃₄₅-SC(S)SPr, see Scheme II.2.4b. The DLS of this polymer (Figure A.0.11) confirmed the expected sample uniformity and size, which did not significantly change after addition of DEGDMA (15 equiv. per chain), with D_z changing from 139.1 nm (PDI = 0.11) to 137.3 nm (PDI = 0.11). The crosslinking reaction proceeded rapidly with nearly complete monomer consumption (NMR monitoring, Figure II.2.25) to yield a latex as a stable colloidal suspension, without any evidence of macrogelation. The ¹H NMR spectrum in D₂O of the polymer particles with CDCl₃-swollen core clearly shows all expected resonances (Figure II.2.26), except those of the central PDEGDMA crosslinked part, which is not unexpected as for the previously published latexes of the related CCM and NG particles with the neutral P(MAA-*co*-PEOMA) shell.^[72, 105a] The reasons could be the small amount of this monomer resulting in low intensity

resonances and the overshadow by the strong water resonance. It is also worth pointing out that the DEGDMA protons, being close to the polymer tight crosslinking points, have more restricted mobility and long correlation time. Therefore, their resonances are expected to be broader.

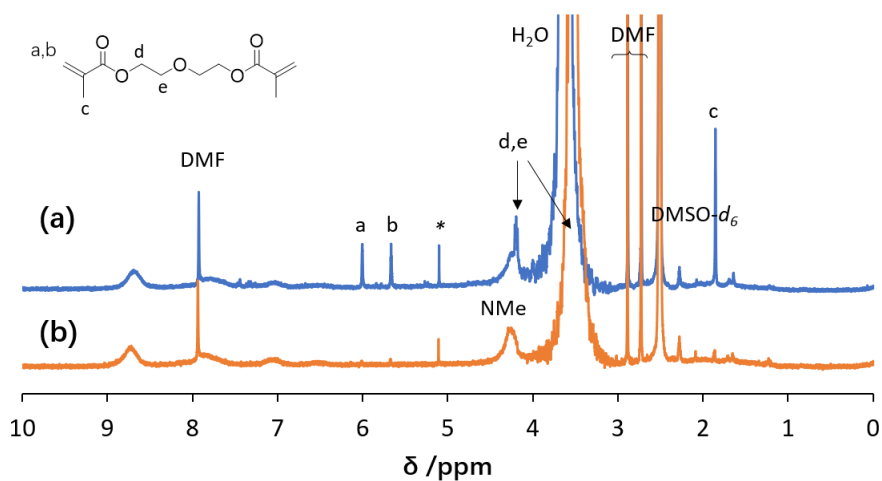


Figure II.2.25 ^1H NMR monitoring in $\text{DMSO-}d_6$ of the crosslinking reaction with pure DEGDMA to yield the $\text{R}_0\text{-(4VPMe}^+\text{I)}_{137}\text{-}b\text{-St}_{345}\text{-}b\text{-DEGDMA}_{15}\text{-SC(S)SPr}$ latex: initial spectrum (a, blue) and final spectrum (b, orange).

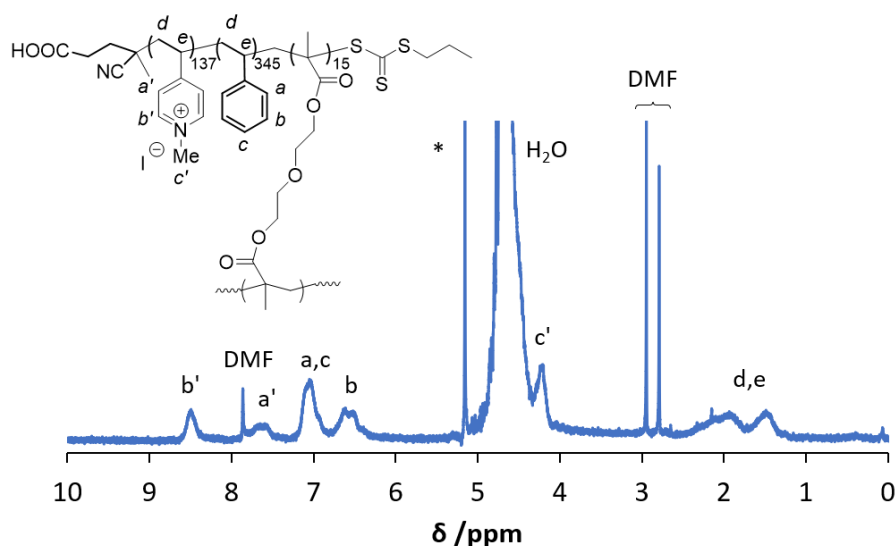


Figure II.2.26 ^1H NMR spectrum of the $\text{R}_0\text{-(4VPMe}^+\text{I)}_{137}\text{-}b\text{-St}_{345}\text{-}b\text{-DEGDMA}_{15}\text{-SC(S)SPr}$ latex with added D_2O and with the PSt core swollen by CDCl_3 .

The DLS and TEM analyses (Figure II.2.27) show the absence of agglomerates

and confirm the quality of the product as particles with a narrow size distribution. The average size obtained from DLS for these particles ($D_z = 148$ nm, PDI = 0.09 for the unswollen sample and $D_z = 162$ nm, PDI = 0.10 for the toluene-swollen sample) is slightly greater than for those obtained when styrene was also used in the crosslinking step. For these particles, the average size increase by swelling is 31.1%, with an average volume increase of 5.29×10^5 nm³ corresponding to 3.0×10^6 toluene molecules per particle. When compared with the previously published crosslinking step, under equivalent conditions, to yield CCM particles with the neutral P(MAA-*co*-PEOMA) hydrophilic shell,^[94] this result demonstrates the positive effect of a charged polycationic shell and of the ensuing Coulombic repulsion to avoid irreversible particle-particle coupling.

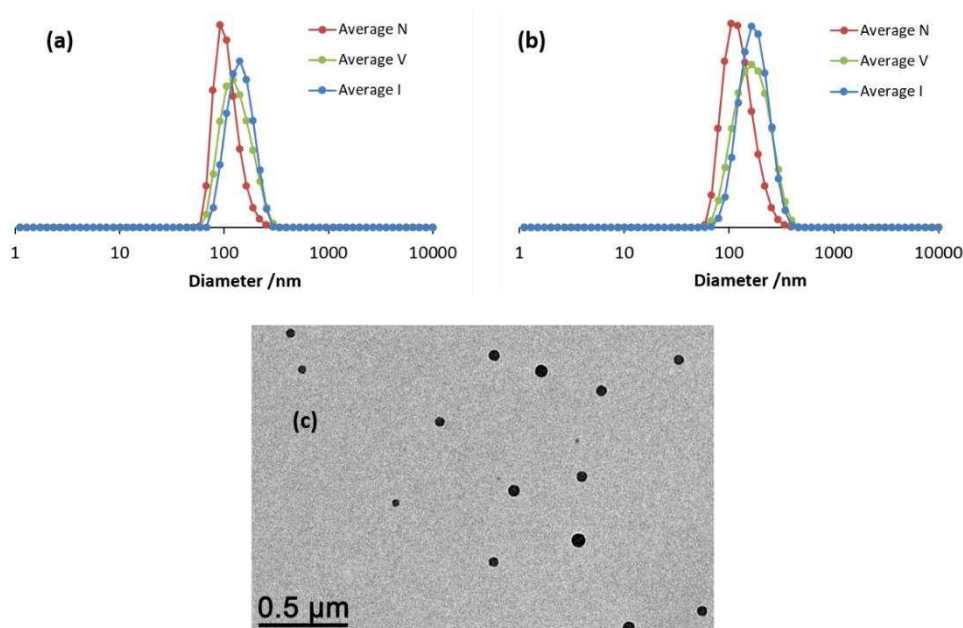


Figure II.2.27 DLS and TEM analyses of the $R_0-(4VPMe^+I^-)_{137}-b-St_{345}-b-DEGDMA_{15}-SC(S)SPr$ CCM latex: (a) DLS (unfiltered sample); (b) DLS after swelling with toluene (unfiltered sample); (c) TEM.

The same thermal stability, freeze-drying, and redispersion experiments described above for the CCM particles crosslinked by the DEGDMA/styrene mixture were also carried out for the $R_0-(4VPMe^+I^-)_{137}-b-St_{345}-b-DEGDMA_{15}-SC(S)SPr$ by DLS

measurements. The results were quite similar, the CCM has a little shrink after heating at 90 °C for 24 h ($D_z = 148$ nm, PDI = 0.09 as synthesized and $D_z = 112.9$ nm, PDI = 0.09 after the treatment), see Figure II.2.28a. Meanwhile, the swollen particles after heating for 24 h at 90 °C showed a size enlargement and a broad distribution ($D_z = 381.0$ nm and PDI = 0.24, Figure II.2.28b) with a formation of larger aggregates (~8000 nm). The aqueous latex after freeze-drying and redispersion showed a size similar to that of the latex as prepared in a narrow distribution, with no evidence of coagulation ($D_z = 129.6$ nm and PDI = 0.13, Figure II.2.28c).

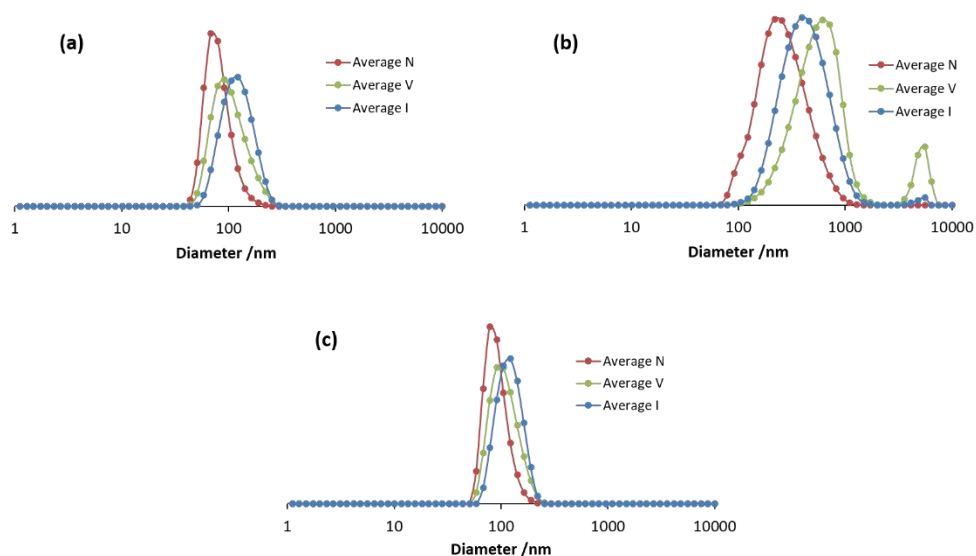


Figure II.2.28 DLS analysis of the $R_0-(4VPMe^+I)_{140}-b-St_{345}-b-DEGDMA_{15}-SC(S)SPr$ latex: (a) after heating at 90 °C for 24 h; (b) swollen with toluene and after heating for 24 h at 90 °C; (c) after freeze-drying and redispersion in water. All measurements were carried out on unfiltered samples.

Compared with the synthesized CCM-C aqueous latex, the freeze-dried polymer redispersed in neat DMSO presented smaller particles at room temperature ($D_z = 104.4$ nm and PDI = 0.06), while the polymer being warmed for at 90 °C 24 h showed a further size decrease ($D_z = 80.6$ nm and PDI = 0.08) without any aggregates (Figure II.2.29b). Notably, this CCM-C $R_0-(4VPMe^+I)_{140}-b-St_{345}-b-DEGDMA_{15}-SC(S)SPr$ still showed similar D_z (110.2 nm and PDI = 0.25) in the DMSO/toluene (80/20, v/v) mixture (Figure

II.2.29c), and reduced D_z (95.9 nm and PDI = 0.12) after heating for 24 h at 90 °C. The absence of a small size single chains indicates again the successful core crosslinking.

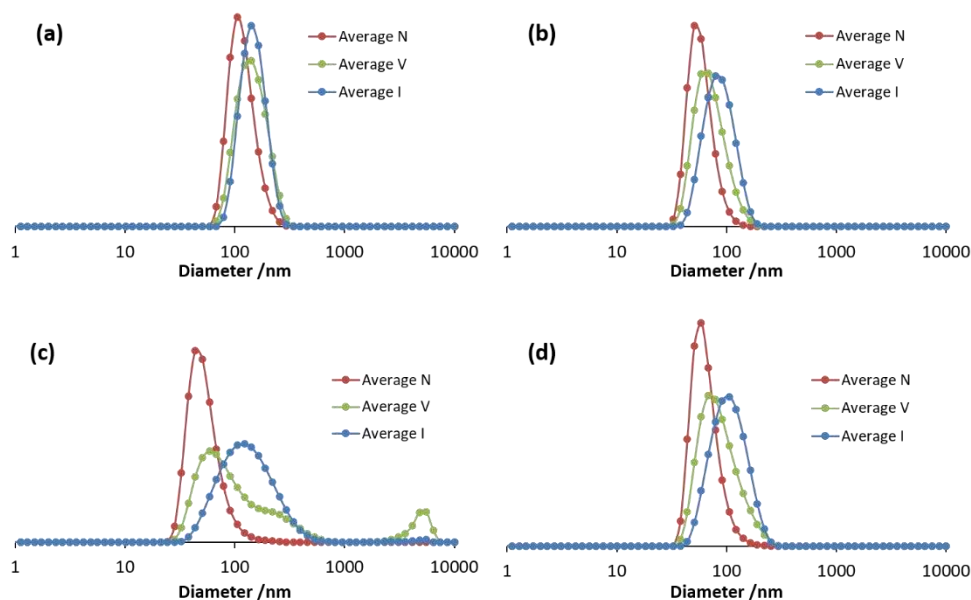


Figure II.2.29 DLS analysis of $R_0-(4VPMe^+I)_{140}-b-St_{345}-b-DEGDMA_{15}-SC(S)SPr$ after freeze-drying and redispersion: (a) in neat DMSO at room temperature; (b) as (a) after heating at 90 °C for 24 h; (c) in DMSO/toluene 80/20 (v/v) at room temperature; (d) as (c) after heating at 90 °C for 24 h. All measurements were carried out on unfiltered samples.

II.2.4 Synthesis of a $P4VPMe^+I^- - b - PSt - b - P(St-co-DEGDMA)$ NG

As a final synthetic application, the $R_0-(4VPMe^+I^-)_{137}-b-St_{48}-SC(S)SPr$ macroRAFT intermediate was used for a one-step synthesis of unimolecular polymers with a NG core. This was accomplished by copolymerization of styrene and the DEGDMA crosslinker with a $P4VPMe^+I^- - b - PSt$ macroRAFT/St/DEGDMA molar ratio of 1:300:15. The 1H NMR monitoring revealed once again complete monomer conversion (Figure II.2.30), yielding the desired $R_0-(4VPMe^+I^-)_{137}-b-St_{48}-b-(St_{300}-co-DEGDMA_{15})-SC(S)SPr$.

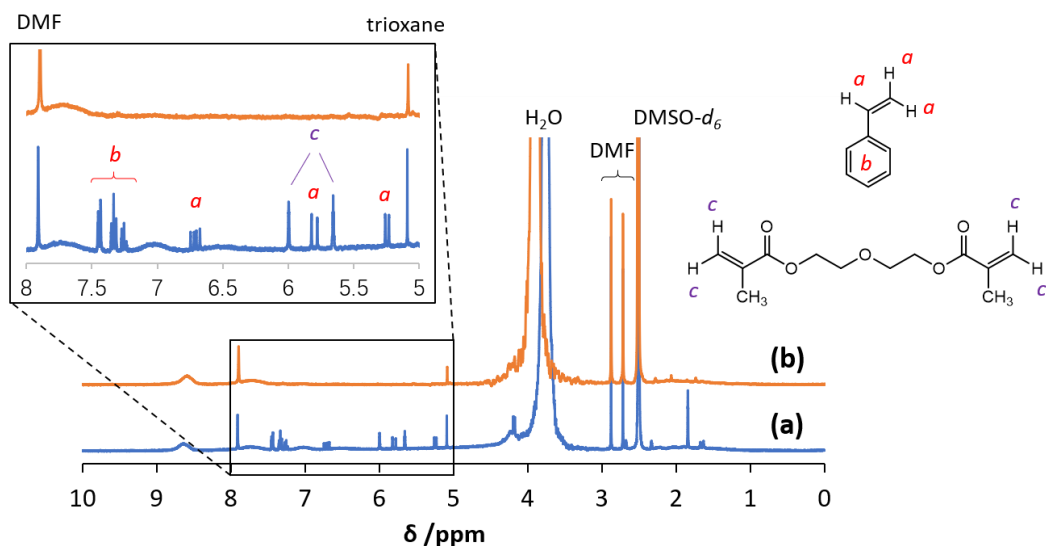


Figure II.2.30 ^1H NMR monitoring in $\text{DMSO-}d_6$ of the $\text{R}_0\text{-(4VPMe}^+\text{I)}_{137}\text{-}b\text{-St}_{48}\text{-}b\text{-(St}_{300}\text{-}co\text{-DEGDMA}_{15}\text{)-SC(S)SPr}$ nanogel synthesis: (a) initial spectrum ($t = 0$) and (b) after 17 h.

The DLS analysis confirms the generation of uniform particles, although it suggests a minor degree of agglomeration, see Figure II.2.31, although this phenomenon is less important as in the corresponding NG with the $\text{P(MAA-}co\text{-PEOMA)}$ shell (Figure A.0.9). The D_z (PDI) is 84.7 nm (0.05) for the unswollen sample, 92.6 nm (0.06) for the CHCl_3 -swollen sample (30.7% volume increase; $\Delta V = 9.76 \times 10^4 \text{ nm}^3$; and 7.3×10^5 molecules per particle), and 88.8 nm (0.06) for the toluene-swollen sample (15.2% volume increase; $\Delta V = 4.85 \times 10^4 \text{ nm}^3$; and 2.7×10^5 molecules per particle). The formation of larger agglomerates was however not evident from the TEM analysis (several images were analyzed), which also confirms the presence of individual spherical particles, indicating that the degree of aggregation is very minor (see a representative image in Figure II.2.32).

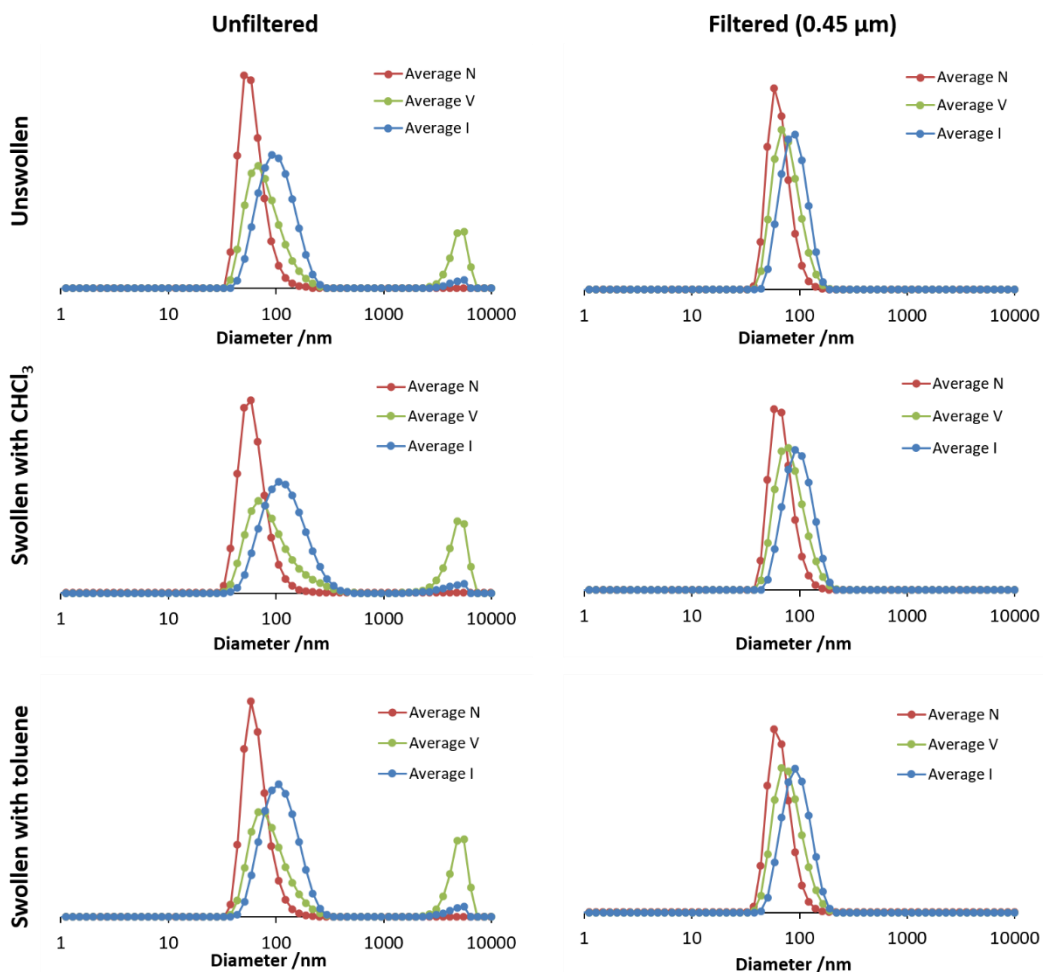


Figure II.2.31 DLS analysis of the nanogel $R_0-(4VPMe^+I)_{137}-b-St_{48}-b-(St_{300}-co-DEGDMA_{15})-SC(S)SPr$ latex, as synthesized or swollen with either $CHCl_3$ or toluene.

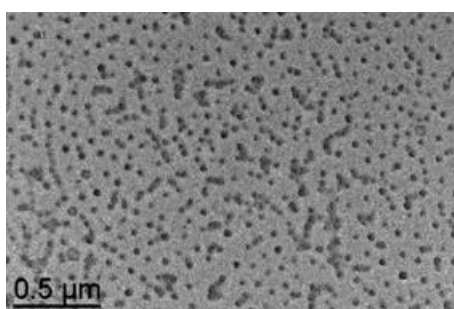


Figure II.2.32 TEM image of the $R_0-(4VPMe^+I)_{137}-b-St_{48}-b-(St_{300}-co-DEGDMA_{15})-SC(S)SPr$ nanogel particles.

This result, in comparison with the absence of particle-particle coupling for the CCM syntheses described in the previous sections, shows that the state of aggregation of the diblock precursor is important. The diblock with the long PSt chain, that is, R_0-

$(4\text{VPMe}^+\text{I}^-)_{137}\text{-}b\text{-St}_{345}\text{-SC(S)SPr}$, is preorganized in the form of individual spherical micelles (Figure II.2.17) and leads to individual particles upon crosslinking, even when using a neat crosslinker. On the other hand, the diblock precursor with the short PSt chain, that is, $\text{R}_0\text{-}(4\text{VPMe}^+\text{I}^-)_{137}\text{-}b\text{-St}_{48}\text{-SC(S)SPr}$, is self-organized in agglomerated micelles with a broader size distribution (Figure II.2.15) and the crosslinking step consequently leads to the formation of a few particle agglomerates. It is important to underline that in this synthesis, as in all other syntheses described above, all components including the initiator were introduced into the reaction flask before starting to heat the mixture.

Since the results described above clearly demonstrate that the state of aggregation is affected by the hydrophilic/hydrophobic component ratio, notably increasing the hydrophobic fraction favors a breakdown of large aggregates into individual spherical micelles, it was reasoned that this NG particle synthesis could be improved by first equilibrating the $\text{R}_0\text{-}(4\text{VPMe}^+\text{I}^-)_{137}\text{-}b\text{-St}_{48}\text{-SC(S)SPr}$ macroRAFT agent with all hydrophobic monomers at the reaction temperature in the absence of an initiator, before the ACPA addition to start the reaction. Indeed, operating in this way, the initial broad distribution of the $\text{R}_0\text{-}(4\text{VPMe}^+\text{I}^-)_{137}\text{-}b\text{-St}_{48}\text{-SC(S)SPr}$ particles (Figure II.2.15), after monomer addition and equilibration, was transformed into a narrower distribution of smaller particles ($D_z = 107.0$ nm and $\text{PDI} = 0.10$, Figure II.2.33a). Subsequent polymerization yielded a stable colloidal suspension of $\text{R}_0\text{-}(4\text{VPMe}^+\text{I}^-)_{137}\text{-}b\text{-St}_{48}\text{-}b\text{-}(\text{St}_{300}\text{-}co\text{-DEGDMA}_{15})\text{-SC(S)SPr}$ without any evidence of residual agglomerates by DLS and TEM analyses, see Figure II.2.33. Notably, the size distribution of the final crosslinked polymer particles ($D_z = 101.4$ nm and $\text{PDI} = 0.06$, see Figure II.2.33b) is relatively close to that of the swollen particles prior to polymerization. The particle size then slightly increased after swelling with toluene ($D_z = 110.5$ nm and $\text{PDI} = 0.15$, see Figure II.2.33c), corresponding to a 29.4% volume increase ($\Delta V = 1.61 \times 10^5$ nm³ and 9.1×10^5 molecules per particle).

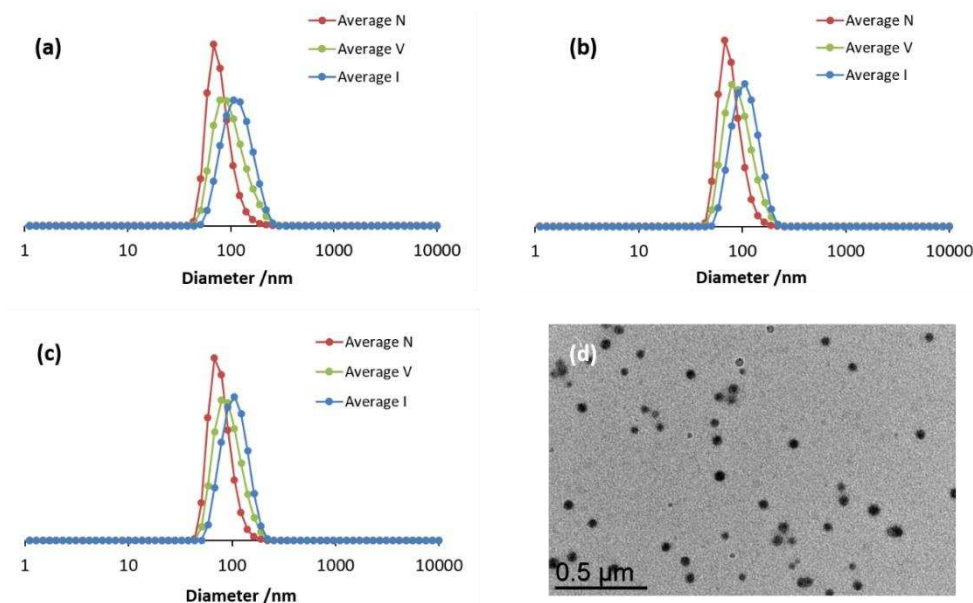


Figure II.2.33 DLS analyses (unfiltered samples) of (a) $R_0-(4VPMe^+I^-)_{137}-b-St_{48}-SC(S)SPr$ macroRAFT agent after equilibration with styrene (300 equiv.) and DEGDMA (15 equiv.) in water at 80 °C for 30 min; (b) $R_0-(4VPMe^+I^-)_{137}-b-St_{48}-b-(St_{300}-co-DEGDMA_{15})-SC(S)SPr$; (c) as (b), after swelling with toluene; (d) TEM image of the final product.

The 1H NMR spectrum of the NG-C particles in D_2O , with the core swollen by $CDCl_3$, is reported in Figure II.2.34. Identical to the 1H NMR spectra of $R_0-(4VPMe^+I^-)_{137}-b-St_{345}-b-(St_{157}-co-DEGDMA_{13})-SC(S)SPr$ and $R_0-(4VPMe^+I^-)_{140}-b-St_{345}-b-DEGDMA_{15}-SC(S)SPr$, this spectrum also shows proton signals from $P4VPMe^+I^-$ shell units solvated by D_2O and PSt core units solvated by $CDCl_3$.

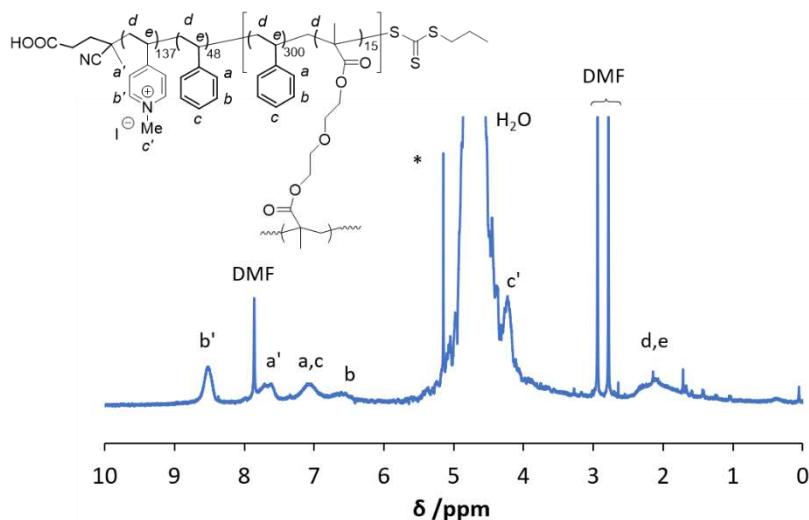


Figure II.2.34 1H NMR spectrum of the $R_0-(4VPMe^+I^-)_{137}-b-St_{48}-b-(St_{300}-co-DEGDMA_{15})-SC(S)SPr$ latex with added D_2O and with the PSt core swollen by $CDCl_3$.

These particles, like the CCM-C particles obtained by crosslinking with the DEGDMA/styrene mixture, showed thermal stability, no alteration by freeze-drying and redispersion in water (Figure II.2.35) or DMSO, and no evidence of single chain release in the DMSO/toluene (80/20, v/v) mixture (Figure II.2.36). By analogy with the CCM-C particles and the precursor diblock copolymer micelles, redispersion of the freeze-dried NG-C particles in DMSO resulted in distributions with a smaller diameter ($D_z = 60.8$ nm and PDI = 0.06) relative to those redispersed in water ($D_z = 116.4$ nm and PDI = 0.14).

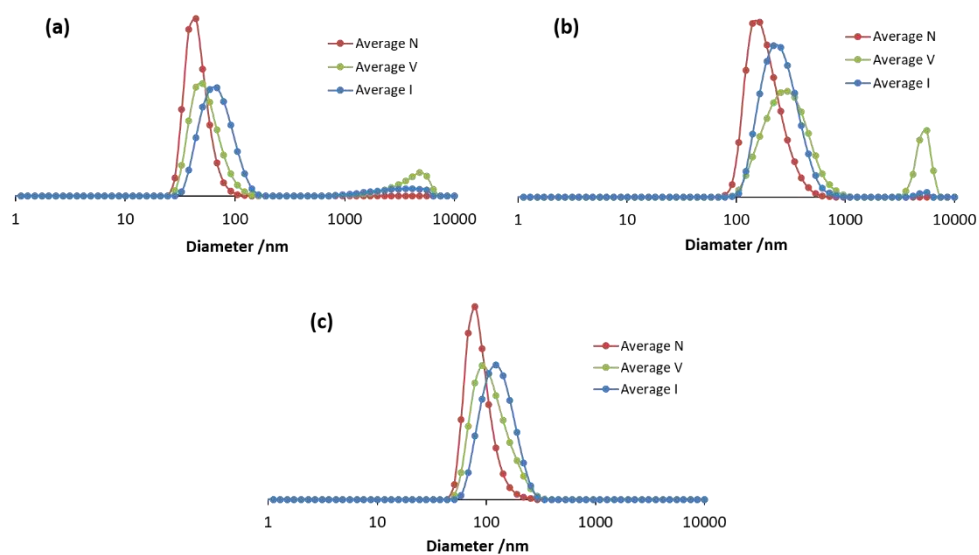


Figure II.2.35 DLS analysis of the $R_0-(4VPMe^+I)_{140}-b-St_{50}-b-(St_{300}-co-DEGDMA_{15})-SC(S)SPr$ nanogel latex: (a) after heating at 90 °C for 24 h ($D_z = 70.0$ nm, PDI = 0.25); (b) swollen with toluene and after heating for 24 h at 90 °C ($D_z = 237.8$ nm, PDI = 0.19); (c) after freeze-drying and redispersion in water. All measurements were carried out on unfiltered samples.

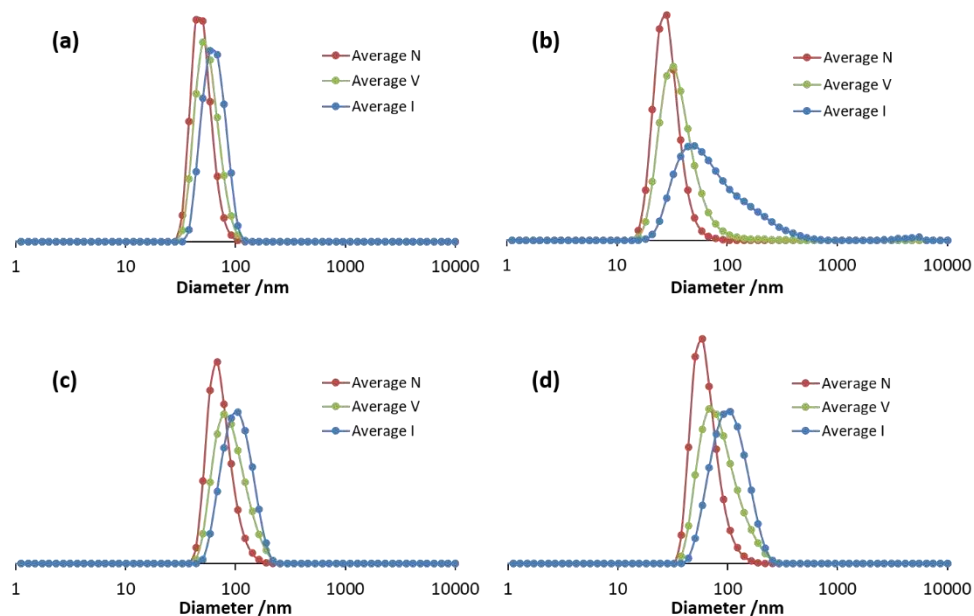
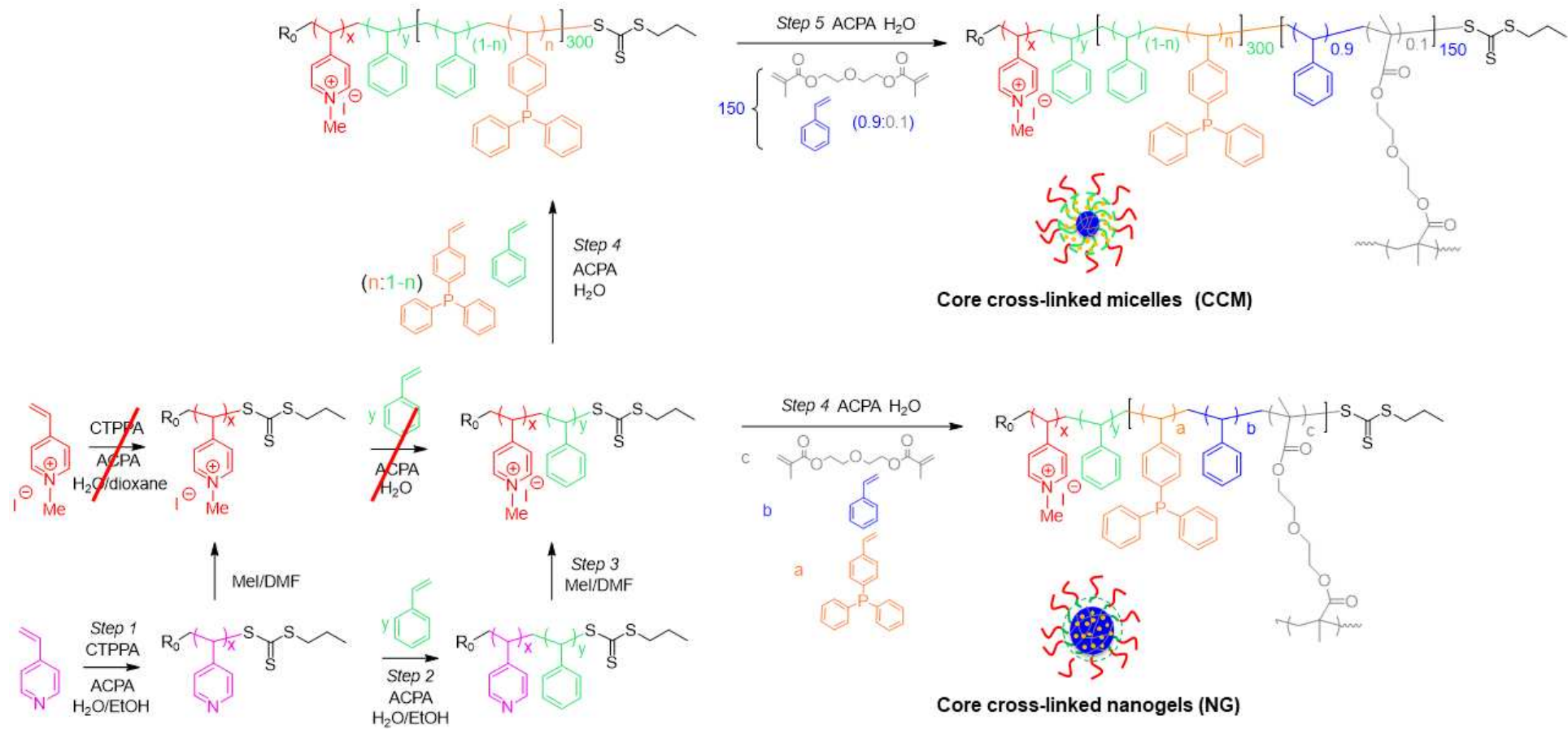


Figure II.2.36 DLS analysis of $R_0-(4VPMe^+I)_{140}-b-St_{50}-b-(St_{300}-co-DEGDMA_{15})-SC(S)SPr$ after freeze-drying and redispersion: (a) in neat DMSO at room temperature; (b) as (a) after heating at 90 °C for 24 h ($D_z = 59.2$ nm, PDI = 0.28); (c) in DMSO/toluene 80/20 (v/v) at room temperature ($D_z = 110.1$ nm, PDI = 0.03); (d) as (c) after heating at 90 °C for 24 h ($D_z = 94.9$ nm, PDI = 0.12). All measurements were carried out on unfiltered samples.

II.3 RAFT polymerization of phosphine-functionalized cationic copolymer

In order to use the second-generation crosslinked polymers with a $P4VPMe^+I^-$ cationic shell (CCM-C and NG-C) described in section II.2 as nanoreactors for aqueous biphasic catalysis, analogous core-functionalized polymers were then developed using DPPS as hydrophobic comonomer, duplicating the strategy used for the first generation neutral-shell nanoreactors.^[72, 94, 100, 102, 105-107, 109, 143]

Scheme II.3.1 Synthesis pathway toward block copolymer nanoreactor with a polycationic shell.



For this CCM synthesis, the macroRAFT agent, $R_0-(4VPMe^+I^-)_{140}-b-St_{50}-SC(S)SPr$ was first chain extended with the appropriate mixture of styrene and DPPS, yielding latexes of the corresponding $R_0-(4VPMe^+I^-)_{140}-b-St_{50}-b-(St_{1-n}-co-DPPS_n)_{300}-SC(S)SPr$ amphiphilic linear chains. In order to simplify the symbol in this thesis, the neutral-shell polymers are acronymized as CCM-N-n and the cationic-shell polymers as CCM-C-n and NG-C-n ($n =$ DPPS fraction in the hydrophobic core). In this step, DPPS was first dissolved in styrene and then the monomer solution was added to the macroRAFT solution. Due to the solubility of DPPS in styrene, the selected n values were limited to 0.05, 0.1 and 0.2, which corresponds to three versions of polymer diblocks: diblock 5%, with an average of 15 ligands per chain, diblock 10%, 30 ligands per chain and diblock 20%, 60 ligands per chain. The 1H NMR spectra obtained after diluting an aliquot of the latex into $DMSO-d_6$ for reaction monitoring, collected in Figure II.3.1, show that these three polymerizations were complete (no residual monomer resonances).

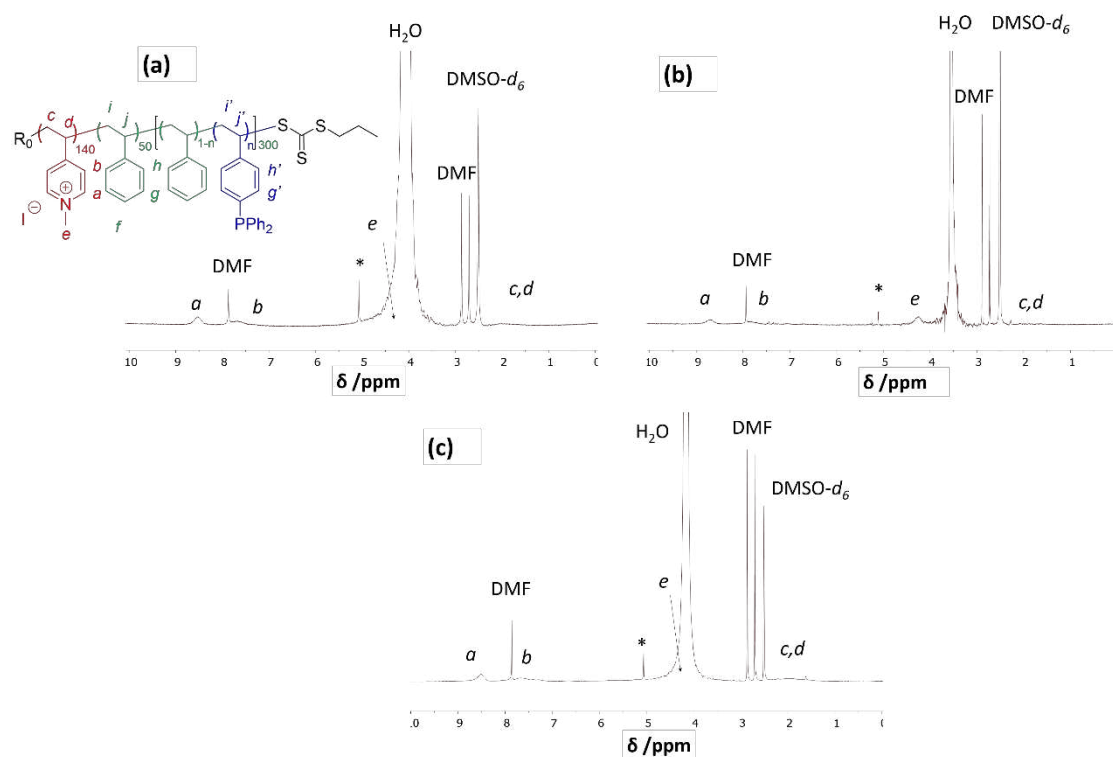


Figure II.3.1 1H NMR spectra of the latex of diblocks $R_0-(4VPMe^+I^-)_{140}-b-St_{50}-b-(St_{1-n}-co-DPPS_n)_{300}-SC(S)SPr$: (a) $n = 0.05$; (b) $n = 0.1$; (c) $n = 0.2$ in $DMSO-d_6$.

Dilution with DMSO- d_6 allowed the monomer consumption to be monitored but the particle core resonances were not revealed, since DMSO is not a good solvent for PSt. On the other hand, after core swelling with $CDCl_3$ (a good solvent for PSt) and dilution into D_2O , the core resonances became observable (Figure II.3.2).

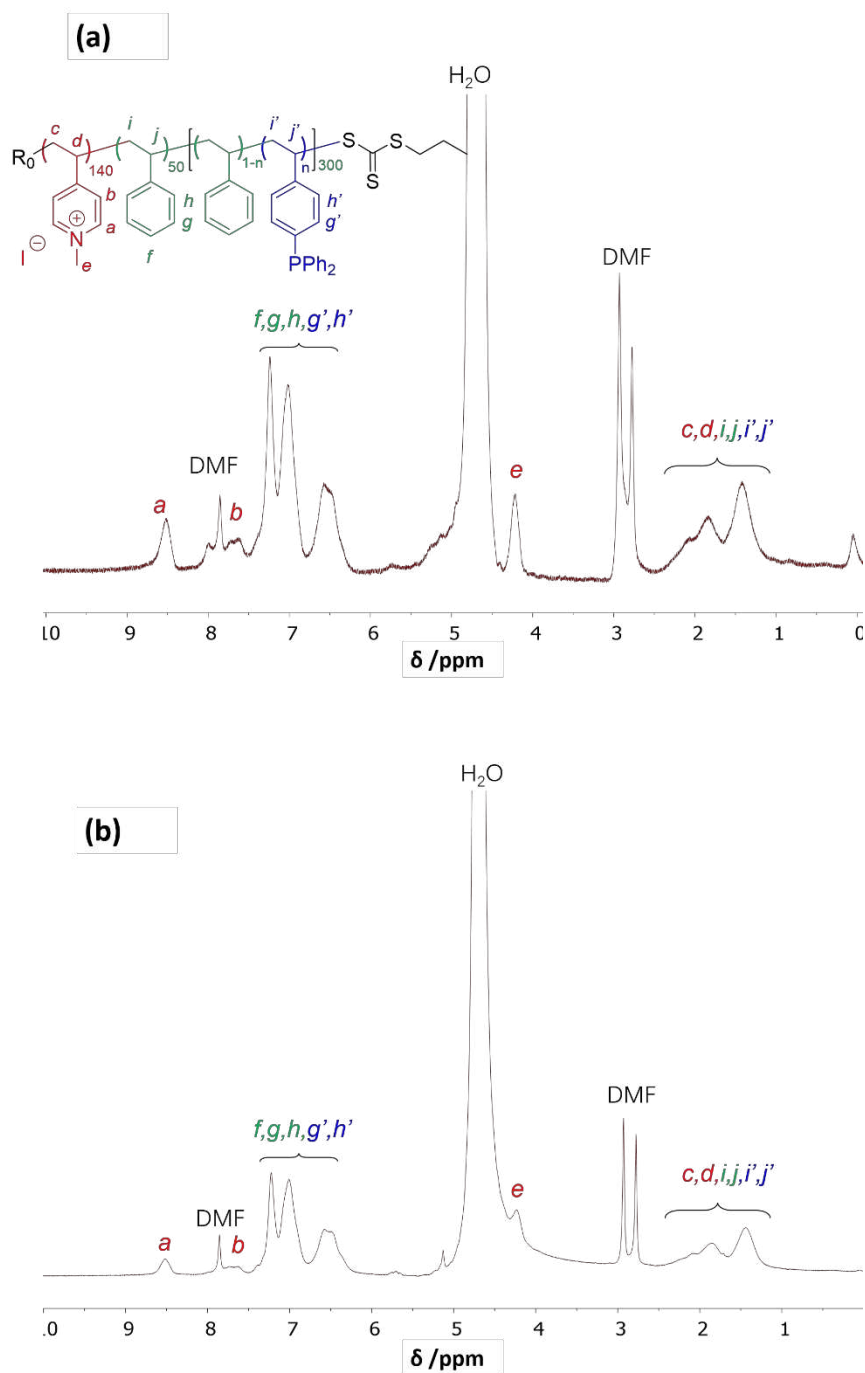


Figure II.3.2 1H NMR spectrum of the latex of (a) diblock 10% and (b) diblock 20% in D_2O , with core swollen by $CDCl_3$.

These polymers were then crosslinked with a DEGDMA/styrene (10/90) mixture in the final step to afford $R_0-(4VPMe^+I^-)_{140}-b-St_{50}-b-(St_{1-n}-co-DPPS_n)_{300}-b-(St_{0.9}-co-DEGDMA_{0.1})_{150}-SC(S)SPr$ (CCM-C-0.05, CCM-C-0.1 and CCM-C-0.2, respectively). The 1H NMR spectra in $DMSO-d_6$ are shown in Figure II.3.3 and those in $D_2O/CDCl_3$ are shown in Figure II.3.4.

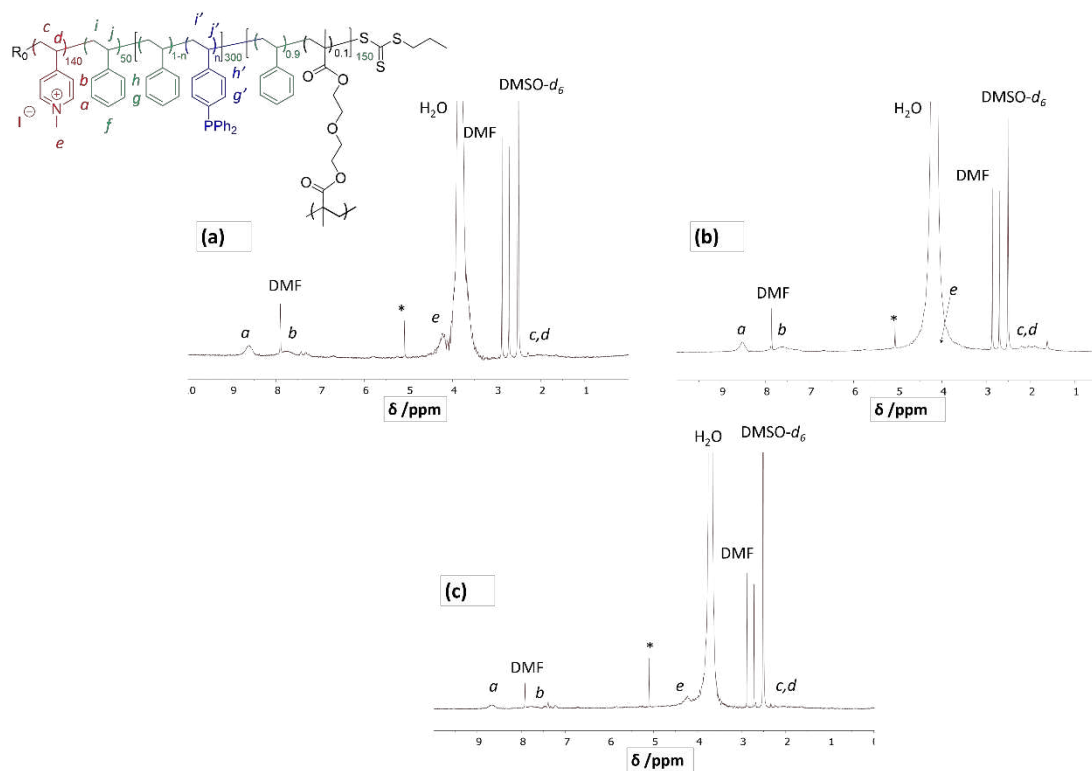


Figure II.3.3 1H NMR spectra of the latex of (a) CCM-C-0.05; (b) CCM-C-0.1; (c) CCM-C-0.2 in $DMSO-d_6$.

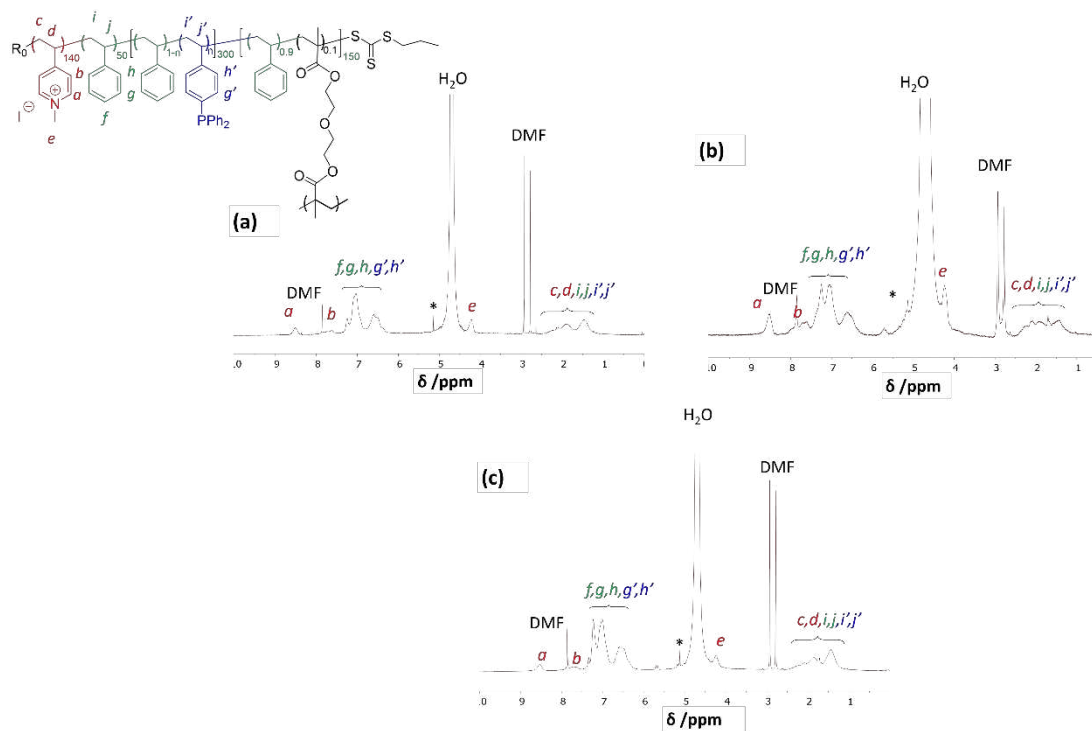


Figure II.3.4 ^1H NMR spectra of the latex of (a) CCM-C-0.05; (b) CCM-C-0.1; (c) CCM-C-0.2 in D_2O , with core swollen by CDCl_3 .

The latex of the NG was obtained in a single step, copolymerizing simultaneously styrene, the ligand-functionalized DPPS monomer, and the DEGDMA crosslinker. Only a version containing on average 30 DPPS monomers per chain, $\text{R}_0\text{-(4VPMe}^+\text{I)}_{140}\text{-}b\text{-St}_{50}\text{-}b\text{-(St}_{426}\text{-}co\text{-DPPS}_{30}\text{-}co\text{-DEGDMA}_{15})\text{-SC(S)SPr}$, like the CCM-C-0.1 product, was developed (Figure II.3.5), although the total amount of styrene and crosslinker per chain is greater and therefore the overall ligand concentration in the hydrophobic core is intermediate between those of CCM-C-0.1 and CCM-C-0.05. All the latexes obtained were low viscosity colloidal dispersions, in spite of the high polymer content (16-24% in weight), with a milky aspect. They were all stable over time, giving no evidence of destabilization or gradient development over several months.

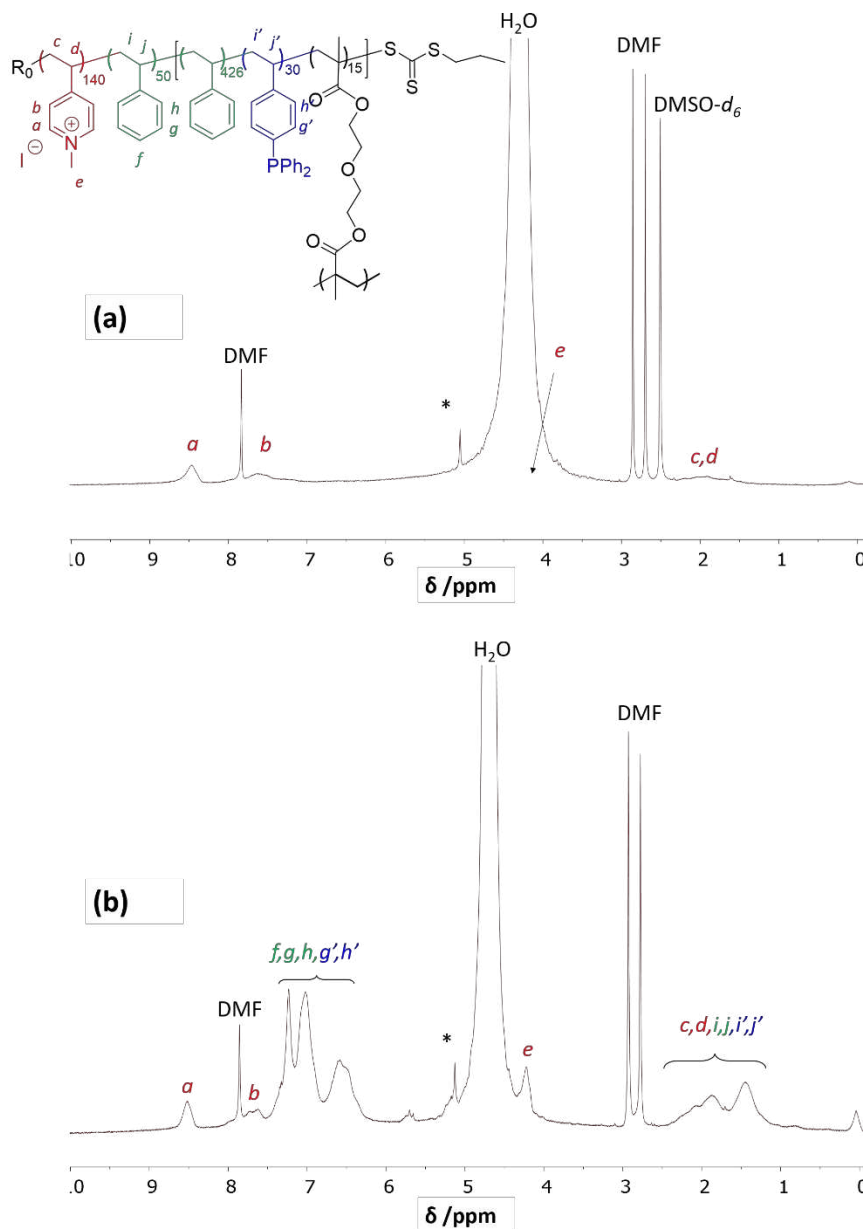


Figure II.3.5 ^1H NMR spectra of the latex of NG: (a) in $\text{DMSO-}d_6$ and (b) in D_2O , with core swollen by CDCl_3 .

The particle size of the final polymers is too large to allow meaningful SEC or DOSY NMR analyses. The DPPS incorporation in the polymer core cannot be assessed from the ^1H NMR spectra because the corresponding resonances cannot be distinguished from those of the styrene units. However, the presence of core-linked DPPS units was clearly indicated by a relatively broad resonance in the ^{31}P NMR spectrum at δ -6.5 ppm, slightly shifted from the resonance of the precursor DPPS in

the same CDCl_3 solvent (Figure II.3.6). The same broadening and resonance shift was previously observed for the incorporation of DPPS in the equivalent polymers with the neutral outer shell.^[72, 105a]

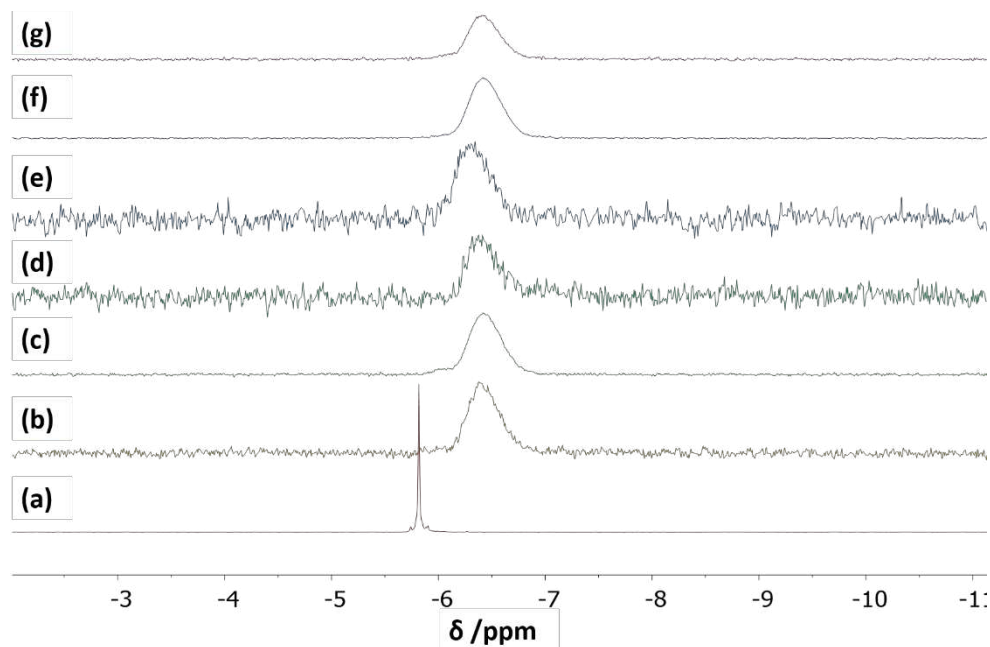


Figure II.3.6 ^{31}P NMR spectra of (a) DPPS in CDCl_3 and (b-g) of the various latexes after swelling with CDCl_3 and dilution in D_2O : (b) diblock 10%; (c) diblock 20%; (d) CCM-C-0.05; (e) CCM-C-0.1; (f) CCM-C-0.2; (g) NG.

The DLS and TEM analyses (Figure II.3.7) showed that all obtained polymers have spherical morphology, with average diameter in the 130-150 nm range and narrow size distributions. In addition, DLS measurements of CCM-C-0.05, CCM-C-0.1 and NG-C after freeze-drying and redispersion in a DMSO/toluene 80/20 (v/v) mixture revealed the absence of non-crosslinked arms (see Figure II.3.8). Indeed, this solvent mixture is able to solvate both blocks and would reveal the presence of single chains at smaller diameters, as shown in section II.2 for the analogous DPPS-free diblock. The particle diameters revealed by the TEM images are smaller than those obtained from the DLS data (see the frequency analysis in Figure II.3.7, right part), because the TEM measures the objects after deposition and drying on the grid support, whereas the DLS data are obtained on the solvated particles and thus reflect the diameter expansion by

the hydrophilic shell solvation.

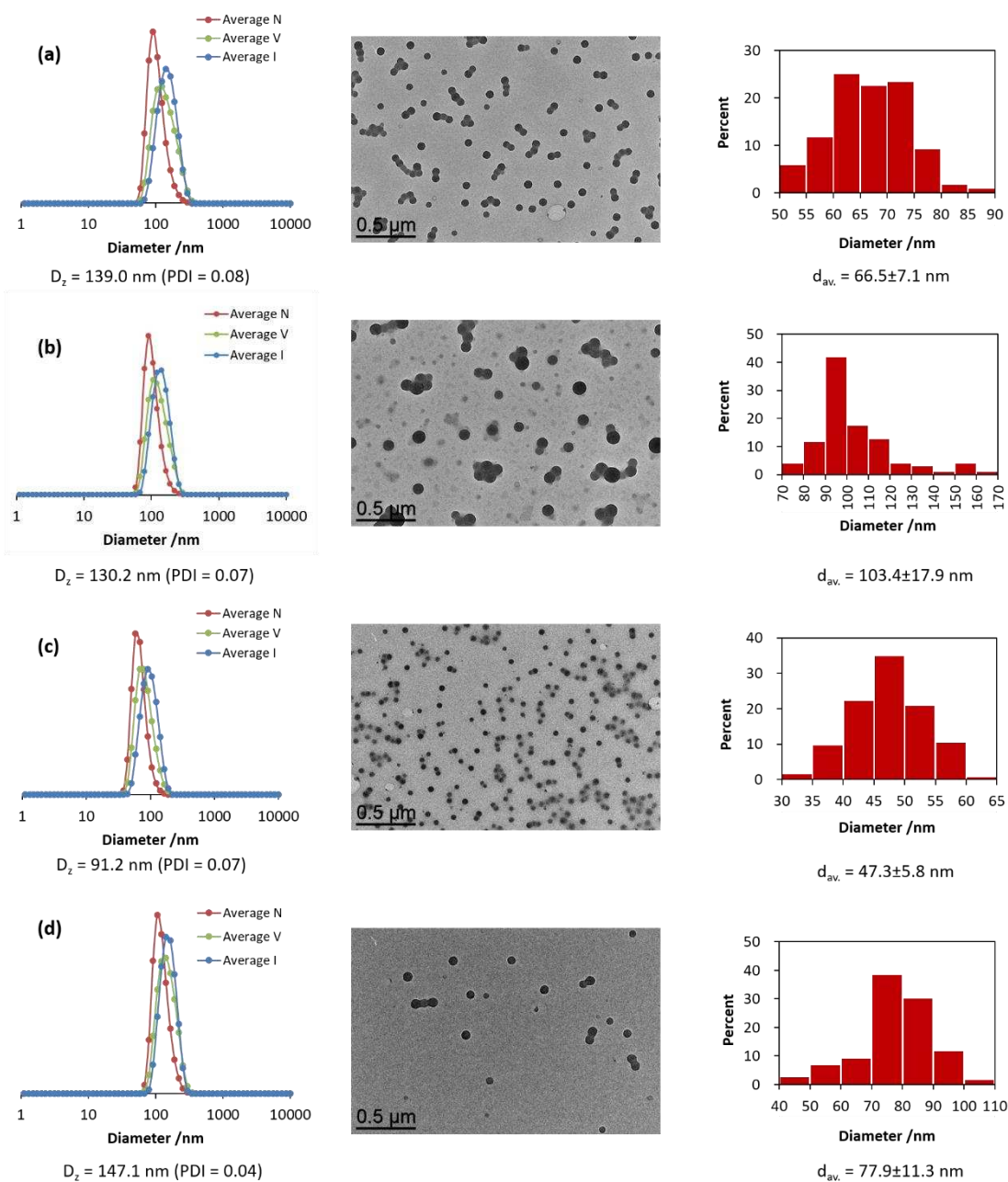


Figure II.3.7 DLS with D_z , PDI (left), representative TEM images (middle) and frequency analysis of the diameters with average and standard deviation from the TEM images (right, > 100 measured particles) for: (a) CCM-C-0.05; (b) CCM-C-0.1; (c) CCM-C-0.2; (d) NG-C. All reported DLS data were obtained on unfiltered samples.

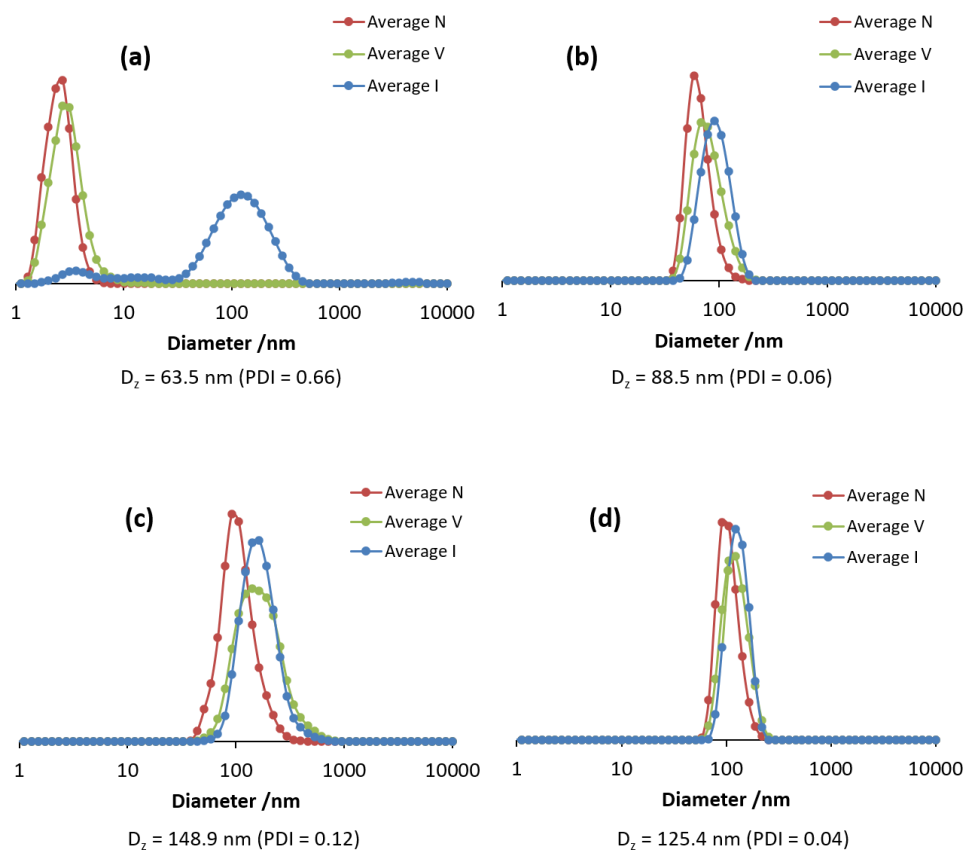
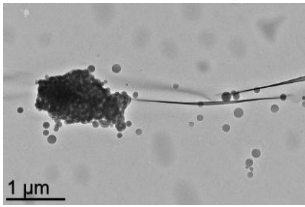
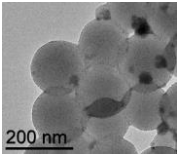
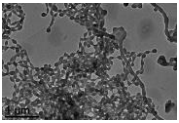
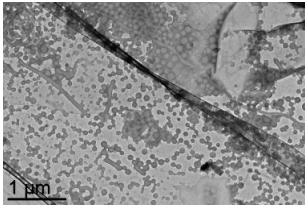
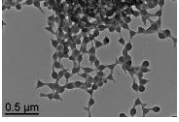
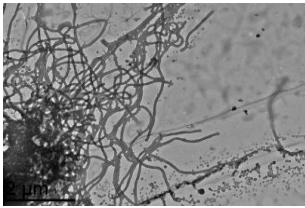
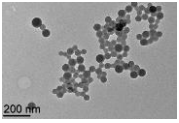
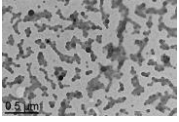
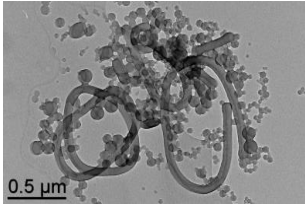
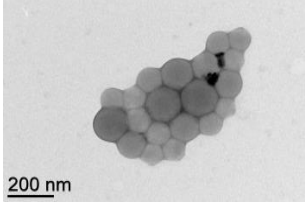
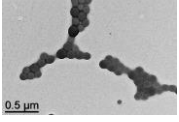
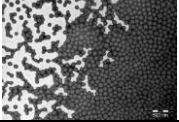
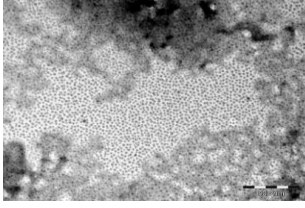
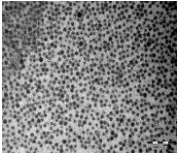


Figure II.3.8 DLS analyses of (a) $R_0-(4VPMe^+I)_{140}-b-St_{50}-b-St_{300}-SC(S)SPr$; (b) CCM-C-0.05; (c) CCM-C-0.1; (d) NG-C, after freeze-drying and redispersion in a DMSO/toluene (80/20, v/v) mixture. The diblock sample (a) was filtered through a $0.45 \mu m$ septum to remove a small fraction of agglomerates with $d > 5000 \text{ nm}$ (visible in the volume and intensity distributions). All other measurements were done on unfiltered samples.

An exploration by TEM analysis (Table II.3.1) of the CCM morphology dependence on the hydrophilic and hydrophobic block molar masses showed that a reduction of the hydrophilic block molar mass (72 or 56 $4VPMe^+I^-$ units), while maintaining a similar molar mass for the hydrophobic part, led to mixtures of cylindrical and spherical micelles for the linear amphiphilic intermediate. This switch in morphology is consistent with the behavior of block copolymers with higher molar mass hydrophobic block and self-assembling during a PISA process.^[144] It indirectly attests to the control of the polymerization during chain extension, indicating that well-defined block copolymers were achieved. Interestingly, rearrangement to spherical CCM particles occurred when using greater amounts of styrene/DEGDMA in the

crosslinking step. The corresponding strong plasticization of the core of the nano-objects probably helps the reorganization of the block copolymers during this step into spherical morphologies, rapidly locked by the crosslinking reaction. Shortening the hydrophobic chain molar mass (*e.g.* R₀-(4VPMe⁺I⁻)₅₆-*b*-St₃₂-*b*-(St_{1-n}-*co*-DPPS_n)₁₁₈-SC(S)SPr) ensured a spherical morphology for the intermediate micelles, although the final crosslinked objects had a less well-defined morphology. The most homogeneous spherical morphology for both the intermediate micelles and the final CCM-C particles was obtained when using the longer outer block (140-150 4VPMe⁺I⁻ monomer units). Since the spherical morphology seems most suitable for applications as nanoreactors in biphasic catalysis, the optimum balance of hydrophilic and hydrophobic parts of the CCM-C nanoreactors was fixed as *ca.* 150 and 300 before crosslinking, and an overall equivalent ratio of hydrophilic/hydrophobic parts was maintained for the NG synthesis.

Table II.3.1 Exploration of the morphology dependence for the diblock $R_0-(4VPMe^+I)_a-b-St_b-b-(St_{1-n-co-DPPS_n})_c-SC(S)SPr$ and for the CCM $R_0-(4VPMe^+I)_a-b-St_b-b-(St_{1-n-co-DPPS_n})_c-b-(St_d-co-DEGDMA_e)-SC(S)SPr$ as a function of hydrophilic and hydrophobic chain lengths (a, b, c) and of the amount of monomers used in the crosslinking step (d, e).

a	b	c (n)	Diblock TEM	d	e	CCM TEM
56	32	246 (0.1)		82	110	
				90	10	
56	32	118 (0.042)		100	10	
72	28	274 (0.09)		180	10	
				148	3	
72	28	160 (0)		Not crosslinked		
138	45	300 (0.083)		158	13	
				0	10	
150	50	300 (0.1)		165	11	

In terms of swelling capacity and mass transport, these polymers do not show any substantial difference relative to the equivalent ones with the neutral P(MAA-*co*-PEOMA) outer shell (Figure A.0.10) or to the non-functionalized ones with the same outer shell described above in section II.2: the incorporation of swelling solvents (toluene or chloroform) was quite rapid (< 1 min) upon shaking the biphasic mixture, as visually assessed by the change of the relative phase volumes, and gave rise to an average diameter increase while maintaining narrow size dispersions (Figure II.3.9). Therefore, changing the hydrophilic shell from neutral P(MAA-*co*-PEOMA) to polycationic P4VPMe⁺I⁻ or the introduction of phosphine ligands do not negatively affect the migration of neutral organic compounds from an external continuous phase to the nanoreactor core.

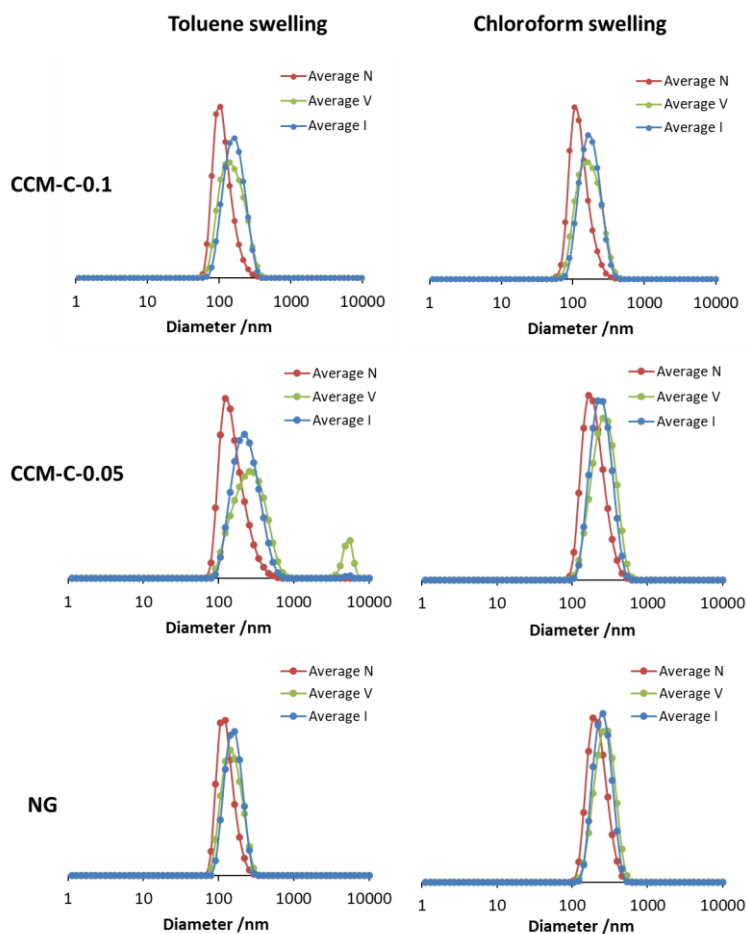


Figure II.3.9 DLS analyses of the aqueous suspensions of CCM-C and NG-C particles after swelling. All measurements were done on unfiltered samples.

II.4 Conclusion

In this chapter, we targeted CCMs or NGs with a P4VPMe⁺I⁻ polycationic outer shell and a PSt core. Our initial approach was based on the use of PISA to chain extend in water a P4VPMe⁺I⁻ polymer, synthesized by RAFT, with a PSt block, followed by crosslinking with DEGDMA. However, neither RAFT polymerization of 4VPMe⁺I⁻ nor chain extension of a preformed P4VPMe⁺I⁻ macroRAFT agent (obtained after cationization of P4VP synthesized by RAFT) with styrene in water was successful. This drove us to develop an alternative strategy, relying on the synthesis of P4VP-*b*-PSt block copolymer particles obtained by PISA in a mixture of ethanol and water, the stabilizing P4VP layer being post-cationized to provide a P4VPMe⁺I⁻-*b*-PSt intermediate. Optimization to efficiently produce the targeted CCM-C or NG-C required fine tuning of the hydrophilic/hydrophobic balance between the two blocks, with an optimum for short PSt block, that is, R₀-(4VPMe⁺I⁻)₁₃₇-*b*-St₄₈-SC(S)SPr chains that were redispersed in water.

For the CCM-C synthesis, these chains were first chain-extended with styrene. Crosslinking successfully took place in a subsequent step using either a mixture of St and DEGDMA or DEGDMA alone. Indeed, in the latter case, particle-particle interpenetration, identified in the previous work on the P(MAA-*co*-PEOMA) shell CCM-N as the main cause of macrogelation, was impeded thanks to the polyelectrolytic nature of the particle shells. Under both experimental conditions, the crosslinking was quantitative as evidenced by the absence of free diblock arms, according to the DLS analysis of freeze-dried polymer suspension in a mixed DMSO/toluene (80/20, v/v) solvent. The NGs were obtained by simultaneous chain extension and crosslinking of the R₀-(4VPMe⁺I⁻)₁₃₇-*b*-St₄₈-SC(S)SPr chains with a mixture of St and DEGDMA.

For both CCMs and NGs, positively charged and spherical particles with average D_z in the 85-150 nm range were obtained as stable polymer dispersions, with polymer content up to 10% in weight. Taking advantage of the flexibility of the PISA process,

the initially encountered difficulties linked to the charged nature of polyelectrolytic shell were circumvented, leading to the successful formation of the targeted polycationic spherical particles.

Finally, equivalent particles with phosphine ligand-functionalized hydrophobic cores have also been prepared by adaptation of the chain extension step that introduces the hydrophobic block. These polymers are still well-controlled when prepared on the basis of the previously optimized hydrophilic/hydrophobic monomer ratio. The investigations of these polymers as nanoreactors in micellar aqueous biphasic catalysis will be described in Chapter III.

Chapter III

Coordination studies and molecular rhodium-catalyzed biphasic hydrogenations

III.1 Introduction

For the purpose of the application of the phosphine-functionalized unimolecular nanoreactors synthesized as described in Chapter II to aqueous biphasic catalysis, the molecular transition metal complex precatalysts must be transferred into the hydrophobic core through the hydrophilic shell with the help of organic solvents and coordinated to the phosphine ligands. As noted in the Chapter II, DLS and NMR spectroscopy demonstrate that the hydrophobic polystyrene core can be swollen by typical organic solvents such as toluene, chloroform, THF and diethyl ether by a short-time stirring at room temperature. In the previous reports on the nanoreactors with neutral P(MAA-*co*-PEOMA) shell in our team^[72, 94, 100, 102, 105-107, 109, 143], a protocol for the coordination reaction was optimized. The particle cores were pre-swollen by toluene or chloroform, before addition of the metal complex as a toluene or chloroform solution to the aqueous latex phase. Upon equilibrating the two phases under vigorous stirring at room temperature, the Rh complex was transferred into the nanoreactor cores quantitatively within 30 min, as optically assessed by the transfer of the complex orange color from the organic to the aqueous phase (Figure III.1.1).

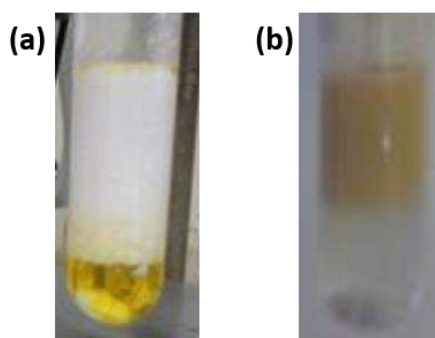
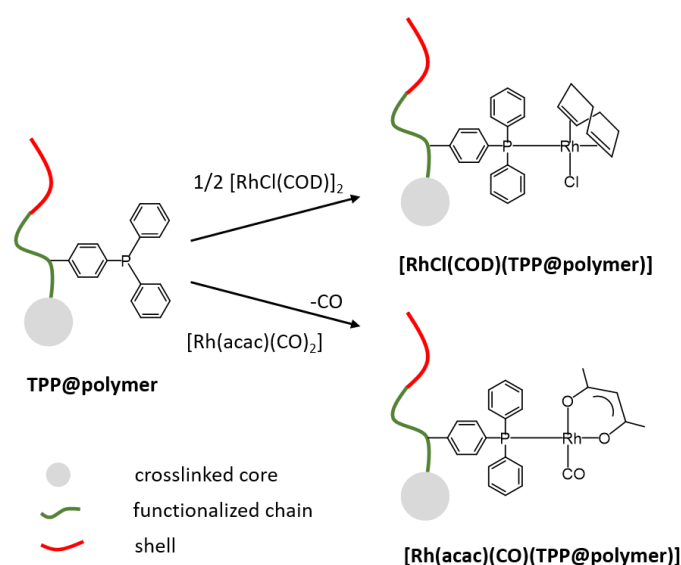


Figure III.1.1 Photos of CCM latex: (a) pre-swelling latex with Rh complex chloroform solution; (c) after stirring and decantation for less than 1 min.

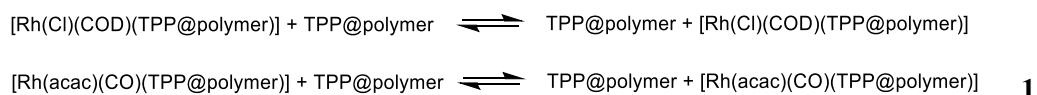
More specifically, the polymers were loaded with either chloro(1,5-cycoctadiene)rhodium(I) dimer ($[\text{RhCl}(\text{COD})]_2$) for the styrene and 1-octene

hydrogenation^[109] or with acetylacetonatodicarbonylrhodium(I) ($[\text{Rh}(\text{acac})(\text{CO})_2]$) for the 1-octene hydroformylation,^[105a] forming the $[\text{RhCl}(\text{COD})(\text{TPP}@\text{polymer})]$ and $[\text{Rh}(\text{acac})(\text{CO})(\text{TPP}@\text{polymer})]$ core-anchored complexes, respectively (Scheme III.1.1). The successful coordination of the rhodium complexes to the phosphine ligands was additionally confirmed by the ^{31}P NMR spectrum: the fully Rh loaded particles ($\text{P}/\text{Rh} = 1:1$) show a doublet resonance at low field (δ 47.5 ppm, $J_{\text{PRh}} = 175$ Hz) while the empty particles ($\text{P}/\text{Rh} = 0$) show a single resonance at high field (δ -6.2 ppm).^[94]



Scheme III.1.1 Coordination reaction between Rh precatalyst and nanoreactor (CCM).

Interestingly, in the spectra recorded for the Rh-charged particles at higher P/Rh ratios (2:1 or 4:1) neither the Rh-P resonance nor the free P resonance was visible because of a fast interparticle exchange reaction^[145] between the coordinated and free phosphine ligands, as indicated in Equation 1, which led to a broadened P signal. This phenomenon occurs for both the intraparticle exchange (TPP ligands within the same core) and for the interparticle exchange (TPP ligands from different cores, which come into contact during particle interpenetration). The latter phenomenon is responsible for interparticle metal migration.^[94, 100, 143] Even in the TPP@NG nanoreactor, the interparticle metal exchange between phosphine ligands from different cores was not blocked by the crosslinked core environment.



Another interesting phenomenon is the immediate coagulation of the Rh-loaded polymer latex after heating. It was inferred that the $[\text{Rh}(\text{acac})(\text{CO})(\text{TPP}@polymer)]$ complex underwent thermal decarbonylation to form $[\text{Rh}(\text{acac})(\text{TPP}@CCM)_2]$ alike to the related molecular species.^[146] Therefore, the vacant coordination site left by the dissociated CO ligand may be saturated, during core-core interpenetration, by a free phosphine ligand of another polymer particle, creating particle-particle crosslinks. Similarly, the Rh leaching to the organic phase observed after the hydroformylation reactions conducted with high P/Rh ratios was accompanied by the observation of big particle aggregates ($D_z = 950 \text{ nm}$) in the organic phase. This was attributed to the generation of lipophilic species $[\text{RhH}(\text{CO})_2(\text{TPP}@polymer)_2]$ for the activated catalyst, in which the Rh atom may act as the crosslinker for phosphine ligands from different particles.^[106] It is of interest to stop this core-core contact, which can lead to the particle-particle coupling through interpenetration after metal complexation, in order to solve the polymer macrogelation and agglomeration problems. For that purpose, the introduction of shell-shell Coulombic repulsion through the presence of permanent charges on the shell is anticipated to be helpful.

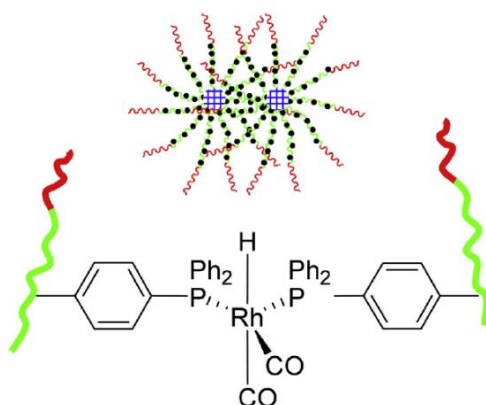


Figure III.1.2 Particle-particle coupling resulting from interpenetration and Rh-TPP coordination.^[72]

Indeed, when the TPP@CCM and [Rh(acac)(CO)(TPP@polymer)] latexes with the neutral P(MAA-*co*-PEOMA) outer shells were mixed at high pH, after addition of NaOH, the metal migration process was stopped. This was the consequence of the complete shell deprotonation, and was evidenced by the observation of both coordinated and free phosphine NMR resonances. The intensities of these peaks decreased quite slowly and remained detectable even after 11 h at room temperature.^[100] This result implies that the negatively charged shells impeded the core-core contact and the interparticle metal exchange. This finding affords an inspiration about a novel polymer nanoreactor with a positively charged shell as described in Chapter II.

In the present chapter, the prepared polymers, namely the CCM-C R₀-(4VPMe⁺I⁻)₁₄₀-*b*-St₅₀-*b*-(St_{1-n}-*co*-DPPS_n)₃₀₀-*b*-(St_{0.9}-*co*-DEGDMA_{0.1})₁₅₀-SC(S)SPr (n = 0.05 or 0.1) and the NG-C R₀-(4VPMe⁺I⁻)₁₄₀-*b*-St₅₀-*b*-(St₄₂₃-*co*-DPPS₃₀-*co*-DEGDMA₁₅)-SC(S)SPr, are investigated as macroligands for the coordination of [RhCl(COD)]₂, with particular focus on the interparticle metal migration using the same protocol optimized in the previous contributions.^[109, 143] Subsequently, they are employed as catalytic nanoreactors in the aqueous biphasic hydrogenation of styrene and 1-octene, demonstrating their superior performance in all respects (activity, speed of decantation, leaching) relative to the first-generation neutral P(MAA-*co*-PEOMA) shell nanoreactors.

III.2 [RhCl(COD)]₂ precatalyst coordination and migration studies

The premise of metal precatalyst loading and the substrates transportation into the cores is the penetration of organic molecules through the P4VPMe⁺I⁻ outer shell. This was verified by NMR spectroscopy. In the same manner as previously done for the P(MAA-*co*-PEOMA) shell polymer, the polymer core was not visible in the ¹H and ³¹P

spectra for the pristine latex, but became visible after swelling with a good solvent for polystyrene, such as CHCl_3 or toluene. This results from the “dissolution” of the polymer chains in the swelling solvent with increase of their mobility (decrease of the correlation time) and consequent sharpening of the NMR lines. Hence, the PSt-anchored TPP ligands can be observed by a characteristic resonance at -6.5 ppm in the ^{31}P NMR spectrum. This results also demonstrates the rapid transport of organic molecules (the swelling solvents) through the $\text{P4VPMe}^+\text{I}^-$ shell. Again by analogy with the neutral-shell polymers, spectroscopic evidence of metal complexation, leading to the core-anchored $[\text{RhCl}(\text{COD})(\text{TPP}@\text{CCM})]$ functions, was possible only when the polymer cores were quantitatively charged with the metal complex ($\text{P/Rh} = 1:1$). The free TPP resonance at -6.5 ppm in the ^{31}P NMR spectrum was fully replaced by a doublet at 32.2 ppm, assigned to the Rh-coordinated TPP (*e.g.* see the spectra for the CCM-C-0.1 particles in Figure III.2.1). Although relatively broad because of the increased correlation time in the polymeric environment, the Rh coupling is clearly discernible with $J_{\text{PRh}} \approx 150$ Hz, consistent with previous studies.^[72, 94, 100, 105b, 106, 143] These spectral parameters agree well with those reported for the molecular model (δ 31.5 ppm, $J_{\text{PRh}} = 152$ Hz)^[147] and for the same complex anchored to the equivalent neutral-shell polymer (δ 29.3 ppm, $J_{\text{PRh}} = 150$ Hz).^[143]

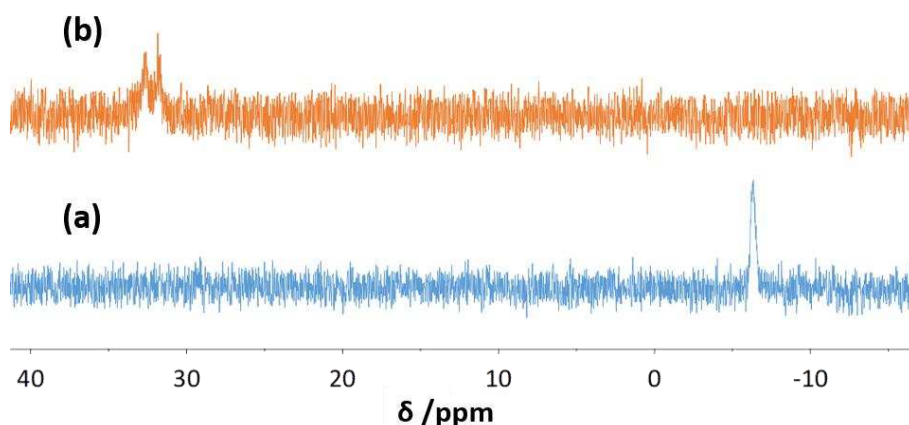


Figure III.2.1 ^{31}P NMR spectrum for the toluene-swollen CCM-C-0.1 latex, before (a) and after (b) equilibration with a $[\text{RhCl}(\text{COD})]_2$ toluene solution at a P/Rh ratio of 1:1.

The present polycationic shell polymers proved to be capable of stopping the metal migration, as demonstrated by the persistence of the simultaneously observable ^{31}P NMR resonances for the free and coordinated TPP ligands in the 1:1 mixture of pristine and 100% loaded TPP@CCM-C latexes (the P-richer CCM-C-0.2 sample was used for this experiment), even after stirring the mixture for over one week at room temperature (Figure III.2.2).

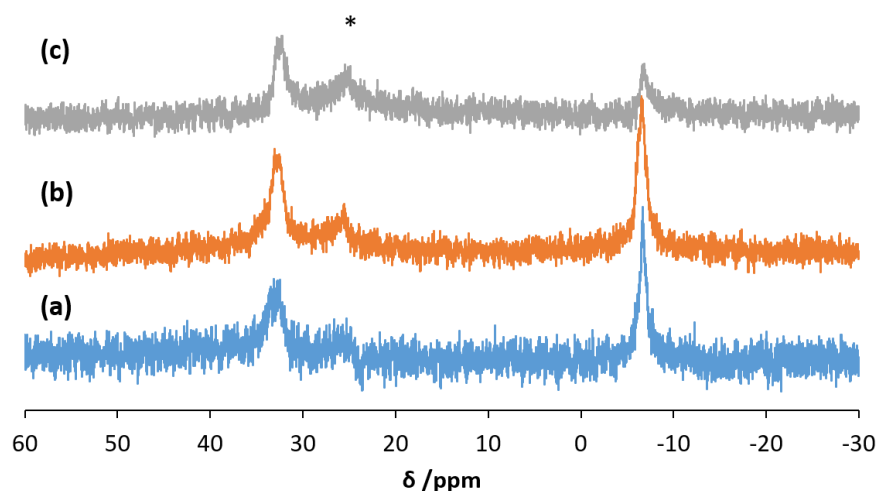


Figure III.2.2 ^{31}P NMR spectra recorded at different times after mixing equivalent amounts of CCM-C-0.2 latexes with 0 and 100% Rh loadings, and stirring at room temperature: (a) 1.5 h; (b) 7 h; (c) 1 week. The starred resonance corresponds to phosphine oxide.

In case of migration, the Rh complex would redistribute among all CCMs ($> 0\%$ in the initially empty polymers, $< 100\%$ in initially fully loaded polymers, tending to an equilibrium 50% loading in all polymers), in which case the signals would be unobservable due to the fast exchange process, as discussed above. Indeed, partially loaded latexes resulted in the absence of any ^{31}P resonance, proving that intraparticle phosphine exchange processes continue to take place. This result demonstrates the efficient confinement of the metal complex within the core of the nanoreactor in which it has initially been anchored.

It is interesting to compare the monitoring of Figure III.2.2 with that of the

corresponding experiment for the polymer with the neutral P(MAA-*co*-PEOMA) shell at high pH, namely after deprotonation of the methacrylic acid monomers and introduction of negative charges. In the latter case, even though the immediate exchange via core-core contact was stopped, a slow change (complete in *ca.* 10 h at room temperature) took place with formation of a single product, [Rh(OH)(CO)(TPP@CCM)₂], indicating a slower metal migration accompanied by a chemical transformation. This phenomenon was shown to involve Rh extraction from the polymer-bound [Rh(acac)(CO)(TPP@CCM)] complex by OH⁻ and migration through the continuous aqueous phase, presumably as anionic [Rh(acac)(OH)(CO)]⁻. In the present case, the insignificant change of the NMR spectrum over one week indicates the absence not only of core-core contact but also of any metal migration through the continuous phase. Namely, the Rh metal does not leach out of the nanoreactor core.

III.3 Biphasic catalytic hydrogenations

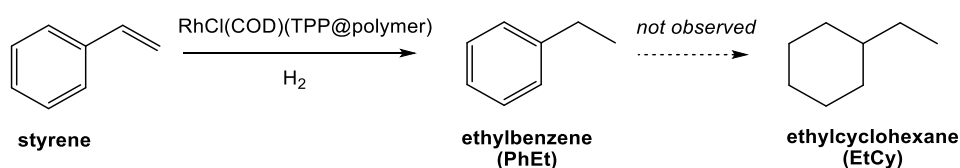
All nanoreactors were used to catalyze the hydrogenation of styrene and 1-octene as representative aromatic and aliphatic unsaturated substrates. Two different protocols were used for styrene, with the substrate introduced either neat or diluted into 1-nonanol. For 1-octene, the neat substrate could not be used because it is not a good solvent for the polystyrene core and is therefore not able to swell it. The core swelling required substrate dilution into a good solvent for polystyrene. The choice of 1-nonanol was guided by the previous optimization study of the same biphasic catalytic reaction with the neutral-shell polymer.^[109] Using 1-nonanol (sparingly soluble in water, good solvent for polystyrene, and able to stabilize transient unsaturated forms of the catalytically active species by coordination) led to successful implementation of the reaction with no polymer coagulation and rapid phase decantation. On the other hand, substrate dilution with toluene (another good solvent for polystyrene) led to decantation

problems because of coagulation in application to styrene hydrogenation.^[109] This phenomenon was attributed to interparticle crosslinking following core-core contact because of the coordinative unsaturation of the active catalyst. It should be underlined that the P/Rh ratio used in that specific catalytic experiment was only 2:1, yielding a stoichiometry of “RhCl(TPP)₂” at the most for the active catalyst. The coordinative unsaturation can be stabilized only by the reagents, product, polymer and solvent. Although the product (an alkane), toluene and the polymer backbone do not have strongly stabilizing donor groups, 1-nonanol can apparently help to keep the system in a stabilized mononuclear form while at the same time maintaining high catalytic activity by its facile dissociation. Neat styrene, on the other hand, did not lead to any decantation problem because it is able, by itself, to provide sufficient stabilization by coordination. Although the polycationic shell of the new nanoreactors should stop the particle interpenetration, the use of 1-nonanol was initially maintained to compare the performance of the cationic and neutral-shell nanoreactors.

III.3.1 Hydrogenation of styrene in 1-nonanol

A first exploratory investigation was carried out to assess the effect of various parameters on the catalytic efficiency: P/Rh ratio (1:1, 2:1 and 4:1, for the CCM-C-0.1 nanoreactor), P content in the CCM (5% vs. 10%) and nanoreactor architecture (CCM vs. NG). In all cases, decantation was very rapid, as previously observed for the equivalent hydrogenation with the neutral-shell nanoreactors. For each experiment, the only detected product was ethylbenzene, showing selective hydrogenation of the vinyl function as expected for a molecular Rh catalyst, shown in Scheme III.3.1. The generation of Rh nanoparticles, which is known to occur from Rh^I precursor in the absence of stabilizing π -acidic ligands, would also lead to significant ring hydrogenation, as shown in previous reports of the reduction of arenes^[148] including

styrene.^[149]



Scheme III.3.1 Products resulting from the hydrogenation of styrene catalyzed by molecular Rh^I.

Catalytic activity and selectivity

Using a 10% (v/v) styrene solution in 1-nonanol, a styrene/Rh ratio of 200, and an H₂ pressure of 20 bar at 25 °C, quantitative substrate conversion was achieved after *ca.* 5 h of stirring in all cases. A representative conversion versus time plot for the CCM-C-0.1 system with a P/Rh ratio of 4:1 is shown in Figure III.3.1 and the full data for all systems are collected in Table III.3.1. Considering the need for single-point kinetic monitoring and the associated experimental errors, leading to a relatively large scatter of the data (Figure A.0.12), no clear trends can be derived from a comparison of the data obtained under different experimental conditions. Thus, all subsequent experiments made use of the CCM-C-0.1 scaffold with a P/Rh ratio of 4:1. With this ratio, each Rh atom should be surrounded by a sufficient number of efficient phosphine ligands to be stabilized. From the initial slope in Figure III.3.1, the TOF can be estimated as 70 h⁻¹.

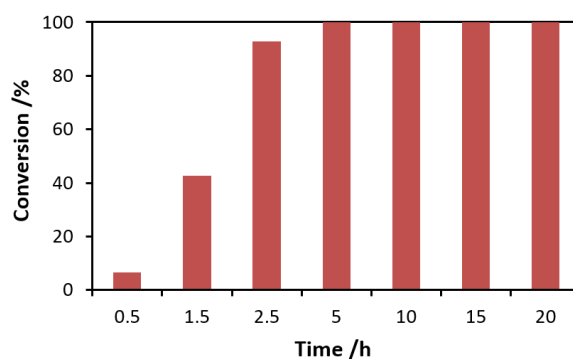


Figure III.3.1 Time dependence of the styrene conversion for the biphasic catalyzed by the CCM-C-0.1 latex with a P/Rh ratio of 4:1 in 1-nonanol. Each point was generated by an independent experiment.

The performance of the CCM-C-0.1 biphasic system was also compared with the homogeneous system in 1-nonanol with free triphenylphosphine as supporting ligand and operated under identical conditions (styrene/1-nonanol = 1/9, v/v; styrene/Rh = 200; T = 25 °C; p(H₂) = 20 bar; stirring rate = 1200 rpm). The two systems differ only by the biphasic vs. monophasic nature, introducing the potential effect of mass transport on the reaction kinetics, and by the effective catalyst concentration. Indeed, for the biphasic nanoreactor implementation, all the Rh active centers are concentrated within the nanoreactor cores, the total volume of which is much smaller than the total volume of the organic phase. From the polymer content in the latex, the nanoreactor swelling capacity and the amounts used in the catalytic experiments, the effective catalyst concentration in the nanoreactors can be estimated. For styrene homogeneous catalysis in 1-nonanol, the Rh concentration was 6.22 μmol ml⁻¹; For CCM-C-0.1 catalysis, from molecular weight (93278 g mol⁻¹), polymer mass content (20.6%), polystyrene density (1.05 g cm⁻³), latex density (1.12 g cm⁻³), the volumetric content of core polymers in CCM latex was calculated as 35.1%. The D_z of CCM latex before (130.2 nm) and after core-swelling (152.7 nm) showed the volumetric increase percentage of CCM particle equals to 61.3%. So, the total volume of organic solution in all cores in 1 ml latex was 0.351 × 0.613 = 0.215 cm³. Derived from this value, the Rh concentration in a particle core was 12.79 μmol ml⁻¹. It was calculated that the effective catalyst concentration in the nanoreactors was 2.3 times greater than that of the homogeneous system. The transformation should therefore be faster for the biphasic nanoreactor implementation, because of the rate dependence on the catalyst concentration, in the absence of mass transport limitations. However, the chemical environment around the catalytic center is not the same for the two systems: substrate/1-nonanol for the homogeneous system and substrate/polystyrene/1-nonanol for the biphasic one.

Table III.3.1 Hydrogenation of styrene in 1-nonanol with different nanoreactors and different P/Rh ratios.^a

Polymer	P/Rh	Time /h	% styrene ^b	% PhEt ^b	% EtCy ^b	[Rh] /ppm ^c
CCM-C-0.1	1:1	0.5	77.5	22.5	0	nd
		1.5	40.4	59.6	0	0.24
		2.5	36.8	63.2	0	1.22
		5	0	100	0	0.11
		10	0	99.9	0.1	0.41
		15	0	99.9	0.1	0.36
		20	0	100	0	nd
	2:1	0.5	73.1	26.9	0	0.16
		1.5	51.1	48.9	0	nd
		2.5	13.5	86.5	0	nd
		5	0	100	0	0.07
		10	0	99.9	0.1	0.11
		15	0	99.9	0.1	0.34
		20	0	100	0	nd
	4:1	0.5	93.4	6.6	0	0.04
		1.5	57.4	42.6	0	0.09
		2.5	7.2	92.8	0	0.04
		5	0	100	0	0.59
		10	0	100	0	0.34
		15	0	100	0	0.05
		20	0	100	0	nd
CCM-C-0.05	4:1	0.5	84.4	15.6	0	0.25
		1.5	49.6	50.4	0	0.06
		2.5	7.3	92.7	0	0.10
		5	0	100	0	0.07
		20	0	100	0	nd
NG-C	4:1	0.5	95.0	5.0	0	0.09
		1.5	75.0	25.0	0	0.58
		2.5	26.5	73.5	0	0.07
		5	0	100	0	0.15
		10	0	100	0	0.39
		15	0	100	0	0.05
		20	0	100	0	nd

^a Reaction conditions: styrene/1-nonanol = 1/9 (v/v); styrene/Rh = 200; T = 25 °C; p(H₂) = 20 bar; stirring rate = 1200 rpm.

^b From the GC analysis of the recovered organic phase.

^c From the ICP-MS analysis of the recovered organic phase; the average standard deviation on the measurements is 10%; nd = not determined.

A comparison of the results obtained for the three different P/Rh ratios (1:1, 2:1 and 4:1) shows an approximately equal reactivity, with complete conversions within *ca.* 2.5 hours (see Figure III.3.2). Once again, each data point comes from a different experiment and thus errors may be large, preventing a more quantitative kinetics comparison. However, the fact that the biphasic system is not significantly faster than the homogeneous one suggests mass transport limitations.

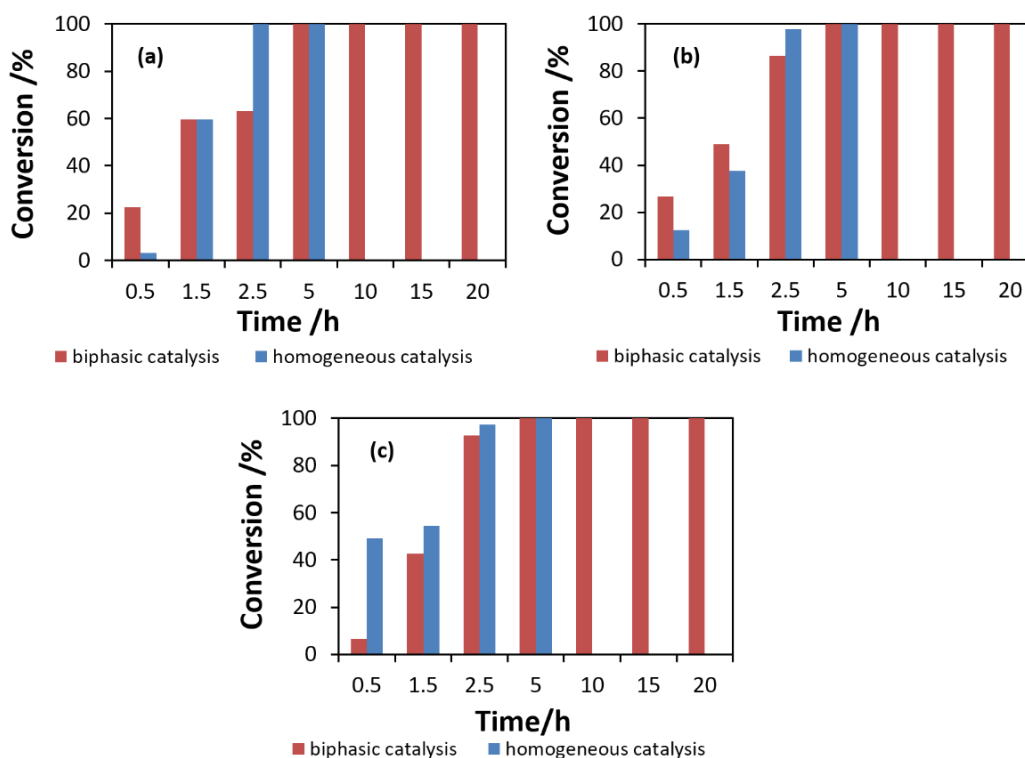


Figure III.3.2 Comparison of the conversion vs. time between the [RhCl(COD)(TPP@CCM-C-0.1)] catalyst under biphasic conditions and the homogeneous [RhCl(COD)@PPh₃] catalyst. The P/Rh ratios were (a) 1:1; (b) 2:1; (c) 4:1.

An interesting comparison can also be made with the performance of the equivalent neutral-shell nanoreactor, [RhCl(COD)(TPP@CCM-N-0.1)]. The hydrogenation of styrene in 1-nonanol (styrene/Rh = 400; room temperature; p(H₂) = 20 bar; stirring rate = 1200 rpm) revealed high activity (95.2% conversion after 18 h) and good recyclability (100% for the 2nd run).^[109] However, the selectivity was relatively low. The yields of ethylbenzene were 85.3% and 83.6% respectively.

Leaching

Another important parameter, which indeed motivated the development of this second-generation cationic-shell nanoreactor series, is catalyst leaching. Relative to the neutral-shell first-generation nanoreactors, in which the PEOMA blocks becomes less hydrophilic at higher temperature, it was hoped that the polycationic P4VPM^{e+}I⁻ shell would reduce the polymer transfer to the organic phase. Indeed, the ICP-MS measurement of the recovered organic phases showed Rh concentrations in most cases much lower than 1 ppm, with an average of 0.24 ppm (see Table III.3.1). There is no significant difference between the average leaching for the CCM-C (0.25 ppm) and NG-C (0.22 ppm) catalysts, whereas the measured leaching for the corresponding neutral-shell particle was much greater and architecture-dependent (1.7-2.7 ppm for the CCM-N^[94, 105a] and 0.4-1.2 ppm for the NG-N^[72] nanoreactors).

Recycling efficiency

The performance of the CCM-C-0.1 nanoreactor with a P/Rh ratio of 4:1 was further assessed in terms of catalyst recycling; the data are collected in Table III.3.2. To properly evaluate the catalyst stability and durability, the reaction time in different cycles was initially set at 2.5 h under conditions identical to those of Figure III.3.1 and Table III.3.1, where a fully quantitative conversion was not yet achieved. The results, shown in Figure III.3.3, suggest high stability, since an essentially quantitative conversion was achieved in all runs after the first recycle after an initial slight drop in the first recycle.

Table III.3.2 Recycling experiments for the hydrogenation of styrene in 1-nonanol with CCM-C-0.1 and P/Rh = 4:1.^a

Run	Time /h	Recycle	% styrene ^b	% PhEt ^b	% EtCy ^b	[Rh] /ppm ^c
1	2.5	0	7.2	92.8	0	0.17
2		1	17.6	82.4	0	0.05
3		2	2.4	97.6	0	0.66
4		3	1.7	98.3	0	0.04
5		4	2.3	97.7	0	0.07
6		5	5.5	94.5	0	0.05
7		6	4.7	95.3	0	nd
8		7	1.1	98.9	0	nd
9		8	0.2	99.8	0	nd
10		9	0.2	99.8	0	nd
11	1.5	0	63.0	37.0	0	0.11
12		1	47.3	52.7	0	0.13
13		2	15.8	84.2	0	0.15
14		3	1.7	98.3	0	0.61
15		4	0	100	0	0.12
16		5	1.4	98.6	0	0.11
17		6	0.2	99.8	0	0.08
18		7	2.3	97.7	0	0.26
19		8	5.0	95.0	0	0.16
20		9	8.0	92.0	0	0.31
21	1.5	0	64.3	35.7	0	0.21
22		1	68.4	31.6	0	0.14
23		2	2.5	97.5	0	0.05
24		3	2.0	98.0	0	0.06
25		4	0.5	99.5	0	0.11
26		5	0.7	99.3	0	0.08
27		6	1.0	99.0	0	0.13
28		7	2.6	97.4	0	0.16
29		8	6.8	93.2	0	0.11
30		9	8.1	91.9	0	0.09

^a Reaction conditions: styrene/1-nonanol = 1/9 (v/v); styrene/Rh = 200; T = 25 °C; p(H₂) = 20 bar; stirring rate = 1200 rpm.

^b From the GC analysis of the recovered organic phase.

^c From the ICP-MS analysis of the recovered organic phase; the average standard deviation on the measurement is 7%; nd = not determined.

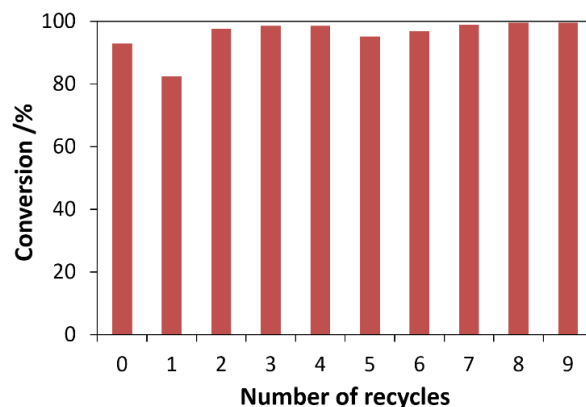


Figure III.3.3 Styrene conversion vs. recycle number for the biphasic catalyzed styrene hydrogenation by the CCM-C-0.1 latex with a P/Rh ratio of 4:1 in 1-nonanol (data in Table III.3.2, runs 1-10).

In order to more easily detect a possible catalyst degradation, a second series of recycles was carried out under the same conditions, except for setting the reaction time at 1.5 h. The corresponding results are shown in Figure III.3.4. This series of experiments clearly revealed the presence of an initial catalyst activation phase, but an essentially quantitative conversion was again achieved after the second recycle and up to the seventh recycle. Subsequently, the last two (8th and 9th) recycles gave evidence for a slight decrease of the final conversion.

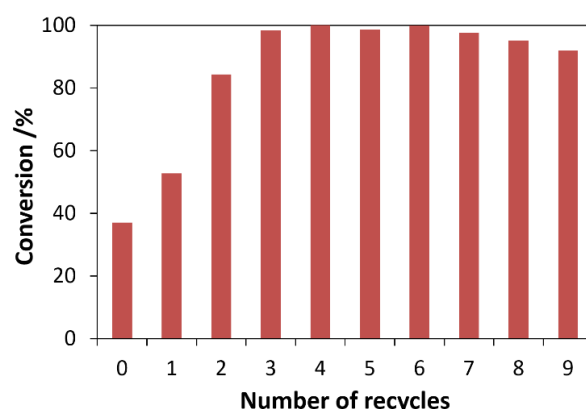


Figure III.3.4 Styrene conversion vs. recycle number for the biphasic catalyzed styrene hydrogenation by the CCM-C-0.1 latex with a P/Rh ratio of 4:1 in 1-nonanol (data in Table III.3.2, runs 11-20).

To verify the reproducibility of these observations, a third recycle run was carried out with a fresh catalytic charge, under the same conditions. The results (Figure III.3.5) indeed faithfully reproduced those of Figure III.3.4, including the slight decrease of final conversion after the seventh recycle. This slight decrease may result either from mechanical losses or from catalyst degradation by adventitious oxygen diffusion during the separation of the decanted phases between subsequent cycles. From the quantitative conversions of the recycles (3-7 in Figure III.3.4 and Figure III.3.5), the lower limit of the catalyst TOF in this hydrogenation process is estimated as 133 h^{-1} . The essentially identical DLS and TEM parameters measured for the latex before catalysis and after 1 and 10 catalytic runs are shown in Figure III.3.6. The particle size remained in the same range around 230 nm with very low PDI, accompanied by the well-defined spherical shape in the course of recycling tests. This indicates that the catalytic nanoreactors are quite stable. DLS and TEM measurements before and after catalysis were also carried out for the NG-C latex, indicating again no alteration (Figure III.3.7). In addition, the ICP-MS measurement of the Rh concentration in the recovered organic product phases gave even lower values than those indicated above (average of 0.16 ppm from Table III.3.1) and without any clear drift for greater recycle numbers.

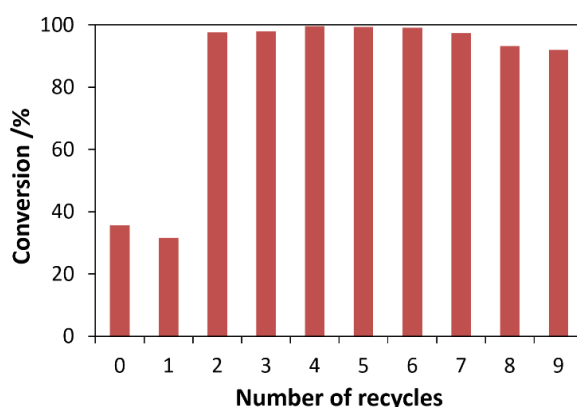


Figure III.3.5 Styrene conversion vs. recycle number for the biphasic catalyzed styrene hydrogenation by the CCM-C-0.1 latex with a P/Rh ratio of 4:1 in 1-nonanol (data in Table III.3.2, runs 21-30).

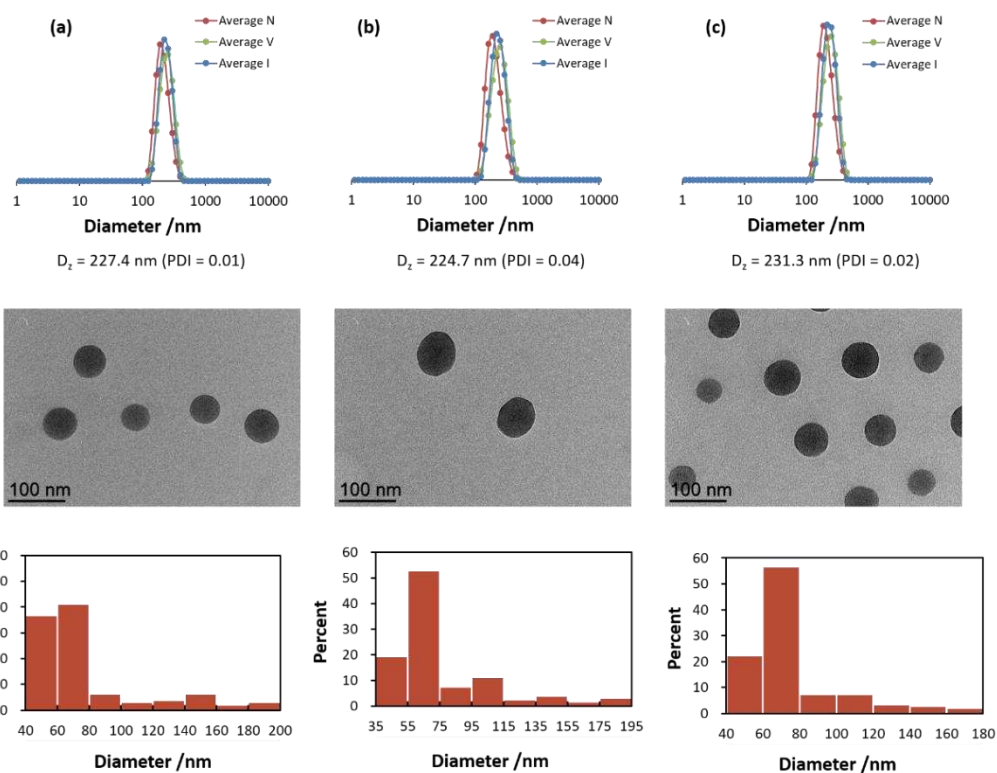


Figure III.3.6 DLS with D_z and PDI values (above), representative TEM images (middle) and frequency analysis of the diameters from the TEM images (> 100 measured particles) of: (a) CCM-C-0.1 latex after charging with $[\text{RhCl}(\text{COD})]_2$ (P/Rh = 4:1); (b) same latex, after one catalytic run at for 20 h (Table III.3.1); (c) same latex, after 9 recycles (runs 1-10 in Table III.3.2). All reported DLS data were obtained on unfiltered samples.

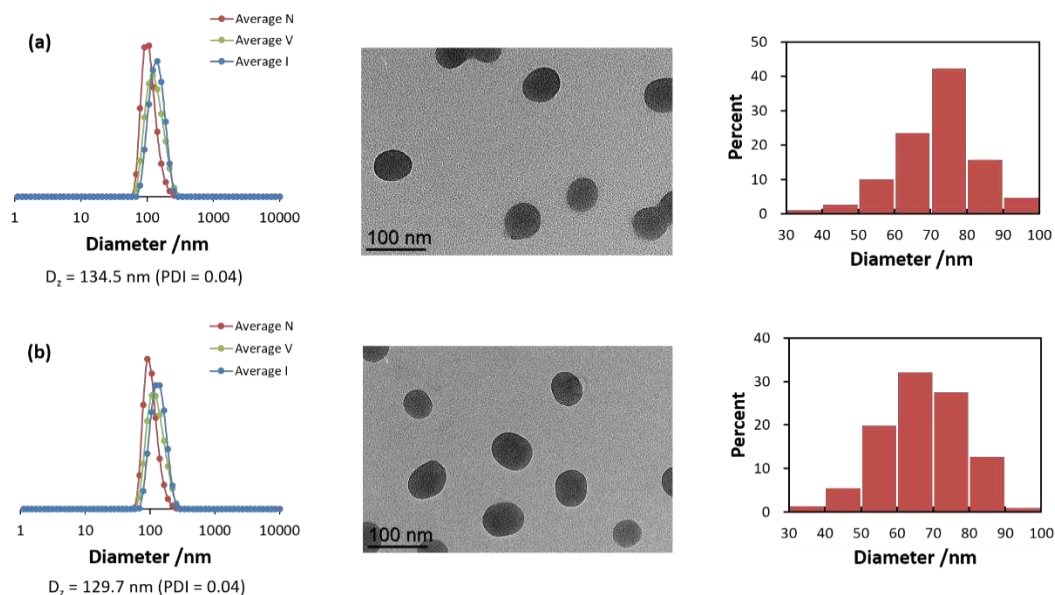


Figure III.3.7 DLS (left), representative TEM (middle) and frequency analysis of the diameters from the TEM images (> 100 measured particles, right) of: (a) NG-C latex after charging with $[\text{RhCl}(\text{COD})]_2$ (P/Rh = 4:1) and (b) same latex, after the catalytic run for 20 h (Table III.3.1).

III.3.2 Hydrogenation of neat styrene

Since styrene is compatible with the polystyrene core and is thus able to swell the nanoreactors by itself, the hydrogenation was also tested for the neat substrate (styrene/Rh = 5000; T = 25 °C; p(H₂) = 20 bar; stirring rate = 1200 rpm). This reaction was only carried out using the CCM-C-0.1 nanoreactors, charged with the precatalysts at a P/Rh ratio of 4:1. The conversion versus time study, see Figure III.3.8 (data in Table III.3.3), confirmed the presence of an initial activation phase, since only a 12.1% conversion was achieved after 5 h (average TOF = 120 h⁻¹). However, the conversion was quantitative after 20 h and the slope of the conversion versus time between 5 and 20 h yields an average TOF of *ca.* 300 h⁻¹. Nine subsequent recycles, with a reaction time of 5 h, demonstrated excellent stability. No strong evidence for an induction phase was shown in this case, probably because the catalyst is already fully activated at the end of the first cycle. For these catalytic runs, the average concentration of Rh leached into the product phase was 0.13 ppm, once again without a clear drift for high recycle numbers. The corresponding neutral-shell CCM gave a similar TOF for the hydrogenation of neat styrene (*ca.* 220 h⁻¹) in the first and second run, but leaching was higher (0.3-0.6 ppm) and a loss of activity was observed for the second recycle.^[109]

Table III.3.3 Hydrogenation of neat styrene with CCM-C-0.1 and P/Rh = 4:1.^a

Time /h	Recycle	% styrene ^b	% PhEt ^b	% EtCy ^b	[Rh] /ppm ^c
0.5		98.8	1.2	0	0.06
1.5		97.2	2.8	0	0.09
2.5		94.2	5.8	0	0.08
5		87.9	12.1	0	0.29
10		55.6	44.4	0	0.31
15		38.9	61.1	0	0.19
20		0	100	0	0.06
	0	87.9	12.1	0	0.22
	1	85.4	14.6	0	0.12
	2	90.9	9.1	0	0.14
	3	88.0	12.0	0	0.04
	4	87.4	12.6	0	0.09
5	5	87.8	12.2	0	0.07
	6	93.2	6.5	0.3	0.10
	7	92.4	7.6	0	0.05
	8	88.0	12.0	0	0.09
	9	93.7	6.3	0	0.14

^a Reaction conditions: styrene/Rh = 5000; T = 25 °C; p(H₂) = 20 bar; stirring rate = 1200 rpm.

^b From the GC analysis of the recovered organic phase.

^c From the ICP-MS analysis of the recovered organic phase; the average standard deviation on the measurements is 5%.

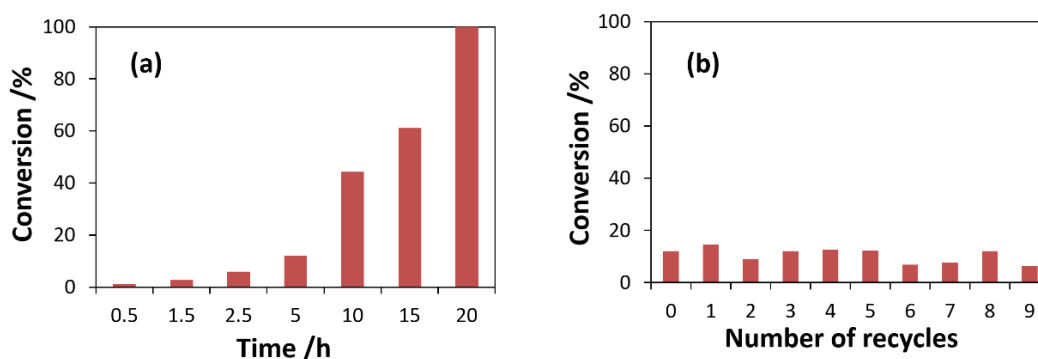
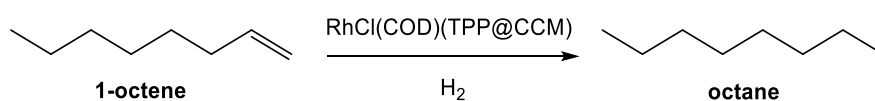


Figure III.3.8 (a) Time dependence of the styrene conversion for the biphasic catalyzed hydrogenation of neat styrene by the CCM-C-0.1 latex with a P/Rh ratio of 4:1. Each point was generated by an independent experiment. (b) recycling under the same conditions as in (a), for t = 5 h.

III.3.3 Hydrogenation of 1-octene

Since 1-octene is not a good solvent for polystyrene, its mass transport to the polymer core is limited unless vectorized by a good solvent such as toluene or 1-nonanol. Indeed, a previously described NMR investigation^[94] did not evidence any core 1-octene incorporation when added as a neat phase to a CCM-N latex, whereas this was confirmed after core swelling by toluene. All subsequent investigations of the biphasic 1-octene hydrogenation with the molecular $[\text{RhCl}(\text{COD})(\text{TPP}@ \text{CCM})]$ precatalyst were carried out with 1-nonanol as vectorizing solvent, both for CCM-N^[150] and for CCM-C (Scheme III.3.2)^[151].

This reaction was again carried out only with the CCM-C-0.1 polymer latex and a 4:1 P/Rh ratio, using identical conditions as for the styrene/1-nonanol studies shown above (substrate concentration of 10% in volume, 25 °C at 20 bar of H₂ pressure under 1200 rpm stirring speed). The resulting activity was quite similar to that observed for the styrene hydrogenation, leading to a nearly quantitative conversion (97.2%) after 5 h and a quantitative one after 20 h (see Table III.3.4 and Figure III.3.9), with octane as the only observed product and an average leaching of 0.13 ppm.



Scheme III.3.2 Products resulting from the hydrogenation of 1-octene catalyzed by molecular Rh^I.

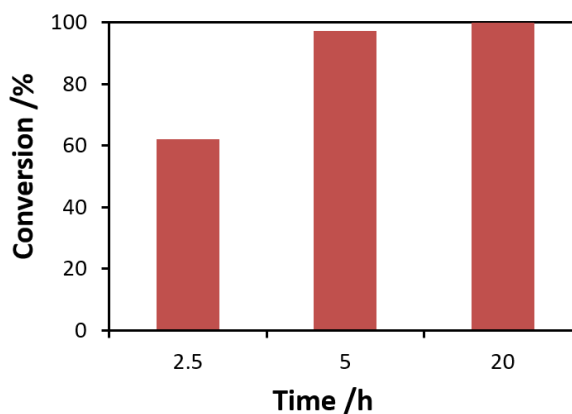
Table III.3.4 Hydrogenation of 1-octene with CCM-C-0.1 and P/Rh = 4:1.^a

Solvent	Time /h	% 1-octene ^b	% octane ^b	[Rh] /ppm ^c
1-nonanol	2.5	37.9	62.1	0.14
	5	2.8	97.2	0.08
	20	0	100	0.17
toluene	20	0	100	0.08

^a Reaction conditions: 1-octene/solvent = 1/9 (v/v); 1-octene/Rh = 200; T = 25 °C; p(H₂) = 20 bar; stirring rate = 1200 rpm.

^b From the GC analysis of the recovered organic phase.

^c From the ICP-MS analysis of the recovered organic phase; the average standard deviation on the measurements is 10%.

**Figure III.3.9 Conversion vs. time for the biphasic hydrogenation of 1-octene in 1-nonanol catalyzed by [RhCl(COD)(TPP@CCM-C-0.1)].**

As stated above, the neutral P(MAA-co-PEOMA) shell CCM led to coagulation when the hydrogenations were carried out with toluene as the carrier organic solvent, due to irreversible particle coupling. In the present case, however, the charged nature of the outer shell blocks the particle interpenetration, as shown above (metal migration study). Indeed, when the hydrogenation of 1-octene catalyzed by the [RhCl(COD)(TPP@CCM-C-0.1)] latex was repeated with the use of toluene as organic solvent, the decantation process was equally fast as for the corresponding reaction with 1-nonanol (see Figure III.3.10). The substrate conversion was again quantitative (Table III.3.4) and leaching was again very low (0.08 ppm).

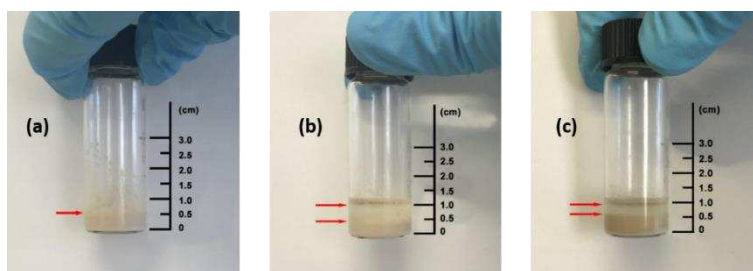


Figure III.3.10 Reaction vial for the biphasic hydrogenation of 1-octene in toluene catalyzed by $[\text{RhCl}(\text{COD})(\text{TPP}@ \text{CCM-C-0.1})]$: (a) starting latex; (b) after addition of the 1-octene/toluene phase; (c) after the reaction (< 2 min after the stirring was stopped).

III.4 Conclusion

The polymer particles with a $\text{P4VPMe}^+\text{I}^-$ polycationic shell were loaded with the $[\text{RhCl}(\text{COD})]_2$ precatalyst to yield $[\text{RhCl}(\text{COD})(\text{TPP}@ \text{CCM-C})]$ or $[\text{RhCl}(\text{COD})(\text{TPP}@ \text{NG-C})]$, respectively. They were used as unimolecular nanoreactors in Rh-catalyzed aqueous biphasic hydrogenation of the model substrates styrene and 1-octene, either neat (for styrene) or in an organic solvent (1-nonanol or toluene). All hydrogenations were rapid (TOF up to 300 h^{-1}) at $25 \text{ }^\circ\text{C}$ and 20 bar of H_2 pressure, the biphasic mixture rapidly decanted at the end of the reaction (< 2 min), the Rh loss was negligible (< 0.1 ppm in the recovered organic phase), and the catalyst phase could be recycled 10 times without significant loss of catalytic activity.

The performance of these cationic-shell nanoreactors is superior to that of the equivalent polymers with a neutral-shell in terms of activity, catalyst stability, recyclability, and catalyst leaching, which can be ascribed to the greater ability of the polycationic shell to confine the nanoreactors in the aqueous phase, while not restricting the mass transport of reactants and products between the continuous organic phase and the nanoreactor core. These nanoreactors (or related ones obtained by the incorporation of other ligand-functionalized monomers) should be suitable to anchor a wide variety of catalytic metals and thus be applied to numerous other catalyzed transformations under aqueous biphasic conditions.

Chapter IV

Rhodium nanoparticles generation and catalyzed biphasic hydrogenations

IV.1 Introduction

In all work published so far by our team, all these polymers were charged with either $[\text{Rh}(\text{acac})(\text{CO})_2]$ or $[\text{RhCl}(\text{COD})]_2$, which coordinated to the core-anchored triphenylphosphine ligands by either CO replacement or Cl-bridge splitting to yield $[\text{Rh}(\text{acac})(\text{CO})(\text{TPP}@CCM)]$ or $[\text{RhCl}(\text{COD})(\text{TPP}@CCM)]$, respectively. The resulting metal-loaded polymers were subsequently used in Rh-catalyzed aqueous biphasic olefin hydroformylation or hydrogenation, showing excellent performance and recyclability with sub-ppm catalyst losses. In further exploratory investigations, the $[\text{RhCl}(\text{COD})(\text{TPP}@CCM)]$ precatalyst was also applied to the hydrogenation of acetophenone. However, contrarily to the observed behavior in styrene hydrogenation, the catalytic mixture unexpectedly turned black (Figure IV.1.1), suggesting that the molecular Rh precatalyst was reduced to the metallic state under these conditions, with the possible formation of metal NPs. It was reasoned that, in a phosphine-poor environment (P/Rh ratios of 1:1 or 2:1 was initially used), styrene might protect the Rh^{I} center from reduction by H_2 because of its π -acidity as a ligand, contrarily to acetophenone.

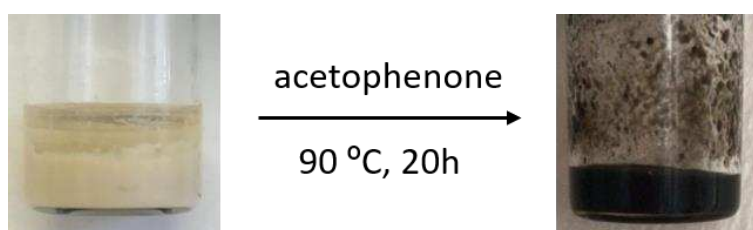


Figure IV.1.1 Reaction vial for the biphasic hydrogenation of acetophenone in toluene catalyzed by $[\text{RhCl}(\text{COD})(\text{TPP}@CCM\text{-C-0.1})]$: (a) starting latex and (b) after the reaction.

Although NPs have been known for a long time, their controlled generation has attracted keen interest only recently,^[152] because of growing awareness that their characteristics such as size and morphology strongly influence their physical and

chemical properties. Much effort is currently devoted to the synthesis of very precisely defined metal nanospecies, up to the atomic precision level.^[153] In addition to fundamental aspects, the specific properties that the metal NPs display relative to bulk metals and molecular complexes make them very attractive for applications in diverse domains, particularly in catalysis. Nanocatalysis is now a well-recognized discipline at the frontier between homogeneous and heterogeneous catalyses.^[154] Metal NPs are highly attractive because of their high surface/volume ratio, especially for diameters of one nanometer or below (subnanoparticles), thus providing a high number of potential active sites (> 90% of surface atoms). Therefore, developing synthetic tools that enable the production of ultra-small NPs is of prime importance. In terms of catalytic performance, in addition to the metal nature and particle size, other important parameters are the crystalline structure, the nature and relative amounts of the exposed faces, edges and corners and the composition and architecture (*e.g.* core-shell) for multimetallic NPs. However, the performance in catalysis may also be influenced or even oriented by the surrounding stabilizer or by the support.^[155]

The choice of the stabilizing agent is critical as it controls both the NP size and dispersion and provides long-term stability during the catalytic process.^[156] Contrarily to heterogeneous catalysis where calcination is usual to suppress organic contaminants and liberate the active sites, but like in molecular catalysis, metal-ligand interactions are of paramount importance^[156b, 156d] as they may improve the activity or even promote more interesting chemoselectivities.^[156c] The challenge is to find capping ligands that at the same time stabilize the metal NPs and allow access to the metal surface for the catalytic transformation.^[156a, 156c] Ligand-stabilized metal NPs may be involved in catalysis as colloidal suspensions in water, polyols or organic solvents and several strategies have been developed to facilitate the catalyst recovery.^[157]

Increased rates have indeed been obtained upon anchoring catalytic NPs on the hydrophilic shell of micelles.^[158] Thermoregulated processes, where the catalyst is anchored on thermosensitive macromolecules (hydrophilic at low temperature and

hydrophobic at high temperature) have also been implemented in metal NP catalysis. Matthias Ballauff *et al.* have described the synthesis of different core-shell polyelectrolytes as the catalyst carrier for Ag, Pd, Au, Pt nanoparticles. The thermosensitive microgel polymer contains a polystyrene core, a poly(N-isopropylacrylamide) (PNIPA) shell and is crosslinked by N,N'-methylenebisacrylamide (BIS). The Ag⁺ ions are localized within the nitrogen atoms of the PNIPA and reduced to nanoparticles by NaBH₄. This shell chains stretch at room temperature and shrink at 32 °C, resulting in the slowing down of the catalytic reaction.^[159] A second type is a nano-tree-type polymer brush, which consists of a polystyrene core and poly(ethylene glycol) methacrylate (PEGMA) shell. It also intended for the generation and immobilization of Ag nanoparticles.^[160] The hydroxyl groups on the shell have a high affinity for Ag⁺ and Ag nanoparticles. Furthermore, the high degree of branching blocks the nanoparticle loss and the aggregation. Nanoparticles have also been deposited on the PAA shell of a third type of brush polyelectrolyte with a polystyrene core.^[161] The small (< 10 nm) and homogeneously distributed nanoparticles located in these polyelectrolytes show different activity in the reduction reaction of 4-nitrophenol with negligible nanoparticles loss.

An alternative solution is to anchor the metallic nanoparticle catalysts to the hydrophobic core of micelles, just as the molecular catalysts described in Chapter III. There are no previous examples of this type of metal NP-polymer architecture, to the best of our knowledge.

I will report herein a systematic investigation of the [RhCl(COD)(TPP@CCM)] reduction and of the effect of various parameters on the size and morphology of the produced Rh NPs. Finally, the performance of the resulting catalytic nanoreactors in acetophenone, styrene and 1-octene hydrogenation will be described, also in terms of catalyst stability and recycling, providing useful new information about the Rh NPs stabilization and mobility in the amphiphilic polymer environment.

IV.2 Generation of rhodium nanoparticles in the CCM-N polymers

A first application of the $[\text{RhCl}(\text{COD})]_2$ -loaded $\text{R}_0\text{-(MAA}_{0.5}\text{-co-PEOMA}_{0.5})_{30}\text{-b-(St}_{1-n}\text{-co-DPPS}_n)_{300}\text{-b-(St}_{0.9}\text{-co-DEGDMA}_{0.1})_{100}\text{-SC(S)SPr}$ (CCM-N-n) latex to the aqueous biphasic catalyzed hydrogenation of acetophenone (90 °C, 20 bar of H_2) led to an unexpected color change of the initially pale cream latex to black, suggesting metal reduction, and to a low extent of substrate reduction (see catalytic results below). On the other hand, the results described in Chapter III have demonstrated very efficient aqueous biphasic styrene or 1-octene hydrogenation with no color change using the same protocol. Metallic rhodium, in the form of small NPs, has previously been obtained by reduction of several molecular Rh^{I} and Rh^{III} precursors,^[162] including $[\text{RhCl}(\text{COD})]_2$ ^[163]. A black latex was again obtained when neat toluene, without any added acetophenone, was used to swell the polymer core, showing that acetophenone is not essential for the metal reduction. When the $[\text{RhCl}(\text{COD})(\text{TPP}@ \text{CCM-N})]$ reduction was carried out at 25 °C (either with or without acetophenone), the latex only turned light grey, suggesting that the reduction may be incomplete under these conditions. However, a black latex was again obtained at 60 °C. Reasoning that the reduction of a $\text{Rh}^{\text{I}}\text{-Cl}$ complex by H_2 also generates an equivalent amount of HCl per Rh atom, the procedure was then repeated in the presence of excess NEt_3 (≥ 5 equiv.). Under these conditions, a black latex was obtained even at 25 °C. These initial studies were carried out with a fully metal-loaded ($\text{P/Rh} = 1:1$) CCM-N-0.1 latex, in which each polymer chain contains on average 30 TPP ligands in the hydrophobic PSt block and 15 PEOMA/15 MAA monomers in the hydrophilic P(MAA-co-PEOMA) block. Therefore, the PEO/Rh ratio is *ca.* 0.5. It should also be pointed out that the NEt_3 excess leads to the transformation of the neutral-shell into an anionic one, containing triethylammonium carboxylate functions, $\text{-COO}^-\text{NHEt}_3^+$. The amount of NEt_3 used is sufficient for the neutralization of all generated HCl and all the shell carboxylic

functions.

The TEM analyses of the recovered latexes, Figure IV.2.1(a, b, c), besides confirming the formation of metal NPs, highlighted a few interesting phenomena. While the grey latex obtained in the absence of base contains isolated small size (< 5 nm) NPs, see Figure IV.2.1a, the black latex obtained in the presence of base contains few individual small NPs together with a dominant fraction of NP agglomerates, Figure IV.2.1b. These agglomerates appear to accumulate mostly on the polymer particle surface (hydrophilic shell). A similar behavior is observed for the NPs formed in the absence of base at 60 °C, Figure IV.2.1c, with an even more evident location of the agglomerates on the CCM-N outer shell. Thus, the protonation state of the shell MAA monomer does not appear to greatly affect neither the aggregation phenomenon nor the preference of the aggregates for the polymer shells. This suggests that the aggregated NPs are mostly stabilized by the shell PEO chains. Indeed, although phosphine ligands have been used as stabilizers of Rh NPs, *e.g.* using $[\text{Rh}(\text{acac})(\text{COD})_2]$ and $[\text{Rh}(\eta^6\text{-C}_3\text{H}_5)_3]$ as precursors,^[148c, 149, 164] PEO has also been described as a stabilizer for the generation of Rh NPs.^[148a, 148d, 165]

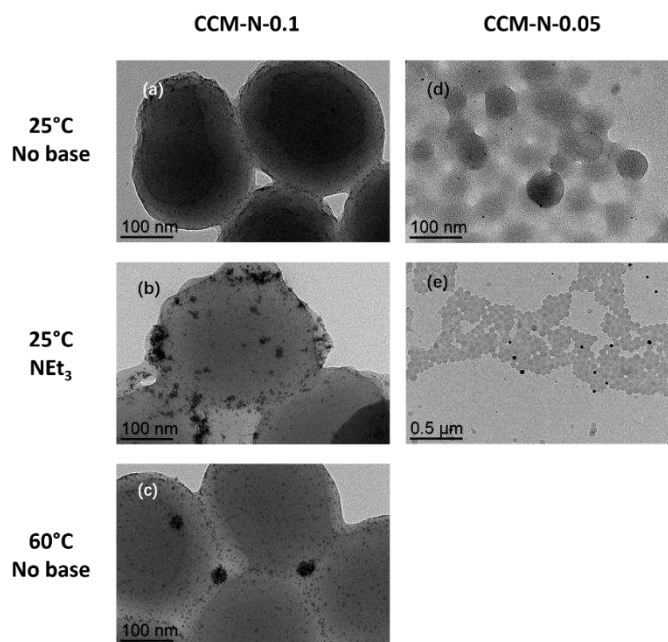


Figure IV.2.1 TEM images of CCM-N-n polymer latexes ($n = 0.1, 0.05$) after loading with $[\text{RhCl}(\text{COD})_2]$ ($\text{P/Rh} = 1:1$) and treatment with H_2 (20 bar) under different conditions for 20 h.

In separate experiments, the Rh NPs were also generated at 25 °C, both in the absence and presence of NEt_3 , using the fully loaded CCM-N-0.05, all other conditions being the same (H_2 pressure, NEt_3/Rh ratio, reaction time). The behavior was qualitatively identical: grey and black latexes in the absence and presence of base, respectively. The TEM images of these products are shown in Figure IV.2.1d and e, respectively. The former looks rather similar to the $\text{RhNP}@CCM\text{-N-0.1}$ latex obtained under the same conditions, with dispersed individual Rh NPs and no aggregates. The latter shows a few large NP aggregates located near a few polymer particles, while most other polymer particles are NP-free and there are no visible individual NPs. Figure IV.2.1e also shows a few Rh NP agglomerates located outside of the CCM-N particles, most probably resulting from mechanical detachment from the CCM-N outer shells during the preparation of the TEM grid. Since the CCM-N-0.05 particles contain on average only 15 TPP functions per chain, these are located farther from each other and the PEO/TPP ratio is twice that of the CCM-N-0.1 particles. The observed trends suggest that while the Rh NPs start to form as small individual particles in the CCM core, the core TPP and the shell PEO functions subsequently compete under the influence of the PEO/TPP ratio. For comparison, Rh have also been generated NPs by reduction of $[\text{RhCl}(\text{COD})]_2$ toluene solutions in the presence of either the PEOMA monomer or the macroRAFT chains $\text{R}_0\text{-(MAA}_{0.5}\text{-}co\text{-PEOMA}_{0.5})_{30}\text{-SC(S)SPr}$ (macroRAFT-N), at various PEO/Rh ratios. The TEM images reveal particle agglomerates very much like those of Figure IV.2.1c and e, see Figure IV.2.2. In particular, at equivalent PEO/Rh ratios, stabilization by the macroRAFT chains produces smaller agglomerates than the free PEOMA monomer, and the agglomerates are smaller when using a greater PEO/Rh ratio, as may be expected. The results of the experiments with the CCM in Figure IV.2.1 also indicate mobility for the Rh NPs, with migration from the core to the shell and from one polymer particle to another. In previous work, we demonstrated that the molecular Rh^{I} complex can rapidly migrate between different particle cores via reversible interpenetration with core-core contact,

in combination with phosphine exchange reactions. This principle can therefore be extended to the metallic NPs.

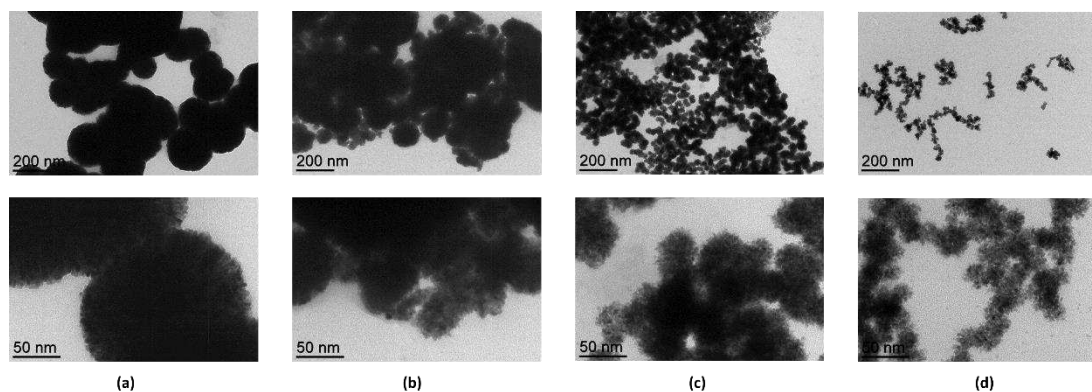


Figure IV.2.2 TEM images of the Rh NPs obtained from a toluene solution of $[\text{RhCl}(\text{COD})]_2$ in the presence of PEOMA ((a) and (b)) or macroRAFT-N ((c) and (d)), H_2 (20 bar) and NEt_3 (10 equiv. per Rh) at 60 °C: (a) and (c): PEO/Rh = 0.5:1. (b) and (d): PEO/Rh = 2:1.

When using an incompletely Rh-loaded CCM-N latex (P/Rh = 4:1), no Rh^{I} reduction occurred at 25 °C, even in the presence of excess NEt_3 . This suggests that the excess phosphine ligand exerts a protective action against reduction to the metallic state, like the styrene and 1-octene substrates in our previous catalyzed hydrogenation study,^[150] and confirms the principle that only a coordinatively unsaturated Rh^{I} center, such as that obtained from $[\text{RhCl}(\text{COD})(\text{TPP}@ \text{CCM})]$ after removal of the COD ligand by hydrogenation in the absence of additional TPP, may be readily reduced by H_2 . When the same procedure was carried out at 60 °C, however, Rh NPs were once again generated. In the absence of base, NPs formed only upon warming to 90 °C. In this case, the TEM characterization shows small NPs in all polymer particles, although they appear to be located mostly near the surface of the polymer particles rather than homogeneously dispersed in the core, see Figure IV.2.3. Therefore, the NPs obtained under these conditions have either reduced mobility or increased thermodynamic stability relative to the particles stabilized by the shell PEO chains.

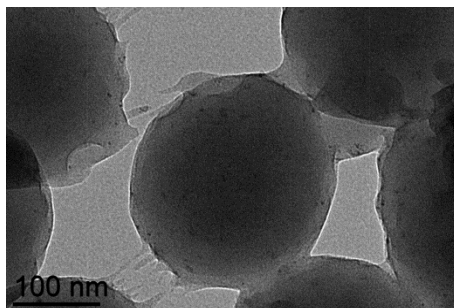


Figure IV.2.3 TEM image of the RhNP@CCM-N-0.1 obtained from a 25% loaded latex (P/Rh = 4:1) without NEt_3 at 90 °C for 20 h.

The same comparative experiments with P/Rh ratios of 1:1 and 4:1 were also carried out for the $[\text{RhCl}(\text{COD})]_2$ -loaded CCM-N-0.2 latex (for which PEO/TPP = 1:4), in the presence of NEt_3 , yielding similar results. Large agglomerates, even larger than those obtained with the CCM-N-0.1 and 0.05 latexes, were produced when using a 1:1 P/Rh ratio at 25 °C ($d_{\text{av}} = 57.3 \pm 18.1$ nm) (Figure IV.2.4a), whereas using a 4:1 ratio at 60 °C led to better dispersed and very small NPs (~ 1 nm), Figure IV.2.4b. These results indicate that the Rh NPs migration is strongly affected by the P/Rh ratio but not by the PEO/Rh ratio.

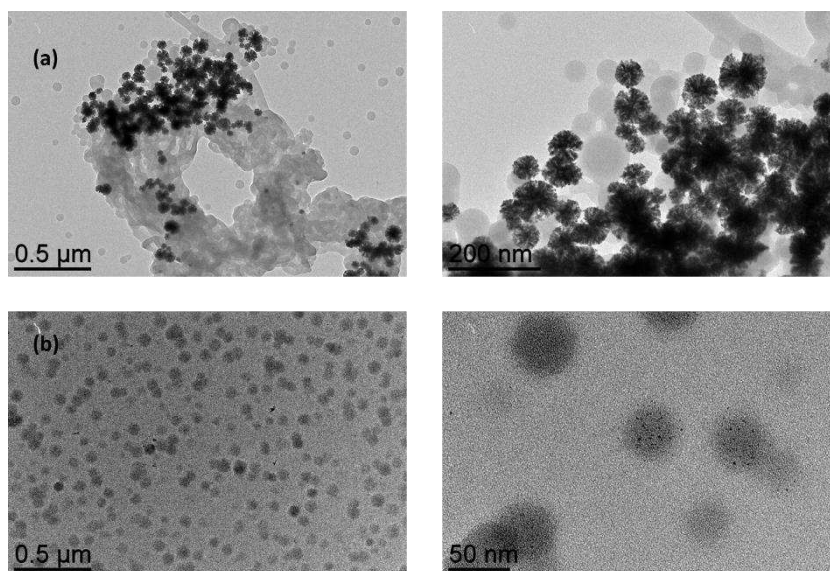


Figure IV.2.4 TEM images of the CCM-N-0.2 polymer latex after loading with $[\text{RhCl}(\text{COD})]_2$ and reduction with H_2 (20 bar) in the presence of NEt_3 (5 equiv. per Rh) for 20 h: (a) P/Rh = 1:1, 25 °C and (b) P/Rh = 4:1, 60 °C.

For comparison, Rh NPs were also generated by $[\text{RhCl}(\text{COD})]_2$ reduction from a homogeneous toluene solution in the presence of PPh_3 , using P/Rh ratio of 1:1 and 4:1, and in the presence of ≥ 5 equiv. of NEt_3 . The reduction rate followed the same trend as observed for the $\text{RhNP}@CCM\text{-N}$ synthesis: rapid at 25 °C for a P/Rh ratio of 1:1 and no reduction at all for a 4:1 ratio, but the latter mixture yielded NPs at 60 °C. The $\text{RhNP}@PPh_3$ obtained at 60 °C with P/Rh = 4:1 is significantly smaller, more narrowly dispersed, and less aggregated than those obtained at 25 °C with P/Rh = 1:1, see Figure IV.2.5. Their size is quite similar to $\text{RhNP}@PPh_3$ previously obtained from $[\text{Rh}(\eta^3\text{-C}_3\text{H}_5)_3]$.^[148c, 164b] Additional control experiments carried out in the absence of H_2 and in the presence of 10 equiv. of NEt_3 per Rh showed no color change over 20 h at 60 °C, whether the P/Rh ratio is 1:1 or 4:1, indicating that the amine does not act as a reducing agent for the Rh^{I} complex and that H_2 is essential to accomplish the Rh NPs formation. The conclusions to be drawn from these investigations are that using a low P/Rh ratio (or no phosphine at all) leads to agglomerated Rh NPs, whereas higher P/Rh ratios yield better dispersed ones. For the experiments with the Rh-loaded CCM polymers, the lower P/Rh ratio leads to extensive NP migration and accumulation as aggregates in the PEO-rich areas.

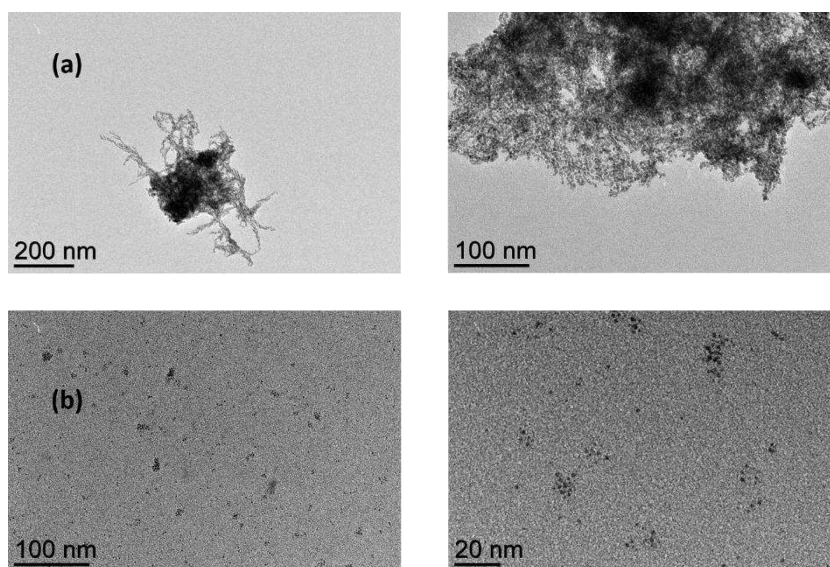


Figure IV.2.5 TEM images of the Rh NPs obtained from a toluene solution of $[\text{RhCl}(\text{COD})]_2$ in the presence of PPh_3 , H_2 (20 bar) and NEt_3 (5 equiv. per Rh): (a) P/Rh = 1:1, 25 °C and (b) P/Rh = 4:1, 60 °C.

IV.3 Generation of rhodium nanoparticles in the CCM-C polymers

The formation of Rh NPs has also been investigated using the cationic-shell CCM particles $R_0-(4VPMe^+I^-)_{140}-b-(St_{1-n}-co-DPPS_n)_{300}-b-(St_{0.9}-co-DEGDMA)_{150}-SC(S)SPr$ (CCM-C-n) as stabilizing matrix. The charged nature of the shell in CCM-C stops the interpenetration of the polymer particles and the interparticle migration of the molecular Rh^I complexes (see Chapter III).^[151] Hence, the Rh NPs migration process may also be stopped. In addition, the chemical nature of the CCM-C outer shell is not expected to strongly stabilize metal NPs, although a potential role of the iodide counterions cannot be discarded.

Under the same conditions (P/Rh ratios, temperature, H_2 pressure, base and reaction time) the Rh NPs generation in the CCM-C-0.1 latex followed the same reactivity trend as in the CCM-N latexes: reduction at 25 °C when P/Rh = 1:1 and only upon warming to 60 °C when P/Rh = 4:1. However, as anticipated, the Rh NPs remained confined in all cases within the polymer core, see Figure IV.3.1. The amount of used base (0, 1 or 5 equiv. per Rh for P/Rh = 1:1) did not affect the NP morphology or their dispersion within the polymer particles, see Figure IV.3.2. In order to evaluate the potential of the outer shell as a stabilizer for the generation of Rh NPs, the reduction of $[RhCl(COD)]_2$ was also carried out in the presence of the amphiphilic diblock macroRAFT agent $R_0-(4VPMe^+I^-)_{140}-b-St_{50}-SC(S)SPr$ (macroRAFT-C), using MeOH as a solvent and equivalent amounts (4VPMe⁺I⁻/Rh ratios) to those of the syntheses with the CCM-C polymer. The resulting Rh NPs are highly agglomerated with agglomerate sizes that are essentially independent on the macroRAFT-C/Rh ratio, in the 10-50 nm range (Figure IV.3.3).

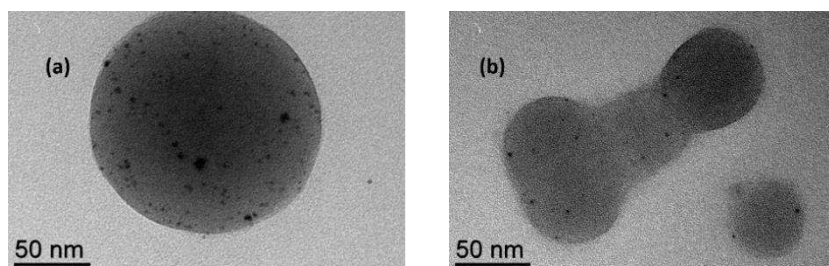


Figure IV.3.1 TEM images of the CCM-C-0.1 polymer latex after loading with $[\text{RhCl}(\text{COD})]_2$ and reduction with H_2 (20 bar) in the presence of NEt_3 (5 equiv. per Rh) for 20 h: (a) P/Rh = 1:1, 25 °C and (b) P/Rh = 4:1, 60 °C.

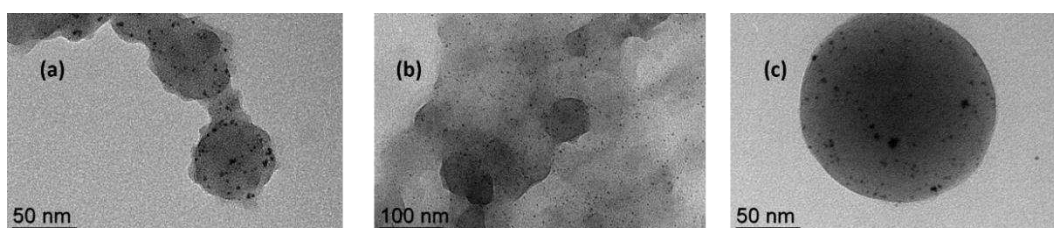


Figure IV.3.2 TEM images of RhNP@CCM-C-0.1 obtained with P/Rh = 1:1 and reduction with H_2 (20 bar) at 25 °C for 20 h with different NEt_3/Rh ratios: (a) 0; (b) 1; (c) 5.

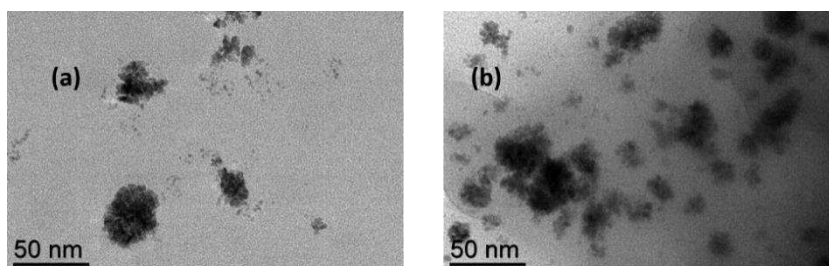


Figure IV.3.3 TEM images of RhNP@macroRAFT-C obtained by $[\text{RhCl}(\text{COD})]_2$ reduction with H_2 (20 bar) at 60 °C in methanol in the presence of NEt_3 (10 equiv. per Rh) for 20 h: (a) $4\text{VPMe}^+\text{I}^-/\text{Rh} = 4.7$ (equivalent to the experiment with CCM-C-0.1 at P/Rh = 1:1) and (b) $4\text{VPMe}^+\text{I}^-/\text{Rh} = 18.8$ (equivalent to the experiment with CCM-C-0.1 at P/Rh = 4:1).

IV.4 Catalyzed hydrogenation of acetophenone

The TEM characterization of the RhNP@CCM shows that the P/Rh ratio and the type of CCM shell (neutral and cationic) affect the NP location (core vs. shell), whereas

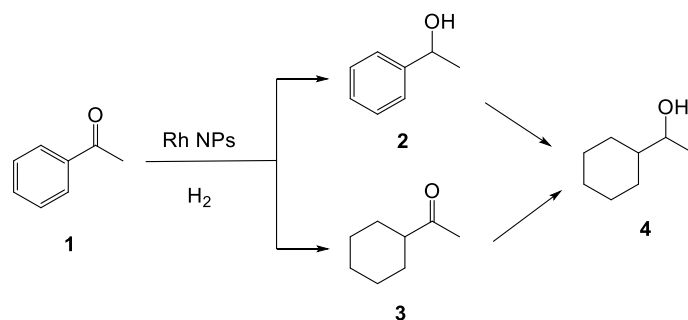
the presence or absence of NEt_3 does not appear to induce significant changes on the synthesized NP morphology and location. The NPs are stabilized by either core-anchored TPP for the CCM-N nanoreactors at high P/Rh ratios and for the CCM-C nanoreactors under any conditions, or by the shell PEO chains for the CCM-N nanoreactors at low P/Rh ratios. Therefore, in order to properly evaluate the catalytic performance of the RhNP@CCM systems, control experiments were run with related Rh NPs, namely RhNP@PPh₃, RhNP@PEOMA, RhNP@macroRAFT-N and RhNP@macroRAFT-C, generated in the presence of the corresponding stabilizers under homogeneous conditions. The catalytic experiments with the RhNP@CCM latexes were carried out under aqueous biphasic conditions using the “as synthesized” latex, diluted with water, as catalyst phase and toluene as the organic carrier phase. The control runs with RhNP@PPh₃, RhNP@PEOMA, RhNP@macroRAFT-N were carried out in toluene without any water phase, whereas methanol was used as a compatible solvent for the control runs with RhNP@macroRAFT-C. All results are collected in Table IV.4.1.

Table IV.4.1 Acetophenone hydrogenation catalyzed by Rh NPs.^{a,b}

Entry	NP stabilizer	P/Rh	PEO/Rh	4VPMe ⁺ I ⁻	T /°C	Conv. /% ^c	TON 2 ^{c,d}	TON 3 ^{c,d}	TON 4 ^{c,d}	TON MeCy ^{c,d}
1	CCM-N-0.1	1 ^e	0.5	-	25	21.0	31.0	9.5	2.0	22.5
2					60	41.4	61.8	13.4	7.0	9.0
3					90	100.0	162.1	16.9	29.1	^k
4		4 ^e	2	-	25	43.5	63.2	20.8	8.6	7.9
5					60	100.0	118.6	33.5	63.8	44.6
6					90	94.8	150.5	24.5	19.7	^k
7	PPh ₃	1	-	-	60 ^g	97.2 (3.7)	146.4 (7.9)	7.6 (3.1)	44.3 (13.4)	23.9 (7.7)
8		4	-	-	60 ^h	78.8 (6.8)	153.8 (13.2)	0.5 (0.8)	1.3 (2.1)	2.8 (0.2)
9	PEOMA	-	0.5	-	60 ^g	93.6 (0.5)	75.3 (47.4)	7.9 (6.5)	105.6 (54.7)	4.3 (0.9)
10			2		60 ⁱ	93.6 (4.7)	152.3 (11.9)	17.5 (4.5)	19.5 (2.4)	29.5 (14.0)
11			8		60 ⁱ	96.0 (0.8)	109.9 (26.7)	21.1 (4.0)	33.0 (10.8)	3.4 (0.1)
12	macroRAFT-N	-	0.5	-	60 ^h	98.8 (1.5)	93.0 (22.0)	42.4 (2.5)	62.5 (25.6)	10.7 (3.5)
13			2		60 ^h	98.8 (0.1)	107.2 (19.4)	34.1 (8.7)	58.9 (11.2)	2.4 (0.4)
14			0.5		60 ^{ij}	97.1 (0.3)	11.2 (4.0)	49.6 (2.1)	133.3 (3.5)	21.6 (4.3)
15			2		60 ^{ij}	96.4 (1.0)	25.0 (6.6)	59.1 (13.8)	109.7 (4.8)	11.7 (2.4)
16	CCM-C-0.1	1 ^l	-	4.7	25	12.9	10.2	4.2	0.0	1.0
17					60	9.1	14.0	4.1	0.0	60.5
18					90	86.5	154.0	9.2	7.2	^k
19		4 ^m	-	18.7	25	5.0	11.5	0.0	0.0	10.3
20					60	18.0	25.3	10.6	0.0	21.1
21					90	23.5	49.8	0.0	0.0	ⁱ
22	macroRAFT-C	-	-	4.7	60 ^g	20.9 (6.5)	32.0 (10.0)	6.9 (1.9)	3.2 (1.5)	2.0 (0.1)
23				18.8	60 ⁱ	12.5 (6.9)	17.0 (7.4)	3.8 (3.5)	2.5 (1.8)	2.0 (0.2)

^a Unless otherwise stated, the Rh NPs were synthesized at 60 °C in the presence of NEt₃ (10 equiv. per Rh) and the indicated support prior to catalysis. ^b Standard conditions: acetophenone/Rh = 200; 0.4 ml of latex, 0.5 ml of toluene; p(H₂) = 20 bar; 20 h. ^c The figures are averages, with standard deviations in parentheses, when multiple runs were carried out. ^d TON is usually defined by the number of reacted molecules to that of an active site. Here, TON = Number of reacted molecules / Number of Rh introduced. ^e 8.07 μmol of Rh. ^f 1.70 μmol of Rh. ^g Average and standard deviation from 3 parallel runs. ^h Average and standard deviation from 5 parallel runs. ⁱ Average and standard deviation from 4 parallel runs. ^j No NEt₃ was used in the NP synthesis. ^k The volatility of methylcyclohexane led to escape of the product from the reaction vials and prevented a reliable measurement of its amount at the end of the reaction. ^l 5.09 μmol of Rh. ^m 1.29 μmol of Rh.

The partial reduction products 1-phenylethanol (**2**, carbonyl reduction) and methyl cyclohexyl ketone (**3**, arene ring reduction) and the fully reduced 1-cyclohexylethanol (**4**) were observed in variable proportions, depending on the stabilizer and conditions (Scheme IV.4.1). A certain amount of methylcyclohexane (MeCy), produced by the ring reduction of the toluene solvent, was also observed (see Table IV.4.1). The arene ring reduction is not surprising, because arene hydrogenation is well-known to be promoted by metal NPs, particularly those of Rh.^[163, 166] A most relevant precedent is the reported biphasic acetophenone (and other functionalized arenes) hydrogenation using buffered water, benzene or cyclohexane as organic phase, and cetyltrimethylammonium bromide or tetrabutylammonium hydrogen sulphate as phase transfer catalyst, which also produced mixtures of all the possible products **2-4**.^[167] Although the authors of that contribution wrote “we are not certain whether the phase-transfer process described herein involves a soluble or insoluble rhodium catalyst”, their molecular precursor ($[\text{RhCl}(\text{1,5-hexadiene})]_2$) and catalytic conditions were quite similar to those used here. The acetophenone hydrogenation catalyzed by Rh NPs has previously been reported for NPs stabilized by polyvinylpyrrolidone (RhNP@PVP)^[168] and by phosphine ligands, including PPh_3 .^[148c] There are also a few reports on the Rh NP-catalyzed transfer hydrogenation of acetophenone by isopropanol, focusing on enantioselectivity, where no ring hydrogenation was mentioned.^[169]



Scheme IV.4.1 Products resulting from the hydrogenation of acetophenone catalyzed by Rh NPs.

For the RhNP@CCM-N-0.1 catalyst, the acetophenone reduction appears faster

for P/Rh = 4:1 (cf. entries 4-6 with 1-3 in Table IV.4.1). In particular, complete substrate consumption was already achieved at 60 °C (entry 5), whereas the conversion was complete only at 90 °C when P/Rh = 1:1. It is important to underline that, due to the uncontrolled and unreliable magnetic stirring, the conversion data (sum of all products = consumed acetophenone) for certain runs may be artificially low and should therefore be considered as a lower limit. Carbonyl reduction is faster than the arene reduction (**2** > **3**). This trend is opposite to that found for the above-mentioned [RhCl(1,5-hexadiene)]₂-catalyzed reduction under phase transfer conditions.^[167] In the two previous reports on the hydrogenation of acetophenone with Rh NPs in a single liquid phase, similar selectivity but greater activity were observed, *e.g.* up to 78 turnovers in only 5 h at 30 °C and 20 bar of H₂ for the PPh₃-stabilized particles^[148c] and 71 turnovers in 2 h at 25 °C and 1 bar of H₂ for the PVP-stabilized particles.^[168] The lower activity observed for the RhNP@CCM catalyst can be attributed, at least in part, to mass transport limitations, as the catalytic performance of NPs in polyelectrolyte brush.^[160]

All control experiments with the RhNP@PPh₃, RhNP@PEOMA and RhNP@macroRAFT-N catalysts were carried out only at 60 °C. The data reported in Table IV.4.1 are averages of parallel runs with standard deviations. In all cases (entries 7-15), the observed conversions were greater (lower residual **1**) than for RhNP@CCM-N-0.1 with P/Rh = 1:1 (entry 2) but lower than for RhNP@CCM-N-0.1 with P/Rh = 4:1 (entry 5). A most interesting comparison concerns the selectivity (carbonyl vs. arene ring reduction). The phosphine stabilizer (RhNP@PPh₃) suppresses arene reduction, particularly for the smaller NPs obtained with P/Rh = 4:1 (entry 8), for which the ring reduction products **3** and **4** were obtained in very small amounts. The NPs stabilized by PEO functions (RhNP@PEOMA and RhNP@macroRAFT-N), on the other hand, gave more extensive arene reduction. The PEO/Rh ratio (from 0.5 to 8 for RhNP@PEOMA, entries 9-11; from 0.5 to 2 for RhNP@macroRAFT-N, entries 12-13) does not appear to significantly alter the activity and selectivity. The absence of NEt₃ for RhNP@macroRAFT-N (hence leaving the methacrylic acid functions protonated (entries 14-15), slightly improves the arene ring reduction (**3** > **2**; increase of **4**). These

selectivities are similar to those reported in the previous studies.^[148c, 168]

For the RhNP@CCM-N catalyst with P/Rh = 1:1, the most interesting comparison is between entries 2, 9 and 12, because the NPs in this catalyst (Figure IV.2.2) are located near the PEO surface functions. The control catalysts (RhNP@PEOMA and RhNP@macroRAFT-N) appear more active and yield a greater fraction of arene reduction products (**3** and **4**). For the RhNP@CCM-N catalyst with P/Rh = 4:1, where the Rh NPs remain confined in the hydrophobic core, the most interesting comparison is between entries 5 and 8. While the activity compares favorably, the large selectivity difference (large amounts of arene reduction products for entry 5, traces in entry 8) suggests a different catalyst organization, raising questions about the stability of the core confinement in RhNP@CCM-N. TEM images for this catalyst recorded after catalysis revealed large NP aggregates outside of the CCM particles, see Figure IV.4.1. Given this result, we can conclude that the CCM-N scaffold is not an appropriate support for the Rh NPs confinement under these catalysis conditions.

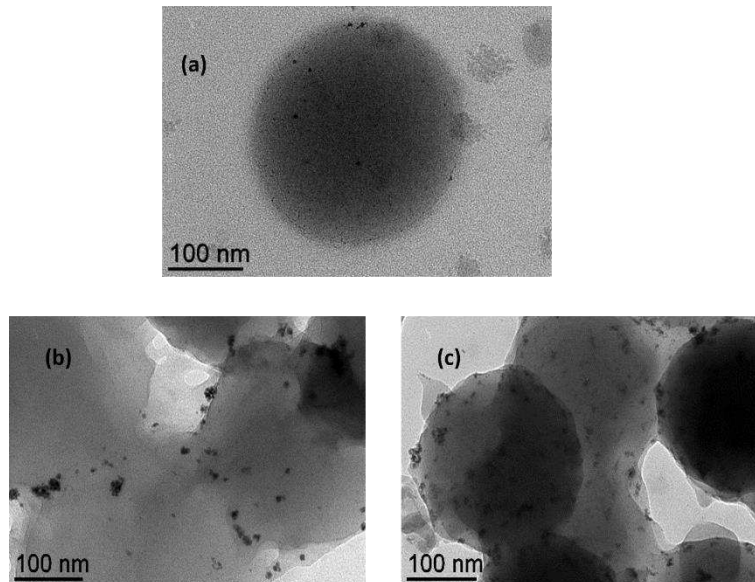


Figure IV.4.1 TEM images of the RhNP@CCM-N-0.1 (P/Rh = 4:1) latex before (a) and after the catalytic runs of entry 4 (b) and 6 (c) in Table IV.4.1.

Moving to the cationic CCM latex (RhNP@CCM-C, entries 16-21 in Table IV.4.1), the substrate conversions were very poor, except at the highest temperature for P/Rh =

1:1 (entry 18). These results may indicate poor mass transport of the substrate towards the CCM core and suggest that the Rh NPs remain trapped within the CCM core under catalytic conditions, contrary to the RhNP@CCM-N latex examined above. A TEM analysis of the latex after catalysis (Figure IV.4.2) confirms this conclusion. These results may seem puzzling, because both CCM-N and CCM-C have shown excellent performance in olefin hydrogenation (notably styrene and 1-octene) by molecular Rh^I@CCM, which is confined within the CCM core (see Chapter III).^[109, 151] Indeed, the CCM-C nanoreactors performed equally well (or better) than CCM-N. Since toluene is a good solvent for polystyrene and efficiently swells the CCM core, it can vectorize substrates toward the catalyst, even those like 1-octene that do not have themselves high affinity for polystyrene. Control experiments run with RhNP@macroRAFT-C (entries 22-23) gave equally poor conversions. In this catalyst, the Rh NPs are possibly stabilized by interaction with the iodide anions associated to the polycationic P4VPMe⁺ chains. Therefore, the only possible way to rationalize these results is that the polycationic nature of the CCM-C and macroRAFT-C, although not affecting the mass transport of the organic solvent (toluene), have a negative effect on the mass transport of the acetophenone substrate, perhaps as a consequence of electrostatic interactions between the 4VPMe⁺I⁻ functions and the substrate carbonyl group. This hypothesis is supported by the results obtained for the hydrogenation of styrene (vide infra).

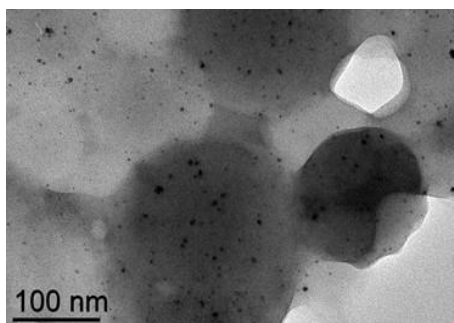
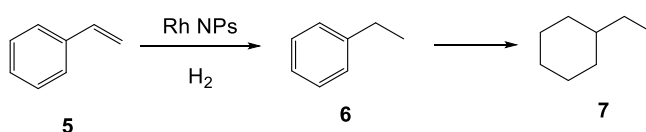


Figure IV.4.2 TEM image of the RhNP@CCM-C-0.1 (P/Rh = 4:1) latex after the catalytic run of entry 19 in Table IV.4.1.

IV.5 Catalyzed hydrogenation of styrene

These reactions were carried out under conditions identical to those of the acetophenone hydrogenation (notably, styrene/Rh = 200), except that 1-nonanol was used as the continuous organic phase instead of toluene, for two reasons. One is to eliminate the competitive ring hydrogenation between styrene (Scheme IV.5.1) and the organic solvent. The second one is to compare the results with those of the previously described molecular hydrogenations, where 1-nonanol was also used as continuous organic phase (Chapter III).^[150] The Rh NP-catalyzed hydrogenation of styrene has only been addressed in one recent report, with NPs stabilized by a phosphine ligand.^[149, 151] Additional contributions have addressed the hydrogenation of other arenes and aromatic heterocycles with Rh NPs stabilized by PEO,^[148a, 148d] cyclic iminium salts^[148e] or phosphines^[148b, 148c]. All our new results are collected in Table IV.5.1.



Scheme IV.5.1 Products from the hydrogenation of styrene catalyzed by Rh NPs.

Table IV.5.1 Styrene hydrogenation catalyzed by Rh NPs.^{a,b}

Entry	NP stabilizer	P/Rh	PEO/Rh	4VPMe ⁺ I/Rh	St/Rh	T /°C	5/% ^c	6/% ^c	7/% ^c
24	CCM-N-0.1	1 ^d	0.5	-	200	25	0.1	99.3	0.6
25						60	0.1	95.9	4.0
26		4 ^e	2	-	200	25	0	100	0
27						60	0	97.0	3.0
28	PPh ₃	1	-	-	200	60 ^f	0 (0)	72.7 (2.4)	27.3 (2.4)
29		4	-	-	200	60 ^g	0 (0)	93.1 (1.4)	6.9 (1.4)
30		4	-	-	2000 ^h	60 ^f	0.1 (0)	98.2 (0.4)	1.7 (0.4)
31	PEOMA	-	0.5	-	200	60 ^g	0 (0)	88.0 (2.3)	12.0 (2.3)
32			2	-	200	60 ^f	0.5 (0.8)	90.6 (0.9)	8.9 (0.8)
33			8	-	200	60 ^g	0 (0)	54.6 (2.0)	45.4 (2.0)
34	macroRAFT-N	-	0.5	-	200	60 ^g	0 (0)	19.1 (9.0)	80.9 (9.0)
35			2	-	200	60 ^f	0 (0)	93.7 (3.3)	6.3 (3.3)
36			0.5	-	200	60 ^{g,i}	5.1 (3.2)	3.6 (5.2)	91.3 (4.4)
37			2	-	200	60 ^{g,i}	2.8 (1.6)	19.9 (10.9)	77.3 (9.4)
38	CCM-C-0.1	1 ^j	-	4.7	200	25	0	99.0	1.0
39						60	0.1	99.6	0.3
40					2000 ^h	25	0	100	0
41						60	0	99.8	0.2
42		4 ^k	-	18.7	200	25	0	100	0
43						60	0	100	0
44					2000 ^h	25	0	100	0
45						60	0	99.9	0.1
46	macroRAFT-C	-	-	200	4.7	60 ^f	0 (0)	99.9 (0.2)	0.1 (0.2)
47					18.8	60 ^g	0 (0)	99.9 (0.1)	0.1 (0.1)
48				19.2	2000 ^h	60 ^l	6.3 (4.0)	93.7 (4.0)	0 (0)
49	CCM-C-0.05	1	-	9.1	200	25	0	100	0
50						60	0	100	0
51		4		37.7		25	0	100	0
52						60	0	100	0

53	CCM-C-0.2	1	-	2.4	200	25	0	99.7	0.3
54				60		0	100	0	
55		4		25		0	99.9	0.1	
56				60		0	100	0	
57	NG-C-0.1	1	-	4.7	200	25	0	91.7	8.3
58				60		0	93.3	6.7	
59		4		25		0	100	0	
60				60		0	100	0	

^a Unless otherwise stated, the Rh NPs were synthesized at 60 °C in the presence of NEt₃ (10 equiv. per Rh) and the indicated support prior to catalysis.

^b Standard conditions: 0.4 ml of latex, 0.5 ml of 1-nonanol; p(H₂) = 20 bar; 20 h.

^c The figures are averages, with standard deviations in parentheses, when multiple runs were carried out.

^d 8.07 μmol of Rh.

^e 1.70 μmol of Rh.

^f Average and standard deviation from 5 parallel runs.

^g Average and standard deviation from 4 parallel runs.

^h Pure styrene was used as organic phase.

ⁱ No NEt₃ was used in the NP synthesis.

^j 5.09 μmol of Rh.

^k 1.29 μmol of Rh.

^l Average and standard deviation from 3 parallel runs.

Since the RhNP@CCM-N catalytic efficiency is very high (entries 24-27 in Table IV.5.1), experiments were carried out only up to 60 °C. Full substrate conversion was already achieved in 20 h at 25 °C, with high selectivity for the vinyl group hydrogenation. Only traces of the final product **7** were observed at 25 °C for the NPs produced with P/Rh = 1:1 (entry 24) and this increased only slightly when operating at 60 °C (entry 25). The RhNP@PPh₃ performed equally well (entries 28-29), with a slightly greater arene hydrogenation, particularly when P/Rh = 1:1. The RhNP@PEOMA also gave full conversion and similar selectivity (entries 31-33). The RhNP@macroRAFT-N also gives full conversions and an even greater proportion of **7**, particularly for the sample obtained with PEO/Rh = 0.5:1 (entry 34). Clearly, a greater amount of stabilizer (either the phosphine or the ethylene oxide functions) negatively affects the ring hydrogenation, probably by reducing the surface accessibility. For the RhNP@macroRAFT-N catalyst, additional runs were carried out in the absence of NEt₃ (both in the NP synthesis and in catalysis; same batch used for the acetophenone hydrogenation; entries 36-37). Like for the acetophenone hydrogenation, the absence of base increases the rate of ring hydrogenation. It is also interesting to compare the much lower extent of ring hydrogenation for styrene (Table IV.5.1) relative to acetophenone (Table IV.4.1). For instance, runs 1 and 24 for RhNP@CCM-N-0.1 at 25 °C and P/Rh = 1:1 show 27% of ring-hydrogenated products (**3** + **4**) for acetophenone vs. only 0.6% (**7**) for styrene. Likewise, these fractions are 60% and 12%, respectively, for runs 9 and 31 involving RhNP@PEOMA at 60 °C and PEO/Rh = 0.5:1. This difference may result from the action of the carbonyl function in acetophenone and the hydroxyl function in the phenylethanol intermediate in keeping the substrate more strongly anchored to the Rh NP surface. However, because of the Rh NPs migration under catalytic conditions, as already demonstrated in the previous section, interest in using this latex is limited. Indeed, a TEM analysis of the CCM-N-0.1 catalyst after styrene hydrogenation with P/Rh = 4:1 (run 27), shown in Figure IV.5.1, reveals a very similar morphology change to that observed after the acetophenone hydrogenation under the same conditions (Figure IV.4.1).

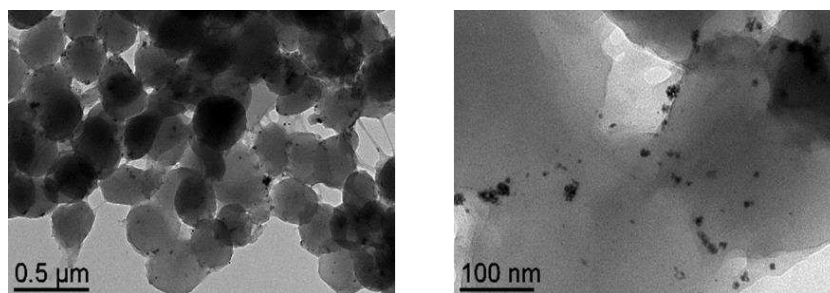


Figure IV.5.1 TEM images of the RhNP@CCM-N-0.1 (P/Rh = 4:1) latex after the catalytic run of entry 27 in Table IV.5.1.

The RhNP@CCM-C catalyst also shows excellent performance (entries 38-45, 49-56), like the RhNP@CCM-N catalyst, with full substrate conversion (up to 2000 equiv. vs. Rh) at both 25 °C and 60 °C within 20 h. This is in stark contrast with the poor performance in acetophenone hydrogenation, confirming the hypothesis of a severe mass transport limitation for the latter. High activities were also observed for the RhNP@macroRAFT-C control runs (entries 46-48). The fraction of ring-hydrogenated product is even lower than that observed for the RhNP@CCM-N-0.1 and RhNP@macroRAFT-N systems. Since neat styrene is a good solvent for polystyrene, the hydrogenation was also carried out in bulk (styrene/Rh = 2000), yielding once again full conversion in 20 h at both 25 °C and 60 °C for both P/Rh ratios (entries 40-41 and 44-45). High activities for the hydrogenation of neat styrene were also observed for the RhNP@PPh₃ (run 30) and RhNP@macroRAFT-C (run 48) control runs. The TEM of latex after 20 h hydrogenation reaction didn't show significant NPs leaching or polymer agglomeration (Figure IV.5.2).

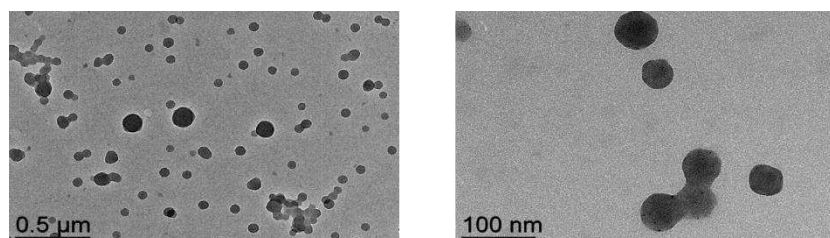


Figure IV.5.2 TEM images of the RhNP@CCM-C-0.1 (P/Rh = 4:1) latex after the catalytic run of entry 42 in Table IV.5.1.

In addition to this conclusion, the catalytic performance of RhNP@NG-C-0.1 showed comparable reactivity and selectivity (entries 57-60), even though the Rh NPs were confined in the crosslinked parts, and the conversions of styrene were quantitative after 20 h at 25 °C for P/Rh = 4:1 and 1:1.

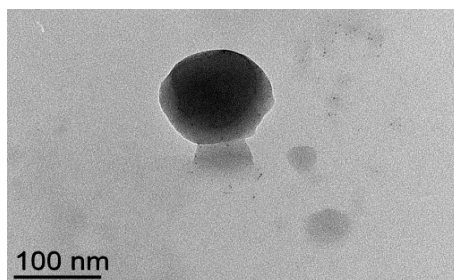


Figure IV.5.3 TEM images of the RhNP@NG-C-0.1 (P/Rh = 4:1) latex after the catalytic run of entry 51 in Table IV.5.1.

In order to better assess the catalyst performance, a series of experiments were also carried out using shorter reaction times with the RhNP@CCM-C-0.1 (P/Rh = 4:1) catalyst, see Table IV.5.2. When operating in 1-nonanol (styrene/Rh = 200), quantitative conversion to ethylbenzene was still achieved down to 1 h (runs 61-65). Lowering the temperature to 25 °C and using neat styrene (conditions identical to those of entry 44 in Table IV.5.1) gave again full conversion after 2 and 1.75 h (runs 66-67). Only for shorter reaction times of 1.5, 1 and 0.5 h (runs 68-70), incomplete conversions were witnessed. From runs 67-70, average TOF values over the entire catalytic runs of 1143, 1020, 994 and 1056 h⁻¹ can be calculated from the TON/time ratios, for an overall average of 1053 ± 46 h⁻¹. In order to assess the possible effect of the TPP concentration in the hydrophobic CCM core, two additional hydrogenations of neat styrene were carried out using a reaction time of 0.5 h under otherwise identical conditions, with RhNP@CCM-C-0.05 and RhNP@CCM-C-0.2 (runs 71-72). The results are quite comparable, indicating that the TPP concentration does not significantly affect the NP catalytic activity. All experiments in Table IV.5.2 show perfect selectivity in favor of the ethylbenzene product **6**. In comparison with the only published example of styrene hydrogenation with Rh NPs (complete conversions in 24 h at R.T and 30 bar of H₂ in

isopropanol with TON up to 756),^[149] the activity appears much greater. However, that investigation did not report runs with shorter reaction time or greater substrate/Rh ratios. It is also of interest to compare these results with those described in Chapter III with the molecular Rh^I system embedded in the same CCM support, which were carried out under the same conditions (aqueous biphasic, neat styrene, 25 °C, 20 bar of H₂), where a TOF of *ca.* 300 h⁻¹ was obtained.^[151] Thus, the catalytic activity of the Rh NPs appears superior to that of the molecular system.

Table IV.5.2 Effect of reaction time, temperature and TPP content on the biphasic hydrogenation of styrene catalyzed by RhNP@CCM-C.^{a,b}

Entry	NP stabilizer	P/Rh	4VPMe ⁺ I /Rh	Styrene/Rh	T /°C	Time /h	5/%	6/%	7/%
61	CCM-C-0.1	3.93 ^c	18.3	200	60	15	0	99.6	0.4
62						10	0	100	0
63						5	0	100	0
64						2	0	100	0
65						1	0	100	0
66						4.05 ^d	18.9	2000 ^g	25
67	1.75	0	100	0					
68	1.5	23.5	76.5	0					
69	1	50.3	49.7	0					
70	0.5	73.6	26.4	0					
71	CCM-C-0.05	4.04 ^e	37.7	2000 ^g	0.5				
72	CCM-C-0.2	4.07 ^f	9.5	2000 ^g	0.5	56.1	43.9	0	
73	NG-C-0.1	3.96	18.5	200	25	1.5	0	100	0
74						0.5	0	100	0
75						2000 ^g	0.5	71.3	28.7

^a The Rh NPs were synthesized at 60 °C in the presence of NEt₃ (10 equiv. per Rh) and the indicated support prior to catalysis.

^b Standard conditions: 0.4 ml of latex; 0.5 ml of 1-nonanol (if used); p(H₂) = 20 bar.

^c 0.96 μmol of Rh.

^d 2.43 μmol of Rh.

^e 0.45 μmol of Rh.

^f 1.89 μmol of Rh.

^g Neat styrene (no 1-nonanol).

Finally, the hydrogenation of neat styrene was repeated under the same conditions

of entry 70 of Table IV.5.2 (P/Rh = 4:1, 25 °C, 0.5 h, 20 bar of H₂) with catalyst recovery and recycling. In a first series of experiments, the product recovery involved extraction of the latex phase (after decanting off the organic layer) with diethyl ether, in order to remove all product and residual substrate from the polymer hydrophobic core prior to the addition of a new substrate charge for the next catalytic run. This extraction procedure is identical to that used in all individual runs of the above tables, as well as to that used for the recycling experiments with the molecular Rh^I catalyst embedded in the CCM as described in Chapter III. The results are shown in Figure IV.5.4a. Again, the selectivity was 100% in favor of ethylbenzene, with no trace of ethylcyclohexane. While the first run gave a higher conversion (66.4%) relative to entry 70 of Table IV.5.2, the subsequent runs indicated significant loss of activity, with a continuous drop of the conversion to less than 5% after the 5th recycle. This decrease cannot be related to metal leaching or to mechanical losses during the separation phase, because the decantation phase was rapid yielding a colorless and transparent organic phase and a sharp interface. In a separate recycle series (Figure IV.5.4b), a catalyst regeneration step was operated after the 1st recycle, consisting of H₂ treatment (20 bar, 80 °C, 2 h) in the absence of substrate. The activity was partially recovered in the 2nd recycle. However, it dropped again in the 3rd recycle. This suggests a NP surface deactivation process, which was only incompletely corrected by the regeneration phase. The TEM analysis of the latex recovered after the 6th recycle (first series), Figure IV.5.4c, reveals large Rh NP agglomerates and empty polymer particles. Therefore, the irreversible (*i.e.*, not recovered by regeneration) activity loss can be attributed at least in part to the loss of Rh NPs active surface associated to the agglomeration.

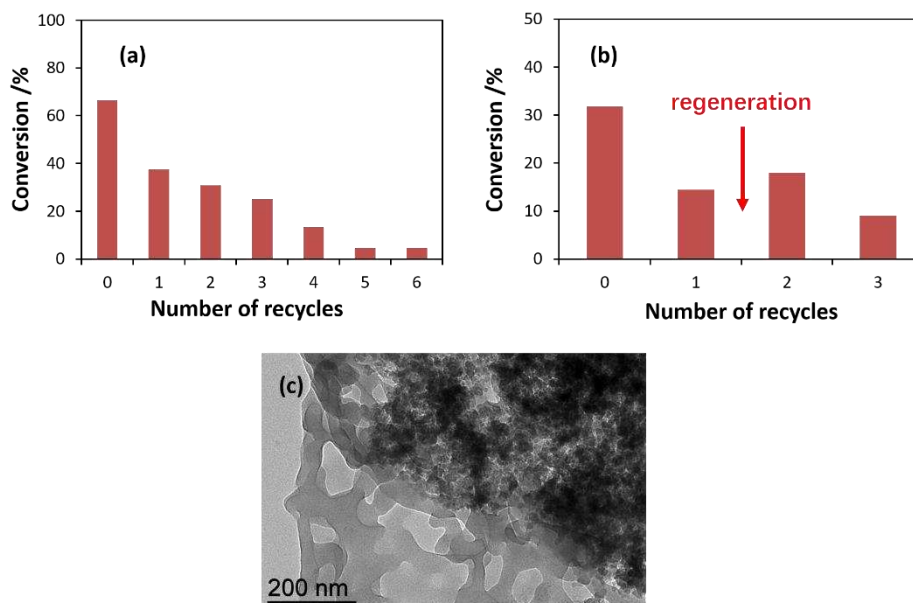


Figure IV.5.4 (a) Conversion vs. recycle number for the hydrogenation of neat styrene catalyzed by RhNP@CCM-C-0.1 (P/Rh = 4:1) and with product recovery by extraction with diethyl ether. Conditions: styrene/Rh = 2000, 25 °C, 0.5 h, 20 bar of H₂ pressure; (b) same as (a), with a catalyst regeneration step (indicated by an arrow) between recycles 1 and 2; (c) TEM image of the recovered latex after the 6th recycle of the series of experiments in (a).

The Rh NPs extraction from the CCM core can be associated to the use of diethyl ether for the product separation. Indeed, the Rh NPs can be expected to interact similarly with Et₂O and with the PEO functions of the CCM-N shell. In order to substantiate this hypothesis, a final series of catalytic runs with recycling was carried out using toluene instead of Et₂O for product extraction, in combination with periodical NP surface regeneration. The results are shown in Figure IV.5.5a. A first catalyst regeneration, conducted immediately after the 1st run, led to greater activity relative to the original one (*ca.* 80% conversion). Without any additional regeneration, the high activity was maintained for the next two recycles and then gradually fell to *ca.* 20% in the 5th recycle. At this point, a second catalyst regeneration led again to a full activity recovery to *ca.* 80% conversion for the next two cycles. The TEM analysis of the recovered latex after the 8th recycles clearly showed that the Rh NPs remained well dispersed inside the CCM particles, see *e.g.* Figure IV.5.5b. The comparison of the activity trend for the recycles with Et₂O and toluene washings and the TEM images of

the recovered catalyst in Figure IV.5.4c and Figure IV.5.5b constitutes indirect proof of the Rh NPs confinement in the CCM-C hydrophobic core. A precise comparison of the Rh NP size before and after catalysis is difficult, but the TEM image clearly evidences the absence of NP agglomeration. The observed behavior confirms the surface deactivation phenomenon during the catalytic runs at 25 °C and the full reactivation by H₂ treatment at 80 °C. Clearly, no surface deactivation would be expected if the catalytic hydrogenations are conducted directly at higher temperatures.

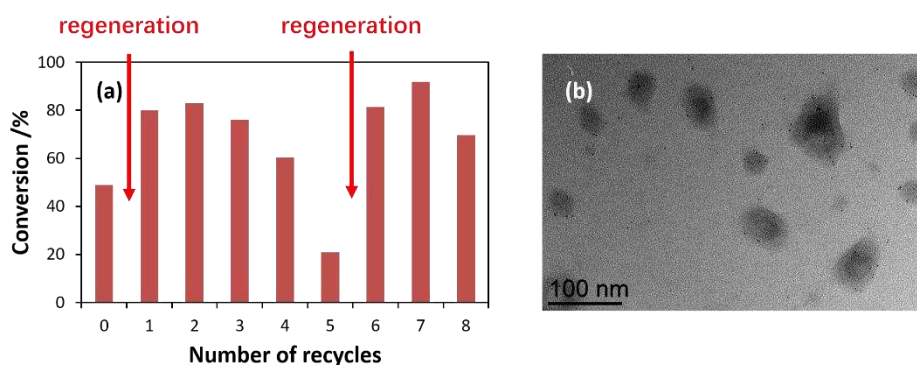


Figure IV.5.5 (a) Conversion vs. recycle number for the hydrogenation of neat styrene catalyzed by RhNP@CCM-C-0.1 (P/Rh = 4:1) and with product recovery by extraction with toluene. Conditions: styrene/Rh = 2000, 25 °C, 0.5 h, 20 bar of H₂ pressure. The arrows indicate additional Rh NPs regeneration steps. (b) TEM image of the recovered latex after the 8th recycle.

The marked difference in behavior between the recycle results with Et₂O and toluene washings provides useful information about the relative aptitude of different NP stabilizers. This difference is in line with the different NP migration behavior observed for the RhNP@CCM-N and RhNP@CCM-C systems. Although the phosphine P lone pairs bind Rh^I much more tightly than the O lone pair in ethers, the same is definitely not true for the Rh⁰ atoms on the Rh NPs surface. Thus, while Et₂O washings did not lead to any significant Rh^I leaching from the supported molecular Rh^I@CCM (N or C) systems,^[150] the Rh NPs could be maintained in the stabilizing environment of the CCM core only in the absence of large concentrations of O-based donor stabilizers. The Rh NPs extraction from the CCM-C core observed during the recycles with Et₂O washings, leading to agglomeration and loss of catalytic activity, is

certainly facilitated by the large Et₂O concentration.

A final series of recycling experiments was conducted with the RhNP@NG-C-0.1 system, with toluene washings and regenerations at 80 °C after 1st and 6th recycle (see Figure IV.5.6). After the 1st regeneration, the reactivity recovered up to 45.7% from the initial 36.6%, and declined to 19.1% by the followed four recycles. At this moment, another Rh NPs regeneration contributed to the revived reactivity to 37.6%. The TEM of latex after the last recycle indicated that all the Rh NPs remained confined in the cores, without any agglomeration problem. A determination of the relative P- and O-donor affinity with respect to the Rh NPs surface would require more detailed quantitative study, which is beyond the scope of the present study.

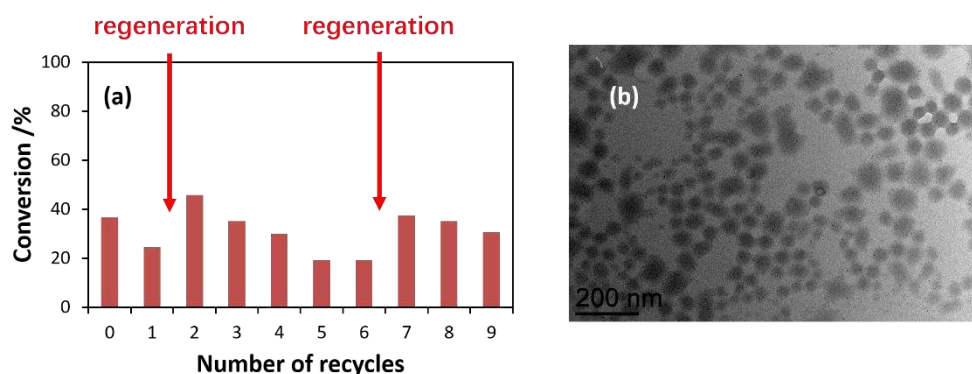


Figure IV.5.6 (a) Conversion vs. recycle number for the hydrogenation of neat styrene catalyzed by RhNP@NG-C-0.1 (P/Rh = 4:1) and with product recovery by extraction with toluene. Conditions: styrene/Rh = 2000, 25 °C, 0.5 h, 20 bar of H₂ pressure. The arrows indicate additional Rh NPs regeneration steps. (b) TEM image of the recovered latex after the 9th recycle.

IV.6 Catalyzed hydrogenation of 1-octene

The main objective of these experiments was to gather additional evidence for the Rh NPs confinement in the CCM-C core. The experiments were only carried out with the CCM-C-0.1 latex, using both the in-situ-activated [RhCl(COD)(TPP@CCM-C-0.1)] precatalyst and the RhNP-containing system, RhNP@CCM-C (see Table IV.6.1).

Before catalysis implementation, the latexes were freeze-dried in order to completely remove toluene (previously used as swelling solvent to load the molecular Rh precursor) and avoid any 1-octene mass transport assistance. The experiment with the molecular catalyst (run 76) unexpectedly yielded a rather efficient hydrogenation. Since this molecular catalyst is unambiguously core-confined, this result demonstrates the occurrence of 1-octene mass transport to the polystyrene core. Consequently, the previously reported absence of ^1H and ^{31}P NMR signatures (of incorporated 1-octene and core-anchored TPP ligands, respectively) after equilibration of the CCM-N particles with neat 1-octene^[94] cannot be attributed to the absence of 1-octene in the core. Rather, the 1-octene amount (a poor polystyrene solvent) at equilibrium is evidently too small to confer sufficient mobility to the polymer and the correlation times remain too long for NMR observation. A new ^1H NMR investigation has confirmed the absence of ^1H and ^{31}P resonances for core-incorporated 1-octene and core-anchored TPP after equilibrating the TPP@CCM-C-0.1 latex with neat 1-octene.

Table IV.6.1 1-octene hydrogenation catalyzed by RhNP@CCM-C-0.1.

Entry	Catalyst	Substrate phase	<i>n</i> -Octane/%
76	[RhCl(COD)(TPP@CCM-C)]	neat 1-octene	62.6
77	RhNP@CCM-C ^b	neat 1-octene	31.1
78	RhNP@CCM-C ^b	1-octene/1-nonanol ^c	100

^a Conditions: 0.4 ml of latex; 0.71 μmol of Rh (P/Rh = 4:1); 158.9 mg of 1-octene (1-octene/Rh = 2000); $p(\text{H}_2) = 20$ bar; 25 $^\circ\text{C}$; 3 h.

^b The Rh NPs were synthesized at 60 $^\circ\text{C}$ in the presence of NEt_3 (10 equiv. per Rh) prior to catalysis.

^c 0.4 ml of 1-nonanol.

As shown in entry 77, the Rh NPs also catalyzed the hydrogenation of 1-octene, but the yield was *ca.* half that of run 76, suggesting that the Rh NPs have lower activity than the molecular catalyst for the hydrogenation of this substrate. This is opposite to the observed trend in styrene hydrogenation. This difference may be rationalized by a different relative affinity of 1-octene and styrene to bind to and be activated by a

coordinatively unsaturated monometallic Rh^{I} center versus the surface of a Rh^0 NP. Finally, the activity was greater (full conversion after 3 h) when 1-octene hydrogenation was carried out in the presence of 1-nonanol (run 78). This phenomenon is clearly related to an increased 1-octene mass transport, resulting from the vectorizing effect of 1-nonanol. This more than compensates the expected negative effects of substrate dilution on the kinetics and the possible 1-nonanol competition for NP surface binding. Thus, these catalysis results provide additional evidence in support of the Rh NPs confinement in the CCM-C hydrophobic core environment.

IV.7 Conclusion

We have extended the nanoreactor application of triphenylphosphine-functionalized core-crosslinked micelle latexes, for the first time, to metal nanoparticle catalysis. These latexes, with either neutral P(MAA-*co*-PEOMA) or polycationic P4VPM e^+I^- chains on the micelle surface and loaded with a Rh precatalyst, $[\text{RhCl}(\text{COD})(\text{TPP}@ \text{CCM})]$, led to the generation of CCM-embedded Rh NPs by H_2 reduction in the absence of olefins. For fully loaded (P/Rh = 1:1) latexes, the core-anchored complexes were readily reduced to Rh NPs by H_2 (20 bar) at 25 °C in the presence of NEt_3 , whereas heating to 60 °C is needed in the absence of base. Partially loaded latexes (P/Rh = 4:1) yield Rh NPs only upon heating and in the presence of excess NEt_3 . The TEM analyses revealed migration of the produced NPs from the core to the shell for $\text{RhNP}@ \text{CCM-N}$ latexes, due to competition between the core TPP ligands and the shell PEO chains as stabilizing functions. During the catalytic applications, even the phosphine-richer (P/Rh = 4:1) $\text{RhNP}@ \text{CCM-N}$ latexes led to NP migration and agglomeration away from the CCM particles, invalidating the CCM-N strategy for catalyst confinement.

For the cationic-shell latexes, on the other hand, the Rh NPs remained well-dispersed and core-confined for all P/Rh ratios after catalysis, but only when toluene, which displays poorer stabilizing power towards the Rh NPs than the core-anchored

triphenylphosphines, was used for product recovery/catalyst recycling. These RhNP@CCM-C latexes are therefore of interest for the catalytic application of Rh NPs under aqueous biphasic conditions with catalyst recycling. The catalytic studies presented here show high activity for the reduction of styrene in bulk (TOF greater than 1000 h^{-1} at $25 \text{ }^\circ\text{C}$ and 20 bar of H_2) and also of 1-octene, although the activity in the latter case is improved when the substrate is vectorized to the CCM core by 1-nonanol, which is a better polystyrene solvent. On the other hand, the polycationic nature of the CCM shell introduced mass transport limitations in the hydrogenation of acetophenone, blocking access to the catalytic NPs. Further investigations are necessary to establish the origin of this blocking effect. It should be possible to implement aqueous biphasic nanocatalysis under a wider array of experimental conditions through the development of nanoreactors with different core functions, *i.e.*, ligands that can better stabilize the metal NPs than TPP while allowing substrate access to the NP surface.

Chapter V

Synthesis and characterization of anionic core-shell amphiphilic copolymer

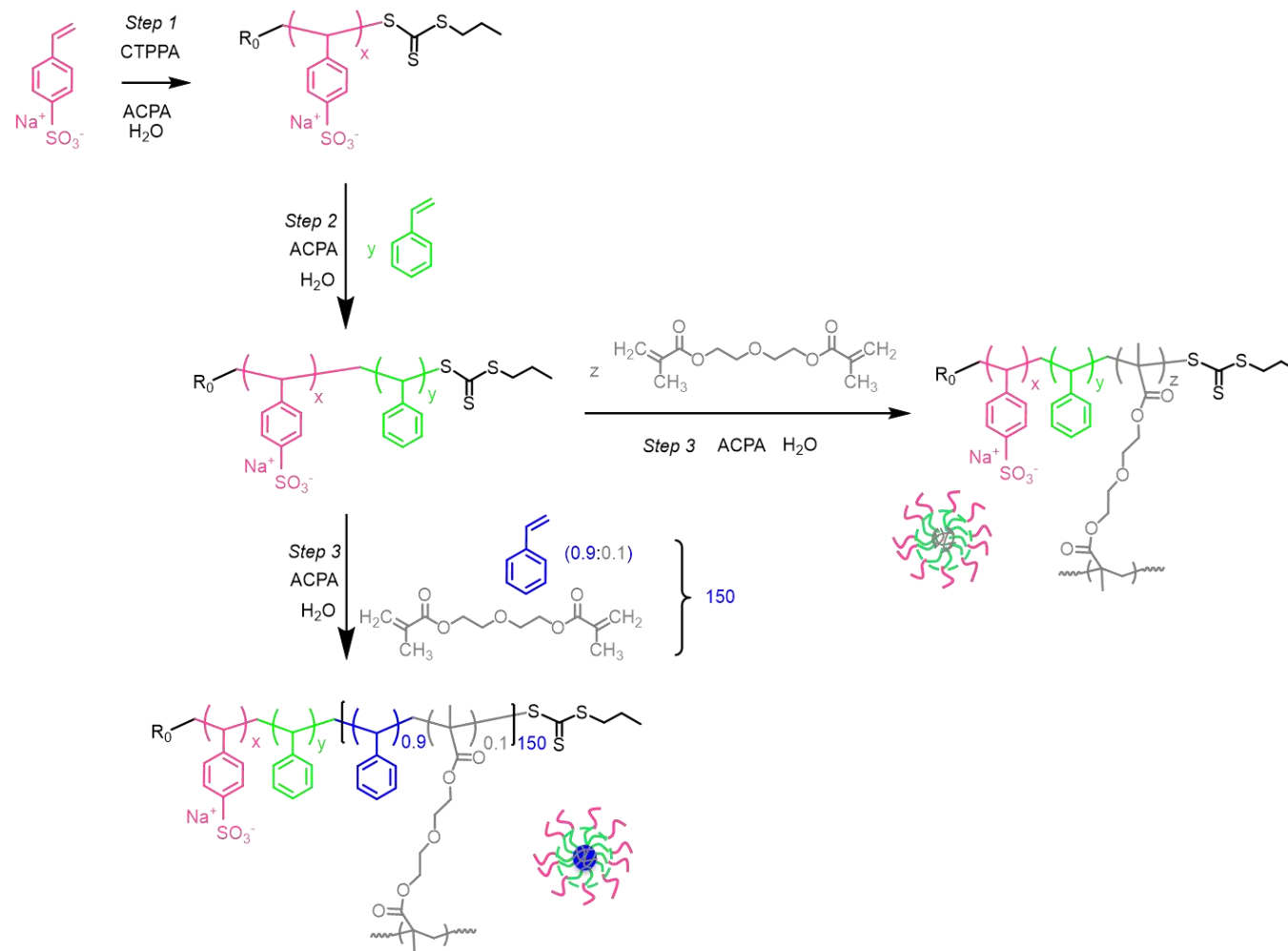
V.1 Introduction

In the previous chapters, it could be concluded that the positively charged shell consisting of P4VPMe⁺I chains brings electrostatic repulsion forces between different particles, which impedes interpenetration and core-core contact after metal precatalyst loading, ultimately leading to particle-particle coupling. This process may result in the formation of agglomeration or even macrogelation. As an added advantage, this polymeric nanoreactor architecture also leads to lower catalyst leaching and improved recyclability.

Enlightened by this work, a novel polymer with a polyanionic shell and a crosslinked core becomes another candidate of interest as catalyst carrier. Micelles with polyanionic shells are less frequent than their polycationic and neutral counterparts. Examples are the diblock copolymer micelles containing P(SPMA⁻K⁺),^[132] P(SPMA⁻K⁺-*co*-HEMA),^[132] PSS⁻Na⁺^[170] and PAMPS⁻Na⁺^[171] outer shells (SPMA⁻K⁺ = potassium 3-sulfopropyl methacrylate; HEMA = hydroxyethyl methacrylate; SS⁻Na⁺ = sodium 4-vinylbenzenesulfonate or *p*-styrenesulfonate; AMPS⁻Na⁺ = sodium 2-acrylamido-2-methylpropane sulfonate).

However, no example of unimolecular (crosslinked) micelles with a permanent polyanionic shell has so far been reported to the best of our knowledge. Anionic-shell CCMs have previously been obtained only by deprotonation of carboxylic acid groups from neutral-shell CCMs at high pH, *e.g.* by deprotonating the MAA monomers in the first generation CCMs developed within our group.^[100, 143] The SS⁻Na⁺ monomer was selected as the chain unit of the negatively charged shell in the new target nanoreactors. A few previous contributions have reported the controlled radical polymerization of SS⁻Na⁺ to generate well-defined architectures, including PSS⁻Na⁺-*b*-PMMA,^[172] PSS⁻Na⁺-*b*-PS,^[173] P(SS⁻Na⁺-*co*-VBC),^[174] P(SS⁻Na⁺-*co*-AANa),^[175] P(SS⁻Na⁺-*co*-*t*-BuAM),^[176] PSS⁻Na⁺-*b*-PNIPAm^[177] and so forth (VBC = 4-vinylbenzyl chloride; AANa = sodium acrylate; BuAM = N-*tert*-butylacrylamide; NIPAm = N-isopropylacrylamide).

Scheme V.1.1 Synthesis pathway toward block copolymer nanoreactor with a polyanionic shell.



We report here the synthesis and characterization of CCMs with a permanent polyanionic shell consisting of PSS^-Na^+ and a non-functionalized polystyrene core by the RAFT-PISA strategy in a one-pot process, following the same optimization strategy used for the polycationic shell particles in Chapter II, prior to the development of the target core-functionalized nanoreactors.

The polymer synthesis, summarized in Scheme V.1.1, followed the same procedure that was previously adopted for the first-generation CCM particles with a neutral hydrophilic P(MAA-*co*-PEOMA) shell.

V.2 PSS^-Na^+ macroRAFT

The first step, SS^-Na^+ RAFT polymerization in a water/ethanol (70/30, v/v) mixture, proceeded to complete conversion (see Figure V.2.1) with good control (low-dispersity and target molar masses, Figure V.2.2) to yield the macroRAFT agents $\text{R}_0\text{-(SS}^-\text{Na}^+)_x\text{-SC(S)SPr}$. Two quite different target degrees of polymerization ($x = 50$ and 140) were used to assess the stability of the final CCM particles with respect to this parameter. The DLS and TEM characterization of the macroRAFT products is available in Figure V.2.3. The DLS of the polymer aqueous solutions shows narrow distributions of small objects ($D_z \approx 1$ nm), probably corresponding to solvated single chains, though a small contribution of large agglomerates ($D_z \approx 300$ nm) is also present but visible only in the intensity mode. The TEM analysis of the solid residue shows only large agglomerates.

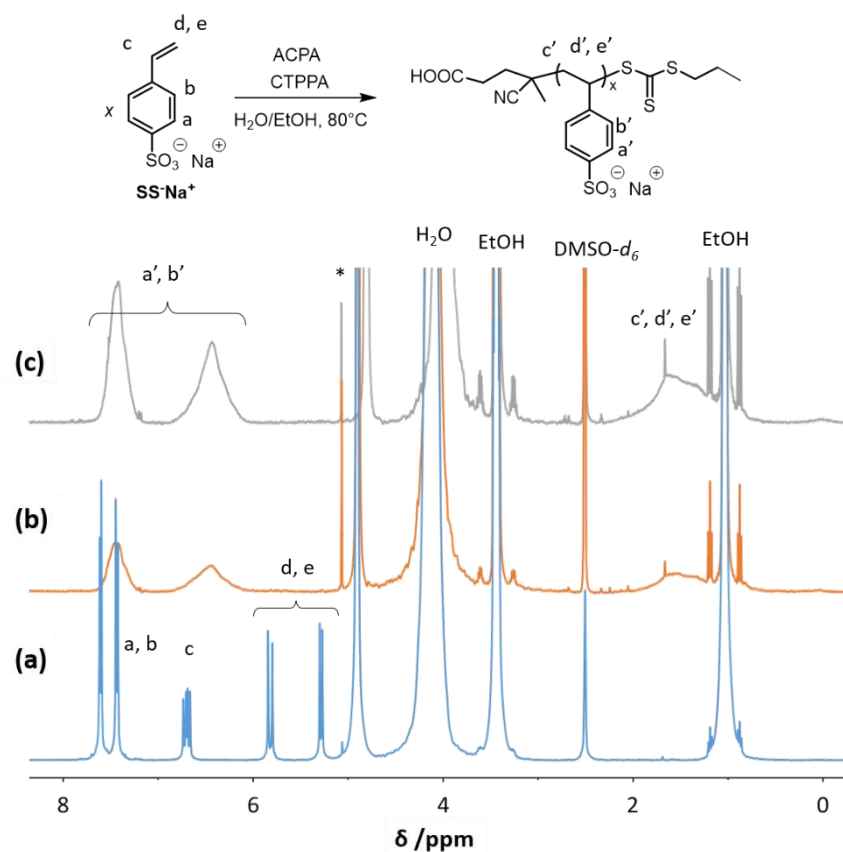


Figure V.2.1 ^1H NMR monitoring of the SS^-Na^+ RAFT polymerization in $\text{DMSO-}d_6$: (a) initial spectrum; (b) final spectrum ($\text{SS}^-\text{Na}^+/\text{CTPPA} = 50$); (c) final spectrum ($\text{SS}^-\text{Na}^+/\text{CTPPA} = 140$).

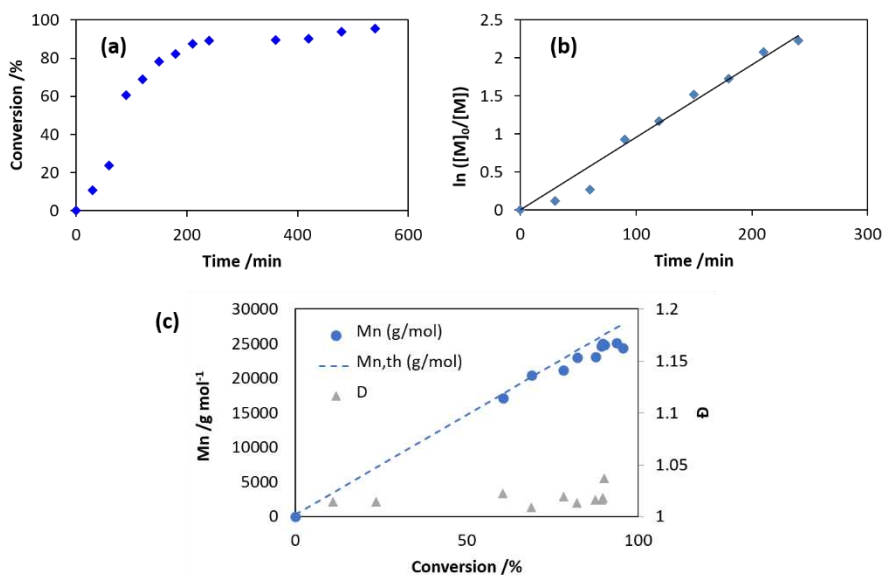


Figure V.2.2 Monitoring of the SS^-Na^+ RAFT polymerization with $\text{SS}^-\text{Na}^+/\text{CTPPA} = 140$: (a) conversion vs. time curve from ^1H NMR; (b) first-order kinetics plot; (c) evolution of the molar mass and D vs. conversion from the SEC analysis in $\text{H}_2\text{O} + \text{CH}_3\text{CN}$ (80/20, v/v) with 0.1 M NaNO_3 .

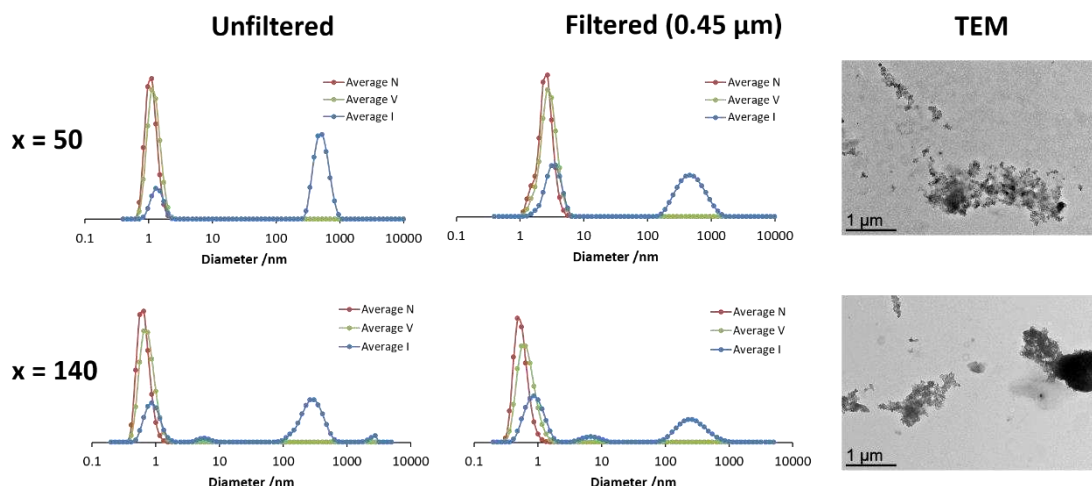


Figure V.2.3 Unfiltered and filtered (0.45 μm) DLS (left and middle) and TEM (right) characterization of the $\text{R}_0\text{-(SS}^-\text{Na}^+)_x\text{-SC(S)SPr}$ macroRAFT products for $x = 50$ (above) and 140 (below).

V.3 PSS $^-\text{Na}^+$ -*b*-PSt diblock macroRAFT

The chain extension of PSS $^-\text{Na}^+$ macroRAFT agents with a polystyrene block in water has previously been described,^[178]. A PSS $^-\text{Na}^+$ -*b*-PSt diblock copolymer was also indirectly obtained by extending a hydrophobic P(SS $^-\text{Oct}_3\text{NH}^+$) macroRAFT agent with styrene in benzene or chlorobenzene, followed by trioctylammonium/sodium exchange,^[179] as well as by chain extension of a PSS $^-\text{Na}^+$ -TEMPO macroinitiator with styrene by NMP.^[173] The chain extension of both $\text{R}_0\text{-(SS}^-\text{Na}^+)_x\text{-SC(S)SPr}$ ($x = 50$ and 140) macroRAFT agents with styrene proceeded without difficulty. This step entails PISA and proceeds up to essentially quantitative styrene conversion (see Figure V.3.1) and with good control (molar masses linearly growing with conversion, low D , see Table V.3.1) to afford translucent dispersions, indicating successful micellization, see Figure V.3.2.

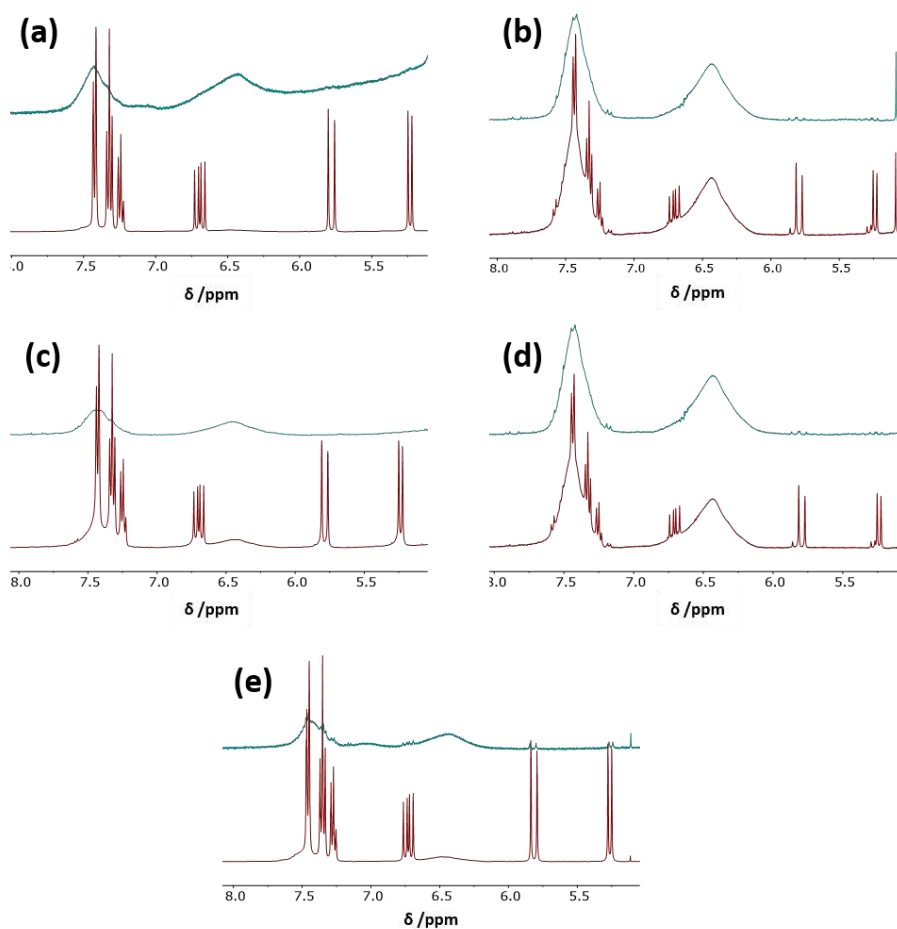


Figure V.3.1 ^1H NMR ($\text{DMSO-}d_6$) monitoring of the $\text{R}_0\text{-(SS}^-\text{Na}^+)_x\text{-SC(S)SPr}$ macroRAFT chain extension with styrene: (a) $x = 50$, $y = 300$; (b) $x = 140$, $y = 50$; (c) $x = 140$; $y = 300$; (d) $x = 140$; $y = 350$; (e) $x = 140$; $y = 380$. Bottom spectrum: t_0 ; above spectrum: final latex.

Table V.3.1 Conversion and polymer characterization during the chain extension of the $\text{R}_0\text{-(SS}^-\text{Na}^+)_{140}\text{-SC(S)SPr}$ macroRAFT agent with 150 equiv. styrene.

Time /min	Conv /%	$M_{n,\text{th}}/\text{g mol}^{-1}$	$M_n/\text{g mol}^{-1}$	\mathcal{D}
0	0.00	20090	20090	1.045
20	58.35	29210	23820	1.131
40	70.02	31035	24060	1.103
80	98.63	35505	26760	1.106
100	99.77	35684	27450	1.131

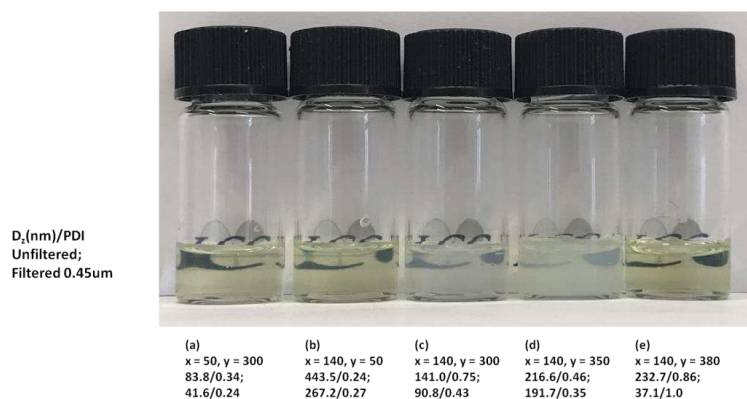


Figure V.3.2 The photos of $R_0\text{-(SS}^-\text{Na}^+)_x\text{-}b\text{-St}_y\text{-SC(S)SPr}$ translucent dispersions.

The DLS and TEM characterization of the resulting diblock macroRAFT latexes revealed interesting phenomena. Chain extension of the short ($x = 50$) PSS^-Na^+ chain with a long ($y = 300$) PS block yielded a relatively large number of particles narrowly distributed around $D_z \approx 40$ nm, but also larger aggregates (low in number but relevant in intensity) around $D_z \approx 200$ nm (Figure V.3.3a). Chain extension of the longer ($x = 140$) PSS^-Na^+ chain with a short ($y = 50$) PSt block yields morphologically unstable latexes. The DLS of the $R_0\text{-(SS}^-\text{Na}^+)_{140}\text{-}b\text{-St}_{50}\text{-SC(S)SPr}$ solution shows relatively homogeneous large aggregates ($D_z > 500$ nm) for the unfiltered solution, whereas after filtration single chains ($D_z \approx 1$ nm) become the dominant distribution in number, while the TEM characterization suggests that the large objects are vesicles (Figure V.3.3b). Extension of the same long PSS^-Na^+ chain with a longer PSt block ($y = 300, 350$ or 380), however, led to more stable and more narrowly distributed small micelles ($D_z \approx 20$ nm), although a small number of larger particles are also present (Figure V.3.3c-e). In conclusion, monomodal distributions of stable micelles were never observed and equilibria between aggregated and small micelles (and even single chains in one case) are always present. The degree of polymerization of the PSS^-Na^+ block ($x = 50$ or 140) does not seem to make a large difference, whereas the micelles appear to be better stabilized by a longer PSt block. These results are similar to those previously obtained for the polycationic $\text{P4VPM}^+\text{T}^-$ CCM particles. Given that the morphology can vary during the crosslinking step, both the shorter and longer PSS^-Na^+ diblock macroRAFT chains were investigated in the crosslinking step.

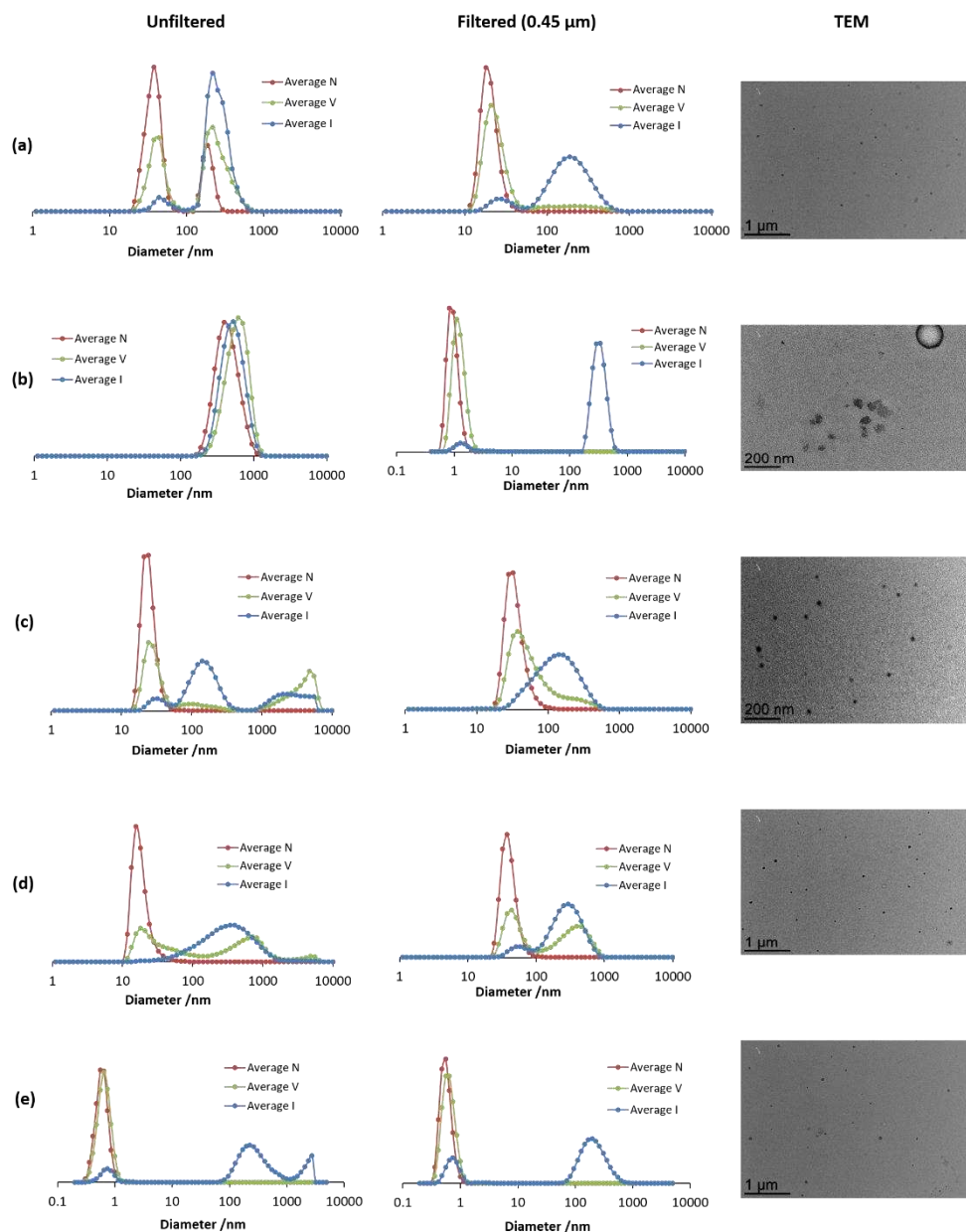


Figure V.3.3 Unfiltered and filtered (0.45 μm) DLS (left and middle) and TEM (right) characterization for the $\text{R}_0\text{-(SS}^-\text{Na}^+\text{)}_x\text{-}b\text{-St}_y\text{-SC(S)SPr}$ diblock macroRAFT agents: (a) $x = 50$, $y = 300$; (b) $x = 140$, $y = 50$; (c) $x = 140$, $y = 300$; (d) $x = 140$, $y = 350$; (e) $x = 140$, $y = 380$.

V.4 Crosslinking of the amphiphilic $\text{PSS}^- \text{Na}^+ \text{-} b \text{-PSt}$ copolymer with high molar mass PSt block

V.4.1 Crosslinking by DEGDMA in the presence of styrene

The initial crosslinking experiments were carried out with the DEGDMA crosslinker diluted in styrene (DEGDMA/styrene = 10/90), the same comonomer mixture previously used to obtain the cationic-shell CCM particles, for a total of 150 monomers per chain. Two diblock copolymer macroRAFT agents, $\text{R}_0\text{-(SS}^-\text{Na}^+)\text{-}b\text{-St}_y\text{-SC(S)SPr}$ ($x = 140$, $y = 300$ and 350), were crosslinked in these experiments. The monomer conversions were quantitative (Figure V.4.1). The obtained polymer particles have spherical morphology (Figure V.4.2) and relatively small size (main distribution in number with $D_z \approx 30$ and 70 nm for $y = 300$ and 350 , respectively, from the DLS), but are contaminated by a larger size distribution.

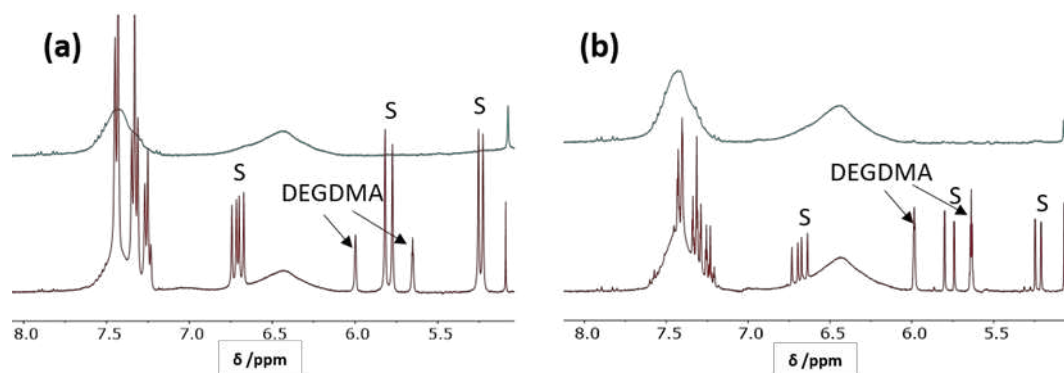


Figure V.4.1 ^1H NMR ($\text{DMSO-}d_6$) monitoring of the crosslinking of the diblock $\text{R}_0\text{-(SS}^-\text{Na}^+)\text{-}b\text{-St}_y\text{-SC(S)SPr}$ macroRAFT micelles: (a) $y = 300$; (b) $y = 350$ with a DEGDMA/styrene mixture (10/90). Brown spectrum: t_0 ; magenta spectrum: final latex.

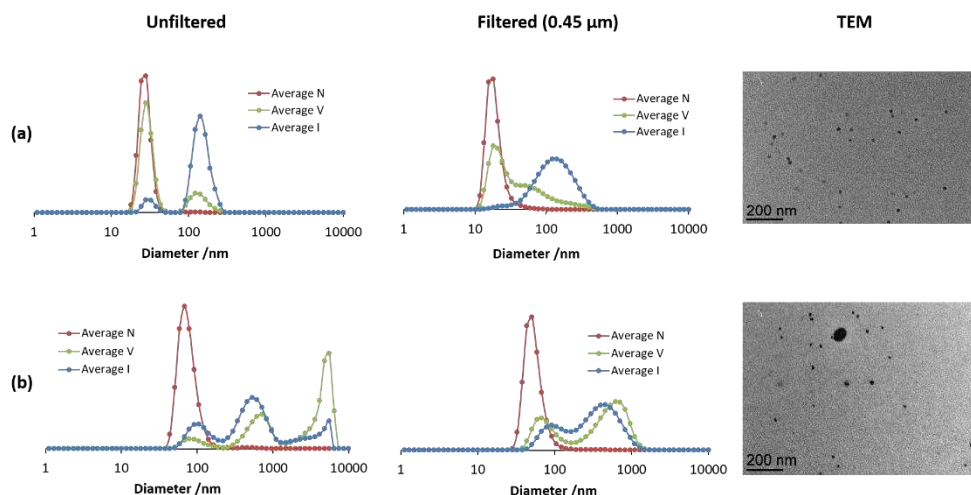


Figure V.4.2 Relevant DLS and TEM data for the $R_0\text{-(SS}^-\text{Na}^+)_{140}\text{-}b\text{-St}_y\text{-}b\text{-(St}_{0.9}\text{-}co\text{-DEGDMA}_{0.1})_{150}\text{-SC(S)SPr CCM: (a) } y = 300$ and (b) $y = 350$.

V.4.2 Crosslinking with pure DEGDMA

Arguing that the anionic-shell CCM particles should benefit from the same Coulombic shell-shell repulsion as the cationic-shell CCMs as mentioned above, the crosslinking step was then tested with neat DEGDMA. The shell-shell repulsion should block the particle interpenetration phenomenon that leads to macrogelation, as previously observed for the neutral-shell particles when using neat DEGDMA. Indeed, in all cases, the crosslinking of $R_0\text{-(SS}^-\text{Na}^+)_{x}\text{-}b\text{-St}_y\text{-SC(S)SPr$ with neat DEGDMA produced stable white latexes. Four CCM products were thus generated, $R_0\text{-(SS}^-\text{Na}^+)_{x}\text{-}b\text{-St}_y\text{-}b\text{-DEGDMA}_z\text{-SC(S)SPr$ with $(x, y, z) = 140, 300, 15$ (a), $140, 350, 15$ (b), $140, 380, 90$ (c), and $50, 300, 15$ (d). The monomer conversion was again quantitative in all cases, as shown by the NMR monitoring (Figure V.4.3). The ^1H NMR spectrum of the final latex after dilution in $\text{DMSO-}d_6$ revealed only the resonances of the PSS^-Na^+ shell (aromatic *ortho* and *meta* H resonances centered at δ 7.4 and 6.4 ppm and broad feature at δ 2-1 ppm for the aliphatic backbone atoms), because the polystyrene core is not sufficiently well-swollen by this solvent. However, the polystyrene core became visible after swelling the latex with CDCl_3 (Figure V.4.4). The overlapping (*o+p*) resonance of

the aromatic polystyrene protons are centered at δ ca. 7.0 ppm, whereas the *m* resonance, expected at δ ca. 6.5 ppm, overlaps with a PSS⁻Na⁺ shell resonance.

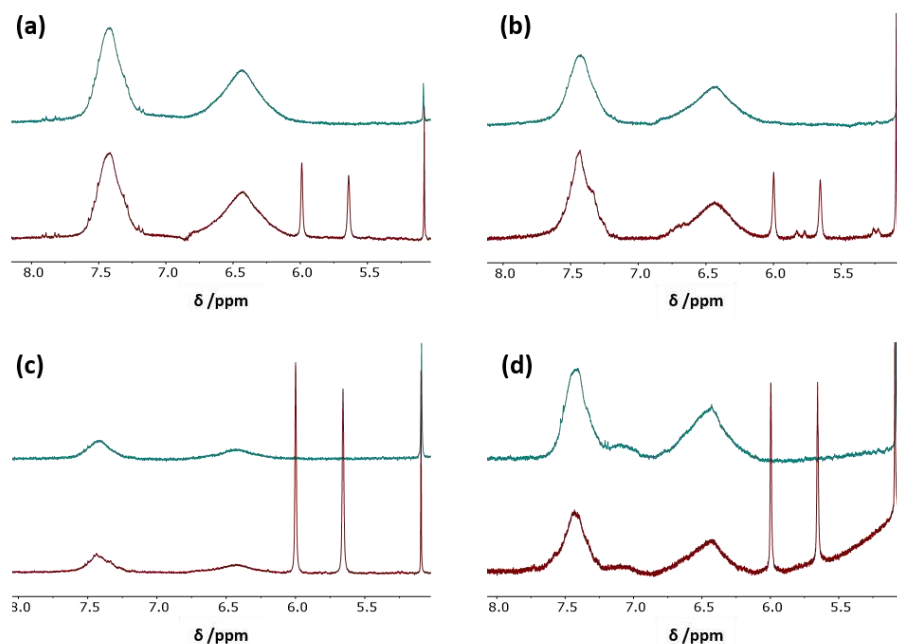


Figure V.4.3 ¹H NMR monitoring of the crosslinking of the diblock R₀-(SS⁻Na⁺)_x-*b*-St_y-SC(S)SPr macroRAFT micelles with neat DEGDMa to produce the R₀-(SS⁻Na⁺)_x-*b*-St_y-*b*-DEGDMA_z-SC(S)SPr CCM: (a) *x* = 140, *y* = 300, *z* = 15; (b) *x* = 140, *y* = 350, *z* = 15; (c) *x* = 140, *y* = 380, *z* = 90; (d) *x* = 50, *y* = 300, *z* = 15. Bottom spectrum: *t*₀; above spectrum: final latex.

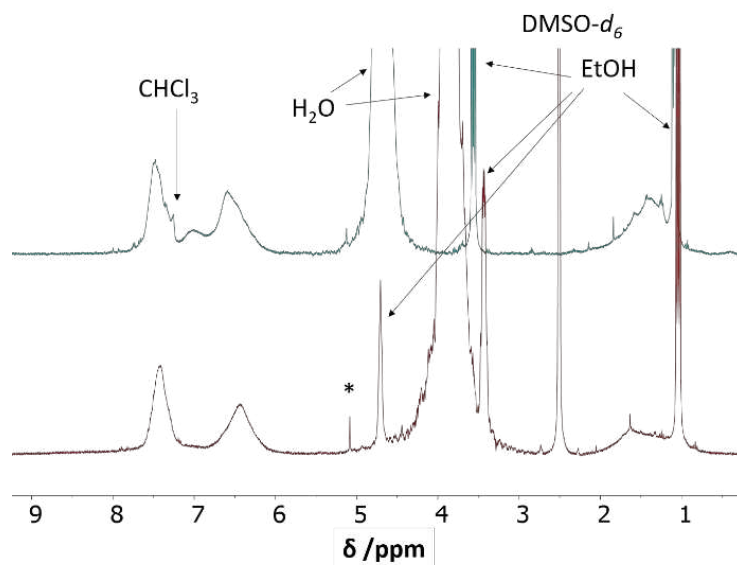


Figure V.4.4 ¹H spectrum of R₀-(SS⁻Na⁺)₁₄₀-*b*-St₃₀₀-*b*-DEGDMA₁₅-SC(S)SPr: (a) in DMSO-*d*₆ and (b) in D₂O/CDCl₃.

The TEM characterization of the obtained latexes confirms in all cases the presence of spherical particles of relatively small size (< 100 nm), see Figure V.4.5. The narrow distribution of the particle size is again confirmed by the DLS analysis. However, a population of larger aggregates ($D_z \approx 350$ nm), small in the number distribution but dominant in the intensity distribution, is again visible for the sample a with $y = 300$ (Figure V.4.5a). This second population is not observed in samples b (Figure V.4.5b) and c (Figure V.4.5c), for which the size distributions is quite narrow ($D_z = 106$ nm, PDI = 0.08 and $D_z = 105$ nm, PDI = 0.11 respectively). Crosslinking of the diblock macroRAFT arms with the shorter PSS⁻Na⁺ block (sample d) yielded again a minor larger size population ($D_z \approx 100$ nm, significant only in the intensity distribution), but the major population is rather narrowly distributed and with a smaller average diameter than the longer-block outer shell particles b and c ($D_z = 41$ nm and PDI = 0.23, Figure V.4.5d). Therefore, even though the R₀-(SS⁻Na⁺)₅₀-*b*-St₃₀₀-SC(S)SPr diblock macroRAFT agent has a rather heterogeneous (bimodal) size distribution for the self-assembled micelles (Figure V.3.3a), the crosslinker addition has the effect of breaking up the larger agglomerates during the crosslinking step. Additional information was sought from a DLS measurement of the R₀-(SS⁻Na⁺)₅₀-*b*-St₃₀₀-SC(S)SPr dispersion in the presence of 15 equiv. per chain of DEGDMA before the crosslinking step. This shows that the distribution is dominated by a population with very small diameter ($D_z \approx 0.6$ nm, see Figure V.4.6), consisting of single chains. Thus, the aqueous dispersion of the PSS⁻Na⁺-*b*-PSt diblock copolymers appears rather unstable, with facile equilibria that respond to minor perturbations (filtration for Figure V.3.3b; addition of DEGDMA for Figure V.4.6) between single chains, single spherical micelles, and larger agglomerates. In most cases, however, the CCMs with spherical morphology are the dominant product obtained from the crosslinking step. It is to be noted that a quite different amount of the DEGDMA crosslinker was used for samples b and c (15 and 90 equivalents per chain, respectively). However, this difference affected neither the crosslinking efficiency nor the particle average size.

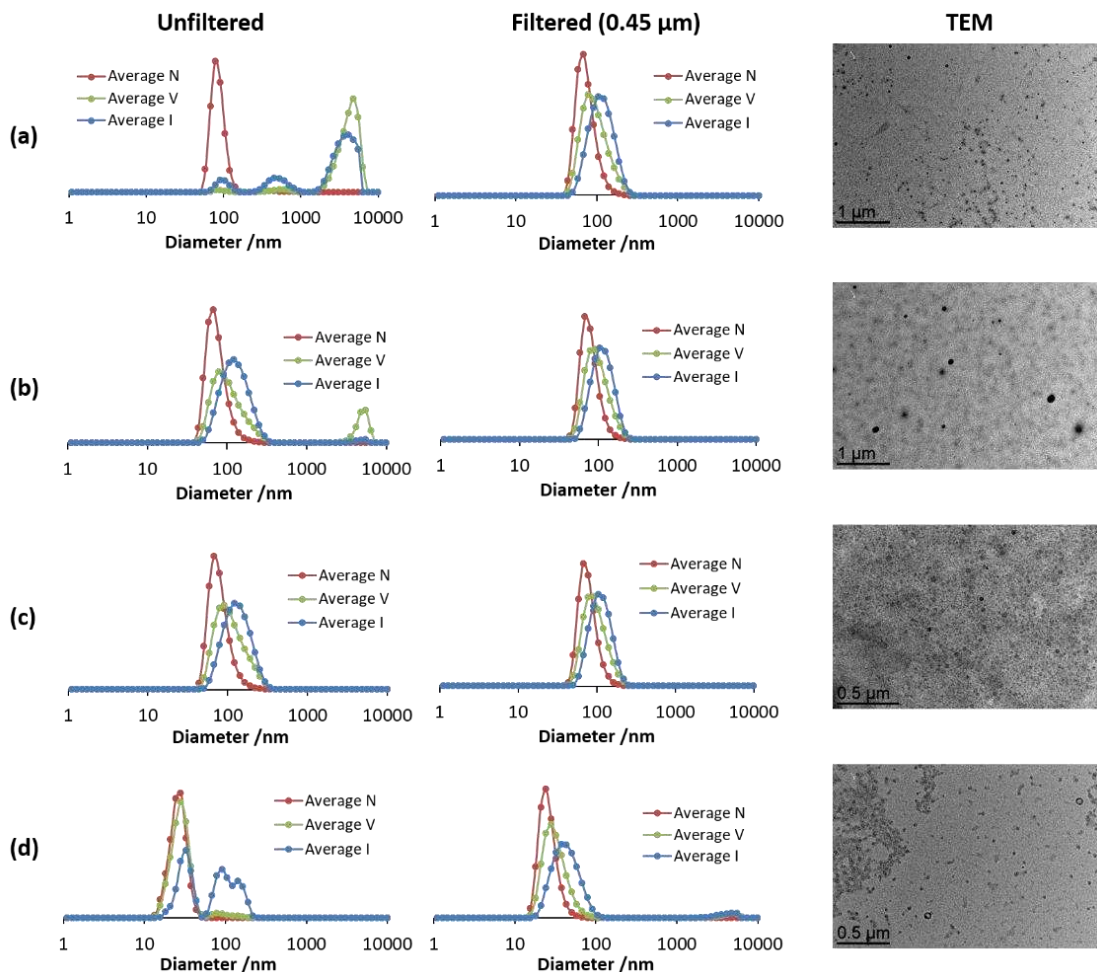


Figure V.4.5 Relevant DLS and TEM data for the $R_0-(SS^-Na^+)_x-b-St_y-b-DEGDMA_z-SC(S)SPr$ CCM: (a) $x = 140, y = 300, z = 15$; (b) $x = 140, y = 350, z = 15$; (c) $x = 140, y = 380, z = 90$; (d) $x = 50, y = 300, z = 15$.

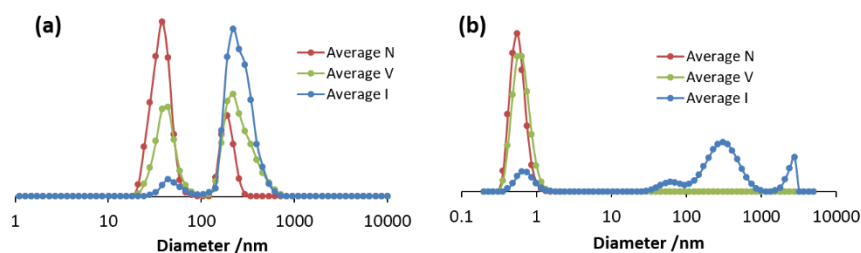


Figure V.4.6 Comparative DLS results of the $R_0-(SS^-Na^+)_{50}-b-St_{300}-SC(S)SPr$ latex without (a) and with (b) 15 equiv. per chain of DEGDMA, prior to crosslinking (unfiltered dispersions).

For a similar size of the hydrophobic PSt blocks, the particle size is similar to those of the neutral particles (*e.g.* $D_z = 79$ nm, PDI = 0.18 for $R_0-(MAA_{0.5}-co-PEOMA_{0.5})_{30}$ -

$b-(\text{St}_{0.9}\text{-}co\text{-DPPS}_{0.1})_{300}\text{-}b-(\text{St}_{0.9}\text{-}co\text{-DEGDMA}_{0.1})_{100}\text{-SC(S)SPr}^{[94]}$ and cationic ones (e.g. $D_z = 109.6$ nm, PDI = 0.04 for $R_0\text{-}(4\text{VPMe}^+\text{I})_{140}\text{-}b\text{-St}_{350}\text{-}b\text{-DEGDMA}_{15}\text{-SC(S)SPr}$). Core-swelling experiments were carried out on the two most homogeneous samples b and c, using toluene and chloroform, both of which are very good solvents for polystyrene, using DLS to assess the particle size increase. The results of these experiments (Figure V.4.7) show that chloroform has greater swelling capacity than toluene. These swelling abilities are again similar to those previously observed for the neutral and cationic-shell analogues.

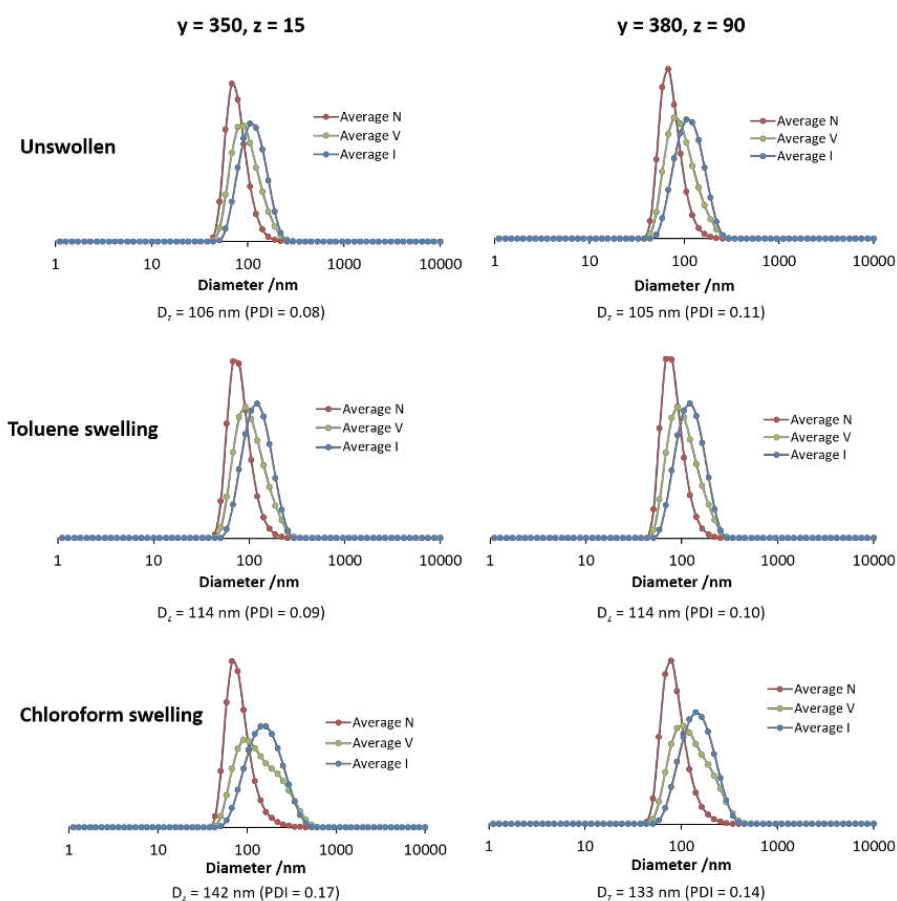


Figure V.4.7 DLS monitoring of the core-swelling by toluene and chloroform for selected $R_0\text{-}(\text{SS}^+\text{Na}^+)_{140}\text{-}b\text{-St}_y\text{-}b\text{-DEGDMA}_z\text{-SC(S)SPr}$ CCMs.

A determination of whether the CCM product contains residual non-crosslinked arms is not simple because any free arm would remain entrapped in the CCM particles by self-assembly and would thus remain undetected by DLS and TEM. In addition, free

arms and crosslinked polymers are indistinguishable by NMR spectroscopy. The separation of non-crosslinked free arms from the crosslinked particles is only possible by dispersion in a medium with good solvent properties for both core and shell. The presence of any free diblock chain can then be assessed by an investigation of size-dependent properties such as diffusion (DOSY NMR) or light scattering (DLS). In this work, the use of the DLS methodology was selected.

V.4.3 Completeness of the crosslinking step

The first task for determining whether the CCM product contains residual non-crosslinked arms was to find a suitable solvent or solvent combination. The hydrophilic PSS⁻Na⁺ block is well-solvated by water but not sufficiently well by neat THF and DMF, which are good solvents for the PSt block. Indeed, the R₀-(SS⁻Na⁺)_x-SC(S)SPr macroRAFT intermediates are insoluble in these solvents. The PSt block compatibility with THF and DMF was verified by a DLS study of a R₀-St₃₀₀-SC(S)SPr homopolymer, made by the ACPA-initiated RAFT polymerization of styrene in water (suspension polymerization) using CTPPA as transfer agent. The as-synthesized aqueous dispersion contains particles of large dimensions ($D_z \approx 350$ nm), but freeze-drying followed by dissolution in THF or DMF gave a narrow distribution of much lower dimensions ($D_z \approx 7.5$ or 6.5 nm) indicating the presence of single chains (see Figure V.4.8). Acetone gave aggregates of much larger dimensions ($D_z \approx 300$ nm) for the R₀-St₃₀₀-SC(S)SPr homopolymer, although in equilibrium with single chains. Therefore, a single solvent for both blocks is not available. The THF/H₂O and DMF/H₂O mixtures were considered and used to investigate the solvation of the diblock R₀-(SS⁻Na⁺)₁₄₀-*b*-St₃₀₀-SC(S)SPr macroRAFT intermediate.

The results of the DLS investigation for the R₀-(SS⁻Na⁺)₁₄₀-*b*-St₃₀₀-SC(S)SPr polymer, after freeze-drying and redispersion in THF/H₂O and DMF/H₂O mixtures of various compositions are summarized in Figure V.4.9. These measurements indicate that large agglomerates are present in the neat organic solvent and when the water

content is < 40%. However, mixtures containing 40% or more water, both with THF or DMF as cosolvent, yielded single chains as the largely dominating distribution. The size of the distribution is larger in THF/H₂O ($D_z \approx 3-10$ nm depending on the composition, the maximum corresponding to the 60/40 composition) than in DMF/H₂O ($D_z \approx 1.5-3$ nm). The best solvent combination to solvate the R₀-(SS⁻Na⁺)₁₄₀-*b*-St₃₀₀-SC(S)SPr single chains thus appears to be the THF/H₂O 60/40 mixture and this was selected for the subsequent investigations of the CCM latexes.

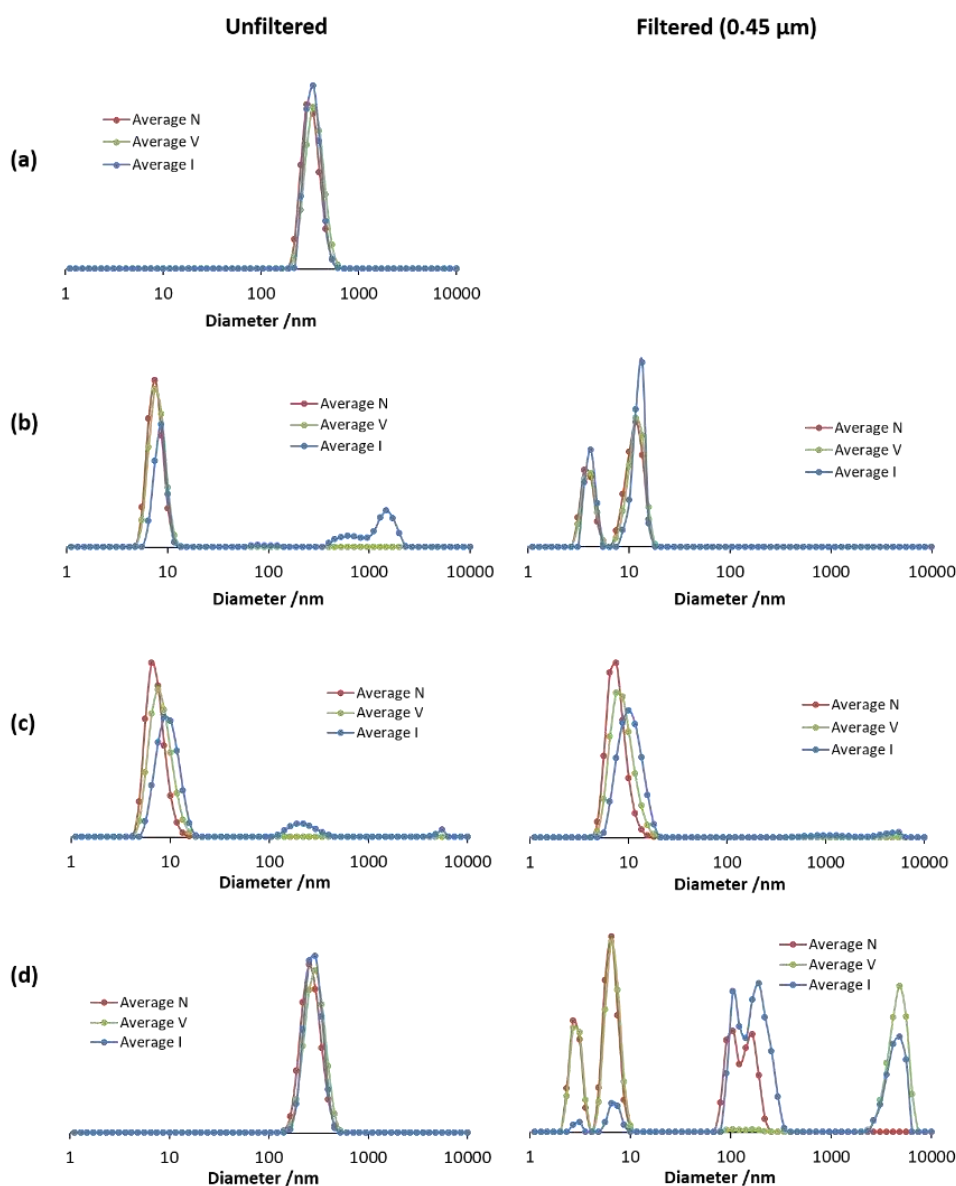


Figure V.4.8 DLS investigations of R₀-St₃₀₀-SC(S)SPr as (a) synthesized in water and after freeze-drying and redispersion (plus sonication for 15 min) in (b) THF; (c) DMF; (d) acetone.

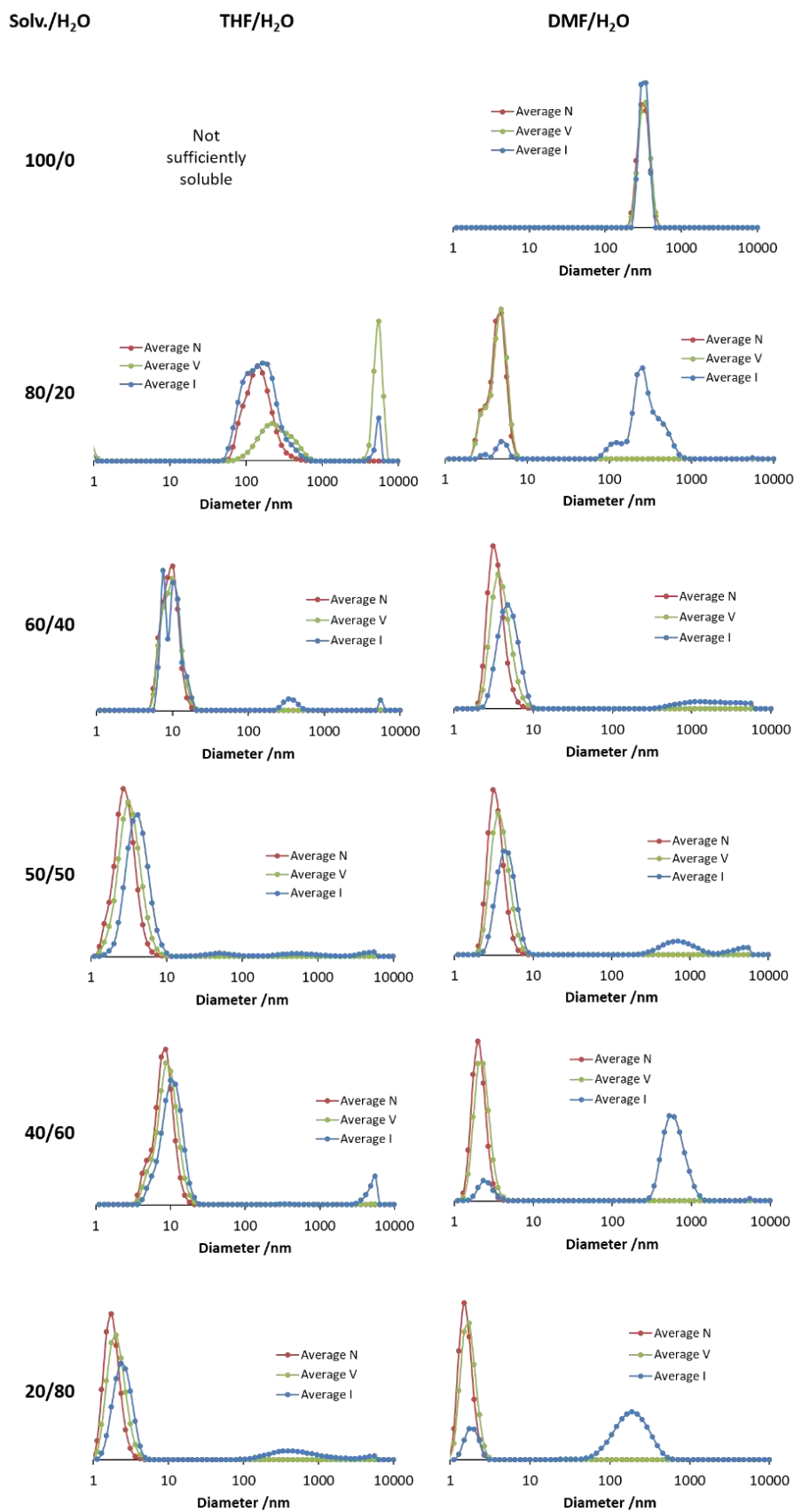


Figure V.4.9 DLS investigations of $R_0-(SS^-Na^+)_{140}-b-St_{300}-SC(S)SPr$ after freeze-drying and redispersion (plus sonication for 15 min) in THF/H₂O and DMF/H₂O mixtures of various compositions.

The investigations in THF/H₂O were carried out for the two better-controlled latexes with a neat DEGDMA core crosslinking, R₀-(SS⁻Na⁺)₁₄₀-*b*-St_y-*b*-DEGDMA_z-SC(S)SPr (y, z = 350, 15 and 380, 90), but also for one of the latexes with a mixed P(*St-co*-DEGDMA) nanogel core. All latexes were freeze-dried and redispersed both in pure water and in the THF/H₂O 60/40 mixture. The results (Figure V.4.10) clearly indicate the absence of detectable populations of single chains. The distributions in THF/H₂O also show the disappearance (or the significant decrease) of the larger-size agglomerates, confirming the nature of the CCM products as single particles with controlled size, which in turn confirms the controlled nature of the chain extension of the hydrosoluble macroRAFT intermediate and of the crosslinking steps.

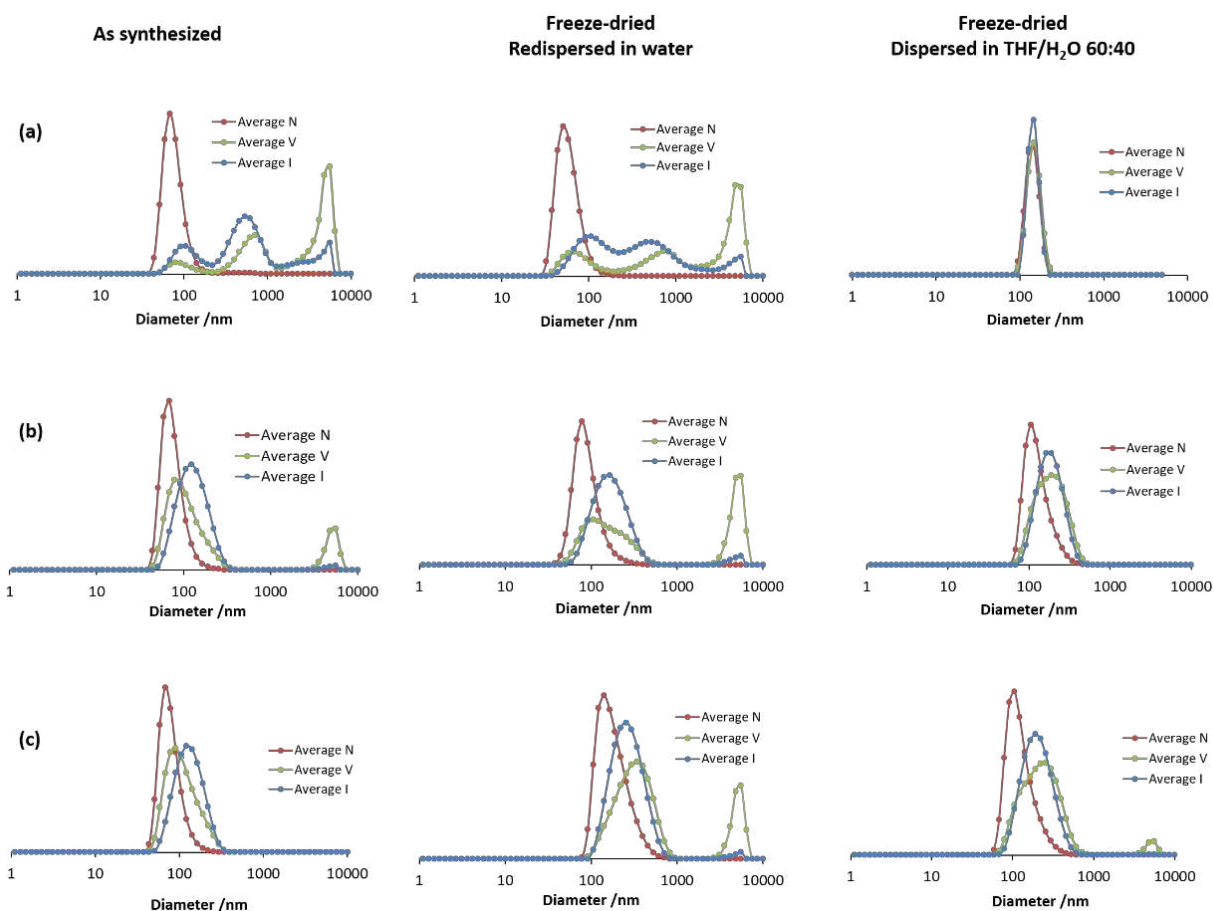


Figure V.4.10 Comparison of the DLS in water and THF/H₂O 60/40 for the R₀-(SS⁻Na⁺)_x-*b*-St_y-*b*-(St_w-*co*-DEGDMA_z)-SC(S)SPr CCMs polymers: (a) x = 140, y = 350, z = 15, w = 135; (b) x = 140, y = 350, z = 15, w = 0; (c) x = 140, y = 380, z = 90, w = 0. The dispersions of the freeze-dried samples were sonicated for 15 min prior to dilution and measurement. All samples were measured from unfiltered solutions.

V.5 Conclusion

Herein, a synthetic route for CCMs with a PSS⁻Na⁺ polyanionic outer shell and a non-functionalized PSt core based on RAFT polymerization via the PISA strategy has been proposed. It was discovered that in RAFT emulsion polymerization of styrene employing R₀-(SS⁻Na⁺)_x-SC(S)SPr, the negative charges on the macroRAFT agent do not perturb the chain extension and micellar self-organization process, contrary to that happens in the polymerization of styrene using the polycationic R₀-(4VPMe⁺I)_x-SC(S)SPr macroRAFT agent.

The latexes of diblock R₀-(SS⁻Na⁺)_x-*b*-St_y-SC(S)SPr ((a) x = 50, y = 300; (b) x = 140, y = 50; (c) x = 140, y = 300; (d) x = 140, y = 350; (e) x = 140, y = 380) showed similar size distributions and indicated the presence of equilibria between small micelles (D_z < 50 nm) and large aggregates (D_z > 200 nm), which depend on the hydrophilic/hydrophobic ratio. The crosslinking was achieved in a subsequent step by either a mixture of styrene and DEGDMA or neat DEGDMA. Thanks to the Coulombic shell-shell repulsion from negatively charged PSS⁻Na⁺ chains, the CCMs crosslinked by DEGDMA alone do not suffer from interparticle penetration or macrogelation. Furthermore, the DEGDMA stoichiometry (number of equivalents per chain) has an insignificant influence on the particle micellization or size range (as proven by DLS and TEM). The solid content of polymer in the final latex was up to 16 wt%. The development of equivalent phosphine-functionalized particles and their complexation with [RhCl(COD)]₂ is a perspective for the continuation of this research.

Chapter VI

Experimental section

VI.1 Materials and characterization

VI.1.1 Materials

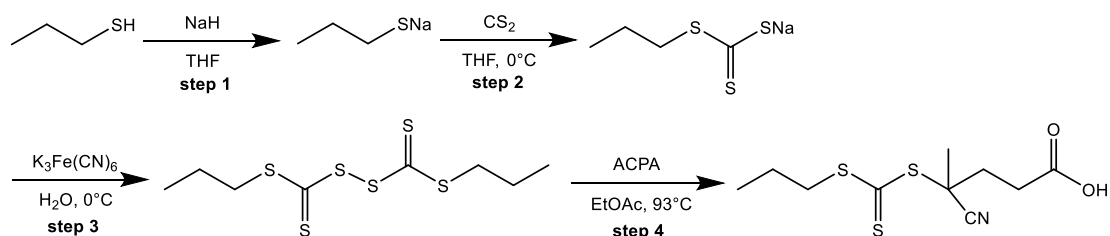
Reagents	Purity	Brand
diethyl ether	RE	Carlo Erba Reagents
anhydrous ethanol	RPE	Carlo Erba Reagents
tetrahydrofuran (THF)	RPE	Carlo Erba Reagents
Acetonitrile (CH ₃ CN)	HPLC	Carlo Erba Reagents
toluene	RPE	Alfa Aesar
N, N-dimethylformamide (DMF)	>99.9% ≥99.5% (HPLC)	Sigma-Aldrich Fisher Scientific
4-vinyl pyridine (4VP)	95%	Sigma-Aldrich
styrene (St)	99%	ACROS Organics
diethylene glycol dimethacrylate (DEGDMA)	95%	Sigma-Aldrich
4-(diphenylphosphino) styrene (DPPS)	97%	Sigma-Aldrich
sodium 4-vinylbenzenesulfonate (SS ⁻ Na ⁺)	>90%	Sigma-Aldrich
methacrylic acid (MAA)	99%	Sigma-Aldrich
poly(ethylene oxide) dimethyl ether (PEOMA)	M _n = 950 g·mol ⁻¹	Sigma-Aldrich
triphenylphosphine (PPh ₃ or TPP)	98.5%	Fluka
4,4'-azobis(4-cyanopentanoic acid) (ACPA)	>98%	Fluka
sodium hydrogen carbonate (NaHCO ₃)	>99%	Alfa Aesar
1,3,5-Trioxane	>99%	Sigma-Aldrich
iodomethane (MeI)	>98%	Sigma-Aldrich

chloro(1,5-cyclooctadiene) rhodium(I) dimer ([RhCl(COD)] ₂)	min. 40.8% Rh	ACROS Organics
triethylamine (NEt ₃)	99%	ACROS Organics
acetophenone	99%	Sigma-Aldrich
1-octene	99%	ACROS Organics
<i>n</i> -Decane	99%	Alfa Aesar
<i>n</i> -Dodecane	99%	Sigma-Aldrich
1-nonanol	99%	TCI Chemicals
hydrogen peroxide (H ₂ O ₂)	50% wt in water	Sigma-Aldrich
phosphoric acid (H ₃ PO ₄)	85% wt in water	Sigma-Aldrich
hydrochloric acid (HCl)	37% wt in water	VWR Chemicals
anhydrous magnesium sulfate (MgSO ₄)	99.6%	VWR Chemicals
lithium bromide (LiBr)	>99%	ACROS Organics
sodium nitrate (NaNO ₃)	>98%	Alfa Aesar
potassium chloride (KCl)	>99%	Sigma-Aldrich
deuterated dimethyl sulfoxide (DMSO- <i>d</i> ₆)	99.8% D	Eurisotop
deuterium oxide (D ₂ O)	99,9% D	Eurisotop
deuteriochloroform (CDCl ₃)	99.8% D	Eurisotop

Purifications: diethyl ether and toluene were dried by Innovative Technology machine and purged by argon prior to use. 4VP and styrene were distilled under reduced pressure prior to use. Anhydrous MgSO₄, LiBr and KCl were dried in the oven (T = 130 °C) for at least 24 h before use. All other purchased chemicals were used as received.

A stock solution of water ACPA/NaHCO₃ was prepared with 5 ml of H₂O and dissolution of ACPA/NaHCO₃ (0.10 g / 0.10 g), [ACPA] = 71.4 mmol l⁻¹. 1-methyl-4-vinylpyridinium iodide (0.35 g, 1.43 mmol).

Compounds RAFT agent 4-cyano-4-thiothiopropyl-sulfanyl pentanoic acid (CTPPA) R_0 -SC(S)SPr was prepared according to the published procedures (Scheme VI.1.1).^[180]



Scheme VI.1.1 Synthesis route of CTPPA RAFT agent.

The polymers with a neutral-shell were prepared as described in the previous publications in our team.^[94] The copolymer R_0 -(MAA_{0.5}-*co*-PEOMA_{0.5})₃₀-*b*-(St_{0.9}-*co*-DPPS_{0.1})₃₀₀-*b*-(St_{0.9}-*co*-DEGDMA_{0.1})₁₀₀-SC(S)SPr was characterized by DLS and TEM shown in Figure VI.1.1. This representative polymer was used as nanoreactor for nanoparticle catalysis.

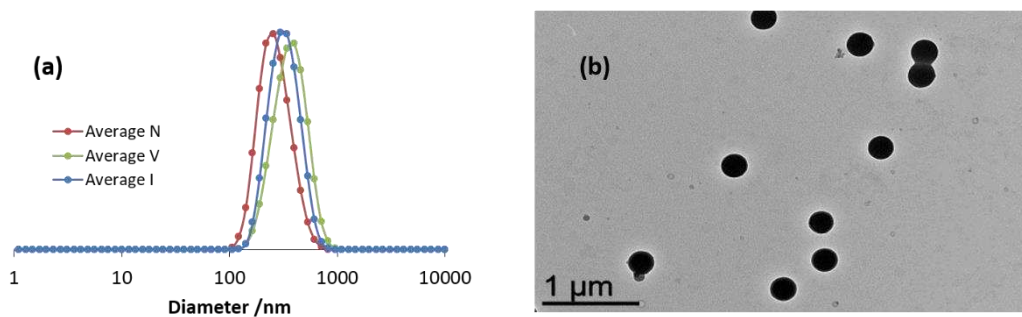


Figure VI.1.1 (a) DLS (unfiltered sample) and (b) TEM characterizations for the R_0 -(MAA_{0.5}-*co*-PEOMA_{0.5})₃₀-*b*-(St_{0.9}-*co*-DPPS_{0.1})₃₀₀-*b*-(St_{0.9}-*co*-DEGDMA_{0.1})₁₀₀-SC(S)SPr latex.

VI.1.2 Characterization techniques

Nuclear magnetic resonance (NMR)

All nuclear magnetic resonance spectra were recorded in 5 mm diameter tubes at 297 K on a Bruker Avance 300 and 400 spectrometers. The ^1H chemical shifts were determined using the residual resonance of the deuterated solvent as internal standard ($\delta = 2.50$ ppm for DMSO- d_6 , 4.79 ppm for D $_2$ O, 7.26 ppm for CDCl $_3$) and are reported in ppm (δ) relative to tetramethylsilane. Peaks are labelled as singlet (s), doublet (d), triplet (t), quadruplet (q), multiplet (m), double doublet (dd) and broad (br). The ^{31}P chemical shifts are reported relative to 85% H $_3$ PO $_4$, which was used as external reference for calibration. To monitor the monomer conversion in the polymerization reactions, 1,3,5-Trioxane (δ 5.20 ppm in DMSO- d_6) was used as an integration reference.

Size exclusion chromatography (SEC)

All polymers were analyzed at a concentration of 3 mg·ml $^{-1}$ after filtration through a 0.22 μm pore size polytetrafluoroethylene (PTFE) membrane. For the synthesis of the P4VP macroRAFT agent (R $_0$ -4VP $_x$ -SC(S)SPr), SEC was performed in DMF (with LiBr) at 60 °C at a flow rate of 1.0 ml·min $^{-1}$ by using a Viscotek TDA305 apparatus (SEC-DMF). The separation was carried out on three columns from PSS GRAM (7 μ , 300 \times 7.5 mm). The setup was equipped with a refractive-index (RI) detector ($\lambda = 670$ nm). The average molar masses (number-average molar mass M_n and weight-average molar mass M_w) and the dispersity ($D = M_w / M_n$) were derived from the RI signal by a calibration curve based on polystyrene standards (PS from Polymer Laboratories). The software used for data collection and calculation was OmniSec version 4.7 from Malvern Instruments.

For the synthesis of the PSS $^-$ Na $^+$ macroRAFT agent, R $_0$ -(SS $^-$ Na $^+$) $_x$ -SC(S)SPr, SEC was performed in water/acetonitrile (80/20, v/v) with 0.1 M NaNO $_3$. The SEC was

coupled with a multi-angle light scattering (MALLS) detector (18 angles) from MALLS Wyatt Dawn Heleos for the dn/dc value (0.199 ml g^{-1}) of PSS^-Na^+ in the eluent. All polymers were analyzed at a concentration of $5 \text{ mg}\cdot\text{ml}^{-1}$ after filtration through $0.45 \mu\text{m}$ pore size membrane. The separation was carried out on two columns from Agilent Aquagel OH Mixed M.

The dn/dc values were determined using a differential refractometer (Waters Associates) associated to a light-scattering diffusion mini Dawn apparatus from Wyatt Technology Corporation. The dn/dc increment values were determined by the iterative method software.

Dynamic light scattering (DLS)

The intensity-weighted harmonic mean particle diameter (Z -Average, D_z) and the polydispersity index (PDI) were obtained on a Malvern Zetasizer NanoZS equipped with a He-Ne laser ($\lambda = 633 \text{ nm}$), operating at $25 \text{ }^\circ\text{C}$. Samples were analyzed after dilution (with deionized water or other solvents mixture) either unfiltered or after filtration through a $0.45 \mu\text{m}$ pore-size PTFE membrane. The procedure without filtration allowed verification of the presence of agglomerates. In a standard DLS measurement, each sample was measured for five times though not all runs were always used for the final calculation of the size and size distribution. Occasionally, one or more runs were removed (*e.g.* runs with larger intensity fluctuation due to dust particles). All samples were measured at a scattering angle of 173° (backscatter) using the “general purpose” analysis model and the default size analysis parameters as well as a refractive index of 1.35 for the micelle matrix as sample parameter.

For the polymer samples that displayed monomodal size distributions, the results of the cumulant fits, namely the D_z and PDI, were used to compare sizes and size distributions of the different samples. For polymer samples displayed multi-distributions, the Average N, Average V and Average I and corresponding PDI values were also presented.

Transmission electron microscopy (TEM)

The morphological analyses of the copolymer nano-objects were performed at the Centre de Microcaractérisation Raimond Castaing (Toulouse, France) with a JEOL JEM 1400 transmission electron microscope working at 120 kV. Diluted latex samples were dropped on a formvar/carbon-coated copper grid and dried under vacuum at 10^{-4} mbar for 24 h. The diameter distributions of the polymer particles and nanoparticles were obtained with the help of the ImageJ software, using images with 100-300 particles.

Gas chromatography (GC)

The GC analyses of residual substrate and products in the organic layer after catalysis were conducted with a Shimadzu GC 2014 chromatograph equipped with a SLB 5ms capillary column (30 m \times 0.32 mm; 0.23 μ m film thickness) for the styrene hydrogenation experiments and with a Hewlett Packard 4890A chromatograph equipped with a SPB 20 capillary column (30 m \times 0.32 mm; 0.25 μ m film thickness) for the acetophenone hydrogenation experiments. The 0.1 ml organic solution was diluted in 0.2 ml distilled toluene for GC analysis. Both GC instruments were coupled to a flame ionization detector (FID) and used helium as carrier gas.

High-resolution inductive couple plasma-mass spectrometry (ICP-MS)

The rhodium catalyst leaching in the organic phase was quantified by high-resolution ICP/MS with a XR Thermo Scientific Element. For the sample preparation, the recovered organic phase was diluted into water using a 10^4 volumetric dilution factor, high enough to ensure complete dissolution. In practice, a 100 ml volumetric flask was filled at 2/3 with Milli-Q water, then 10 μ l of the organic product phase was introduced using a precision pipette. The borders were rinsed and the flask was

introduced into an ultrasound bath for 15 min. The dilution was then completed with Milli-Q water to the 100 ml mark, followed by further sonication for 45 min. Standards were prepared using $[\text{RhCl}(\text{COD})]_2$ and triphenylphosphine dissolved in toluene, attaining Rh concentrations in aqueous solution in the 1-100 ppt range. The relative standard deviation on the measurements used for the calibration was 3%.

VI.2 Synthesis and characterization of core-shell amphiphilic nanoreactors with a polycationic shell

VI.2.1 Preliminary optimization studies on phosphine-free copolymers with a cationic P4VPMe⁺I⁻ shell

Attempted polymerization of 1-methyl 4-vinylpyridinium iodide (4VPMe⁺I⁻)

The CTPPA RAFT agent (7.8 mg, 28.2 μmol) and a degassed ACPA/ NaHCO_3 stock solution (0.9 ml, 18 mg ACPA, 64.2 μmol) were dissolved in a mixture of dioxane (2 ml) and water (3 ml) in a Schlenk tube under Ar. The mixture was cooled to 0 °C and degassed with Ar for 40 min. Heating the mixture at 80 °C for 19 h did not lead to any polymerization (absence of monomer conversion evidenced by the NMR analysis).

RAFT polymerization of 4-vinylpyridine

A portion of an ACPA stock solution (0.4 g, 4.2 mg ACPA, 0.015 mmol), CTPPA (44.2 mg, 0.16 mmol), 4VP (998 mg, 9.49 mmol; 4VP/CTPPA = 59.3), ethanol (1 ml) and deionized water (1.67 ml) were added to a 50 ml flask with a magnetic stirrer bar.

1,3,5-Trioxane (19.0 mg, 0.211 mmol) was also added to the flask as an internal reference for the determination of the monomer conversion as a function of time by ^1H NMR. The solution in the septum-sealed flask was purged for 45 min with argon and then heated to 70 °C during 330 min in a thermostated oil bath under stirring, leading to a 93% monomer conversion (56 4VP units per chain). Theoretical molar mass for the resulting $\text{R}_0\text{-4VP}_{56}\text{-SC(S)SPr} = 6165 \text{ g mol}^{-1}$. SEC (THF): $M_n = 5800 \text{ g mol}^{-1}$, $D = 1.09$.

Attempted chain extension starting from $\text{R}_0\text{-P4VPMe}^+\text{I-SC(S)SPr}$

1. Preparation of the $\text{R}_0\text{-(4VPMe}^+\text{I)}_{56}\text{-SC(S)SPr}$ macroRAFT agent.

The macroRAFT agent prepared as described above (0.58 g, 0.1 mmol or 5.6 mmol of 4VP units) was dissolved in 10 ml of DMF. Then CH_3I (7.48 g, 52.68 mmol; $\text{CH}_3\text{I}/4\text{VP} = ca. 10$) was added at room temperature and the resulting solution was stirred overnight. A yellow precipitate was recovered and purified by dialysis against pure water, then dried by freeze-drying. Theoretical molar mass for $\text{R}_0\text{-(4VPMe}^+\text{I)}_{56}\text{-SC(S)SPr} = 14114 \text{ g mol}^{-1}$. ^1H NMR in $\text{DMSO-}d_6$: δ 8.77 (br) *ca.* 8 (br) for the aromatic protons and 4.2 for the methyl protons.

2. RAFT polymerization of styrene in the presence of $\text{R}_0\text{-(4VPMe}^+\text{I)}_{56}\text{-SC(S)SPr}$.

The $\text{R}_0\text{-(4VPMe}^+\text{I)}_{56}\text{-SC(S)SPr}$ macroRAFT agent from the previous step (0.14 g, 0.01 mmol), styrene (0.31 g, 2.98 mmol), 0.06 g of the ACPA solution (10 mg g^{-1} , 0.6 mg ACPA, 0.002 mmol) and 1.41 g of a $\text{H}_2\text{O}/\text{EtOH}$ (70/30, v/v) mixture (~ 1.5 ml) were added to a 10 ml flask. The mixture was purged with argon at 0 °C for 40 min then heated to 80 °C overnight. The polymerization was quenched by immersion of the flask in iced water. The overall styrene conversion (determined by gravimetric analysis) was < 5%.

Synthesis of a R₀-4VP₅₆-*b*-St₂₄₇-SC(S)SPr diblock copolymer in a one-pot two-step process

A P4VP macroRAFT agent was first synthesized as described above ($M_n = 5800$ g mol⁻¹, $D = 1.09$). In a separate flask, styrene (4.959 g, 48 mmol) was dispersed in 14.3 g of deionized water and 4.91 g of EtOH, to which was also added the ACPA stock solution (0.4 g containing 4 mg of ACPA, 0.014 mmol). The resulting mixture was purged for 45 min with argon at 0 °C and then injected into the flask containing the macroRAFT agent (16.62 mg, 0.16 mmol) under argon at 80 °C. After 3 h, a 0.5 ml aliquot was withdrawn for analysis and the polymerization was quenched by immersion of the flask in iced water. The overall styrene conversion (82%) was determined by gravimetric analysis. The composition of the resulting R₀-4VP₅₆-*b*-St₂₄₇-SC(S)SPr product was verified by NMR, SEC and TEM analyses.

Synthesis of the R₀-(4VPMe⁺I⁻)₁₃₇-*b*-St₃₄₄-SC(S)SPr diblock copolymer

1. Synthesis of the R₀-4VP₁₃₇-SC(S)SPr macroRAFT agent.

This macroRAFT agent was synthesized as described above, using an ACPA/NaHCO₃ stock solution (1.0 ml, 20 mg ACPA, 71.4 μmol), CTPPA (0.11 g, 0.39 mmol), 1,3,5-Trioxane (0.49 g, 5.44 mmol) and degassed 4VP (5.89 ml, 5.74 g, 54.6 mmol; 4VP/CTPPA = 140), in 15 ml of a degassed H₂O/EtOH mixture (70/30, v/v) (total volume = 21.9 ml). The reaction took 7 h at 80 °C to reach a 98% 4VP conversion. Aliquots were withdrawn periodically for monitoring by ¹H NMR in DMSO-*d*₆. This yields a polymer with average composition R₀-4VP₁₃₇-SC(S)SPr (theoretical molar mass = 14681 g mol⁻¹).

*2. MacroRAFT chain extension with styrene. Preparation of R₀-4VP₁₃₇-*b*-St₃₄₄-SC(S)SPr:*

To the solution of R₀-4VP₁₃₇-SC(S)SPr obtained in the previous step were

successively added degassed styrene (15.7 ml, 14.2 g, 136.5 mmol; St/macroRAFT = 350), the degassed ACPA/NaHCO₃ stock solution (7.0 ml, 140 mg ACPA, 499.5 μmol) and 47 ml of a degassed H₂O/EtOH mixture (70/30, v/v). The resulting reaction mixture (total volume = 92.1 ml) was stirred at 80 °C for 3 h. Aliquots were withdrawn periodically for monitoring by ¹H NMR in DMSO-*d*₆. Styrene consumption was almost complete (98.4%) and was accompanied by transformation of the initial suspension into a stable latex as a white opalescent stable dispersion. Theoretical molar mass for R₀-4VP₁₃₇-*b*-St₃₄₄-SC(S)SPr = 50526 g mol⁻¹.

3. *Methylation of the poly(4-vinylpyridine) block. Preparation of R₀-(4VPMe⁺I)₁₃₇-*b*-St₃₄₄-SC(S)SPr.*

In a 250 ml round-bottom flask, the total volume of the R₀-4VP₁₃₇-*b*-St₃₄₄-SC(S)SPr latex obtained above (0.39 mmol of polymer, corresponding to 53.4 mmol of 4VP units) was diluted with DMF (90 ml) and CH₃I (33.2 ml, 75.8 g, 534 mmol, *ca.* 10 equiv. *vs.* 4VP) was slowly added via syringe. The reaction mixture was then stirred at room temperature for 86.5 h, yielding a yellowish suspension. Vacuum filtration left the product as a yellow paste, which was further washed with distilled water (5 × 20 ml) and then extensively dried under vacuum, to afford 33.3 g of a yellow gummy solid, [R₀-(4VPMe⁺I)₁₃₇-*b*-St₃₄₄-SC(S)SPr]·24(DMF) (theoretical molar mass = 71726 g mol⁻¹). The amount of residual DMF was determined by ¹H NMR in DMSO-*d*₆. The sticky nature of the polymer rendered the washing, mother liquor decanting and drying processes rather problematic.

Preparation of a latex of a P4VPMe⁺I-*b*-PSt amphiphilic block copolymer in four steps

Step 1: Preparation of R₀-4VP₁₃₇-SC(S)SPr.

This polymer was prepared as described above, from 0.39 mmol of CTPPA in a total volume of 21.9 ml (70/30, v/v H₂O/EtOH mixture), yielding a polymer with theoretical molar mass = 14681 g mol⁻¹.

Step 2. MacroRAFT chain extension with styrene. Preparation of R₀-4VP₁₃₇-b-St₄₈-SC(S)SPr:

To the solution of R₀-4VP₁₃₇-SC(S)SPr obtained in the previous step were successively added degassed styrene (2.24 ml, 2.03 g, 19.5 mmol; St/macroRAFT = 50) and the degassed ACPA/NaHCO₃ stock solution (1.0 ml, 20 mg ACPA, 71.4 μmol). The resulting reaction mixture (total volume = 25.1 ml) was stirred at 80 °C for 4.5 h. Aliquots were withdrawn periodically for monitoring by ¹H NMR in DMSO-*d*₆. Styrene consumption was almost complete (98%) and was accompanied by transformation of the initial suspension into a stable latex of R₀-4VP₁₃₇-b-St₄₈-SC(S)SPr macromolecules, self-assembled in the form of micelles to yield a white opalescent stable dispersion (DLS: D_z = 24.4 nm and PDI = 0.14). At this stage, the NMR spectrum in DMSO-*d*₆ allowed to determine the styrene conversion (97.5%), while the use of CDCl₃ (CDCl₃/D₂O emulsion) allowed verifying the molar 4VP/St ratio per chain (*ca.* 3/1), which approximates the theoretical value (137/48). Theoretical molar mass calculated for R₀-4VP₁₃₇-b-St₄₈-SC(S)SPr = 19683 g mol⁻¹. The theoretical total polymer mass obtained was 7.68 g in a total volume of 25.1 ml (32.9 wt% solid content).

Step 3. Methylation of the poly(4-vinylpyridine) block. Preparation of R₀-(4VPMe⁺I⁻)₁₃₇-b-St₄₈-SC(S)SPr:

In a 250 ml round-bottom flask, the total volume of the R₀-4VP₁₃₇-b-St₄₈-SC(S)SPr latex obtained in step 2 (0.39 mmol of polymer, corresponding to 53.4 mmol of 4VP units) were diluted with DMF (84 ml) and CH₃I (33.2 ml, 75.8 g, 534 mmol, *ca.* 10 equiv. *vs.* 4VP) was slowly added via syringe. The reaction mixture was then stirred at room temperature for 117 h, resulting in the formation of yellow precipitate that could be isolated from a yellowish solution by centrifugation. The yellow solid was further washed with DMF (5 × 6.0 ml), followed by diethyl ether (2 × 5.0 ml), and dried under vacuum to afford 8.15 g of a yellow powder, [R₀-(4VPMe⁺I⁻)₁₃₇-b-St₄₈-SC(S)SPr]·38(DMF) (formula determined by ¹H NMR in DMSO-*d*₆, theoretical molar mass = 41906 g mol⁻¹, 49.9% yield). All attempts to remove the residual 38 molecules of DMF per polymer chain were unsuccessful.

Step 4. Extension with a polystyrene block. Preparation of R₀-(4VPMe⁺I⁻)₁₃₇-b-

St₃₄₅-SC(S)SPr

A portion of the [R₀-(4VPMe⁺I)₁₃₇-*b*-St₄₈-SC(S)SPr]·38(DMF) polymer resulting from step 3 (0.3 g, 7.16 μmol) was dispersed in 6 ml of degassed water under Ar in a Schlenk tube to afford a pale yellow turbid suspension (DLS: D_z = 276 nm and PDI = 0.25). To this solution was added 1,3,5-Trioxane (2.8 mg, 31.1 μmol) and degassed styrene (0.25 ml, 0.224 g, 2.15 mmol; 300 equiv. per chain). Then the degassed ACPA/NaHCO₃ stock solution (0.25 ml, 4.9 mg ACPA, 17.5 μmol) was added and the resulting reaction mixture was stirred at 80 °C for 5 h, yielding a white opalescent stable dispersion. Styrene conversion = 99% (by ¹H NMR in DMSO-*d*₆). The resulting polymer, R₀-(4VPMe⁺I)₁₃₇-*b*-St₃₄₅-SC(S)SPr, has a theoretical molar mass of 70076 g mol⁻¹. DLS: D_z = 139.1 nm and PDI = 0.11.

Crosslinking of the P4VPMe⁺I-*b*-PSt amphiphilic block copolymer by DEGDMA

(a) *In the presence of styrene. Preparation of R₀-(4VPMe⁺I)₁₃₇-*b*-St₃₄₅-*b*-(St₁₅₇-*co*-DEGDMA₁₃)-SC(S)SPr.*

To the Schlenk tube containing the entire aqueous suspension of the R₀-(4VPMe⁺I)₁₃₇-*b*-St₃₄₅-SC(S)SPr polymer, prepared as described in the previous section starting from a R₀-(4VPMe⁺I)₁₃₇-*b*-St₄₈-SC(S)SPr (11.8 μmol) were successively added degassed styrene (0.193 g, 1.85 mmol; 157 equiv. per chain), DEGDMA (37 mg, 0.15 mmol; 13 equiv. per chain), and the degassed ACPA/NaHCO₃ stock solution (0.5 ml, 10 mg ACPA, 35.7 μmol). The resulting reaction mixture was stirred at 80 °C for 2.5 h. After NMR monitoring (DMSO-*d*₆), a second (0.1 ml, + 3.5 h at 80 °C) and a third batch of the ACPA/NaHCO₃ stock solution (0.1 ml, overnight at 80 °C) were added to reach complete conversion of the monomers. The final polymer, [R₀-(4VPMe⁺I)₁₃₇-*b*-St₃₄₅-*b*-(St₁₅₇-*co*-DEGDMA₁₃)-SC(S)SPr]·38(DMF) (1.09 g, 12.2 μmol) has a theoretical molar mass of 89406 g mol⁻¹. The polymer content in the latex is 9.7 wt%. DLS (unfiltered): D_z = 143 nm and PDI = 0.09. DLS after swelling with toluene by

shaking for < 1 min at room temperature (unfiltered): $D_z = 156$ nm and PDI = 0.04. Volume increase: $(4/3)\pi[(156/2)^3 - (143/2)^3] = 4.57 \cdot 10^5$ nm³ (29.8% of the original volume).

(b) *With neat DEGDMA. Preparation of $R_0-(4VPMe^+I)_{137-b-St_{345-b-DEGDMA_{15-SC(S)SPr}}$.*

A new batch of $[R_0-(4VPMe^+I)_{137-b-St_{345-SC(S)SPr}] \cdot 38(DMF)$ polymer (7.16 μ mol) was prepared as described above. To the Schlenk tube containing the entire aqueous suspension were successively added DEGDMA (25.9 mg, 0.107 mmol; 15 equiv. per chain), and the degassed ACPA/NaHCO₃ stock solution (0.08 ml, 1.7 mg ACPA, 6.07 μ mol). The resulting reaction mixture was stirred at 80 °C for 5 h resulting in nearly complete monomer consumption (< 1% by ¹H NMR monitoring in DMSO-*d*₆) to yield $[R_0-(4VPMe^+I)_{137-b-St_{345-b-DEGDMA_{15-SC(S)SPr}] \cdot 38(DMF)$. The polymer content in the latex is 7.9 wt%. DLS (unfiltered): $D_z = 148$ nm and PDI = 0.09. DLS after swelling with toluene by shaking for < 1 min at room temperature (unfiltered): $D_z = 162$ nm and PDI = 0.10. Volume increase: $(4/3)\pi[(162/2)^3 - (148/2)^3] = 5.28 \cdot 10^5$ nm³ (23.7% of the original volume).

Preparation of a latex of a P4VPMe⁺I-*b*-PSt amphiphilic nanogel copolymer

(a) *Without pre-heating.*

A $R_0-(4VPMe^+I)_{137-b-St_{48-SC(S)SPr}$ macroRAFT agent was first synthesized as described above. To the Schlenk tube containing a suspension of the precursor (7.16 μ mol) in 6 ml of H₂O were successively added degassed styrene (0.25 ml, 0.224 g, 2.15 mmol; 300 equiv. per chain), DEGDMA (25.9 mg, 0.107 mmol; 15 equiv. per chain), and the degassed ACPA/NaHCO₃ stock solution (0.5 ml, 10 mg ACPA, 35.7 μ mol). The resulting reaction mixture was stirred at 80 °C for 17 h to reach complete conversion of all monomers (¹H NMR monitoring in DMSO-*d*₆), to yield $[R_0-(4VPMe^+I)_{137-b-St_{48-b-(St_{300-co-DEGDMA_{15-SC(S)SPr}] \cdot 38(DMF)$. The polymer content in the latex is 7.6

wt%. D_z (PDI) obtained from DLS (filtered through a 0.45 μm pore filter): unfiltered sample 84.7 nm (0.05), toluene-swollen sample 88.8 nm (0.06), CHCl_3 -swollen sample 92.6 nm (0.06).

(b) *With pre-heating.*

A second polymerization was carried out starting from the same macroRAFT agent and using the same amounts of all reagents. The only different is that the ACPA stock solution was not introduced initially. The reaction mixture was pre-heated with stirring at 80 °C for 30 min. A sample of this mixture was withdrawn and used for a DLS analysis ($D_z = 107.0$ nm and PDI = 0.10). The ACPA solution was then introduced and stirring was continued at 80 °C for 4 h (complete monomer consumption). The polymer content in the latex is 7.6 wt%. DLS (unfiltered): $D_z = 101.4$ nm and PDI = 0.06. DLS after swelling with toluene by shaking for < 1 min at room temperature (unfiltered): $D_z = 110.5$ nm and PDI = 0.15. Volume increase: $(4/3)\pi[(110.5/2)^3 - (101.4/2)^3] = 1.61 \cdot 10^5 \text{ nm}^3$ (29.4% of the original volume).

VI.2.2 Preparation of phosphine-functionalized polymers with a cationic $\text{P4VPMe}^+\text{I}^-$ shell

Preparation of latexes of the $\text{R}_0\text{-(4VPMe}^+\text{I}^-)_a\text{-}b\text{-St}_b\text{-}b\text{-(St}_{1-n}\text{-}co\text{-DPPS}_n)_c\text{-SC(S)SPr}$ amphiphilic copolymers

The synthesis of all latexes of this type followed the same procedure, which is detailed here only for the product with a, b, c, n = 140, 50, 300, 0.1 (diblock 10%). The $[\text{R}_0\text{-(4VPMe}^+\text{I}^-)_{140}\text{-}b\text{-St}_{50}\text{-SC(S)SPr}] \cdot 38(\text{DMF})$ macroRAFT agent (2 g, 49.9 mmol) was dissolved in 15 ml of degassed water under Ar in a Schlenk tube to afford a pale-yellow dispersion. To this mixture was added 1,3,5-Trioxane (11.9 mg, 0.13 mmol), degassed styrene (1.55 ml, 1.40 g, 13.48 mmol; 270 equiv. per chain) and DPPS (0.43 g, 1.50 mmol; 30 equiv. per chain). A portion of the degassed ACPA/ NaHCO_3 stock solution (1.4 ml, 28.02 mg ACPA, 0.1 mmol) was then added and the resulting reaction

mixture was stirred at 80 °C for 3 h, yielding a white opalescent stable dispersion. The resulting polymer has a theoretical molar mass of 76847 g mol⁻¹. The weight percent of polymer in the latex is 18.9 wt%. Using the same amounts of [R₀-(4VPMe⁺I⁻)₁₄₀-*b*-St₅₀-SC(S)SPr]·38(DMF), ACPA solution, water and trioxane but different amounts of degassed styrene and DPPS led to latexes of the product with different DPPS content (5% or 20%) in the hydrophobic block. Diblock 5% (a, b, c, n = 140, 50, 300, 0.05): styrene (1.64 ml, 1.48 g, 14.25 mmol; 285 equiv. per chain), DPPS (0.22 g, 0.75 mmol; 15 equiv. per chain), M_{n,th} = 74090 g mol⁻¹, polymer content = 18.4 wt%. Diblock 20% (a, b, c, n = 140, 50, 300, 0.2): styrene (1.38 ml, 1.25 g, 13.48 mmol; 240 equiv. per chain), DPPS (0.86 g, 3.0 mmol; 60 equiv. per chain), M_{n,th} = 82361 g mol⁻¹, polymer content = 20.0 wt%.

Latexes with other a, b, c, n values (as reported in Table VI.2.1) were obtained by the same procedure from the appropriate R₀-(4VPMe⁺I⁻)_a-*b*-St_b-SC(S)SPr macroRAFT agents, using suitable molar amounts of styrene and DPPS for the chain extension.

Preparation of R₀-(4VPMe⁺I⁻)_a-*b*-St_b-*b*-(St_{1-n}-*co*-DPPS_n)_c-*b*-(St_{1-y}-*co*-DEGDMA_y)_d-SC(S)SPr core-crosslinked micelles (CCM)

The same general procedure was used for all CCM particles and will be described in detail only for the product with a, b, c, d, n, y = 140, 50, 300, 140, 0.1, 0.1 (CCM-C-0.1). To the Schlenk tube containing the entire aqueous suspension of the R₀-(4VPMe⁺I⁻)₁₄₀-*b*-St₅₀-*b*-(St_{0.9}-*co*-DPPS_{0.1})₃₀₀-SC(S)SPr (diblock 10%) polymer, prepared as described in the previous section, were successively added degassed styrene (0.702 g, 6.74 mmol; 135 equiv. per chain), DEGDMA (0.17 ml, 0.18 g, 0.75 mmol; 15 equiv. per chain), and 1.4 ml of the degassed ACPA/NaHCO₃ stock solution (28.02 mg ACPA, 0.1 mmol). The resulting reaction mixture was stirred at 80 °C for 8.5 h. The monomer conversions were 91.0% for styrene and 100% for DEGDMA (by ¹H NMR in DMSO-*d*₆). The final polymer has a theoretical molar mass of 93278 g mol⁻¹ and the polymer content in the latex is 20.6 wt% ([TPP] = 73.8 mmol ml⁻¹).

The same procedure, starting from the latex of either diblock 5% or diblock 20%, gave a latex of CCM-C-0.05 or CCM-C-0.2, respectively. For CCM-C-0.05: styrene (0.72 ml, 0.656 g, 6.30 mmol; 126 equiv. per chain), DEGDMA (0.16 ml, 0.17 g, 0.75 mmol; 14 equiv. per chain), and degassed ACPA/NaHCO₃ stock solution (1.4 ml, 28.02 mg ACPA, 10.0 mmol); stirring at 80 °C for 4 h; conversions = 99.0% for styrene and 100% for DEGDMA; $M_{n,th} = 90508 \text{ g mol}^{-1}$; polymer content in the latex = 20.2 wt% ([TPP] = 40.3 mmol ml⁻¹). For CCM-C-0.2: styrene (0.72 ml, 0.655 g, 6.29 mmol; 126 equiv. per chain), DEGDMA (0.16 ml, 0.17 g, 0.75 mmol; 14 equiv. per chain) and the degassed ACPA/NaHCO₃ stock solution (1.4 ml, 28.02 mg ACPA, 10.0 mmol); stirring at 80 °C for 4 h; conversions were nearly 100% for styrene and 100% for DEGDMA; $M_{n,th} = 98878 \text{ g mol}^{-1}$; polymer content in the latex = 21.6 wt% ([TPP] = 148.7 mmol ml⁻¹).

Latexes of CCM particles with other a, b, c, d, n, y values (as reported in Table VI.2.1) were obtained by the same procedure from the appropriate amphiphilic diblock precursors, using suitable molar amounts of styrene and DEGDMA for the crosslinking step.

Preparation of a latex of a P4VPM⁺I⁻-*b*-P(St-*co*-DPPS) amphiphilic nanogel copolymer

To the Schlenk tube containing an aqueous suspension of [R₀-(4VPM⁺I⁻)₁₄₀-*b*-St₅₀-SC(S)SPr]·38(DMF) polymer (0.5 g, 12.5 mmol), prepared as described previously, in 6 ml of distilled water were added 1,3,5-Trioxane (10.6 mg, 0.12 mmol), degassed styrene (0.62 ml, 56.2 mg, 5.39 mmol), DPPS (0.109 g, 0.38 mmol) and DEGDMA (42 ml, 45.4 mg, 187.8 mmol), and finally the degassed ACPA/NaHCO₃ stock solution (0.38 ml, 7.5 mg ACPA, 27.1 mmol). The reaction mixture was stirred at 80 °C for 4 h. The NMR (DMSO-*d*₆) indicated the complete conversion of all monomers. The final polymer has a theoretical molar mass of 96732 g mol⁻¹ and the latex has a polymer content of 16.0 wt% ([TPP] = 53.2 mmol ml⁻¹).

Table VI.2.1 List of all polymers synthesized in this study and reference to their characterization.

Formula	SEC	NMR	DLS	TEM
R ₀ -4VP ₅₆ -SC(S)SPr	Figure II.2.2	Figure II.2.3(a)	-	-
R ₀ -(4VPMe ⁺ I ⁻) ₅₆ -SC(S)SPr	-	Figure II.2.3(b)	-	-
R ₀ -4VP ₅₆ - <i>b</i> -St ₂₄₇ -SC(S)SPr	Figure II.2.5	-	Figure II.2.6(a)	Figure II.2.6(b)
R ₀ -4VP ₁₃₇ -SC(S)SPr	Figure II.2.7	Figure II.2.8	-	-
R ₀ -4VP ₁₃₇ - <i>b</i> -St ₃₄₄ -SC(S)SPr	-	Figure II.2.9 Figure A.0.3	Figure A.0.1(a)	Figure A.0.1(b)
R ₀ -(4VPMe ⁺ I ⁻) ₁₃₇ - <i>b</i> -St ₃₄₄ -SC(S)SPr	-	Figure A.0.2	Figure II.2.10(a)	Figure II.2.10(b)
R ₀ -4VP ₁₃₇ - <i>b</i> -St ₄₈ -SC(S)SPr	Figure A.0.4	Figure II.2.11 Figure II.2.12	Figure II.2.13(a) (b)	Figure II.2.13(c)
R ₀ -(4VPMe ⁺ I ⁻) ₁₃₇ - <i>b</i> -St ₄₈ -SC(S)SPr	-	Figure II.2.14 Figure A.0.5	Figure II.2.15(a)	Figure II.2.15(b)
R ₀ -(4VPMe ⁺ I ⁻) ₁₃₇ - <i>b</i> -St ₄₈ - <i>b</i> -St ₂₉₇ -SC(S)SPr	-	Figure II.2.16	Figure II.2.17(a) Figure II.2.18 Figure II.2.19 Figure A.0.6 Figure A.0.7(b)	Figure II.2.17(b)
R ₀ -(4VPMe ⁺ I ⁻) ₁₃₇ - <i>b</i> -St ₃₄₅ - <i>b</i> -(St ₁₅₇ - <i>co</i> -DEGDMA ₁₃)-SC(S)SPr	-	Figure II.2.20 Figure II.2.21	Figure II.2.22(a) (b)	Figure II.2.22(c)
R ₀ -(4VPMe ⁺ I ⁻) ₁₃₇ - <i>b</i> -St ₃₅₀ - <i>b</i> -(St ₁₃₅ - <i>co</i> -DEGDMA ₁₅)-SC(S)SPr	-	-	Figure II.2.23 Figure II.2.24	-
R ₀ -(4VPMe ⁺ I ⁻) ₁₃₇ - <i>b</i> -St ₃₄₅ -SC(S)SPr			Figure A.0.11	
R ₀ -(4VPMe ⁺ I ⁻) ₁₃₇ - <i>b</i> -St ₃₄₅ - <i>b</i> -DEGDMA ₁₅ -SC(S)SPr	-	Figure II.2.25 Figure II.2.26	Figure II.2.27(a) (b) Figure II.2.28 Figure II.2.29	Figure II.2.27(c)
R ₀ -(4VPMe ⁺ I ⁻) ₁₃₇ - <i>b</i> -St ₄₈ - <i>b</i> -(St ₃₀₀ - <i>co</i> -DEGDMA ₁₅)-SC(S)SPr (direct heating with ACPA)	-	Figure II.2.30	Figure II.2.31	Figure II.2.32
R ₀ -(4VPMe ⁺ I ⁻) ₁₃₇ - <i>b</i> -St ₄₈ - <i>b</i> -(St ₃₀₀ - <i>co</i> -DEGDMA ₁₅)-SC(S)SPr (ACPA addition after thermal equilibration)	-	Figure II.2.34	Figure II.2.33 Figure II.2.35 Figure II.2.36	-

VI.3 RAFT synthesis of core-crosslinked micelles and nanogels with an anionic PSS⁻Na⁺ shell

VI.3.1 Preparation of phosphine-free polymer with an anionic PSS⁻Na⁺ shell

RAFT polymerization of styrene sulfonate

A portion of the ACPA stock solution (1 ml, 20 mg of ACPA, 0.071 mmol), CTPPA (0.1 g, 0.36 mmol), SS⁻Na⁺ (10.42 g, 50.54 mmol; SS⁻Na⁺/CTPPA = 140), ethanol (27 ml) and deionized water (63 ml) were added to a 250 ml Schlenk tube with a magnetic stirrer bar. An internal reference (1,3,5-Trioxane, 0.16 g, 1.84 mmol) was also added as for the determination of the monomer conversion as a function of time by ¹H NMR. The solution was purged for 45 min with argon and then heated to 80 °C during 20 h in a thermostatic oil bath under stirring, leading to nearly quantitative monomer conversion. The experimental molar mass (from SEC) for the final polymer is $M_n = 24400 \text{ g mol}^{-1}$ with $D = 1.04$, versus a theoretical molar mass of 29100 g mol^{-1} . The polymer content in the latex is 11.0 wt%.

Synthesis of the R₀-(SS⁻Na⁺)₁₄₀-*b*-St₃₀₀-SC(S)SPr diblock copolymer

In a 100 ml Schlenk tube, 10 ml R₀-(SS⁻Na⁺)₁₄₀-SC(S)SPr latex obtained in the previous step (0.04 mmol of polymer, corresponding to 5.46 mmol of SS⁻Na⁺ units) were diluted with 3 ml H₂O. To this solution was added degassed styrene (1.346 ml, 1.219 g, 11.70 mmol; 300 equiv. per chain) slowly *via* syringe. Then a portion of the degassed ACPA/NaHCO₃ stock solution (0.11 ml, 2.2 mg ACPA, 7.99 μmol) was added and the resulting reaction mixture was stirred at 80 °C for 4 h. The styrene consumption was complete and was accompanied by the transformation of the initial suspension into a stable latex of R₀-(SS⁻Na⁺)₁₄₀-*b*-St₃₀₀-SC(S)SPr macromolecules, self-assembled in

the form of micelles to yield a light yellow opalescent stable dispersion (DLS: $D_z = 91.8$ nm and PDI = 0.41, filtered through a 0.45 μm pore filter). The molar mass calculated for $R_0\text{-(SS}^-\text{Na}^+)_{140}\text{-}b\text{-St}_{300}\text{-SC(S)SPr}$ is 60360 g mol^{-1} . The polymer content in the latex is 16.1 wt%.

Crosslinking of the PSS⁻Na⁺-*b*-PSt amphiphilic block copolymer by DEGDMA

(a) *In the presence of styrene. Preparation of $R_0\text{-(SS}^-\text{Na}^+)_{140}\text{-}b\text{-St}_{300}\text{-}b\text{-(St}_{0.9}\text{-}co\text{-DEGDMA}_{0.1})_{150}\text{-SC(S)SPr}$.*

To the total amount of the $R_0\text{-(SS}^-\text{Na}^+)_{140}\text{-}b\text{-St}_{300}\text{-SC(S)SPr}$ latex obtained in step 2 (0.04 mmol of polymer) were successively added 3 ml H₂O, degassed styrene (0.606 ml, 0.549 g, 5.27 mmol; 135 equiv. per chain), DEGDMA (0.131 ml, 141.6 mg, 0.59 mmol; 15 equiv. per chain), and a degassed ACPA/NaHCO₃ stock solution (0.11 ml, 2.2 mg of ACPA, 7.99 μmol). The resulting reaction mixture was stirred at 80 °C for 2 h resulting in an essentially quantitative monomer consumption (< 1% of residual styrene by ¹H NMR monitoring in DMSO-*d*₆) to yield $R_0\text{-(SS}^-\text{Na}^+)_{140}\text{-}b\text{-St}_{300}\text{-}b\text{-(St}_{0.9}\text{-}co\text{-DEGDMA}_{0.1})_{150}\text{-SC(S)SPr}$. The polymer content in the latex is 16.4 wt%. The calculated for molar mass per chain is 78070 g mol^{-1} .

(b) *With neat DEGDMA. Preparation of $R_0\text{-(SS}^-\text{Na}^+)_{140}\text{-}b\text{-St}_{300}\text{-}b\text{-DEGDMA}_{15}\text{-SC(S)SPr}$.*

The total volume of the $R_0\text{-(SS}^-\text{Na}^+)_{140}\text{-}b\text{-St}_{300}\text{-SC(S)SPr}$ latex obtained in step 2 (0.04 mmol of polymer) was successively added 3 ml H₂O, DEGDMA (0.131 ml, 141.6 mg, 0.59 mmol; 15 equiv. per chain), and the degassed ACPA/NaHCO₃ stock solution (0.11 ml, 2.2 mg ACPA, 7.99 μmol). The resulting reaction mixture was stirred at 80 °C for 2 h resulting in an essentially quantitative monomer consumption (< 1% of residual DEGDMA by ¹H NMR monitoring in DMSO-*d*₆) to yield $R_0\text{-(SS}^-\text{Na}^+)_{140}\text{-}b\text{-St}_{300}\text{-}b\text{-DEGDMA}_{15}\text{-SC(S)SPr}$. The polymer content in the latex is 13.8 wt%. The calculated for molar mass per chain is 63990 g mol^{-1} .

VI.4 General procedure for Rh complexation to the phosphine ligand within CCM or NG core

All metal complexation reactions were carried out using the same procedures, which is described here in detail for the CCM-C-0.1 polymer with a P/Rh ratio of 4:1. In a Schlenk tube was added 1 ml of the CCM-C-0.1 polymer latex (containing 73.8 mmol of TPP) and 3 ml of H₂O. Toluene (3 ml) was added and the mixture was stirred for 5 min, resulting in the CCM particle core swelling. Then a separately prepared solution of [RhCl(COD)]₂ (4.6 mg, 9.23 mmol) in toluene (1 ml) was added to the latex and the mixture was vigorously stirred at room temperature, stopping the stirring at regular intervals (decantation was rapid, < 1 min) to assess the progress of the reaction. The aqueous phase progressively became yellow while the toluene phase became completely colorless after 30 minutes of stirring. For the procedure with a P/Rh ratio of 1:1, since a slight excess of [RhCl(COD)]₂ was used to ensure quantitative complexation of the TPP ligands, the resulting latex was extracted with toluene until the organic phase was colorless to remove the metal precursor excess. The measured latex volume was 5.8 ml ([TPP] = 12.7 mmol ml⁻¹).

VI.5 General procedure for molecular rhodium-catalyzed biphasic hydrogenations

VI.5.1 Hydrogenation of styrene or 1-octene in solvent

In a vial containing a magnetic stirrer was added 1 ml of the Rh-charged latex (CCM-C-0.1, CCM-C-0.05 or NG-C-0.1), prepared as described in the previous sections. The desired amount of substrate (styrene or 1-octene), mixed with 1-nonanol or toluene (10% v/v), was layered on top of the latex.

VI.5.2 Hydrogenation of neat styrene

In a vial containing a magnetic stirrer was added 0.4 ml of CCM-C-0.1 (5.09 mmol of TPP; 1.27 mmol of Rh) and then neat styrene (0.73 ml, 664 g, 6.37 mmol). For all experiments, irrespective of the substrate/Rh ratio, *n*-Decane (internal standard) was then added to the organic layer (substrate/decane molar ratio *ca.* 4). The vial was then placed inside an autoclave, which was subsequently charged with dihydrogen (20 bar), placed in a thermostatic oil bath, and stirred at 1200 rpm. At the set reaction time, the stirring was stopped, the autoclave was vented and the vial was taken out under argon. The latex decantation was rapid (< 1 min). An aliquot of the organic phase was used for ICP-MS analysis of the Rh leaching. After phase separation, the latex was extracted with diethyl ether or toluene (3 × 0.3 ml). The combined organic phases were used for the GC analysis. For the recycling experiments, a fresh substrate solution (same amounts as in the initial run) was added to the same vial, followed by reaction and product separation according to the same protocol.

VI.6 Rhodium nanoparticles generation and general procedure for biphasic hydrogenations

VI.6.1 General procedure for the synthesis of Rh nanoparticles within the nanoreactors

In a vial containing a magnetic stirrer under argon was added 0.4 ml of the desired L/M@CCM latex (see above), 0.5 ml of degassed toluene and an excess of triethylamine (*ca.* 5-10 equiv. per metal). The vial was placed into an autoclave, which was then charged with 20 bar of H₂. The autoclave was placed in a thermostatic oil bath at the desired temperature and stirred at 1200 rpm. After the set reaction time, the vial was taken out of the autoclave under argon. The resulting black latex was allowed to

decant until yielding a neat phase separation (*ca.* 5-7 min for CCM-N, < 3 min for CCM-C) and then the upper toluene was removed by pipette, leaving a latex of toluene-swollen CCM particles containing the metallic nanoparticles. The products were characterized by TEM.

VI.6.2 General procedure for Rh nanoparticles synthesis from a homogeneous phase

With PEOMA stabilization

In a vial containing 10 mg of PEOMA (10.5 μmol , 210 μmol of EO units) was added a solution of $[\text{RhCl}(\text{COD})]_2$ (either 5.2 mg, 10.5 μmol , or 1.3 mg, 2.6 μmol) in 0.5 ml of degassed toluene, to yield an EO/Rh ratio of 10:1 or 40:1, respectively. The vial was placed into the autoclave, which was then sealed, charged with 20 bar of H_2 and placed in an oil bath at 60 $^\circ\text{C}$ with magnetic stirring at 1200 rpm for 20 h.

With PPh_3 stabilization.

In a vial containing 23.6 mg of triphenylphosphine (0.09 mmol) was added a solution of $[\text{RhCl}(\text{COD})]_2$ (either 22.19 mg, 0.045 mmol, or 5.4 mg, 0.011 mmol) in 0.5 ml of degassed toluene, to yield a P/Rh ratio of 1:1 or 4:1, respectively. The vial was placed into the autoclave, which was then sealed, charged with 20 bar of H_2 and placed in an oil bath at 60 $^\circ\text{C}$, with magnetic stirring at 1200 rpm for 20 h.

With macroRAFT-N $\text{R}_0\text{-(MAA}_{0.5}\text{-}co\text{-PEOMA}_{0.5})_{30}\text{-SC(S)SPr}$ stabilization

In a vial containing 0.1 ml of macroRAFT-N $\text{R}_0\text{-(MAA}_{0.5}\text{-}co\text{-PEOMA}_{0.5})_{30}\text{-}$

SC(S)SPr solution (1.29 μmol) or 0.4 ml of macroRAFT-N $\text{R}_0\text{-(MAA}_{0.5}\text{-}co\text{-PEOMA}_{0.5})_{30}\text{-SC(S)SPr}$ solution (5.17 μmol) was added a solution of $[\text{RhCl}(\text{COD})]_2$ (1.92 mg, 3.89 μmol) in 0.1 ml of 1-nonanol, to yield a same PEOMA/Rh ratio in the case of Rh loaded CCM-C with P/Rh ratio of 1:1 or 4:1, respectively. The vial was placed into the autoclave, which was then sealed, charged with 20 bar of H_2 and placed in an oil bath at 60 $^\circ\text{C}$, with magnetic stirring at 1200 rpm for 20 h.

With macroRAFT-C $\text{R}_0\text{-(4VPMe}^+\text{I)}_{140}\text{-}b\text{-St}_{50}\text{-SC(S)SPr}$ stabilization

In a vial containing 50 mg or 210 mg of macroRAFT-C $\text{R}_0\text{-(4VPMe}^+\text{I)}_{140}\text{-}b\text{-St}_{50}\text{-SC(S)SPr}$ (1.21 μmol) was added a solution of $[\text{RhCl}(\text{COD})]_2$ (1.8 mg, 7.22 μmol) in 0.1 ml of 1-nonanol, to yield a same P4VP/Rh ratio in the case of Rh loaded CCM-C with P/Rh ratio of 1:1 or 4:1, respectively. The vial was placed into the autoclave, which was then sealed, charged with 20 bar of H_2 and placed in an oil bath at 60 $^\circ\text{C}$, with magnetic stirring at 1200 rpm for 20 h.

VI.6.3 General procedure for the catalytic hydrogenation

Biphasic catalytic hydrogenations with nanoparticles stabilized within nanoreactor

In a vial containing the desired RhNP@CCM-C-0.1 latex (1 ml, 8.7 μmol of TPP, 3 μmol of metal), the desired amount of an acetophenone/toluene, styrene/toluene mixture or neat styrene was layered on top. *n*-Decane or dodecane (internal standard) was then added to the organic layer (substrate/internal standard molar ratio = *ca.* 4). The vial was then placed inside an autoclave, which was subsequently charged with 20 bar of H_2 , placed in a thermostatic oil bath and stirred at 1200 rpm. At the set reaction time, the stirring was stopped, the autoclave was vented and the vial was taken out under argon and allowed to decant until a neat phase separation was obtained (*ca.* 15

min with CCM-N, < 3 min with CCM-C). After phase separation, the latex was extracted with diethyl ether (5×0.3 ml). The combined organic phases were used for the GC analysis.

Homogeneous catalytic hydrogenations with nanoparticles stabilized by PEOMA, PPh₃ or a macroRAFT agent

To the vial containing the PEOMA, PPh₃, macroRAFT-N R₀-(MAA_{0.5}-*co*-PEOMA_{0.5})₃₀-SC(S)SPr or macroRAFT-C R₀-(4VPM⁺I)₁₄₀-*b*-St₅₀-SC(S)SPr stabilized rhodium nanoparticles were added the desired amounts of styrene, 1-nonanol and the *n*-Decane internal standard. The vial was then placed inside an autoclave, which was sealed, charged with 20 bar dihydrogen and placed in a thermostatic oil bath with magnetic stirring at 1200 rpm. At the set reaction time, the stirring was stopped, the autoclave was vented and the vial was taken out under argon to allow the nanoparticles to decant. A solution aliquot was withdrawn and diluted with diethyl ether for the GC analysis.

Procedure used for the latex separation, recovery and recycling

At the set reaction time, the stirring was stopped, the autoclave was vented and the vial was taken out under argon and allowed to decant until a neat phase separation was obtained (< 3 min with CCM-C). After phase separation, the latex was extracted with 0.3 ml diethyl ether or 0.3 ml toluene. After 5 min of stirring and 5 min of decantation, the organic solution was withdrawn. The washing was repeated 5 times under argon. The combined organic phases were used for the GC analysis. For the recycling experiments, a fresh substrate solution (same amounts as in the initial run) was added to the same vial, followed by reaction and product separation according to the same protocol. To regenerate NPs, 0.5 ml toluene and 5 equiv. per metal of triethylamine were added into the vial. The vial was placed into an autoclave charged with 20 bar of

dihydrogen. The autoclave was placed in a thermostatic oil bath at the desired temperature (80 °C or 90 °C) and stirred at 1200 rpm for 20 h or 2 h.

Conclusions and perspectives

The principal objective of this thesis was the preparation of amphiphilic core-shell unimolecular polymers with polycationic and polyanionic outer shells as nanoreactors for aqueous biphasic catalysis. The catalysts were anchored in the hydrophobic core through coordinative bonds to core-linked phosphine ligands and the organic substrates diffused from the bulk organic phase to the catalytic sites in the core by migration through the shell. Meanwhile, the hydrophilic shell enabled the particles to be dispersed as a stable colloidal suspension in the aqueous phase. This method was expected to solve the copolymer particle agglomeration and catalyst leaching problems which were observed in case of the neutral-shell polymeric nanoreactors.

Initially, polycationic shell copolymers were developed via the same RAFT-PISA strategy as already used for the neutral shell copolymers. This kind of polymers contain a hydrophilic P4VPM⁺₄T⁻ shell and a polystyrene-based hydrophobic core followed by crosslinking. The first investigations led to the preparation of non-functionalized copolymers, in order to optimize the preparation method and the copolymer composition, leading to stable particles with spherical morphology and a narrow size distribution. The DLS results of the polymers demonstrated the complete crosslinking without any residual free single chains and, in combination with TEM, confirmed the well-defined spherical morphology and narrow size distribution. Then DPPS ligands were introduced into the polymer core by copolymerization. These functionalized polymers also exhibited the expected characteristics and good stability for their colloidal dispersions.

In this thesis, the [RhCl(COD)]₂ complex was used as precatalyst for the hydrogenation of olefins. This metal complex could be transported into the micelle core and coordinated to the TPP ligands situated in the hydrophobic chains. The ³¹P NMR spectra indicated the absence of interparticle metal exchange, which is attributed to the lack of particle interpenetration with core-core contact, thanks to the repulsive Coulombic forces introduced by the positive charges on the outer shell.

The core-confined molecular Rh^I catalyst was used for styrene and 1-octene hydrogenation under aqueous biphasic conditions. The catalytic results indicated high

activity (TOF > 1000 h⁻¹) and high selectivity. The phase decantations were fast (< 2 min) and the ICP-MS showed lower metal leachings to the organic phase, relative to the values previously obtained with the related neutral-shell nanoreactor.

The molecular Rh^I catalyst in the micelle core of both neutral-shell and cationic-shell nanoreactors was found to be reduced to Rh⁰ small-diameter nanoparticles in the absence of protecting π -acidic ligands (TPP for high P/Rh ratios, olefins) and the reduction was faster in the presence of base. It is worth noting that, for the cationic-shell nanoreactors, all Rh nanoparticles remained confined in the cores, in contrast to the case of the neutral-shell nanoreactors, where the Rh⁰ nanoparticles were prone to migrate toward the outer shell, where they can be stabilized by the PEOMA chains. This core-confinement was quite important to avoid metal loss during catalysis. The nanoreactor-embedded Rh⁰-NPs exhibited excellent activity in styrene and 1-octene hydrogenations with low metal leaching, facile catalyst recovery and efficient recycling, whereas acetophenone was efficiently hydrogenated only with the neutral-shell nanoreactor-embedded catalyst. An interesting observation was the loss the Rh⁰ NPs from the polymer cores by migration toward the bulk liquid phase when using diethyl ether for the product extraction during the catalyst recovery and recycling procedure, leading to catalyst loss and to an activity decrease. On the other hand, the NPs remained in the core and the catalytic activity was maintained when toluene was used as the extraction solvent.

It can be concluded that the use of the polycationic P4VPMe^{+I} shell nanoreactors in aqueous biphasic catalysis has clear advantages relative to the neutral P(MAA-co-PEOMA) shell nanoreactors: faster decantation and lower catalyst loss, thus lower cost and more environment-friendly, hence more suitable for large scale production.

Inspired by the results obtained with the P4VPMe^{+I} shell nanoreactors, the last part of this thesis was dedicated to the design of hierarchically organized unimolecular polymeric nanoreactors with a polyanionic PSS^{-Na}⁺ shell. The preparation was conducted once again by a one-pot RAFT-PISA process. The corresponding characterization showed the successful synthesis and self-assembly of well-defined

micelles in water.

On the basis of these investigations, a perspective for further development of this topic would be the preparation of phosphine-functionalized PSS⁻Na⁺ shell copolymer, and its metal precatalyst complexation, coordination chemistry and applications as catalytic nanoreactor in aqueous biphasic catalysis. On the other hand, the investigations of the coordination of a variety of other metal complexes to the core TPP functions for different catalytic reactions would also be a topic worthy of investigation. To solve the metal nanoparticles leaching problem occurring in the diethyl ether washings, ligands with greater affinity as metal nanoparticle stabilizers could be introduced into the cores. Apart from these potential investigations, other polymeric micelles with different compositions, architectures and ligand sites are also a promising direction for further work in this area.

References

- [1]. Ye, T.; Park, S.; Lu, Y.; Li, J.; Sasase, M.; Kitano, M.; Hosono, H. Contribution of nitrogen vacancies to ammonia synthesis over metal nitride catalysts. *J. Am. Chem. Soc.*, **2020**, 142(33), 14374-14383.
- [2]. Rahmati, M.; Safdari, M.-S.; Fletcher, T. H.; Argyle, M. D.; Bartholomew, C. H. Chemical and thermal sintering of supported metals with emphasis on cobalt catalysts during Fischer–Tropsch synthesis. *Chem. Rev.*, **2020**, 120(10), 4455-4533.
- [3]. Kumawat, J.; Gupta, V. K. Fundamental aspects of heterogeneous Ziegler–Natta olefin polymerization catalysis: An experimental and computational overview. *Polym. Chem.*, **2020**, 11(38), 6107-6128.
- [4]. Wang, Z.; van Oers, M. C. M.; Rutjes, F. P. J. T.; van Hest, J. C. M. Polymersome colloidosomes for enzyme catalysis in a biphasic system. *Angew. Chem. Int. Edit.*, **2012**, 51(43), 10746-10750.
- [5]. Anastas, P. T.; Warner, J. C. Green Chemistry: Theory and practice. *Abstracts of Papers of the American Chemical Society*, **1998**, 244(48), 19758-19771.
- [6]. (a) Cornils, B. Industrial aqueous biphasic catalysis: Status and directions. *Org. Process. Res. Dev.*, **1998**, 2(2), 121-127; (b) Joo, F. Aqueous biphasic hydrogenations. *Accounts Chem. Res.*, **2002**, 35(9), 738-745.
- [7]. Cole-Hamilton, D. J.; Tooze, R. P. Catalyst separation, recovery and recycling: Chemistry and process design. Springer Science & Business Media: 2006; Vol. 30.
- [8]. Najdanovic-Visak, V.; Serbanovic, A.; Esperança, J. M.; Guedes, H. J.; Rebelo, L. P.; Nunes da Ponte, M. Supercritical carbon dioxide-induced phase changes in (ionic liquid, water and ethanol mixture) solutions: Application to biphasic catalysis. *ChemPhysChem*, **2003**, 4(5), 520-522.
- [9]. Olivier-Bourbigou, H.; Favre, F.; Forestière, A.; Hugues, F. Ionic liquids and catalysis: The IFP biphasic Difasol process. *Handbook of Green Chemistry: Online*, **2010**, 101-126.
- [10]. Kohlpaintner, C. W.; Fischer, R. W.; Cornils, B. Aqueous biphasic catalysis: Ruhrchemie/Rhone-Poulenc oxo process. *Appl. Catal. A*, **2001**, 221(1-2), 219-225.
- [11]. Ostwald, W. Studien über die Bildung und Umwandlung fester Körper. *Zeitschrift für physikalische Chemie*, **1897**, 22(1), 289-330.
- [12]. (a) Fischer, E. K. Colloidal dispersions. Wiley: 1950; (b) Russel, W. B.; Russel, W.; Saville, D. A.; Schowalter, W. R. Colloidal dispersions. Cambridge university press: 1991.
- [13]. (a) Joó, F. Biphasic catalysis-Homogeneous. *Encyclopedia of Catalysis*, **2002**; (b) Keim, W. Multiphase catalysis and its potential in catalytic processes: The story of biphasic homogeneous catalysis. *Green Chem.*, **2003**, 5(2), 105-111.
- [14]. Paulik, F.; Roth, J. Novel catalysts for the low-pressure carbonylation of methanol to acetic acid. *Chemical Communications (London)*, **1968**, (24), 1578a-1578a.
- [15]. Pinault, N.; Bruce, D. W. Homogeneous catalysts based on water-soluble phosphines. *Coordin. Chem. Rev.*, **2003**, 241(1-2), 1-25.
- [16]. Dijkstra, H. P.; Van Klink, G. P.; Van Koten, G. The use of ultra-and nanofiltration

- techniques in homogeneous catalyst recycling. *Accounts Chem. Res.*, **2002**, 35(9), 798-810.
- [17]. Kozur, A.; Burk, L.; Thomann, R.; Lutz, P. J.; Mülhaupt, R. Graphene oxide grafted with polyoxazoline as thermoresponsive support for facile catalyst recycling by reversible thermal switching between dispersion and sedimentation. *Polymer*, **2019**, 178, 121553.
- [18]. Sowden, R.; Sellin, M.; Blasio, N.; Cole-Hamilton, D. Carbonylation of methanol in supercritical CO₂ catalysed by a supported rhodium complex. *Chem. Commun.*, **1999**, (24), 2511-2512.
- [19]. H. Clark, J.; J. Macquarrie, D. Catalysis of liquid phase organic reactions using chemically modified mesoporous inorganic solids. *Chem. Commun.*, **1998**, (8), 853-860.
- [20]. Gutmann, T.; Ratajczyk, T.; Xu, Y.; Breitzke, H.; Grünberg, A.; Dillenberger, S.; Bommerich, U.; Trantzschel, T.; Bernarding, J.; Buntkowsky, G. Understanding the leaching properties of heterogenized catalysts: A combined solid-state and PHIP NMR study. *Solid State Nucl. Mag.*, **2010**, 38(4), 90-96.
- [21]. Bianchini, C.; Burnaby, D. G.; Evans, J.; Frediani, P.; Meli, A.; Oberhauser, W.; Psaro, R.; Sordelli, L.; Vizza, F. Preparation, characterization, and performance of tripodal polyphosphine rhodium catalysts immobilized on silica via hydrogen bonding. *J. Am. Chem. Soc.*, **1999**, 121(25), 5961-5971.
- [22]. Reetz, M. T. Entrapment of biocatalysts in hydrophobic sol-gel materials for use in organic chemistry. *Adv. Mater.*, **1997**, 9(12), 943-954.
- [23]. Hübner, S.; de Vries, J. G.; Farina, V. Why does industry not use immobilized transition metal complexes as catalysts? *Adv. Synth. Catal.*, **2016**, 358(1), 3-25.
- [24]. Zhang, M.; Wei, L.; Chen, H.; Du, Z.; Binks, B. P.; Yang, H. Compartmentalized droplets for continuous flow liquid-liquid interface catalysis. *J. Am. Chem. Soc.*, **2016**, 138(32), 10173-10183.
- [25]. Manassen, J.; Basolo, F.; Burwell, R. Catalysis: progress in research. *F. Bassolo, RL Burwell, (Eds.)*, **1973**, 177.
- [26]. Joó, F.; Beck, M. Formation and catalytic properties of water-soluble phosphine complexes. *React. Kinet. Catal. L.*, **1975**, 2(3), 257-263.
- [27]. (a) W. Keim; T. M. Shryne; R. S. Bauer; H. Chung; P. W. Glockner; Zwet, H. v. Shell international research. DE 2.054.009, 1969; (b) Keim, W. Vor- und Nachteile der homogenen Übergangsmetallkatalyse, dargestellt am SHOP-Prozeß. *Chemie Ingenieur Technik*, **1984**, 56(11), 850-853.
- [28]. Keim, W. Oligomerization of ethylene to α -olefins: Discovery and development of the shell higher olefin process (SHOP). *Angew. Chem. Int. Edit.*, **2013**, 52(48), 12492-12496.
- [29]. Kuntz, E. G. *CHEMTECH*, **1987**, 17(9), 570-575.
- [30]. (a) Cornils, B.; Kuntz, E. G. Introducing TPPTS and related ligands for industrial biphasic processes. *J. Organomet. Chem.*, **1995**, 502(1-2), 177-186; (b) Beller, M.; Cornils, B.; Frohning, C. D.; Kohlpaintner, C. W. Progress in hydroformylation and carbonylation. *J. Mol. Catal. A Chem.*, **1995**, 104(1), 17-85; (c) Cornils, B.; Wiebus, E. Virtually no environmental impact: the biphasic oxo process. *Recueil des Travaux*

- Chimiques des Pays-Bas*, **1996**, 115(4), 211-215.
- [31]. Yoshimura, N.; Tamura, M. Process for producing normal-octanol. Google Patents: 1983.
- [32]. Tuba, R.; Corrêa da Costa, R.; Bazzi, H. S.; Gladysz, J. A. Phase transfer activation of fluorinated analogs of Grubbs' second-generation catalyst: Ring-opening metathesis polymerization. *ACS Catalysis*, **2012**, 2(1), 155-162.
- [33]. Keim, W.; Vogt, M.; Wasserscheid, P.; Driessen-Hölscher, B. Perfluorinated polyethers for the immobilisation of homogeneous nickel catalysts. *J. Mol. Catal. A Chem.*, **1999**, 139(2-3), 171-175.
- [34]. Gu, Y.; Jérôme, F. Bio-based solvents: An emerging generation of fluids for the design of eco-efficient processes in catalysis and organic chemistry. *Chem. Soc. Rev.*, **2013**, 42(24), 9550-9570.
- [35]. Herriott, A. W.; Picker, D. Phase transfer catalysis. Evaluation of catalysis. *J. Am. Chem. Soc.*, **1975**, 97(9), 2345-2349.
- [36]. Landini, D.; Maia, A.; Montanari, F. Phase-transfer catalysis. Nucleophilicity of anions in aqueous organic two-phase reactions catalyzed by onium salts. A comparison with homogeneous organic systems. *J. Am. Chem. Soc.*, **1978**, 100(9), 2796-2801.
- [37]. Leclercq, L.; Lacour, M.; Sanon, S. H.; Schmitzer, A. R. Thermoregulated microemulsions by cyclodextrin sequestration: A new approach to efficient catalyst recovery. *Chem. Eur. J.*, **2009**, 15(26), 6327-6331.
- [38]. Pera-Titus, M.; Leclercq, L.; Clacens, J.-M.; De Campo, F.; Nardello-Rataj, V. Pickering interfacial catalysis for biphasic systems: From emulsion design to green reactions. *Angew. Chem. Int. Edit.*, **2015**, 54(7), 2006-2021.
- [39]. Olivier, H. Recent developments in the use of non-aqueous ionic liquids for two-phase catalysis. *J. Mol. Catal. A Chem.*, **1999**, 146(1-2), 285-289.
- [40]. Jessop, P. G. Homogeneous catalysis using supercritical fluids: Recent trends and systems studied. *J. Supercrit. Fluid.*, **2006**, 38(2), 211-231.
- [41]. Kolbeck, C.; Paape, N.; Cremer, T.; Schulz, P. S.; Maier, F.; Steinrück, H.-P.; Wasserscheid, P. Ligand effects on the surface composition of Rh-containing ionic liquid solutions used in hydroformylation catalysis. *Chem. Eur. J.*, **2010**, 16(40), 12083-12087.
- [42]. Sharma, A.; Lebigue, C. J.; Deshpande, R. M.; Kelkar, A. A.; Delmas, H. Hydroformylation of 1-octene using [Bmim][PF₆]⁻decane biphasic media and rhodium complex catalyst: Thermodynamic properties and kinetic study. *Ind. Eng. Chem. Res.*, **2010**, 49(21), 10698-10706.
- [43]. Chauvin, Y.; Gilbert, B.; Guibard, I. Catalytic dimerization of alkenes by nickel complexes in organochloroaluminate molten salts. *J. Chem. Soc., Chem. Commun.*, **1990**, (23), 1715-1716.
- [44]. Reichardt, C. Solvents and solvent effects in organic chemistry. VCH, Weinheim: 1990.
- [45]. Horváth, I. T.; Rábai, J. Facile catalyst separation without water: Fluorous biphasic hydroformylation of olefins. *Science*, **1994**, 266(5182), 72-75.
- [46]. Dobbs, A. P.; Kimberley, M. R. Fluorous phase chemistry: A new industrial

- technology. *J. Fluorine Chem.*, **2002**, 118(1), 3-17.
- [47]. Leitner, W. Recent advances in catalyst immobilization using supercritical carbon dioxide. *Pure Appl. Chem.*, **2004**, 76(3), 635-644.
- [48]. Liu, F.; Abrams, M. B.; Baker, R. T.; Tumas, W. Phase-separable catalysis using room temperature ionic liquids and supercritical carbon dioxide. *Chem. Commun.*, **2001**, (5), 433-434.
- [49]. (a) Starks, C. M. Phase-transfer catalysis. I. Heterogeneous reactions involving anion transfer by quaternary ammonium and phosphonium salts. *J. Am. Chem. Soc.*, **1971**, 93(1), 195-199; (b) Albanese, D., Liquid-liquid phase transfer catalysis: basic principles and synthetic applications. In *Interfacial Catalysis*, CRC Press: 2002; pp 209-232.
- [50]. Tokitoh, Y.; Yoshimura, N. Method for production of α,ω -dialdehydes. US: 1989.
- [51]. Mercier, C.; Chabardes, P. Organometallic chemistry in industrial vitamin A and vitamin E synthesis. *Pure Appl. Chem.*, **1994**, 66(7), 1509-1518.
- [52]. (a) Bohnen, H.-W.; Cornils, B., Hydroformylation of alkenes: An industrial view of the status and importance. In *Advances in Catalysis*, Academic Press: 2002; Vol. 47, pp 1-64; (b) Franke, R.; Selent, D.; Börner, A. Applied hydroformylation. *Chem. Rev.*, **2012**, 112(11), 5675-5732.
- [53]. Haber, S.; Kleinert, H. DE 19527118, 1997, S. *Haber, HJ Kleinert (Hoechst AG), DE*, **1997**, 19535528.
- [54]. Goubet, D.; Meric, P.; Dormoy, J.-R.; Moreau, P. New practical syntheses of 4'-methylbiphenyl-2-carbonitrile and -2-carbaldehyde. *J. Org. Chem.*, **1999**, 64(12), 4516-4518.
- [55]. Desset, S. L.; Reader, S. W.; Cole-Hamilton, D. J. Aqueous-biphasic hydroformylation of alkenes promoted by "weak" surfactants. *Green Chem.*, **2009**, 11(5), 630-637.
- [56]. Kania, N.; Léger, B.; Fourmentin, S.; Monflier, E.; Ponchel, A. Activated carbon as a mass-transfer additive in aqueous organometallic catalysis. *Chem. Eur. J.*, **2010**, 16(21), 6138-6142.
- [57]. (a) Hamamoto, H.; Suzuki, Y.; Yamada, Y. M. A.; Tabata, H.; Takahashi, H.; Ikegami, S. A recyclable catalytic system based on a temperature-responsive catalyst. *Angew. Chem. Int. Edit.*, **2005**, 44(29), 4536-4538; (b) Chen, T.; Xu, Z.; Zhou, L.; Qiu, J.; Wang, M.; Wang, J. Highly efficient polymer-based nanoreactors for selective oxidation of alcohols in water. *Mol. Catal.*, **2019**, 474, 110422.
- [58]. Azoui, H.; Baczko, K.; Cassel, S.; Larpent, C. Thermoregulated aqueous biphasic catalysis of Heck reactions using an amphiphilic dipyrindyl-based ligand. *Green Chem.*, **2008**, 10(11), 1197-1203.
- [59]. Osburn, P. L.; Bergbreiter, D. E. Molecular engineering of organic reagents and catalysts using soluble polymers. *Prog. Polym. Sci.*, **2001**, 26(10), 2015-2081.
- [60]. (a) Sheldon, R. A. Green solvents for sustainable organic synthesis: State of the art. *Green Chem.*, **2005**, 7(5), 267-278; (b) Liu, S.; Xiao, J. Toward green catalytic synthesis-transition metal-catalyzed reactions in non-conventional media. *J. Mol. Catal. A Chem.*, **2007**, 270(1), 1-43.
- [61]. Behr, A.; Henze, G.; Schomäcker, R. Thermoregulated liquid/liquid catalyst

- separation and recycling. *Adv. Synth. Catal.*, **2006**, 348(12-13), 1485-1495.
- [62]. (a) Obrecht, L.; Kamer, P. C.; Laan, W. Alternative approaches for the aqueous-organic biphasic hydroformylation of higher alkenes. *Catal. Sci. Technol.*, **2013**, 3(3), 541-551; (b) Hapiot, F.; Bricout, H.; Menuel, S.; Tilloy, S.; Monflier, E. Recent breakthroughs in aqueous cyclodextrin-assisted supramolecular catalysis. *Catal. Sci. Technol.*, **2014**, 4(7), 1899-1908.
- [63]. (a) Nur, H.; Ikeda, S.; Ohtani, B. Phase-boundary catalysis: A new approach in alkene epoxidation with hydrogen peroxide by zeolite loaded with alkylsilane-covered titanium oxide. *Chem. Commun.*, **2000**, (22), 2235-2236; (b) Nur, H.; Ikeda, S.; Ohtani, B. Phase-boundary catalysis of alkene epoxidation with aqueous hydrogen peroxide using amphiphilic zeolite particles loaded with titanium oxide. *J. Catal.*, **2001**, 204(2), 402-408.
- [64]. (a) Ding, H.; Hanson, B. E.; Bartik, T.; Bartik, B. Two-phase hydroformylation of octene-1 with rhodium complexes of $P[C_6H_4(CH_2)_mC_6H_4-p-SO_3Na]_3$ ($m = 3, 6$). Rate and selectivity enhancement with surface-active phosphines. *Organometallics*, **1994**, 13(10), 3761-3763; (b) Monteil, F.; Queau, R.; Kalck, P. Behaviour of water-soluble dinuclear rhodium complexes in the hydroformylation reaction of oct-1-ene. *J. Organomet. Chem.*, **1994**, 480(1), 177-184; (c) Purwanto, P.; Delmas, H. Gas-liquid-liquid reaction engineering: Hydroformylation of 1-octene using a water soluble rhodium complex catalyst. *Catal. Today*, **1995**, 24(1), 135-140; (d) Pagar, N. S.; Deshpande, R. M. Kinetics of 1-decene hydroformylation in an aqueous biphasic medium using a water-soluble Rh-sulfoxantphos catalyst in the presence of a cosolvent. *Int. J. Chem. Kinet.*, **2021**, 53(3), 333-344.
- [65]. Jagtap, S.; Deshpande, R. True water soluble palladium-catalyzed Heck reactions in aqueous-organic biphasic media. *Tetrahedron Lett.*, **2013**, 54(21), 2733-2736.
- [66]. Tang, J.; Cao, S.; Wang, J. CO₂-switchable Pickering emulsions: Efficient and tunable interfacial catalysis for alcohol oxidation in biphasic systems. *Chem. Commun.*, **2019**, 55(74), 11079-11082.
- [67]. Byun, H. S.; Lee, D. H. Phase behavior of binary and ternary mixtures of poly(decyl acrylate)-supercritical solvents-decyl acrylate and poly(decyl methacrylate)-CO₂-decyl methacrylate systems. *Ind. Eng. Chem. Res.*, **2006**, 45(10), 3373-3380.
- [68]. Lu, A.; O'Reilly, R. K. Advances in nanoreactor technology using polymeric nanostructures. *Curr. Opin. Biotech.*, **2013**, 24(4), 639-645.
- [69]. Dwars, T.; Paetzold, E.; Oehme, G. Reactions in micellar systems. *Angew. Chem. Int. Edit.*, **2005**, 44(44), 7174-7199.
- [70]. Hamerla, T.; Rost, A.; Kasaka, Y.; Schomäcker, R. Hydroformylation of 1-dodecene with water-soluble rhodium catalysts with bidentate ligands in multiphase systems. *ChemCatChem*, **2013**, 5(7), 1854-1862.
- [71]. Deraedt, C.; Salmon, L.; Etienne, L.; Ruiz, J.; Astruc, D. "Click" dendrimers as efficient nanoreactors in aqueous solvent: Pd nanoparticle stabilization for sub-ppm Pd catalysis of Suzuki-Miyaura reactions of aryl bromides. *Chem. Commun.*, **2013**, 49(74), 8169-8171.
- [72]. Lobry, E.; Cardozo, A. F.; Barthe, L.; Blanco, J.-F.; Delmas, H.; Chen, S.; Gayet, F.; Zhang, X.; Lansalot, M.; D'Agosto, F.; Poli, R.; Manoury, E.; Julcour, C. Core

- phosphine-functionalized amphiphilic nanogels as catalytic nanoreactors for aqueous biphasic hydroformylation. *J. Catal.*, **2016**, 342, 164-172.
- [73]. Galetti, M.; Rossi, S.; Caffarra, C.; Gerboles, A. G.; Miragoli, M., Chapter 9 - Innovation in nanomedicine and engineered nanomaterials for therapeutic purposes. In *Exposure to Engineered Nanomaterials in the Environment*, Marmiroli, N.; White, J. C.; Song, J., Eds. Elsevier: 2019; pp 235-262.
- [74]. Nabid, M. R.; Bide, Y. H40-PCL-PEG unimolecular micelles both as anchoring sites for palladium nanoparticles and micellar catalyst for Heck reaction in water. *Appl. Catal. A: Gen.*, **2014**, 469, 183-190.
- [75]. Lu, J.; Dimroth, J.; Weck, M. Compartmentalization of incompatible catalytic transformations for tandem catalysis. *J. Am. Chem. Soc.*, **2015**, 137(40), 12984-12989.
- [76]. Sambou, S. S.; Hromov, R.; Ruzhylo, I.; Wang, H.; Allandrieu, A.; Sabatier, C.; Coppel, Y.; Daran, J.-C.; Gayet, F.; Labande, A.; Manoury, E.; Poli, R. Amphiphilic polymeric nanoreactors containing Rh(I)-NHC complexes for the aqueous biphasic hydrogenation of alkenes. *Catal. Sci. Technol.*, **2021**.
- [77]. Herrmann, W. A.; Frey, G. D.; Herdtweck, E.; Steinbeck, M. Synthesis and characterization of N-heterocyclic carbene substituted phosphine and phosphite rhodium complexes and their catalytic properties in hydrogenation reactions. *Adv. Synth. Catal.*, **2007**, 349(10), 1677-1691.
- [78]. (a) Delaittre, G.; Dire, C.; Rieger, J.; Putaux, J.-L.; Charleux, B. Formation of polymer vesicles by simultaneous chain growth and self-assembly of amphiphilic block copolymers. *Chem. commun.*, **2009**, (20), 2887-2889; (b) Blanazs, A.; Madsen, J.; Battaglia, G.; Ryan, A. J.; Armes, S. P. Mechanistic insights for block copolymer morphologies: How do worms form vesicles? *J. Am. Chem. Soc.*, **2011**, 133(41), 16581-16587.
- [79]. Fendler, E. J.; Fendler, J. H., Micellar catalysis in organic reactions: Kinetic and mechanistic implications. In *Advances in Physical Organic Chemistry*, Gold, V., Ed. Academic Press: 1970; Vol. 8, pp 271-406.
- [80]. (a) Holmberg, K. Organic reactions in microemulsions. *Eur. J. Org. Chem.*, **2007**, 2007(5), 731-742; (b) Mancin, F.; Scrimin, P.; Tecilla, P.; Tonellato, U. Amphiphilic metalloaggregates: Catalysis, transport, and sensing. *Coordin. Chem. Rev.*, **2009**, 253(17), 2150-2165; (c) Buurma, N. J. Reactivity in organised assemblies. *Annual Reports Section "B" (Organic Chemistry)*, **2012**, 108(0), 316-333; (d) La Sorella, G.; Strukul, G.; Scarso, A. Recent advances in catalysis in micellar media. *Green Chem.*, **2015**, 17(2), 644-683; (e) Shen, T.; Zhou, S.; Ruan, J.; Chen, X.; Liu, X.; Ge, X.; Qian, C. Recent advances on micellar catalysis in water. *Adv. Colloid Interfac.*, **2021**, 287, 102299.
- [81]. Charleux, B.; Delaittre, G.; Rieger, J.; D'Agosto, F. Polymerization-induced self-assembly: From soluble macromolecules to block copolymer nano-objects in one step. *Macromolecules*, **2012**, 45(17), 6753-6765.
- [82]. (a) Zhang, L.; Eisenberg, A. Multiple morphologies of "Crew-Cut" aggregates of polystyrene-b-poly(acrylic acid) block copolymers. *Science*, **1995**, 268(5218), 1728-1731; (b) Thurmond, K. B.; Kowalewski, T.; Wooley, K. L. Water-soluble knedel-

- like structures: The preparation of shell-cross-linked small particles. *J. Am. Chem. Soc.*, **1996**, 118(30), 7239-7240.
- [83]. Liu, Y.; Piñón, V.; Weck, M. Poly (norbornene) block copolymer-based shell cross-linked micelles with Co (III)–salen cores. *Polym. Chem.*, **2011**, 2(9), 1964-1975.
- [84]. (a) Sugihara, S.; Ito, S.; Irie, S.; Ikeda, I. Synthesis of thermoresponsive shell cross-linked micelles via living cationic polymerization and UV irradiation. *Macromolecules*, **2010**, 43(4), 1753-1760; (b) Liu, Y.; Wang, Y.; Wang, Y.; Lu, J.; Piñón III, V.; Weck, M. Shell cross-linked micelle-based nanoreactors for the substrate-selective hydrolytic kinetic resolution of epoxides. *J. Am. Chem. Soc.*, **2011**, 133(36), 14260-14263.
- [85]. Delaittre, G.; Save, M.; Charleux, B. Nitroxide-mediated aqueous dispersion polymerization: From water-soluble macroalkoxyamine to thermosensitive nanogels. *Macromol. Rapid Comm.*, **2007**, 28(15), 1528-1533.
- [86]. Liu, S.; Weaver, J. V. M.; Save, M.; Armes, S. P. Synthesis of pH-responsive shell cross-Linked micelles and their use as nanoreactors for the preparation of gold nanoparticles. *Langmuir*, **2002**, 18(22), 8350-8357.
- [87]. (a) Zhang, Y.; Han, G.; Cao, M.; Guo, T.; Zhang, W. Influence of solvophilic homopolymers on RAFT polymerization-induced self-assembly. *Macromolecules*, **2018**, 51(11), 4397-4406; (b) Zhou, L.; Qiu, J.; Wang, M.; Xu, Z.; Wang, J.; Chen, T. Fabrication of nanoreactors based on end-functionalized polymethacrylate and their catalysis application. *J. Inorg. Organomet. P.*, **2020**, 30(11), 4569-4577; (c) Zhao, Q.; Liu, Q.; Li, C.; Cao, L.; Ma, L.; Wang, X.; Cai, Y. Noncovalent structural locking of thermoresponsive polyion complex micelles, nanowires, and vesicles via polymerization-induced electrostatic self-assembly using an arginine-like monomer. *Chem. Commun.*, **2020**, 56(36), 4954-4957.
- [88]. Chaduc, I.; Crepet, A. s.; Boyron, O.; Charleux, B.; D'Agosto, F.; Lansalot, M. Effect of the pH on the RAFT polymerization of acrylic acid in water. Application to the synthesis of poly (acrylic acid)-stabilized polystyrene particles by RAFT emulsion polymerization. *Macromolecules*, **2013**, 46(15), 6013-6023.
- [89]. Chen, T.; Xu, Z.; Zhou, L.; Hua, L.; Zhang, S.; Wang, J. Temperature responsive polymer-supported TEMPO: An efficient and recoverable catalyst for the selective oxidation of alcohols. *Tetrahedron Lett.*, **2019**, 60(5), 419-422.
- [90]. Cotanda, P.; Lu, A.; Patterson, J. P.; Petzetakis, N.; O'Reilly, R. K. Functionalized organocatalytic nanoreactors: Hydrophobic pockets for acylation reactions in water. *Macromolecules*, **2012**, 45(5), 2377-2384.
- [91]. Qiu, J.; Meng, F.; Wang, M.; Huang, J.; Wang, C.; Li, X.; Yang, G.; Hua, Z.; Chen, T. Recyclable DMAP-functionalized polymeric nanoreactors for highly efficient acylation of alcohols in aqueous systems. *Polymer*, **2021**, 222, 123660.
- [92]. Gall, B.; Bortenschlager, M.; Nuyken, O.; Weberskirch, R. Cascade reactions in polymeric nanoreactors: Mono (Rh)- and bimetallic (Rh/Ir) micellar catalysis in the hydroaminomethylation of 1-octene. *Macromol. Chem. Phys.*, **2008**, 209(11), 1152-1159.
- [93]. Boucher-Jacobs, C.; Rabnawaz, M.; Katz, J. S.; Even, R.; Guironnet, D. Encapsulation of catalyst in block copolymer micelles for the polymerization of

- ethylene in aqueous medium. *Nat. Commun.*, **2018**, 9(1), 841-849.
- [94]. Zhang, X.; Cardozo Perez, A. F.; Chen, S.; Zhang, W.; Julcour-Lebigue, C.; Lansalot, M.; Blanco, J.-F.; Gayet, F.; Delmas, H.; Charleux, B.; Manoury, E.; D'Agosto, F.; Poli, R. Core-shell nanoreactors for efficient aqueous biphasic catalysis. *Chem. Eur. J.*, **2014**, 20(47), 15505-15517.
- [95]. (a) Takanobu, S.; Yuya, O.; Yuriko, N.; Masato, T.; Hideki, S. Metal nanoparticles derived from polysilane shell cross-linked micelle templates. *Chem. Lett.*, **2003**, 32(10), 980-981; (b) Okamoto, K.; Akiyama, R.; Yoshida, H.; Yoshida, T.; Kobayashi, S. Formation of nanoarchitectures including subnanometer palladium clusters and their use as highly active catalysts. *J. Am. Chem. Soc.*, **2005**, 127(7), 2125-2135; (c) Ievins, A. D.; Wang, X.; Moughton, A. O.; Skey, J.; O'Reilly, R. K. Synthesis of core functionalized polymer micelles and shell cross-linked nanoparticles. *Macromolecules*, **2008**, 41(9), 2998-3006.
- [96]. Liu, R.; Wang, S.; Yao, J.; Xu, W.; Li, H. Cross-linked reverse micelles with embedded water pools: a novel catalytic system based on amphiphilic block copolymers. *RSC Adv.*, **2014**, 4(72), 38234-38240.
- [97]. Moore, B. L.; Moatsou, D.; Lu, A.; O'Reilly, R. K. Studying the activity of the MacMillan catalyst embedded within hydrophobic cross-linked polymeric nanostructures. *Polym. Chem.*, **2014**, 5(10), 3487-3494.
- [98]. (a) Terashima, T.; Kamigaito, M.; Baek, K.-Y.; Ando, T.; Sawamoto, M. Polymer catalysts from polymerization catalysts: direct encapsulation of metal catalyst into star polymer core during metal-catalyzed living radical polymerization. *J. Am. Chem. Soc.*, **2003**, 125(18), 5288-5289; (b) Terashima, T.; Ouchi, M.; Ando, T.; Sawamoto, M. In situ hydrogenation of terminal halogen in poly(methyl methacrylate) by ruthenium-catalyzed living radical polymerization: Direct transformation of "polymerization catalyst" into "hydrogenation catalyst". *J. Am. Chem. Soc.*, **2006**, 128(34), 11014-11015; (c) Terashima, T.; Ouchi, M.; Ando, T.; Kamigaito, M.; Sawamoto, M. Metal-complex-bearing star polymers by metal-catalyzed living radical polymerization: Synthesis and characterization of poly(methyl methacrylate) star polymers with Ru(II)-embedded microgel cores. *J. Polym. Sci., Polym. Chem.*, **2006**, 44(17), 4966-4980; (d) Terashima, T.; Nomura, A.; Ito, M.; Ouchi, M.; Sawamoto, M. Star-polymer-catalyzed living radical polymerization: Microgel-core reaction vessel by tandem catalyst interchange. *Angew. Chem. Int. Edit.*, **2011**, 50(34), 7892-7895.
- [99]. Terashima, T.; Ouchi, M.; Ando, T.; Sawamoto, M. Thermoregulated phase-transfer catalysis via PEG-armed Ru(II)-bearing microgel core star polymers: Efficient and reusable Ru(II) catalysts for aqueous transfer hydrogenation of ketones. *J. Polym. Sci., Polym. Chem.*, **2010**, 48(2), 373-379.
- [100]. Chen, S.; Gayet, F.; Manoury, E.; Joumaa, A.; Lansalot, M.; D'Agosto, F.; Poli, R. Coordination chemistry inside polymeric nanoreactors: Interparticle metal exchange and ionic compound vectorization in phosphine-functionalized amphiphilic polymer latexes. *Chem. Eur. J.*, **2016**, 22(18), 6302-6313.
- [101]. Carletto, A.; Cardozo, A. F.; Suriano, R.; Manoury, E.; Turri, S.; Poli, R. Core cross-linked amphiphilic star-block copolymers with (meth)acrylic acid shells prepared by

- atom transfer radical polymerization. *Isr. J. Chem.*, **2012**, 52(3-4), 328-338.
- [102]. Cardozo, A. F.; Manoury, E.; Julcour, C.; Blanco, J.-F.; Delmas, H.; Gayet, F.; Poli, R. Preparation of polymer supported phosphine ligands by metal catalyzed living radical copolymerization and their application to hydroformylation catalysis. *ChemCatChem*, **2013**, 5(5), 1161-1169.
- [103]. Cardozo, A. F.; Manoury, E.; Julcour, C.; Blanco, J.-F.; Delmas, H.; Gayet, F.; Poli, R. Preparation of phosphine-functionalized polystyrene stars by metal catalyzed controlled radical copolymerization and their application to hydroformylation catalysis. *Dalton T.*, **2013**, 42(25), 9148-9156.
- [104]. (a) Zhang, W.; D'Agosto, F.; Boyron, O.; Rieger, J.; Charleux, B. One-pot synthesis of poly(methacrylic acid-co-poly(ethylene oxide) methyl ether methacrylate)-b-polystyrene amphiphilic block copolymers and their self-assemblies in water via RAFT-mediated radical emulsion polymerization. A kinetic study. *Macromolecules*, **2011**, 44(19), 7584-7593; (b) Zhang, W.; D'Agosto, F.; Boyron, O.; Rieger, J.; Charleux, B. Toward a better understanding of the parameters that lead to the formation of nonspherical polystyrene particles via RAFT-mediated one-pot aqueous emulsion polymerization. *Macromolecules*, **2012**, 45(10), 4075-4084.
- [105]. (a) Cardozo, A. F.; Julcour, C.; Barthe, L.; Blanco, J.-F.; Chen, S.; Gayet, F.; Manoury, E.; Zhang, X.; Lansalot, M.; Charleux, B.; D'Agosto, F.; Poli, R.; Delmas, H. Aqueous phase homogeneous catalysis using core-shell nanoreactors: Application to rhodium-catalyzed hydroformylation of 1-octene. *J. Catal.*, **2015**, 324, 1-8; (b) Poli, R.; Chen, S.; Zhang, X.; Cardozo, A.; Lansalot, M.; D'Agosto, F.; Charleux, B.; Manoury, E.; Gayet, F.; Julcour, C.; Blanco, J.-F.; Barthe, L.; Delmas, H. One-pot RAFT synthesis of triphenylphosphine-functionalized amphiphilic core-shell polymers and application as catalytic nanoreactors in aqueous biphasic hydroformylation. *ACS Symp. Ser.*, **2015**, 1188, 203-220.
- [106]. Chen, S.; Cardozo, A. F.; Julcour, C.; Blanco, J.-F.; Barthe, L.; Gayet, F.; Lansalot, M.; D'Agosto, F.; Delmas, H.; Manoury, E.; Poli, R. Amphiphilic core-cross-linked micelles functionalized with bis(4-methoxyphenyl)phenylphosphine as catalytic nanoreactors for biphasic hydroformylation. *Polymer*, **2015**, 72, 327-335.
- [107]. Joumaa, A.; Gayet, F.; Garcia-Suarez, E. J.; Himmelstrup, J.; Riisager, A.; Poli, R.; Manoury, E. Synthesis of nixantphos core-functionalized amphiphilic nanoreactors and application to rhodium-catalyzed aqueous biphasic 1-octene hydroformylation. *Polymers*, **2020**, 12(5), 1107-1124.
- [108]. Manoury, E.; Gayet, F.; D'Agosto, F.; Lansalot, M.; Delmas, H.; Julcour, C.; Blanco, J.-F.; Barthe, L.; Poli, R., Core-cross-linked micelles and amphiphilic nanogels as unimolecular nanoreactors for micellar-type, metal-based aqueous biphasic catalysis. In *Effects of Nanoconfinement on Catalysis*, Poli, R., Ed. Springer: New York, 2017; pp 147-172.
- [109]. Ahmad, J.; Si, C.; Sandrine, V.; Florence, G.; Rinaldo, P.; Eric, M. Rhodium-catalyzed aqueous biphasic hydrogenation of alkenes with amphiphilic phosphine-containing core-shell polymers. *Mol. Cat.*, **2017**, 438, 267-271.
- [110]. (a) Chai, W.; Zhang, Y.; Hou, Y. Well-defined cationic polyacrylamides with dot-charges: Synthesis via an aqueous living RAFT polymerization, characterization, and

- intrinsic viscosity. *Polym. Chem.*, **2013**, 4(4), 1006-1013; (b) Chakrabarty, A.; Singha, N. K. Tunable morphology and hydrophobicity of polyfluoroacrylate/clay nanocomposite prepared by in situ RAFT polymerization in miniemulsion. *Macromol. Chem. Phys.*, **2015**, 216(6), 650-661; (c) Huang, B.; Jiang, J.; Kang, M.; Liu, P.; Sun, H.; Li, B.; Wang, W. Synthesis of block cationic polyacrylamide precursors using an aqueous RAFT dispersion polymerization. *RSC Adv.*, **2019**, 9(22), 12370-12383; (d) Bravo-Anaya, L. M.; Rosselgong, J.; Fernández-Solís, K. G.; Xiao, Y.; Vax, A.; Ibarboure, E.; Ruban, A.; Lebleu, C.; Joucla, G.; Garbay, B.; Garanger, E.; Lecommandoux, S. Coupling of RAFT polymerization and chemoselective post-modifications of elastin-like polypeptides for the synthesis of gene delivery hybrid vectors. *Polym. Chem.*, **2021**, 12(2), 226-241.
- [111]. Yusa, S.-i.; Konishi, Y.; Mitsukami, Y.; Yamamoto, T.; Morishima, Y. pH-responsive micellization of amine-containing cationic diblock copolymers prepared by reversible addition-fragmentation chain transfer (RAFT) radical polymerization. *Polym. J.*, **2005**, 37(7), 480-488.
- [112]. Sponchioni, M.; Capasso Palmiero, U.; Manfredini, N.; Moscatelli, D. RAFT copolymerization of oppositely charged monomers and its use to tailor the composition of nonfouling polyampholytes with an UCST behaviour. *React. Chem. Eng.*, **2019**, 4(2), 436-446.
- [113]. Cao, X.; An, Z. RAFT synthesis in water of cationic polyelectrolytes with tunable UCST. *Macromol. Rapid Comm.*, **2015**, 36(23), 2107-2110.
- [114]. (a) Scales, C. W.; Huang, F.; Li, N.; Vasilieva, Y. A.; Ray, J.; Convertine, A. J.; McCormick, C. L. Corona-stabilized interpolyelectrolyte complexes of SiRNA with nonimmunogenic, hydrophilic/cationic block copolymers prepared by aqueous RAFT polymerization. *Macromolecules*, **2006**, 39(20), 6871-6881; (b) Gurbuz, N.; Demirci, S.; Yavuz, S.; Caykara, T. Synthesis of cationic N-[3-(dimethylamino)propyl]methacrylamide brushes on silicon wafer via surface-initiated RAFT polymerization. *J. Polym. Sci. Pol. Chem.*, **2011**, 49(2), 423-431.
- [115]. (a) Lowe, A. B.; Sumerlin, B. S.; Donovan, M. S.; Thomas, D. B.; Hennaux, P.; McCormick, C. L., RAFT polymerization in homogeneous aqueous media. In *Advances in controlled/living radical polymerization*, American Chemical Society: 2003; Vol. 854, pp 586-602; (b) Vasilieva, Y. A.; Thomas, D. B.; Scales, C. W.; McCormick, C. L. Direct controlled polymerization of a cationic methacrylamido monomer in aqueous media via the RAFT process. *Macromolecules*, **2004**, 37(8), 2728-2737; (c) Demirci, S.; Caykara, T. High density cationic polymer brushes from combined “click chemistry” and RAFT-mediated polymerization. *J. Polym. Sci. Pol. Chem.*, **2012**, 50(15), 2999-3007.
- [116]. Borguet, Y. P.; Tsarevsky, N. V. Controlled radical polymerization of a styrenic sulfonium monomer and post-polymerization modifications. *Polym. Chem.*, **2013**, 4(6), 2115-2124.
- [117]. Yang, J.; Sun, W.; Lin, W.; Shen, Z. Synthesis and magnetic properties of comb-like copolymeric complexes based on thiazole ring and ionic liquid. *J. Polym. Sci. Pol. Chem.*, **2008**, 46(15), 5123-5132.
- [118]. Vijayakrishna, K.; Jewrajka, S. K.; Ruiz, A.; Marcilla, R.; Pomposo, J. A.;

- Mecerreyes, D.; Taton, D.; Gnanou, Y. Synthesis by RAFT and ionic responsiveness of double hydrophilic block copolymers based on ionic liquid monomer inits. *Macromolecules*, **2008**, 41(17), 6299-6308.
- [119]. Mori, H.; Yahagi, M.; Endo, T. RAFT polymerization of N-vinylimidazolium salts and synthesis of thermoresponsive ionic liquid block copolymers. *Macromolecules*, **2009**, 42(21), 8082-8092.
- [120]. Mertoglu, M.; Laschewsky, A.; Skrabania, K.; Wieland, C. New water soluble agents for reversible addition-fragmentation chain transfer polymerization and their application in aqueous solutions. *Macromolecules*, **2005**, 38(9), 3601-3614.
- [121]. Destarac, M.; Guinaudeau, A.; Geagea, R.; Mazieres, S.; Van Gramberen, E.; Boutin, C.; Chadel, S.; Wilson, J. Aqueous MADIX/RAFT polymerization of diallyldimethylammonium chloride: Extension to the synthesis of poly(DADMAC)-based double hydrophilic block copolymers. *J. Polym. Sci. Pol. Chem.*, **2010**, 48(22), 5163-5171.
- [122]. Chaduc, I.; Zhang, W.; Rieger, J.; Lansalot, M.; D'Agosto, F.; Charleux, B. Amphiphilic block copolymers from a direct and one-pot RAFT synthesis in water. *Macromol. Rapid Comm.*, **2011**, 32(16), 1270-1276.
- [123]. (a) Salamone, J. C.; Mahmud, M. U.; Watterson, A. C.; Olson, A. P.; Ellis, E. J. Polymerization of vinylpyridinium salts. XII. Occurrence of radical polymerization in spontaneous reactions. *Journal of Polymer Science: Polymer Chemistry Edition*, **1982**, 20(5), 1153-1167; (b) Benjelloun, A.; Damas, C.; Brembilla, A.; Lochon, P. N-alkyl-3-vinylpyridinium salts: Homopolymerization of the hexadecyl derivative and behaviour study of the polymer in aqueous media. *Polym. Bull.*, **1994**, 33(5), 513-520; (c) Navrotskii, A. V.; Novakov, I. A.; Zauer, E. A.; Orlyanskii, V. V.; Navrotskii, V. A. Kinetics of 1,2-dimethyl-5-vinylpyridinium methylsulfate polymerization initiated by tert-butylperoxypropanol. *Polym. Sci. Ser. A*, **1999**, 41(4), 384-388; (d) Navrotskii, A. V.; Makeev, S. M.; Orlyanskii, M. V.; Navrotskii, V. A.; Novakov, I. A. Specific features of 1,2-dimethyl-5-vinylpyridinium methyl sulfate polymerization in the presence of α -amino acids. *Polym. sci., Ser. B*, **2003**, 45(7-8), 213-215.
- [124]. Medjahed, K.; Tennouga, L.; Mansri, A. Series of poly(4-vinylpyridine) containing quaternary alkyl bromides: Synthesis and determination percentage of quaternization. *Macromol. Symp.*, **2014**, 339(1), 130-133.
- [125]. Tennouga, L.; Bensalah, W.; Mansri, A. Poly (N-octyl-4-vinylpyridinium bromide) copolymers in aqueous solutions: Potentiometric and thermodynamic studies. *e-Polymers*, **2018**, 18(6), 551-558.
- [126]. Convertine, A. J.; Sumerlin, B. S.; Thomas, D. B.; Lowe, A. B.; McCormick, C. L. Synthesis of block copolymers of 2- and 4-vinylpyridine by RAFT polymerization. *Macromolecules*, **2003**, 36(13), 4679-4681.
- [127]. Božović-Vukić, J.; Mañon, H. T.; Meuldijk, J.; Koning, C.; Klumperman, B. SAN-*b*-P4VP block copolymer synthesis by chain extension from RAFT-functional poly(4-vinylpyridine) in solution and in emulsion. *Macromolecules*, **2007**, 40(20), 7132-7139.
- [128]. (a) Wan, W.; Pan, C. One-pot synthesis of polymeric nanomaterials via RAFT

- dispersion polymerization induced self-assembly and re-organization. *Polym. Chem.*, **2010**, 1(9), 1475-1484; (b) Dong, S.; Zhao, W.; Lucien, F. P.; Perrier, S.; Zetterlund, P. B. Polymerization induced self-assembly: Tuning of nano-object morphology by use of CO₂. *Polym. Chem.*, **2015**, 6(12), 2249-2254.
- [129]. Liu, H.; Ding, M.; Ding, Z.; Gao, C.; Zhang, W. In situ synthesis of the Ag/poly(4-vinylpyridine)-block-polystyrene composite nanoparticles by dispersion RAFT polymerization. *Polym. Chem.*, **2017**, 8(20), 3203-3210.
- [130]. Zhang, W.; Hong, C.; Pan, C. Fabrication of spaced concentric vesicles and polymerizations in RAFT dispersion polymerization. *Macromolecules*, **2014**, 47(5), 1664-1671.
- [131]. Carlsson, L.; Fall, A.; Chaduc, I.; Wågberg, L.; Charleux, B.; Malmström, E.; D'Agosto, F.; Lansalot, M.; Carlmark, A. Modification of cellulose model surfaces by cationic polymer latexes prepared by RAFT-mediated surfactant-free emulsion polymerization. *Polym. Chem.*, **2014**, 5(20), 6076-6086.
- [132]. Semsarilar, M.; Ladmiral, V.; Blanazs, A.; Armes, S. P. Anionic polyelectrolyte-stabilized nanoparticles via RAFT aqueous dispersion polymerization. *Langmuir*, **2012**, 28(1), 914-922.
- [133]. (a) Semsarilar, M.; Ladmiral, V.; Blanazs, A.; Armes, S. P. Cationic polyelectrolyte-stabilized nanoparticles via RAFT aqueous dispersion polymerization. *Langmuir*, **2013**, 29(24), 7416-7424; (b) Williams, M.; Penfold, N.; Armes, S. Cationic and reactive primary amine-stabilised nanoparticles via RAFT aqueous dispersion polymerisation. *Polym. Chem.*, **2016**, 7(2), 384-393.
- [134]. Zhang, B.; Yan, X.; Alcouffe, P.; Charlot, A.; Fleury, E.; Bernard, J. Aqueous RAFT polymerization of imidazolium-type ionic liquid monomers: En route to poly(ionic liquid)-based nanoparticles through RAFT polymerization-induced self-assembly. *ACS Macro Letters*, **2015**, 4(9), 1008-1011.
- [135]. Fischer, A.; Brembilla, A.; Lochon, P. Synthesis of new amphiphilic cationic block copolymers and study of their behaviour in aqueous medium as regards hydrophobic microdomain formation. *Polymer*, **2001**, 42(4), 1441-1448.1.
- [136]. (a) Zamfir, M.; Patrickios, C. S.; Montagne, F.; Abetz, C.; Abetz, V.; Oss-Ronen, L.; Talmon, Y. Styrene-vinyl pyridine diblock copolymers: Synthesis by RAFT polymerization and self-assembly in solution and in the bulk. *J. Polym. Sci. Pol. Chem.*, **2012**, 50(8), 1636-1644; (b) Chen, A.; Blakey, I.; Whittaker, A. K.; Peng, H. The influence of casting parameters on the surface morphology of PS-*b*-P4VP honeycomb films. *J. Polym. Sci. Pol. Chem.*, **2016**, 54(23), 3721-3732.
- [137]. Derry, M. J.; Fielding, L. A.; Armes, S. P. Polymerization-induced self-assembly of block copolymer nanoparticles via RAFT non-aqueous dispersion polymerization. *Prog. Polym. Sci.*, **2016**, 52, 1-18.
- [138]. Ponnusamy, K.; Babu, R. P.; Dhamodharan, R. Synthesis of block and graft copolymers of styrene by raft polymerization, using dodecyl-based trithiocarbonates as initiators and chain transfer agents. *J. Polym. Sci. Pol. Chem.*, **2013**, 51(5), 1066-1078.
- [139]. Wan, W.; Pan, C. Formation of polymeric yolk/shell nanomaterial by polymerization-Induced self-assembly and reorganization. *Macromolecules*, **2010**, 43(6), 2672-2675.

- [140]. Di Grandi, M. J.; Curran, K. J.; Baum, E. Z.; Bebernitz, G.; Ellestad, G. A.; Ding, W.-D.; Lang, S. A.; Rossi, M.; Bloom, J. D. Pyrimido[1,2-b]-1,2,4,5-tetrazin-6-ones as HCMV protease inhibitors: a new class of heterocycles with flavin-like redox properties. *Bioorg. Med. Chem. Lett.*, **2003**, 13(20), 3483-3486.
- [141]. Mai, Y.; Eisenberg, A. Self-assembly of block copolymers. *Chem. Soc. Rev.*, **2012**, 41(18), 5969-5985.
- [142]. Rieger, J.; Grazon, C.; Charleux, B.; Alaimo, D.; Jérôme, C. Pegylated thermally responsive block copolymer micelles and nanogels via in situ RAFT aqueous dispersion polymerization. *J. Polym. Sci. Pol. Chem.*, **2009**, 47(9), 2373-2390.
- [143]. Chen, S.; Manoury, E.; Gayet, F.; Poli, R. Coordination chemistry inside polymeric nanoreactors: Metal migration and cross-exchange in amphiphilic core-shell polymer latexes. *Polymers*, **2016**, 8(2), 26-43.
- [144]. (a) D'Agosto, F.; Rieger, J.; Lansalot, M. RAFT-vermittelte polymerisationsinduzierte Selbstorganisation (PISA). *Angew. Chem.*, **2020**, 132(22), 8444-8470; (b) D'Agosto, F.; Rieger, J.; Lansalot, M. RAFT-mediated polymerization-induced self-assembly. *Angew. Chem. Int. Edit.*, **2020**, 59(22), 8368-8392.
- [145]. Trzeciak, A.; Jon, M.; Ziolkowski, J. Effect of free phosphine on the reactivity of phosphine-containing rhodium (I) complexes. *React. Kinet. Catal. L.*, **1982**, 20(3-4), 383-387.
- [146]. Mukhedkar, A. J.; Mukhedkar, V. A.; Green, M.; Stone, F. G. A. Reactions of low-valent metal complexes with fluorocarbons. Part XV. Acetylacetonatobis(methyldiphenyl- or triphenyl-phosphine)rhodium. **1970**, (0), 3166-3171.
- [147]. Naaktgeboren, A. J.; Nolte, R. J. M.; Drenth, W. Phosphorus-31 nuclear magnetic resonance studies of polymer-anchored rhodium(I) complexes. *J. Am. Chem. Soc.*, **1980**, 102(10), 3350-3354.
- [148]. (a) Lu, Y. D.; Wang, Y. H.; Jin, Z. L. Rh nanoparticles stabilized by PEG-substituted triphenyl-phosphine: A highly active and recyclable catalyst for aqueous biphasic hydrogenation of benzene. *Chinese Chem. Lett.*, **2010**, 21(9), 1067-1070; (b) Snelders, D. J. M.; Yan, N.; Gan, W.; Laurenczy, G.; Dyson, P. J. Tuning the chemoselectivity of Rh nanoparticle catalysts by site-selective poisoning with phosphine ligands: The hydrogenation of functionalized aromatic compounds. *ACS Catal.*, **2012**, 2(2), 201-207; (c) Llop Castelbou, J.; Bresó-Femenia, E.; Blondeau, P.; Chaudret, B.; Castellón, S.; Claver, C.; Godard, C. Tuning the selectivity in the hydrogenation of aromatic ketones catalyzed by similar ruthenium and rhodium nanoparticles. *ChemCatChem*, **2014**, 6(11), 3160-3168; (d) Niu, M.; Wang, Y.; Chen, P.; Du, D.; Jiang, J.; Jin, Z. Highly efficient and recyclable rhodium nanoparticle catalysts for hydrogenation of quinoline and its derivatives. *Catal. Sci. Technol.*, **2015**, 5(10), 4746-4749; (e) Tran, B. L.; Fulton, J. L.; Linehan, J. C.; Lercher, J. A.; Bullock, R. M. Rh(CAAC)-catalyzed arene hydrogenation: Evidence for nanocatalysis and sterically controlled site-selective hydrogenation. *ACS Catalysis*, **2018**, 8(9), 8441-8449.
- [149]. Ibrahim, M.; Wei, M. M.; Deydier, E.; Manoury, E.; Poli, R.; Lecante, P.; Philippot, K. Rhodium nanoparticles stabilized by ferrocenyl-phosphine ligands: Synthesis and

- catalytic styrene hydrogenation. *Dalton T.*, **2019**, 48(20), 6777-6786.
- [150]. Joumaa, A.; Chen, S.; Vincendeau, S.; Gayet, F.; Poli, R.; Manoury, E. Rhodium-catalyzed aqueous biphasic hydrogenation of alkenes with amphiphilic phosphine-containing core-shell polymers. *Mol. Cat.*, **2017**, 438, 267-271.
- [151]. Wang, H.; Vendrame, L.; Fliedel, C.; Chen, S.; Gayet, F.; D'Agosto, F.; Lansalot, M.; Manoury, E.; Poli, R. Triphenylphosphine-functionalized core-cross-linked micelles and nanogels with a polycationic outer shell: Synthesis and application in rhodium-catalyzed biphasic hydrogenations. *Chem. Eur. J.*, **2021**, 27(16), 5205-5214.
- [152]. (a) Schmid, G. Nanoparticles: From theory to application. John Wiley & Sons: 2011; (b) Talapin, D. V.; Shevchenko, E. V. Introduction: Nanoparticle chemistry. *Chem. Rev.*, **2016**, 116(18), 10343-10345; (c) Wu, L.; Mendoza-Garcia, A.; Li, Q.; Sun, S. Organic phase syntheses of magnetic nanoparticles and their applications. *Chem. Rev.*, **2016**, 116(18), 10473-10512; (d) Gilroy, K. D.; Ruditskiy, A.; Peng, H.-C.; Qin, D.; Xia, Y. Bimetallic nanocrystals: Syntheses, properties, and applications. *Chem. Rev.*, **2016**, 116(18), 10414-10472.
- [153]. (a) Jin, R.; Zeng, C.; Zhou, M.; Chen, Y. Atomically precise colloidal metal nanoclusters and nanoparticles: Fundamentals and opportunities. *Chem. Rev.*, **2016**, 116(18), 10346-10413; (b) Kang, X.; Zhu, M. Transformation of atomically precise nanoclusters by ligand-exchange. *Chem. Mater.*, **2019**, 31(24), 9939-9969; (c) Du, Y.; Sheng, H.; Astruc, D.; Zhu, M. Atomically precise noble metal nanoclusters as efficient catalysts: A bridge between structure and properties. *Chem. Rev.*, **2020**, 120(2), 526-622.
- [154]. (a) Roucoux, A.; Philippot, K.; de Vries, J.; Elsevier, C. The handbook of homogeneous hydrogenation. Wiley-VCH, Weinheim: 2007; (b) Bernhardt, T.; Heiz, U.; Landman, U., Chemical and catalytic properties of size-selected free and supported clusters. In *Nanocatalysis*, Heiz, U.; Landman, U., Eds. Springer Berlin Heidelberg: Berlin, Heidelberg, 2007; pp 1-191; (c) Serp, P.; Philippot, K. Nanomaterials in catalysis. Wiley Online Library: 2013.
- [155]. (a) Tao, A. R.; Habas, S.; Yang, P. Shape control of colloidal metal nanocrystals. *Small*, **2008**, 4(3), 310-325; (b) Chen, G.; Zhang, J.; Gupta, A.; Rosei, F.; Ma, D. Shape-controlled synthesis of ruthenium nanocrystals and their catalytic applications. *New J. Chem.*, **2014**, 38(5), 1827-1833; (c) Xia, Y.; Xia, X.; Peng, H.-C. Shape-controlled synthesis of colloidal metal nanocrystals: Thermodynamic versus kinetic products. *J. Am. Chem. Soc.*, **2015**, 137(25), 7947-7966.
- [156]. (a) Yuan, Y.; Yan, N.; Dyson, P. J. Advances in the rational design of rhodium nanoparticle catalysts: Control via manipulation of the nanoparticle core and stabilizer. *ACS Catalysis*, **2012**, 2(6), 1057-1069; (b) Zhukhovitskiy, A. V.; MacLeod, M. J.; Johnson, J. A. Carbene ligands in surface chemistry: From stabilization of discrete elemental allotropes to modification of nanoscale and bulk substrates. *Chem. Rev.*, **2015**, 115(20), 11503-11532; (c) Chen, T.; Rodionov, V. O. Controllable catalysis with nanoparticles: Bimetallic alloy systems and surface adsorbates. *ACS Catalysis*, **2016**, 6(6), 4025-4033; (d) Heuer-Jungemann, A.; Feliu, N.; Bakaimi, I.; Hamaly, M.; Alkilany, A.; Chakraborty, I.; Masood, A.; Casula, M. F.; Kostopoulou, A.; Oh, E.; Susumu, K.; Stewart, M. H.; Medintz, I. L.; Stratakis, E.;

- Parak, W. J.; Kanaras, A. G. The role of ligands in the chemical synthesis and applications of inorganic nanoparticles. *Chem. Rev.*, **2019**, 119(8), 4819-4880.
- [157]. Denicourt-Nowicki, A.; Roucoux, A. Odyssey in polyphasic catalysis by metal nanoparticles. *Chem. Rec.*, **2016**, 16(4), 2127-2141.
- [158]. (a) Sharma, G.; Ballauff, M. Cationic spherical polyelectrolyte brushes as nanoreactors for the generation of gold particles. *Macromol. Rapid Comm.*, **2004**, 25(4), 547-552; (b) Schrunner, M.; Polzer, F.; Mei, Y.; Lu, Y.; Haupt, B.; Ballauff, M.; Göldel, A.; Drechsler, M.; Preussner, J.; Glatzel, U. Mechanism of the formation of amorphous gold nanoparticles within spherical polyelectrolyte brushes. *Macromol. Chem. Phys.*, **2007**, 208(14), 1542-1547; (c) Schrunner, M.; Proch, S.; Mei, Y.; Kempe, R.; Miyajima, N.; Ballauff, M. Stable bimetallic gold-platinum nanoparticles immobilized on spherical polyelectrolyte brushes: Synthesis, characterization, and application for the oxidation of alcohols. *Adv. Mater.*, **2008**, 20(10), 1928-1933; (d) Malysheva, Y. B.; Gushchin, A. V.; Mei, Y.; Lu, Y.; Ballauff, M.; Proch, S.; Kempe, R. C-C coupling reaction of triphenylbismuth (V) derivatives and olefins in the presence of palladium nanoparticles immobilized in spherical polyelectrolyte brushes. WILEY-VCH Verlag Weinheim: 2008; (e) Schrunner, M.; Ballauff, M.; Talmon, Y.; Kauffmann, Y.; Thun, J.; Möller, M.; Breu, J. Single nanocrystals of platinum prepared by partial dissolution of Au-Pt nanoalloys. *Science*, **2009**, 323(5914), 617-620.
- [159]. Lu, Y.; Mei, Y.; Drechsler, M.; Ballauff, M. Thermosensitive core-shell particles as carriers for Ag nanoparticles: Modulating the catalytic activity by a phase transition in networks. *Angew. Chem. Int. Edit.*, **2006**, 45(5), 813-816.
- [160]. Lu, Y.; Mei, Y.; Walker, R.; Ballauff, M.; Drechsler, M. 'Nano-tree'-type spherical polymer brush particles as templates for metallic nanoparticles. *Polymer*, **2006**, 47(14), 4985-4995.
- [161]. Lu, Y.; Mei, Y.; Schrunner, M.; Ballauff, M.; Möller, M. W.; Breu, J. In situ formation of Ag nanoparticles in spherical polyacrylic acid brushes by UV irradiation. *J. Phys. Chem. C*, **2007**, 111(21), 7676-7681.
- [162]. Miguel, G.; Nguyet, T.; Sebastien, N.; Audrey, D. N.; Frederic, H.; Alain, R.; Eric, M.; Karine, P. About the use of rhodium nanoparticles in hydrogenation and hydroformylation reactions. *Curr. Org. Chem.*, **2013**, 17(4), 364-399.
- [163]. Duan, Z.; Hampden-Smith, M. J.; Sylwester, A. P. Room-temperature catalytic hydrogenation of aromatic hydrocarbons using rhodium complex [(1,5-COD)RhH]₄ [COD = 1,5-cyclooctadiene] as a catalyst precursor. *Chem. Mater.*, **1992**, 4(6), 1146-1148.
- [164]. (a) Ramirez-Meneses, E. Synthèse et caractérisation de nanoparticules métalliques à base de rodhium, platine et palladium, stabilisés par des ligands. Université Paul Sabatier Toulouse 3, Toulouse, 2004; (b) Ibrahim, M.; Garcia, M. A.; Vono, L. L.; Guerrero, M.; Lecante, P.; Rossi, L. M.; Philippot, K. Polymer versus phosphine stabilized Rh nanoparticles as components of supported catalysts: Implication in the hydrogenation of cyclohexene model molecule. *Dalton T.*, **2016**, 45(44), 17782-17791; (c) Garcia, M. A. S.; Ibrahim, M.; Costa, J. C. S.; Corio, P.; Gusevskaya, E. V.; dos Santos, E. N.; Philippot, K.; Rossi, L. M. Study of the influence of PPh₃ used

- as capping ligand or as reaction modifier for hydroformylation reaction involving Rh NPs as precatalyst. *Appl. Catal. A Gen.*, **2017**, 548, 136-142.
- [165]. Sun, Z.; Wang, Y.; Niu, M.; Yi, H.; Jiang, J.; Jin, Z. Poly(ethylene glycol)-stabilized Rh nanoparticles as efficient and recyclable catalysts for hydroformylation of olefins. *Catal. Commun.*, **2012**, 27, 78-82.
- [166]. (a) Nasar, K.; Fache, F.; Lemaire, M.; Béziat, J.-C.; Besson, M.; Gallezot, P. Stereoselective reduction of disubstituted aromatics on colloidal rhodium. *J. Mol. Catal.*, **1994**, 87(1), 107-115; (b) James, B.; Wang, Y.; Hu, T. Hydrogenation of substituted aromatics. *Chemical Industries New York Marcel Dekker*, **1996**, 423-428; (c) Hu, T.; James, B.; Lee, C.-L. Towards inhibition of yellowing of mechanical pulps. Part II: Water-soluble catalysts for the hydrogenation of lignin model compounds. *J. Pulp. Pap. Sci.*, **1997**, 23(5), J200-J205; (d) Hu, T. Q.; Lee, C.-L.; James, B. R.; Rettig, S. J. Stereoselective hydrogenation of lignin degradation model compounds. *Can. J. Chem.*, **1997**, 75(9), 1234-1239; (e) Weddle, K. S.; Aiken, J. D.; Finke, R. G. Rh(0) nanoclusters in benzene hydrogenation catalysis: Kinetic and mechanistic evidence that a putative $[(C_8H_{17})_3NCH_3]^+[RhCl_4]^-$ ion-pair catalyst is actually a distribution of Cl^- and $[(C_8H_{17})_3NCH_3]^+$ stabilized Rh(0) nanoclusters. *J. Am. Chem. Soc.*, **1998**, 120(23), 5653-5666; (f) James, B. R.; Wang, Y.; Alexander, C. S.; Hu, T. Catalytic hydrogenation of aromatic rings of lignin. *Chemical Industries T New York-Marcel Dekker*, **1998**, 233-242; (g) Bonilla, R. J.; James, B. R.; Jessop, P. G. Colloid-catalysed arene hydrogenation in aqueous/supercritical fluid biphasic media. *Chem. Commun.*, **2000**, 11(11), 941-942; (h) Roucoux, A.; Schulz, J.; Patin, H. Arene hydrogenation with a stabilised aqueous rhodium(0) suspension: A major effect of the surfactant counter-anion. *Adv. Synth. Catal.*, **2003**, 345(1-2), 222-229; (i) Park, K. H.; Jang, K.; Kim, H. J.; Son, S. U. Near-monodisperse tetrahedral rhodium nanoparticles on charcoal: The shape-dependent catalytic hydrogenation of arenes. *Angew. Chem.*, **2007**, 119(7), 1170-1173; (j) Zhou, K.; Li, Y. Catalysis based on nanocrystals with well-defined facets. *Angew. Chem. Int. Edit.*, **2012**, 51(3), 602-613.
- [167]. Januszkiewicz, K. R.; Alper, H. Exceedingly mild, selective and stereospecific phase-transfer-catalyzed hydrogenation of arenes. *Organometallics*, **1983**, 2(8), 1055-1057.
- [168]. Ibrahim, M.; Poreddy, R.; Philippot, K.; Riisager, A.; Garcia-Suarez, E. J. Chemoselective hydrogenation of arenes by PVP supported Rh nanoparticles. *Dalton T.*, **2016**, 45(48), 19368-19373.
- [169]. (a) Nindakova, L. O.; Badyrova, N. M.; Smirnov, V. V.; Kolesnikov, S. S. Asymmetric transfer hydrogenation of carbonyl compounds catalyzed by rhodium nanoparticles. *J. Mol. Catal. A Chem.*, **2016**, 420, 149-158; (b) Nindakova, L. O.; Badyrova, N. M.; Smirnov, V. V.; Strakhov, V. O.; Kolesnikov, S. S. Enantioselective hydrogen transfer hydrogenation on rhodium colloid systems with optically active stabilizers. *Russ. J. Gen. Chem.*, **2016**, 86(6), 1240-1249; (c) Jiang, H.; Cheng, H.; Bian, F. Heterogeneous enantioselective hydrogenation of aromatic ketones catalyzed by Rh nanoparticles immobilized in ionic liquid. *Catal. Lett.*, **2019**, 149(7), 1975-1982.
- [170]. (a) Velasquez, E.; Rieger, J.; Stoffelbach, F.; D'Agosto, F.; Lansalot, M.; Dufils, P.-E.; Vinas, J. Surfactant-free poly(vinylidene chloride) latexes via one-pot RAFT-

- mediated aqueous polymerization. *Polymer*, **2016**, 106, 275-284; (b) Tang, B.; Li, J.; Ren, Q.; Wang, C. Synthesis of poly(sodium styrene sulfonate)-b-poly(butyl acrylate) block copolymers via RAFT emulsifier-free emulsion polymerization and their application in PEDOT aqueous dispersions. *Synthetic Met.*, **2019**, 258, 116188.
- [171]. Gurnani, P.; Bray, C. P.; Richardson, R. A. E.; Peltier, R.; Perrier, S. Heparin-mimicking sulfonated polymer nanoparticles via RAFT polymerization-induced self-assembly. *Macromol. Rapid Comm.*, **2019**, 40(2), 1800314.
- [172]. Tyllianakis, M.; Dalas, E.; Christofidou, M.; Kallitsis, J.; Chrissanthopoulos, A.; Koutsoukos, P.; Bartzavali, C.; Gourdoupi, N.; Papadimitriou, K.; Oikonomou, E. Novel composites materials from functionalized polymers and silver coated titanium oxide capable for calcium phosphate induction, control of orthopedic biofilm infections: An “in vitro” study. *J. Mater. Sci. Mater. M.*, **2010**, 21(7), 2201-2211.
- [173]. Fan, Z.; Zhao, Y.; Preda, F.; Clacens, J.-M.; Shi, H.; Wang, L.; Feng, X.; De Campo, F. Preparation of bio-based surfactants from glycerol and dodecanol by direct etherification. *Green Chem.*, **2015**, 17(2), 882-892.
- [174]. Koromilas, N. D.; Lainioti, G. C.; Oikonomou, E. K.; Bokias, G.; Kallitsis, J. K. Synthesis and self-association in dilute aqueous solution of hydrophobically modified polycations and polyampholytes based on 4-vinylbenzyl chloride. *Eur. Polym. J.*, **2014**, 54, 39-51.
- [175]. Wang, X.; An, Q.; Zhao, Q.; Lee, K.; Qian, J.; Gao, C. Preparation and pervaporation characteristics of novel polyelectrolyte complex membranes containing dual anionic groups. *J. Membrane Sci.*, **2012**, 415-416, 145-152.
- [176]. Ran, F.; Wu, J.; Niu, X.; Li, D.; Nie, C.; Wang, R.; Zhao, W.; Zhang, W.; Chen, Y.; Zhao, C. A new approach for membrane modification based on electrochemically mediated living polymerization and self-assembly of N-tert-butyl amide- and β -cyclodextrin-involved macromolecules for blood purification. *Mater. Sci. Eng. C*, **2019**, 95, 122-133.
- [177]. Matsuoka, H.; Moriya, S.; Yusa, S.-i. Fundamental properties, self-assembling behavior, and their temperature and salt responsivity of ionic amphiphilic diblock copolymer having poly(N-isopropylacrylamide) in aqueous solution. *Colloid Polym. Sci.*, **2018**, 296(1), 77-88.
- [178]. (a) Yeole, N.; Hundiwale, D. Effect of hydrophilic macro-RAFT agent in surfactant-free emulsion polymerization. *Colloid Surface A*, **2011**, 392(1), 329-334; (b) Yeole, N.; Hundiwale, D.; Jana, T. Synthesis of core-shell polystyrene nanoparticles by surfactant free emulsion polymerization using macro-RAFT agent. *J. Colloid Interf. Sci.*, **2011**, 354(2), 506-510; (c) Yeole, N.; Hundiwale, D. Effect of varying hydrophobic monomers and their copolymerization in surfactant-free emulsion polymerizations using a macro-RAFT agent. *RSC Adv.*, **2013**, 3(44), 22213-22218; (d) Yeole, N.; Kutcherlapati, S. N. R.; Jana, T. Polystyrene-graphene oxide (GO) nanocomposite synthesized by interfacial interactions between RAFT modified GO and core-shell polymeric nanoparticles. *J. Colloid Interf. Sci.*, **2015**, 443, 137-142.
- [179]. Liu, Y.; Pollock, K. L.; Cavicchi, K. A. Synthesis of poly(trioctylammonium p-styrenesulfonate) homopolymers and block copolymers by RAFT polymerization. *Polymer*, **2009**, 50(26), 6212-6217.

- [180]. (a) Bouhadir, G.; Legrand, N.; Quiclet-Sire, B.; Zard, S. Z. A new practical synthesis of tertiary S-alkyl dithiocarbonates and related derivatives. *Tetrahedron Lett.*, **1999**, 40(2), 277-280; (b) Thang, S. H.; Chong, Y. K.; Mayadunne, R. T. A.; Moad, G.; Rizzardo, E. A novel synthesis of functional dithioesters, dithiocarbamates, xanthates and trithiocarbonates. *Tetrahedron Lett.*, **1999**, 40(12), 2435-2438.

Annexes

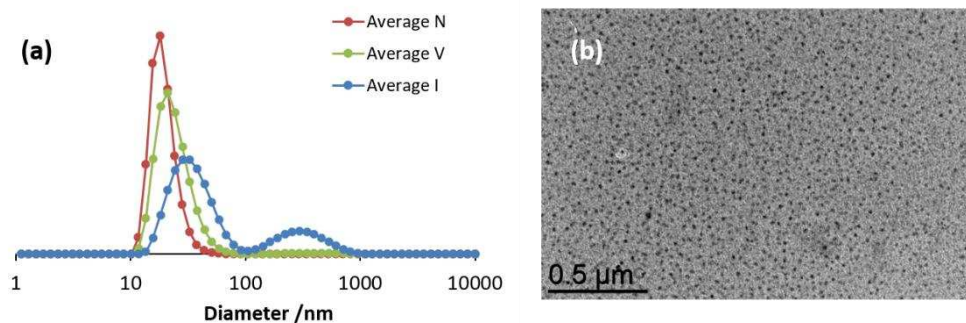


Figure A.0.1 (a) DLS in 75/25 (v/v) water/EtOH (unfiltered sample) and (b) TEM characterization of the R_0 -4VP₁₃₇-*b*-St₃₄₄-SC(S)SPr latex.

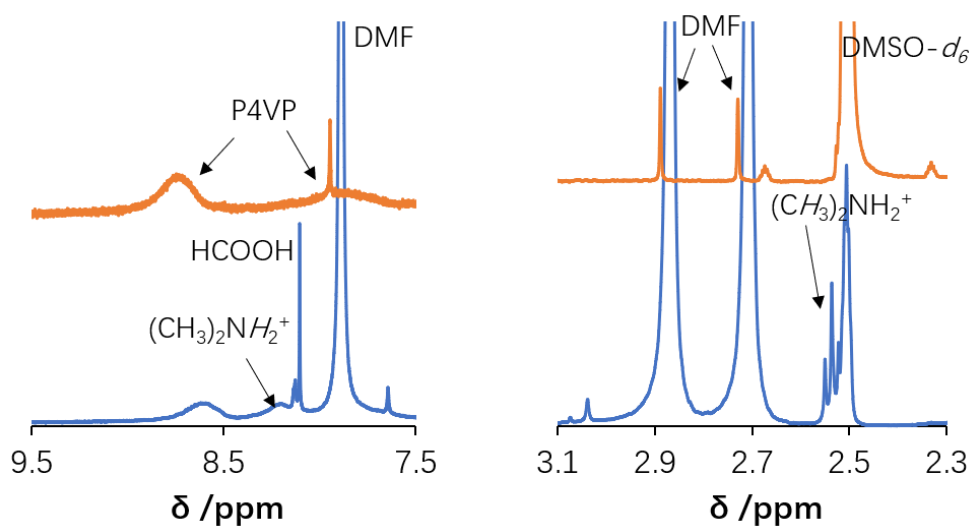


Figure A.0.2 Excerpt in selected regions of the ¹H NMR spectra in DMSO-*d*₆ of R_0 -(4VPMe⁺I)₁₃₇-*b*-St₃₄₄-SC(S)SPr. Below (blue): crude reaction mixture; above (orange): isolated polymer after washing with DMF (full spectrum in Figure A.0.3).

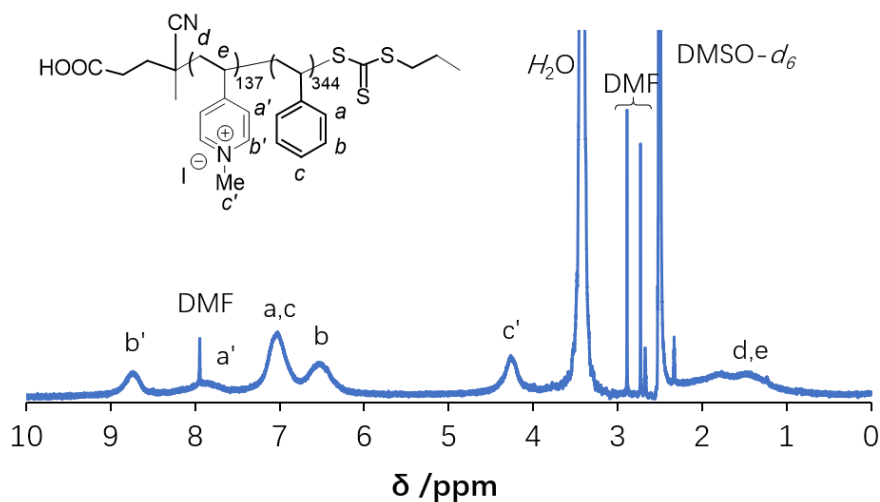


Figure A.0.3 ^1H NMR spectrum in $\text{DMSO-}d_6$ of $[\text{R}_0\text{-(4VPMe}^+\text{I)}_{137}\text{-}b\text{-St}_{344}\text{-SC(S)SPr}]\cdot 24(\text{DMF})$. Note that the PSt block is visible for this polymer in neat $\text{DMSO-}d_6$, presumably thanks to the presence of DMF, whereas it is not visible for the $\text{R}_0\text{-4VP}_{137}\text{-}b\text{-St}_{344}\text{-SC(S)SPr}$ precursor in a $\text{DMSO-}d_6/\text{EtOH}/\text{H}_2\text{O}$ mixture (Figure II.2.9b).

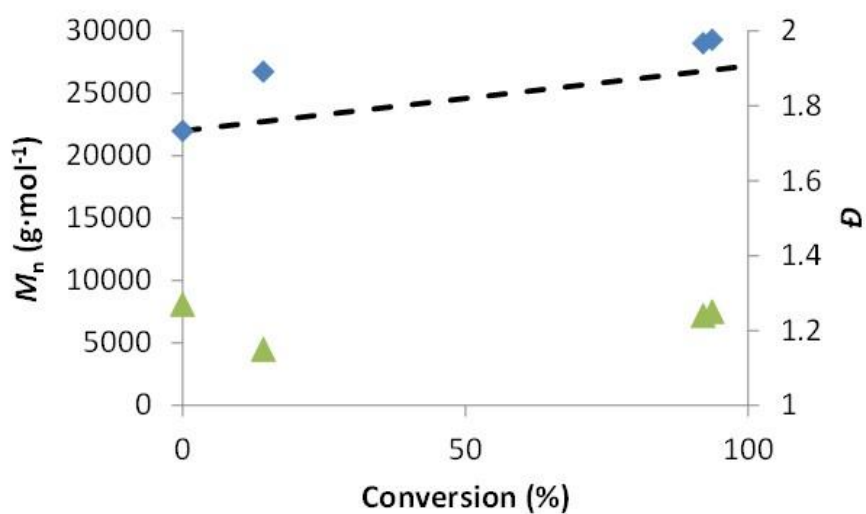


Figure A.0.4 Molar mass and dispersity as a function of conversion, from the SEC monitoring in DMF with 10 mM LiBr, for the chain extension of the $\text{R}_0\text{-4VP}_{137}\text{-SC(S)SPr}$ macroRAFT agent leading to $\text{R}_0\text{-4VP}_{137}\text{-}b\text{-St}_{48}\text{-SC(S)SPr}$.

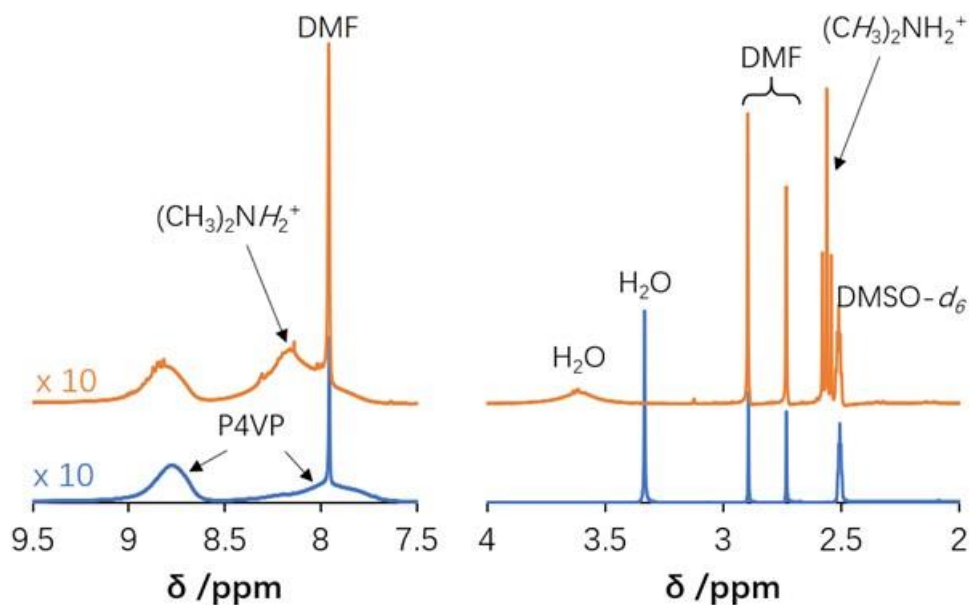


Figure A.0.5 Excerpt in selected regions of the ^1H NMR spectra in $\text{DMSO-}d_6$ of $\text{R}_0\text{-(4VPMe}^+\text{I)}_{137}\text{-}b\text{-St}_{48}\text{-SC(S)SPr}$. Above (orange): crude reaction mixture; below (blue): isolated polymer after washings with DMF and ether (full spectrum in Figure II.2.14). Note how the water resonance is displaced and broadened by the presence of Me_2NH_2^+ .

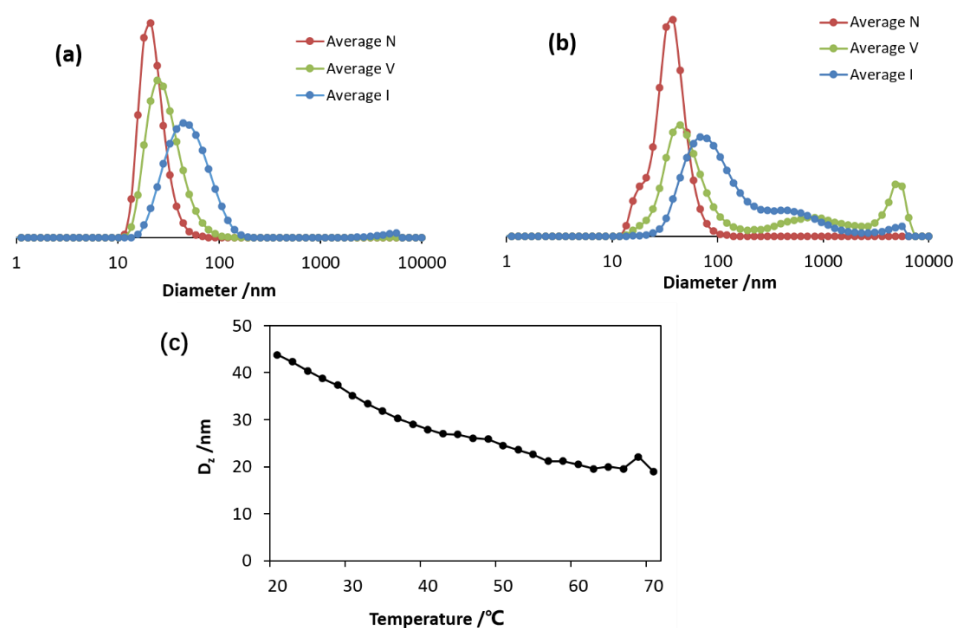


Figure A.0.6 DLS of $\text{R}_0\text{-(4VPMe}^+\text{I)}_{137}\text{-}b\text{-St}_{48}\text{-}b\text{-St}_{297}\text{-SC(S)SPr}$: (a) after freeze-drying and dispersion in DMSO at room temperature; (b) after heating for 24 h at $90\text{ }^\circ\text{C}$; (c) dependence of D_z on temperature.

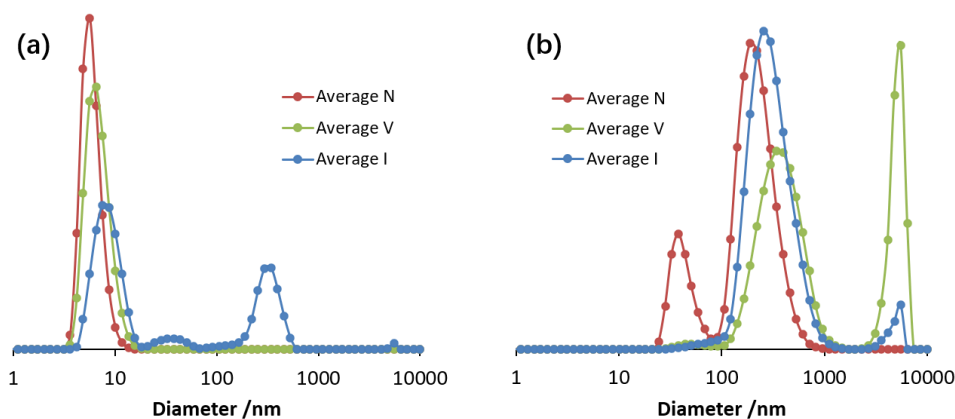


Figure A.0.7 (a) DLS of $R_0\text{-St}_{263}\text{-SC(S)SPr}$ in toluene and (b) DLS of $R_0\text{-(4VPMe}^+\text{I)}_{137}\text{-}b\text{-St}_{48}\text{-}b\text{-St}_{297}\text{-SC(S)SPr}$ after freeze-drying, dispersion in a DMSO/toluene 80/20 (v/v) mixture, and heating for 24 h at 90 °C ($D_z = 253.7$ nm, PDI = 0.36). Both samples were unfiltered.

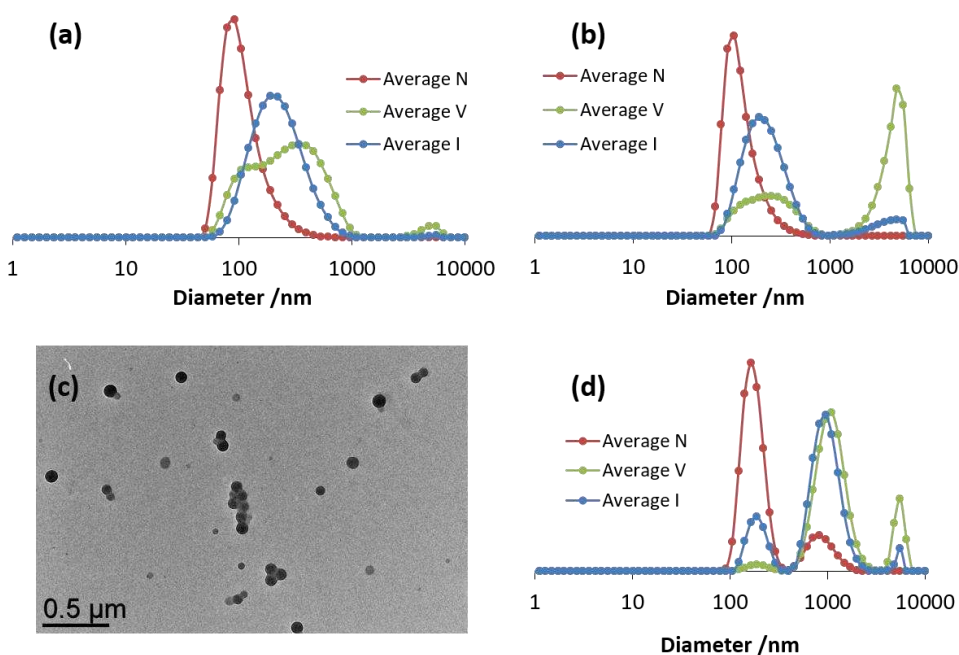


Figure A.0.8 DLS and TEM analyses of the $R_0\text{-(MAA}_{0.5}\text{-}co\text{-PEOMA}_{0.5})_{30}\text{-}b\text{-St}_{350}\text{-}b\text{-(St}_{0.9}\text{-}co\text{-DEGDMA}_{0.1})_{100}\text{-SC(S)SPr}$ CCM latex: (a) DLS ($D_z = 192.6$ nm, PDI = 0.21); (b) DLS after swelling with toluene ($D_z = 212.8$ nm, PDI = 0.30). Both samples were unfiltered; (c) TEM; (d) swollen with toluene and after heating for 24 h at 90 °C ($D_z = 890.4$ nm, PDI = 0.60).

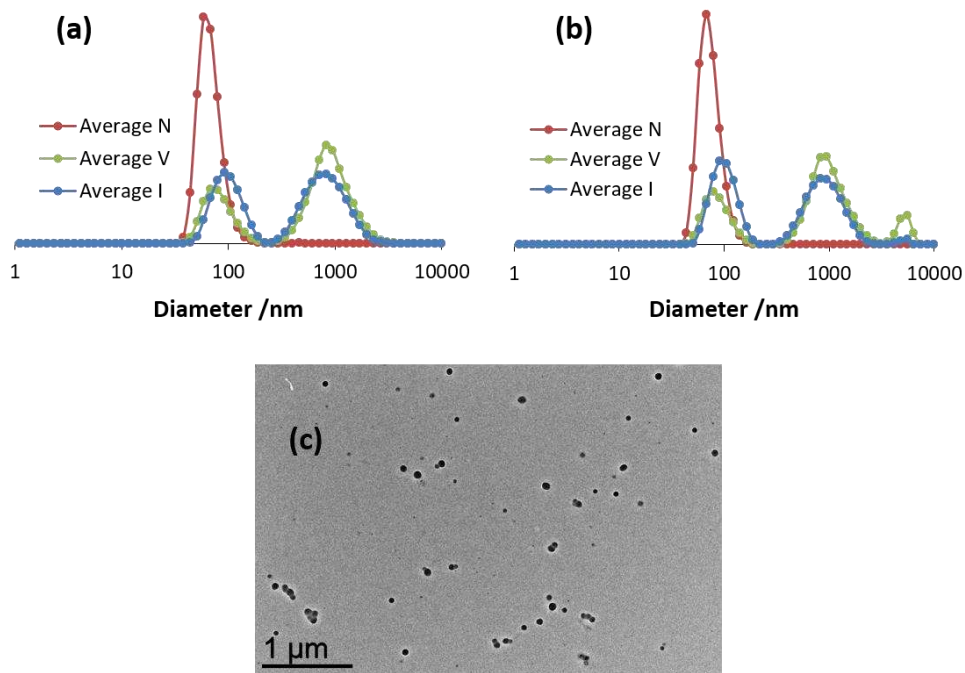


Figure A.0.9 DLS and TEM analyses of the R_0 -(MAA_{0.5}-*co*-PEOMA_{0.5})₃₀-*b*-(St₃₄₀-*co*-DEGDMA₁₀)-SC(S)SPr NG latex: (a) DLS ($D_z = 210.0$ nm, PDI = 0.55); (b) DLS after swelling with toluene ($D_z = 195.8$ nm, PDI = 0.66). Both samples were unfiltered; (c) TEM.

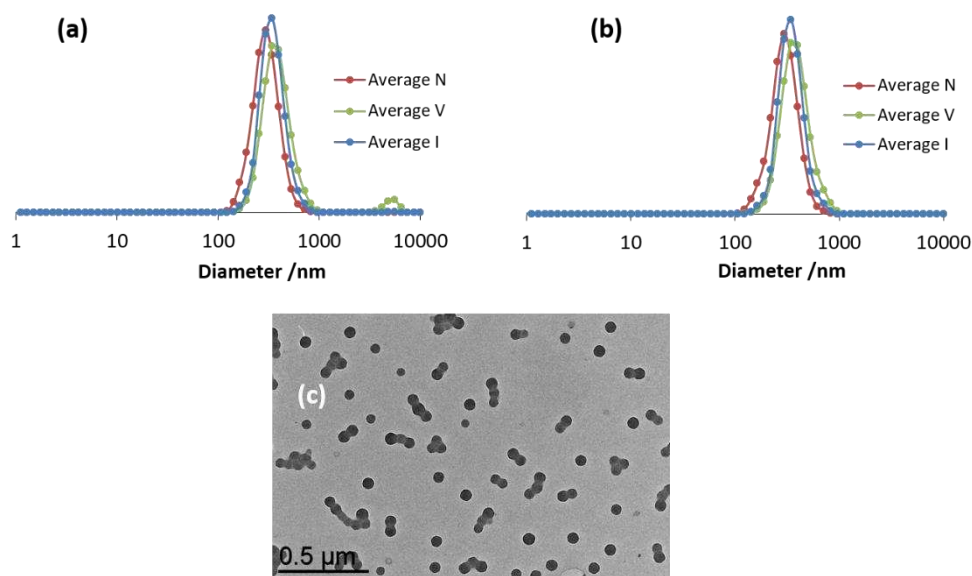


Figure A.0.10 DLS and TEM analyses of the R_0 -(MAA_{0.5}-*co*-PEOMA_{0.5})₃₀-*b*-(St_{0.1}-*co*-DPPS_{0.9})₃₀₀-*b*-(St_{0.9}-*co*-DEGDMA_{0.1})₁₀₀-SC(S)SPr CCM latex: (a) DLS ($D_z = 305.0$ nm, PDI = 0.10); (b) DLS after swelling with toluene ($D_z = 331.8$ nm, PDI = 0.08). Both samples were unfiltered; (c) TEM.

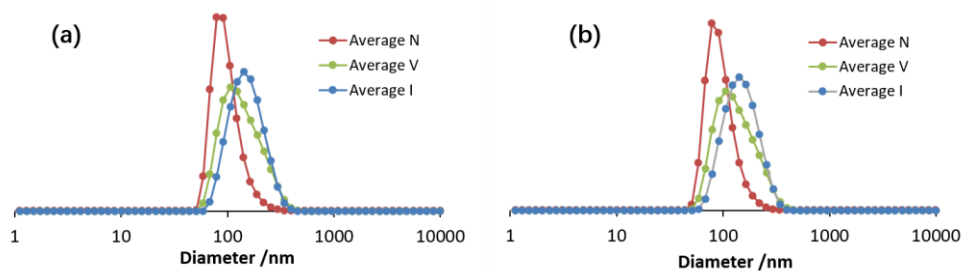


Figure A.0.11 DLS analysis of the $R_0-(4VPMe^+I)_{137}-b-St_{345}-SC(S)SPR$ latex used for the crosslinking with pure DEGDMA: (a) Before addition of DEGDMA and (b) After addition of DEGDMA. All measurements were carried out on unfiltered samples.

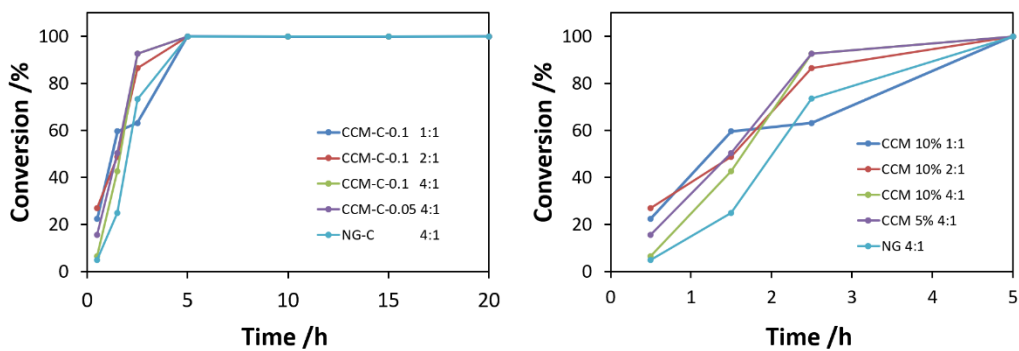


Figure A.0.12 Graphic representation of the data in Table III.3.1.